



UNIVERSITY OF  
LIVERPOOL

TOWARDS AN UNDERSTANDING OF HOW HIP  
MUSCULATURE MODIFIES FALL-RELATED STRESS  
PATTERNS IN THE AGEING FEMUR: A COMPUTER  
SIMULATION APPROACH

---

Thesis submitted in accordance with the requirements of the University of  
Liverpool for the degree of Doctor of Philosophy.

By

David P. Collins

September 2017

## ACKNOWLEDGEMENTS

---

I would like to thank my supervisors Professor Robin Crompton, Dr Karl Bates, Professor Richard Eastell and Dr Lang Yang for giving me the opportunity to study such a fascinating project across two universities and offering me guidance and support throughout. In particular I would like to thank Robin and Karl: Robin for your continued support, brilliant insights, kindness in the difficult times and the time spent helping me to complete this thesis, and Karl for your continued investment of time (despite having none for yourself), putting up with my unnecessarily long emails, words of motivation and all your help in getting me to this point. You're truly one of the good guys. I'd also like to thank Richard for welcoming me into the AUBM lab group in Sheffield and Lang for versing me in the Matlab dark arts. I'm incredibly grateful to everyone in the gait lab, especially the late Russ Savage whose bright mind underpinned much of the work we've undertaken as a group, but also Kris, Ali, Rory and Lyn – your cheeriness always made work that little bit better.

Thanks must also go to those within the CIMA community, notably Louise, for her continued patience despite my many last minute requests and aptitude for missing deadlines but also to the friends I've made along the way and to my other CIMA colleagues who have provided me with a fantastic research environment. I must also give thanks to those in HARC, especially Lyn and Neil, who both gave up their time to help me meet my research goals. To Paul, Paul and Matt, you've been both pillars of support when I've needed it and also led me astray. For both of those things, thank you. To Ewy who I met on day one, it's been a pleasure and long may the cakes continue. And of course, to Rach (and the rest of the Ghadiali clan), who I also met on day one, you've been my rock and I'm eternally grateful for the encouragement, scrambled eggs and massive amounts of self-belief you've given me.

Finally, I would like to say a huge thank you to my family. Even when it's been difficult, you've gone above and beyond in supporting me and pushing me towards my goals. Without that (and little Willow's smile), I wouldn't have got to this point.

Thank you to you all.

## ABSTRACT

---

Hip fracture is one of the most severe complications of falls in older people and is considered a major public health issue. Current clinical assessment tools for hip fracture include measurements of bone mineral density (BMD) via dual energy x-ray absorptiometry (DEXA). Decreased BMD is associated with decreased bone strength and thus increased fracture risk. However, BMD is insufficient for predicting fracture risk and many individuals who suffer fracture are considered to have normal, healthy values of BMD.

Subject-specific finite element (FE) models constructed from patient computed-tomography (CT) scans offer an alternative approach for assessing bone strength and fracture risk. Finite element analysis (FEA) is an increasingly mature technique that shows improved performance in the prediction of fracture risk compared to assessments of BMD. Nonetheless there are still inconsistencies between experimental results and those obtained through FEA.

This thesis explores the effect of concurrent, sideways fall-related impact and hip muscle forces on femoral neck stresses in orthotropic FE models of the ageing femur. This is achieved by integrating data from the following three independent, computational methods: 1) three-dimensional micro-computed tomography imaging and analysis to determine structural anisotropy of older peoples' femoral trabecular bone, 2) multibody dynamic analysis (MDA) to determine a range of potential impact and muscle forces resulting from sideways falls and 3) FEA to determine stress patterns within orthotropic FE models (constructed using data obtained using method 1) of the ageing proximal femora as a result of impact and muscle forces (derived from method 2).

The results from this thesis demonstrate that 1) the architectural arrangement of trabecular bone in the head and neck regions of the ageing proximal femur is region specific but that there exists a high degree of inter-specimen similarity for each of these regions, 2) impact and, in particular, muscle forces at impact are heterogeneous in nature and finally, despite this heterogeneity, 3) impact forces from sideways falls consistently produce highest stresses in the superior femoral neck while contraction of hip muscle forces concurrent with an impact force act to increase femoral neck stress magnitudes resulting from a sideways-fall impact and create principal stress trajectories that are sub-optimally aligned with cortical and trabecular bone principal fabric directions. These findings have relevance for future work, particularly FEA, seeking to investigate the aetiology of and predict hip fracture.

# TABLE OF CONTENTS

---

|   |    |
|---|----|
| Towards an Understanding of How Hip Musculature Modifies Fall-Related Stress Patterns in the Ageing Femur: A Computer Simulation Approach ..... | 1  |
| Acknowledgements.....   | 2  |
| Abstract.....   | 3  |
| List of Figures .....   | 9  |
| 1 Introduction .....  | 11 |
| 1.1 Summary .....   | 11 |
| 1.2 Falls in Older People .....   | 12 |
| 1.3 Hip Fracture .....  | 12 |
| 1.3.1 Hip Fracture Statistics .....   | 12 |
| 1.3.2 Hip Fracture Types .....  | 13 |
| 1.3.3 Hip Fracture Risk Factors .....   | 14 |
| 1.4 Identification and Diagnosis of Individuals at Risk of Hip Fracture .....   | 16 |
| 1.4.1 Tools for Assessing Fracture Risk – DEXA.....   | 17 |
| 1.4.2 Tools for Assessing Fracture Risk – FRAX.....   | 17 |
| 1.4.3 Tools for Assessing Fracture Risk – Computational Methods.....  | 18 |
| 1.5 Thesis Aims and Objectives.....   | 20 |
| 1.5.1 Aims.....   | 21 |
| 1.5.2 Objectives.....   | 21 |
| 1.6 Thesis Outline.....   | 22 |
| 1.6.1 Chapter 2.....  | 22 |
| 1.6.2 Chapter 3.....  | 22 |
| 1.6.3 Chapter 4.....  | 22 |
| 1.6.4 Chapter 5.....  | 23 |
| 1.6.5 Chapter 6.....  | 23 |
| 1.6.6 Chapter 7.....  | 23 |
| 2 Anatomical and Biomechanical Background.....  | 24 |
| 2.1 Human Bone .....  | 24 |
| 2.1.1 The Structural Organisation of Human Bone .....   | 24 |
| 2.1.2 Hierarchical Structure of Bone .....  | 24 |
| 2.1.3 Trabecular Bone .....   | 24 |
| 2.1.4 Cortical Bone .....   | 25 |
| 2.2 Biomechanics of Trabecular and Cortical .....   | 26 |
| 2.3 Bone .....  | 26 |

|       |   |    |
|-------|---|----|
| 2.3.1 | Stress.....   | 26 |
| 2.3.2 | Strain .....  | 27 |
| 2.3.3 | Bone Elastic Constants .....  | 27 |
| 2.3.4 | Directional Dependence of Linear Elasticity .....   | 29 |
| 2.3.5 | The Material Complexity of Bone .....   | 31 |
| 2.3.6 | The Relationship between Trabecular Bone Structural and Linear Elastic Properties.....  | 31 |
| 2.3.7 | The Relationship between Cortical Bone Structural and Linear Elastic Properties.....  | 32 |
| 2.3.8 | Other Properties of Cortical and Trabecular Bone .....  | 33 |
| 2.3.9 | The Relationship between Bone Elastic Constants and Bone Density.....   | 34 |
| 2.4   | Human Skeletal Muscle.....  | 34 |
| 2.4.1 | The Hierarchical Structure of Skeletal Muscle.....  | 35 |
| 2.4.2 | Muscle Strength .....   | 36 |
| 2.4.3 | Tendons.....  | 39 |
| 2.5   | Musculoskeletal Anatomy of the Hip Joint.....   | 40 |
| 2.5.1 | Hip Bones .....   | 41 |
| 2.5.2 | Hip Musculature.....  | 42 |
| 2.5.3 | Hip Musculature – Biomechanical Significance .....  | 43 |
| 3     | <i>Literature Review</i> .....  | 45 |
| 3.1   | $\mu$ CT .....  | 45 |
| 3.1.1 | Aims: .....   | 50 |
| 3.1.2 | Objectives:.....  | 50 |
| 3.2   | MDA .....   | 50 |
| 3.2.1 | Aims: .....   | 54 |
| 3.2.2 | Objectives:.....  | 55 |
| 3.3   | FEA .....   | 55 |
| 3.3.1 | Aims: .....   | 60 |
| 3.3.2 | Objectives:.....  | 60 |
| 4     | Determining the Anisotropy and Bone Volume Fraction of Trabecular Bone in the Ageing Proximal Femur Using Micro-Computed Tomography ..... | 62 |
| 4.1   | Introduction .....  | 62 |
| 4.2   | Methods.....  | 63 |
| 4.2.1 | Study Sample.....   | 63 |
| 4.2.2 | $\mu$ CT Scanning.....  | 64 |
| 4.2.3 | Splitting of $\mu$ CT Scans into Cubes.....   | 64 |

|        |  |     |
|--------|--|-----|
| 4.2.4  | Trabecular Bone Parameters .....   | 66  |
| 4.2.5  | Calculating Trabecular Architectural Anisotropy Using the MIL Method .....                                     | 66  |
| 4.2.6  | Calculating Bone Volume Fraction .....   | 71  |
| 4.2.7  | Plotting Trabecular Orientations.....  | 71  |
| 4.2.8  | Analysis of Trabecular Orientations.....   | 73  |
| 4.2.9  | Defining Femoral Neck Axis .....   | 74  |
| 4.2.10 | Combining Approaches .....   | 75  |
| 4.2.11 | Statistical Analysis.....  | 75  |
| 4.3    | RESULTS.....   | 76  |
| 4.3.1  | Validation .....   | 76  |
| 4.3.2  | Trabecular Orientations in the Femoral Head .....  | 78  |
| 4.3.3  | Trabecular Orientations in the Inferior Femoral Neck.....  | 82  |
| 4.3.4  | Trabecular Orientations in the Superior Femoral Neck.....  | 85  |
| 4.4    | Discussion.....  | 88  |
| 4.5    | Limitations.....   | 94  |
| 4.6    | Conclusions .....  | 95  |
| 5      | Using Multibody Dynamic Analysis to Model and Predict Sideways Fall-Related Hip Muscle and Impact Forces ..... | 96  |
| 5.1    | INTRODUCTION.....  | 96  |
| 5.2    | METHODS.....   | 97  |
| 5.2.1  | Simulations.....   | 98  |
| 5.2.2  | Forwards Dynamics.....   | 98  |
| 5.2.3  | Genetic Algorithm Optimisation .....   | 100 |
| 5.2.4  | Kinematic Data Collection.....   | 101 |
| 5.2.5  | Musculoskeletal Model.....   | 104 |
| 5.2.6  | Simulation Protocol.....   | 110 |
| 5.2.7  | Parameters Quantified.....   | 114 |
| 5.2.8  | Statistical Analysis.....  | 115 |
| 5.3    | RESULTS.....   | 116 |
| 5.3.1  | Kinematic Data .....   | 116 |
| 5.3.2  | Musculoskeletal Model.....   | 118 |
| 5.3.3  | Impact Forces.....   | 119 |
| 5.3.4  | Muscle Forces .....  | 125 |
| 5.3.5  | Tendon Length Changes.....   | 131 |
| 5.4    | DISCUSSION.....  | 131 |
| 5.5    | Limitations.....   | 135 |

|        |  |     |
|--------|--|-----|
| 5.5.1  | Falls .....  | 135 |
| 5.5.2  | Musculoskeletal Model.....   | 136 |
| 5.5.3  | Simulation Protocol.....   | 137 |
| 5.6    | Conclusion.....  | 137 |
| 6      | The Effect of Hip Musculature and Fall Configuration on Stress Patterns in Orthotropic Finite Element Models of the Ageing Proximal Femur: Implications for Risk of Femoral Neck Fracture..... | 139 |
| 6.1    | Introduction .....   | 139 |
| 6.2    | Methods.....   | 141 |
| 6.2.1  | Subject Specific FE Model Construction.....  | 141 |
| 6.2.2  | Segmentation of $\mu$ CT Scans.....  | 141 |
| 6.2.3  | Creation and Optimisation of Surface Meshes .....  | 147 |
| 6.2.4  | Non-Manifold Assembly Creation.....  | 148 |
| 6.2.5  | Generation of the finite element models .....  | 149 |
| 6.2.6  | Material Property Assignment.....  | 151 |
| 6.2.7  | Muscle-Tendon Units .....  | 161 |
| 6.2.8  | Impact Forces .....  | 169 |
| 6.2.9  | Finite Element Simulations .....   | 171 |
| 6.2.10 | Boundary Conditions – Femoral Models.....  | 172 |
| 6.2.11 | Boundary Conditions – Spring Elements.....   | 172 |
| 6.2.12 | Analysis .....   | 173 |
| 6.3    | Results.....   | 173 |
| 6.3.1  | Creation of Fully Orthotropic FE models.....   | 173 |
| 6.3.2  | FE Simulations – General Remarks.....  | 174 |
| 6.3.3  | Impact-Only Simulations.....   | 175 |
| 6.3.4  | Muscle-Only Simulations .....  | 179 |
| 6.3.5  | Impact plus Muscle Force Simulations.....  | 183 |
| 6.4    | Discussion.....  | 189 |
| 6.4.1  | Material and Structural Properties .....   | 189 |
| 6.4.2  | Impact-Only Simulations.....   | 191 |
| 6.4.3  | Muscle-Only Simulations .....  | 194 |
| 6.4.4  | Combined Muscle and Impact Simulations.....  | 195 |
| 6.5    | Limitations.....   | 198 |
| 6.5.1  | Experimental Validation.....   | 198 |
| 6.5.2  | Cortical Bone Density .....  | 198 |
| 6.5.3  | Muscle and Impact Loads.....   | 199 |

|       |                         |     |
|-------|-------------------------|-----|
| 6.5.4 | Insertion Sites.....    | 199 |
| 6.5.5 | MTU Properties.....     | 200 |
| 6.6   | Conclusion.....         | 200 |
| 7     | Concluding Remarks..... | 202 |
|       | References .....        | 208 |
|       | Appendix A.....         | 231 |
|       | Appendix B .....        | 232 |
|       | Appendix C .....        | 244 |
|       | Appendix D.....         | 245 |
|       | Appendix E1 .....       | 277 |
|       | Appendix E2 .....       | 278 |
|       | Appendix F .....        | 279 |
|       | Appendix G .....        | 280 |
|       | Appendix H.....         | 282 |
|       | Appendix I .....        | 284 |

## LIST OF FIGURES

---

|  |     |
|--|-----|
| Figure 1.1 Hip fracture types.....   | 14  |
| Figure 2.1 Hierarchical structure of trabecular bone .....                         | 25  |
| Figure 2.2 Hierarchical structure of cortical bone .....                           | 25  |
| Figure 4.1 Virtual splitting of $\mu$ CT scans into cubes .....                    | 65  |
| Figure 4.2 Bone boundaries .....   | 65  |
| Figure 4.3 MIL method .....  | 66  |
| Figure 4.4 Binarisation of trabecular cubes.....                                   | 67  |
| Figure 4.5 MIL point cloud.....  | 70  |
| Figure 4.6 3D plot of trabecular orthotropic directions .....                      | 72  |
| Figure 4.7 Slice plot of trabecular directions.....                                | 73  |
| Figure 4.8 Comparison of actual and modelled trabecular directions.....            | 77  |
| Figure 4.9 Slice plot comparison of actual and modelled trabecular directions..... | 77  |
| Figure 4.10 Kruskal-Wallis box plot for femoral head angular data.....             | 79  |
| Figure 4.11 Eigenvector paired plots.....  | 81  |
| Figure 4.12 Canonical analysis of eigenvectors .....                               | 81  |
| Figure 4.14 MANOVA dendrogram plot - eigenvectors, inferior femoral neck .....     | 84  |
| Figure 4.15 Scheffe's procedure - superior femoral neck.....                       | 86  |
| Figure 4.16 MANOVA dendrogram plot - eigenvectors, superior femoral neck.....      | 87  |
| Figure 5.1 Kinematic data collection .....   | 103 |
| Figure 5.2 The musculoskeletal model .....   | 104 |
| Figure 5.3 Hill-type muscle model .....  | 106 |
| Figure 5.4 Geoms. ....   | 107 |
| Figure 5.6 Static match.....   | 112 |
| Figure 5.7 Paired plots of linear velocity components .....                        | 117 |
| Figure 5.8 MANOVA dendrogram plot for linear velocities of real-world falls. ....  | 118 |
| Figure 5.9 Successful falls.....   | 118 |
| Figure 5.10 Mean impact forces.....  | 119 |
| Figure 5.11 Average impact force component contributions.....                      | 120 |
| Figure 5.12 Average percentage impact force component contributions.....           | 120 |
| Figure 5.13 Absolute component contributions.....                                  | 121 |
| Figure 5.14 Brown-Forsythe - impact force magnitudes. ....                         | 122 |
| Figure 5.15 Scheffe's procedure - impact force magnitudes.....                     | 123 |
| Figure 5.16 Paired plots of impact force components. ....                          | 124 |
| Figure 5.17 MANOVA dendrogram - impact force components .....                      | 124 |
| Figure 5.18 Kendall tau matrix plot - gluteus maximus.....                         | 128 |
| Figure 5.19 Kendall tau matrix plot - iliopsoas.....                               | 129 |
| Figure 5.20 Scheffe's procedure - iliopsoas.....                                   | 130 |
| Figure 5.21 Kendall tau matrix plot - all muscles.....                             | 130 |
| Figure 6.1 Bone masks.....   | 141 |
| Figure 6.2 Whole bone mask.....  | 143 |
| Figure 6.3 Cortical mask creation .....  | 144 |
| Figure 6.4 Three-dimensional cortical shell.....                                   | 144 |
| Figure 6.5 Trabecular mask. ....   | 146 |
| Figure 6.6 Surface mesh .....  | 147 |
| Figure 6.7 Non-manifold assembly.....  | 149 |

|  |            |
|--|------------|
| Figure 6.8 Finite element mesh.....  | 150        |
| Figure 6.9 Cortical bone material property assignment.....                   | 153        |
| Figure 6.10 FE model cortical bone orthotropy.....                           | 156        |
| Figure 5.11 Trabecular bone material property assignment.....                | 158        |
| Figure 6.12 Cube plot.....   | 159        |
| Figure 6.13 FE cubic regions.....  | 160        |
| Figure 6.14 Trabecular material orientations.....                            | 161        |
| Figure 6.15 Muscle-tendon unit origins.....                                  | 162        |
| <b>Figure 6.16 Femoral head centre.....</b>                                  | <b>163</b> |
| Figure 6.17 Muscle insertion.....  | 164        |
| Figure 6.18 Spring elements.....   | 165        |
| Figure 6.19 Muscle-tendon unit lines of action.....                          | 166        |
| Figure 6.20 Muscle force vectors.....  | 168        |
| Figure 6.21 Continuum distributing coupling constraints.....                 | 169        |
| Figure 6.22 Impact forces.....   | 170        |
| Figure 6.23 Coordinate System.....   | 174        |
| Figure 6.24 VM stress plot.....  | 175        |
| Figure 6.25 Principal stress plots – impact forces.....                      | 176        |
| Figure 6.26 Principal stress plots – impact forces.....                      | 177        |
| Figure 6.27 Principal stress plots – impact forces.....                      | 178        |
| Figure 6.28 Principal stress directions – impact forces.....                 | 179        |
| Figure 6.30 VM stress plot – muscle forces.....                              | 181        |
| Figure 6.31 Principal stress plots – muscle forces.....                      | 181        |
| Figure 6.32 Principal stress directions – muscle forces.....                 | 182        |
| Figure 6.33 VM stress plot – impact plus muscle.....                         | 183        |
| Figure 6.34 Principal stress plots – impact plus muscle.....                 | 184        |
| Figure 6.35 Compressive principal stress increases - impact plus muscle..... | 185        |
| Figure 6.36 Tensile principal stress increases - impact plus muscle.....     | 185        |
| Figure 6.37 Compressive stress distributions - impact plus muscle.....       | 186        |
| Figure 6.38 Tensile stress distributions - impact plus muscle.....           | 187        |
| Figure 6.39 Principal stress directions – impact plus muscle.....            | 188        |
| Figure 6.40 Principal stress comparison - all.....                           | 189        |
| Figure 6.41 Resultant impact forces at the hip.....                          | 192        |
| Figure 6.42 Thin cortex at the superior femoral neck.....                    | 192        |

# 1 INTRODUCTION

---

## 1.1 SUMMARY

Hip fracture is a significant problem within the ageing population. During ageing skeletal muscle and bone become weaker due to age-related biological processes. This leads to lack of independence, an increased risk of mortality and frailty. One of the consequences of frailty is an increased risk and occurrence of falls, which within ageing populations, often leads to hip fracture. The prognosis for hip fracture is poor in terms of quality and length of life and consequently there is a considerable amount of research focused on understanding, predicting and preventing its occurrence. Computational and numerical methods in particular have proved powerful tools for modelling hip fracture to help predict its occurrence and understand its aetiology. Nonetheless, there are still discrepancies between experimental and real-world outcomes vs. results obtained via these computational and numerical modelling techniques. This discrepancy may reflect the fact that the loading conditions to which the ageing femur is subject during a fall, as well as its material properties, are simplified during the modelling process. Using a suite of computational and numerical techniques this thesis aims to address these issues and act as an exploratory analysis into the underlying mechanisms contributing to hip fracture risk.

## 1.2 FALLS IN OLDER PEOPLE

A main consequence of frailty in older people is falls and for these individuals, falls are a leading cause of death and disability (Stevens *et al.*, 1999). The number of falls is expected to grow; numerous studies across developing countries show statistically significant annual increases in rates of fall-related deaths and injuries in older adults (Kannus *et al.*, 2005; Stinchcombe, Kuran and Powell, 2014).

When falls do not result in fatality, they are often accompanied by injuries requiring medical attention or hospitalisation (Alamgir, Muazzam and Nasrullah, 2012). Out of a reported 1.5 million falls in older people (+75 years) in the USA in 2007, 400,000 of these required hospitalisation (Siracuse *et al.*, 2012). Similarly, according to the Centres for Disease Control and Prevention in the US, the preceding year saw 2.1 million emergency department admissions as a result of fall incidents in older people with 560,000 of these patients requiring further hospitalisation (Center for Disease Control, 2015).

And in the UK, a third of over 65's and a half of over 80's fall at least once a year (NICE, 2013). Falls are the most common cause of death from injury in the over 65's and cost the NHS £2 billion and four million bed days annually (Tian *et al.*, 2013). The wider UK economy also incurs significant indirect costs due to work absence and associated carer time (Darnell, Mason and Snooks, 2012). Hip fractures comprise one of the most common serious types of fall-related injury (Kannus and Parkkari, 2006).

## 1.3 HIP FRACTURE

### 1.3.1 Hip Fracture Statistics

Annually, major morbidity from falls includes 1.6 million hip fractures world-wide (Johnell and Kanis, 2006). It is predicted that by 2050, hip fractures globally could total between 4.5 – 6.3 million each year (Cooper, Campion and Melton, 1992; Gullberg, Johnell and Kanis, 1997). Furthermore, for certain geographical regions such as Latin America, hip fracture is predicted to rise by a staggering 400 – 700% in men and women (Cooper, Campion and Melton, 1992). And in the UK alone, hip fractures are estimated to cost the NHS over £1 billion (Svedbom *et al.*, 2013). These costs are expected to rise by as much as 24% in the next 10 years (Svedbom *et al.*, 2013).

Perhaps more important than the socioeconomic costs, is the cost to the individual in terms of quality and length of life following hip fracture. Complications arising from hip fracture mean that 20-24% of individuals die within a year of the initial fracture and remain at a greater risk of death for the following five years (Cooper *et al.*, 1993; Magaziner *et al.*, 1997; Leibson *et al.*, 2002; Haentjens *et al.*, 2010). In the European Union (EU) in 2010, a total estimated 26,300 life years were lost due to incident fractures (Hernlund *et al.*, 2013). Given that around 50% of all fracture related deaths are attributed to hip fractures in both men (47%) and women (50%) (Hernlund *et al.*, 2013), it could be assumed that approximately 13,000 life years were lost to hip fracture in the EU alone, in a single year.

Those who go on to survive hip fracture can still face profound difficulties in later life. Less than half of those who survive regain their previous level of function and suffer either lifelong minor or major impairments (Magaziner *et al.*, 1990). Indeed, 33% of hip fracture patients become totally dependent or reside in a nursing home in the first year following fracture (Riggs and Melton, 1995; Leibson *et al.*, 2002; Johnell and Kanis, 2005) whilst 10 – 20% of formerly community-dwelling patients require long term nursing care (Autier *et al.*, 2000; Cree *et al.*, 2000; Kiebzak *et al.*, 2002). Additionally, 40% of hip fracture survivors lose the ability to walk independently and 60% still require assistance over a year later (Magaziner *et al.*, 1990). Although total rates of hip fracture are lower in men (25%) than women (75%) (Cooper, Campion and Melton, 1992; Becker and Ogon, 2008), resulting morbidity and loss of normal functioning are often experienced to a more significant degree in males with men also experience higher rates of fracture related mortality (Center *et al.*, 1999).

### **1.3.2 Hip Fracture Types**

Hip fractures are categorised by type. The type of fracture is usually defined by the anatomical location in which it occurs. There are three types of hip fracture that are generally described in the literature – femoral neck, trochanteric and subtrochanteric (Haentjens *et al.*, 2007) – all of which occur in the proximal femur (figure 1.1).

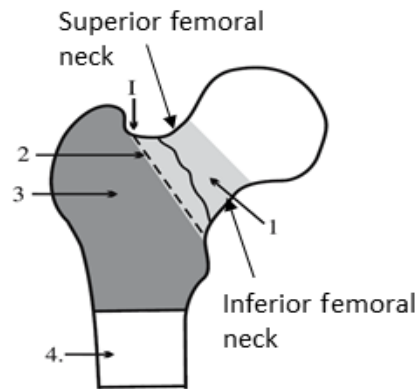


**Figure 1.1 Hip fracture types.** 1. The boundary between the femoral neck and trochanteric region. 1. Region for femoral neck fractures. 2 & 3. Region for trochanteric fractures. 4. Region for subtrochanteric fractures. Superior and inferior portions of the femoral neck are also defined (Adapted from Manninger *et al.*, [2007]).

### 1.3.3 Hip Fracture Risk Factors

Although the specific combinations of risk factors associated with each of these fracture types differs (Pulkkinen *et al.*, 2006; Cauley *et al.*, 2009; Jokinen *et al.*, 2010), there appear to be common risk factors associated with all types of hip fracture, a number of which have been identified by Marks, (2010). Of particular relevance to this thesis are falls and bone-related risk factors. These are briefly discussed below.

#### 1.3.3.1 Falls

Hip fractures make up only a small proportion of fall-related fractures (1 – 2%) but they are almost exclusively caused by falls (Greenspan *et al.*, 1994; Hayes *et al.*, 1996; Jarvinen *et al.*, 2008). Indeed, approximately 90% of all hip fractures are caused by a fall (Grisso *et al.*, 1991). Despite their proportionately small incidence rate amongst fallers hip fractures are undoubtedly amongst the more serious in terms of socioeconomic costs to national economies and prognosis for the individual

#### 1.3.3.2 Bone-related risk factors

##### 1.3.3.2.1 Bone Mineral Density

Increasing age is often accompanied by decreasing bone mineral density (BMD). BMD is correlated to bone strength and as a result, it is often used to determine an individual's chance

of sustaining a hip fracture. The World Health Organisation (WHO) approaches the issue of bone strength from the perspective of BMD and defines osteoporosis as a metabolic bone disease resulting in a BMD 2.5 standard deviations below the population norm for a given anatomical region, such as the femur (World Health Organization, 2004). There is therefore an implicit assumption when using this definition that BMD is directly related to bone strength: the higher the BMD, the stronger a bone is and vice versa.

However, studies have been inconsistent in showing that low BMD necessarily confers a greater risk of hip fracture. The prevalence of hip fracture incidence in older individuals with and without osteoporosis supports this notion well, with many of those who suffer a fall-related hip fracture in old age are falling outside of the osteoporotic range of BMD values (Wickham *et al.*, 1989; Cumming, 1997; Cummings and Melton, 2002). In other words, these individuals are often older people but are, based on BMD, only at low to moderate risk of fracture. Additionally, Asian populations have a lower incidence of hip fracture compared to Caucasians, despite having similar or lower BMD (Yan *et al.*, 1999).

Taking these findings into account and the fact that BMD often occurs alongside other risk factors such as reduced functional mobility (Wei *et al.*, 2001), it is difficult to conclude BMD is an independent, *de facto* risk factor for hip fracture. There appears to be increasing recognition of this with some organisations like The National Institutes of Health Consensus Development Panel on Osteoporosis Prevention, Diagnosis and Therapy now defining diseases adversely affecting BMD such as osteoporosis merely as a skeletal disorder characterized by low bone strength and increased risk of fracture (NIH, 2001).

#### 1.3.3.2.2 Bone Geometry and Structure

The cortex of the femoral neck exhibits significant thinning with increasing age, even when BMD within the neck region is maintained (Ito *et al.*, 2011; Lee *et al.*, 2012). This region also experiences high loads during a fall-induced impact (Lotz, Cheal and Hayes, 1995; Mayhew *et al.*, 2005). Taking these factors together has led some researchers to conclude the superior femoral neck (figure 1.1), is implicated in a higher risk of fracture (Mayhew *et al.*, 2005). Cortical porosity also increases with age and is thought to be a major determinant of bone strength (Malo *et al.*, 2013); increases in porosity ultimately results in weaker bone and thus an enhanced risk of hip fracture.

Trabecular bone also undergoes microstructural deterioration with ageing (Ito *et al.*, 2011; Milovanovic, Potocnik, *et al.*, 2012; Huayue Chen *et al.*, 2013). This deterioration is expressed as decreased bone volume fraction (a measure of the ratio of bone per total unit volume of a specimen), trabecular thinning, reduced connectivity between individual trabeculae, reduced numbers of trabeculae and an increase in inter-trabecular distance (Thomsen, Ebbesen and Mosekilde, 2002; Stauber and Müller, 2006; Eckstein *et al.*, 2007; Chen *et al.*, 2008, 2010; Cui *et al.*, 2008; Myers *et al.*, 2008; H Chen *et al.*, 2013).

Geometry at the organ level can also affect the likelihood of fracture. Assuming the magnitude of loading and bone structural and density parameters to be equal, larger femoral specimens will be less likely to fracture as they have a greater energy absorbing capacity.

#### 1.3.3.2.3 Bone Mechanical Properties

Because of the relationship between bone mineral density, geometry and structural properties with bone's mechanical properties, hip fracture risk can also be analysed within the context of bone mechanical properties. With ageing, due to the density, geometric and structural changes outlined in sections 1.3.3.3.1 & 1.3.3.3.2, declines in the tensile strength, the ultimate tensile strain and impact strength of human femoral bone occur. In other words, older bone becomes weaker and more brittle and this confers with it an increased chance of hip fracture.

## 1.4 IDENTIFICATION AND DIAGNOSIS OF INDIVIDUALS AT RISK OF HIP FRACTURE

As identified in section 1.3.1, in order to prevent against hip fracture there is a real need to be able to identify at risk individuals. It can be appreciated from section 1.3.3 that a large number of risk factors associated with hip fracture have been identified in the literature. Because of this, if it is possible to identify the presence or absence of single or multiple risk factors in individual it becomes possible to assess that individual's risk of fracture. Several assessment tools have been developed for clinical use to achieve exactly this:

1. Dual Energy X-Ray Absorptiometry (DEXA)
2. The Fracture Risk Assessment Tool (FRAX)

These assessment tools use a number of risk factors outlined in section 1.3.3 to predict an individual's chance of fracture over a given time period. They are utilised by clinicians within and across multiple national healthcare systems to predict hip fracture risk. Both are briefly discussed below.

#### **1.4.1 Tools for Assessing Fracture Risk – DEXA**

Currently, DEXA scans are the most widely used tool in clinical practice for the diagnosis of osteoporosis and identification of individuals at risk of fracture (Cummings, Bates and Black, 2002). DEXA scans quantify the areal BMD of bone regions and compare values of BMD against that of a reference value for young adults of the same sex. Osteoporosis is diagnosed when an individual's BMD for a given anatomical region is -2.5 standard deviations below the reference value (World Health Organization, 2004). Fracture risk increases two-fold for every standard deviation below the reference value so low BMD is considered an indicator of fracture risk.

However, there are a number of limitations associated with DEXA scans. BMD is a two-dimensional measurement of a three-dimensional structure and as a consequence, BMD represents only an areal projection, rather than a true volumetric assessment, of bone (Ohnaru *et al.*, 2013). Therefore, DEXA scans do not take account of a number important three-dimensional structural features of bone relevant to bone strength (Topoliński *et al.*, 2012). This implies that BMD cannot account for all of the variation observed in bone strength (Ammann and Rizzoli, 2003) which, as discussed in section 1.3.3.3.1., is reflected by the fact that the majority of people who suffer fragility fractures are not osteoporotic (Bouxsein and Seeman, 2009).

Ultimately these factors make DEXA an inadequate assessment tool for the accurate estimation of bone strength and thus for predicting the likelihood of fracture (see sections 2.2.7 – 2.2.9 for a more detailed discussion of the relevance of bone three-dimensional structural parameters for bone strength) (Cody *et al.*, 1999).

#### **1.4.2 Tools for Assessing Fracture Risk – FRAX**

FRAX was introduced to help address some of the limitations associated with DEXA scans (Kanis *et al.*, 2004, 2007, 2008; Kanis JA on behalf of the World Health Organization Scientific

Group, 2007; McCloskey *et al.*, 2016). FRAX can be used as an assessment method for predicting the probability of a major osteoporotic fracture over a ten-year period using pre-defined clinical risk factors. These clinical risk factors can be considered with or without an assessment of BMD (Kanis *et al.*, 2012) and include age, sex, race, height, history of fragility fracture, parental history of hip fracture, smoking, alcohol intake, rheumatoid arthritis, and use of glucocorticoids.

However, the FRAX model is subject to a number of limitations (Unnanuntana, 2010). It does not consider a number of other important risk factors, lacks generalizability of data from population-based cohorts, may underestimate the likelihood of fracture, cannot be used for patients already receiving treatment and can recommend treatment that contradicts conventional guidelines (Silverman and Calderon, 2010; Unnanuntana, 2010; Giangregorio *et al.*, 2012; Gogate and Bhadada, 2012).

#### **1.4.3 Tools for Assessing Fracture Risk – Computational Methods**

Partly in response to the inadequacies of DEXA and FRAX and partly in response to the increasing need to address the problem of hip fracture, computational models of the hip joint and of hip fracture have been developed to increase understanding about the mechanics and mechanisms of fracture. Such *in silico* models have performed relatively well in their prediction of hip fracture occurrence and type and show promise as an effective, patient-specific tool for the prediction and prevention of hip fracture.

Three computational methods that have been applied in the study of hip fracture are include:

1. Micro-computed tomography ( $\mu$ CT) scanning.
2. Finite element analysis (FEA).
3. Multibody Dynamic Analysis (MDA).

##### **1.4.3.1 $\mu$ CT**

$\mu$ CT is a non-destructive imaging technique that facilitates three-dimensional reconstructions of objects.  $\mu$ CT scanning creates a series of cross-sectional image slices of an object. Although each cross-sectional image slice is two-dimensional in nature, the image set is stacked to form a three-dimensional representation of the imaged object. High image resolutions (typically 5

– 100 microns) are obtainable with  $\mu$ CT scanning and are therefore sufficient to capture bone micro-architectural parameters. This makes it an excellent imaging modality for bone imaging and analysis. However, owing to high radiation doses and small fields of view, its applicability is often limited to pre-clinical animal studies or *ex-vivo* analyses of biological tissues.

#### 1.4.3.2 FEA

FEA is a numerical method used by engineers to investigate the behaviour of physical systems. Increasingly it has been employed within a biological context to model the response (e.g. via stress or strain analysis) of complex biological structures to applied loads. As such FEA has been widely applied to model three-dimensional femoral bone geometry and biomechanical properties to, through the application of simulated loads to these models, measure bone strength and understand the process and predict the likelihood of fracture.

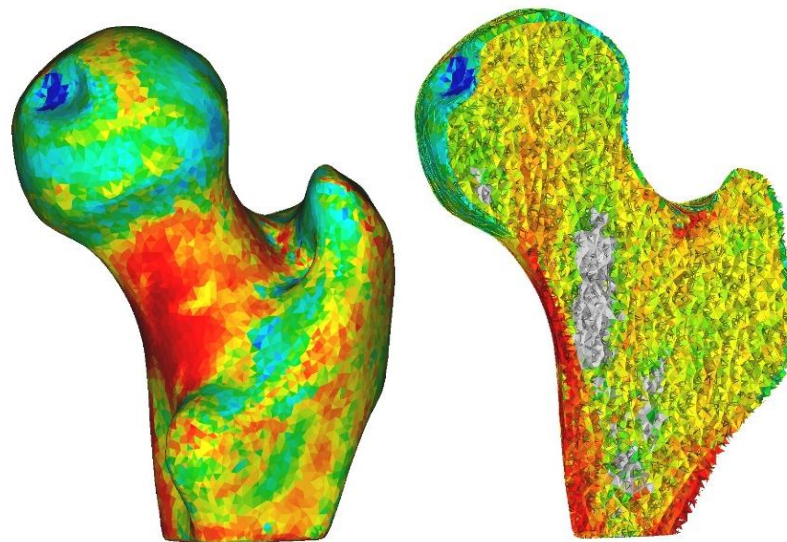


**Figure 1.2 Finite element models of the femur with material properties.** **Left:** Exterior surface of an FE femoral model constructed in chapter 6 with a value for bone density assigned to each element from which the model is made. Red elements are areas of highest bone density, blue elements areas of lowest. Using density, it becomes possible to assign material properties to the FE model. **Right:** Sagittal slice through the same model showing its interior and the individual discrete but interconnected elements (with density values) from which the model is constructed.

#### 1.4.3.3 MDA

MDA is a numerical method that is used to study and model the dynamic behaviour of a system of interconnected bodies undergoing translational and rotational movements (e.g. the human body (figure 1.4)). It has been widely applied to the study of human movement and can be used to predict and quantify a wide array of parameters associated with human

movement including angular and linear velocities of body segments, contact forces, joint reaction forces, muscle forces and ground reaction forces. More specifically, MDA has been applied to the modelling of falls in humans to predict fall related parameters such as fall velocities and impact force magnitudes.

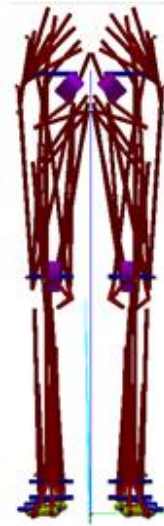


**Figure 1.3 Human musculoskeletal model used for MDA.** The human musculoskeletal model used for MDA in chapter 5 of this thesis. During MDA simulations, the model moves through three-dimensional space and multiple parameters (e.g. muscle forces) required to produce model kinematics can be predicted.

## 1.5 THESIS AIMS AND OBJECTIVES

Bone fails when the stresses it experiences exceed its ultimate strength. An essential step in understanding hip fracture risk is therefore understanding and accurately predicting the stresses the ageing femur is subjected to during a fall-related impact. How accurately femoral stresses can be predicted depends on a proper understanding of ageing femoral bone structural and material properties as well as the loading conditions to which the ageing femur is subjected to during a fall-related impact.

$\mu$ CT, MDA and FEA, although independent experimental approaches, can be combined to help investigate, quantify and understand fall-related femoral stresses by allowing appropriate structural and material properties of the ageing femur to be derived ( $\mu$ CT), appropriate fall-related mechanical loads to be quantified (MDA) and the incorporation of these properties and loads in simulations to quantify femoral stresses (FEA). Taking this into account, the specific aims and objectives of this thesis are outlined below:

### 1.5.1 Aims

1. Use  $\mu$ CT to map, quantify and explore variation in trabecular bone orthotropic fabric throughout multiple ageing proximal femora.
2. Use MDA to simulate, quantify and explore variation in impact and hip muscle forces that might occur during a sideways fall onto the hip.
3. Use FEA to simulate, quantify and explore the effect of combined hip and muscle forces on stress patterns in orthotropic models of the ageing proximal femur.

### 1.5.2 Objectives

1. Use micro-computed tomography ( $\mu$ CT) to scan multiple ageing proximal femur with sufficient resolution to capture trabecular architectural arrangement.
2. Develop a protocol to map trabecular orthotropic fabric for multiple, discrete regions throughout the proximal femoral specimens.
3. Statistically explore variation within and between specimens for regions of interest.
4. Record real-world kinematics of sideways falls.
5. Use MDA to simulate recorded real-world falls and quantify MDA-predicted impact and muscle forces that occur at simulated impact.
6. Statistically explore variation in impact and muscle forces between simulated falls.
7. Construct FE models of the ageing femur using the same  $\mu$ CT scans employed to derive trabecular orthotropy.
8. Construct orthotropic FE models of ageing femora by developing a protocol that incorporates  $\mu$ CT-derived trabecular orthotropic data and cortical orthotropy based on femoral surface geometry.
9. Implement appropriate boundary conditions within FE simulations to facilitate application of MDA-derived impact and hip muscle forces on orthotropic FE models.
10. Explore the biomechanical response of FE models to combined impact and muscle loading by analysing von Mises and principal stress patterns in the femoral neck region.

It is hoped that by combining the results of each experimental approach into a coherent, integrated analysis it will be possible to shed light on the potential role of sideways fall-related, concurrent impact and hip muscle forces in modifying and potentially increasing stress

magnitudes in the femoral neck at impact. The implications of this for hip fracture risk and future FEA work investigating fall-related femoral loading will be discussed.

## **1.6 THESIS OUTLINE**

Following the present introductory chapter, the structure of the remainder of the thesis will be as follows:

### **1.6.1 Chapter 2**

Chapter 2 will describe the structural arrangement of human bone, how its' structure relates to its material properties and the general concepts governing the relationship between structural and material properties. The chapter will then go on to consider the structure and function of human skeletal muscle and tendon. Finally, the gross musculoskeletal anatomy of the human hip joint will be considered.

### **1.6.2 Chapter 3**

Chapter 3 reviews and discusses literature at the forefront of advancing knowledge and methodologies relevant to the study of hip fracture and to each of the three independent experimental approaches employed in the results chapters (chapters 4, 5 and 6) of this thesis. Therefore, discussions surrounding femoral trabecular orthotropic properties, MDA modelling of falls and FEA modelling of sideways falls are included. The specific aims and objectives of each of the chapters addressing each of these areas are also outlined.

### **1.6.3 Chapter 4**

Chapter 4 presents a  $\mu$ CT-based study of older peoples' proximal femora to determine their structural anisotropic properties. It establishes a procedure for determining the principal directions of trabecular bone throughout the proximal femur and explores variation in the principal directions of trabeculae within and between femoral specimens.

#### **1.6.4 Chapter 5**

Chapter 5 presents kinematic data collection, analysis and subsequent MDA modelling of real-world sideways falls onto the hip. An MDA musculoskeletal model is defined and a simulation protocol is established that enables the musculoskeletal model to match the collected real-world kinematics of a sideways fall. Impact and hip muscle force data are quantified and analysed for variation.

#### **1.6.5 Chapter 6**

In chapter 6, FE models of the proximal femur are built using the  $\mu$ CT scans from chapter 4. A method is established to incorporate anisotropic femoral properties obtained in chapter 4 into FE models. Impact and muscle forces obtained in chapter 5 are incorporated into FE simulations. Multiple FE simulations are run and stress distributions within the proximal femur are used to quantify the biomechanical response of the femur to the combined effect of a variety of muscle and impact forces. The findings are placed within the context of the aetiology and prediction of femoral neck fracture.

#### **1.6.6 Chapter 7**

Chapter 7 entails a final discussion summarising the main findings and conclusions arising from this work. The thesis's primary contributions are emphasized and recommendations for future work are discussed.

## 2 ANATOMICAL AND BIOMECHANICAL BACKGROUND

---

### 2.1 HUMAN BONE

#### 2.1.1 The Structural Organisation of Human Bone

Bone differs to other tissues in the human body due to its greater stiffness, strength and the presence of its constituent organic and inorganic elements. In terms of total bone weight and volume the organic phase of bone accounts for 30% and 35% respectively, the inorganic phase 60% and 40% respectively, with the remainder being made up by water (Gong, Arnold and Cohn, 1964). Both inorganic and organic constituents combine to form the extra-cellular matrix (ECM) and it is this unique composition of the ECM that gives bone its increased stiffness and strength compared to other human biological tissues.

#### 2.1.2 Hierarchical Structure of Bone

Bone can be thought of as a hierarchical, composite material (Weiner and Traub, 1992; Rho, Kuhn-Spearing and Zioupos, 1998) (figure 2.1). This essentially means that bone has different levels and types of structural organization, at different length scales. These scales generally range from 0.1 microns to several centimetres.

At the largest hierarchical level of one to 5mm, two types of bone exist; trabecular bone (also called cancellous bone) and cortical bone (also known as compact bone). Cortical bone is made from tightly packed, concentrically arranged lamellar, Haversian and woven bone while trabecular bone is very porous and made from less well organised packets of lamellae.

#### 2.1.3 Trabecular Bone

Trabecular bone is a hierarchical, composite material made of hydroxyapatite, collagen, water and trace amounts of other proteins (Lowenstam and Weiner, 1989) (figure 2.1). It is found at the end of long bones in the appendicular skeleton, the vertebral bodies of the spine and other flat, irregular bones like the sternum or pelvis. It has a very complex, porous spatial arrangement that helps facilitate optimal strength for minimum mass.

Trabecular bone is formed from individual trabeculae that are frequently idealised as rod or plate like shapes (Moreno, Borga and Ö. Smedby, 2012a). Generally, trabecular bone is made from interstitial bone and arranged and joined together in an irregular lattice-like network. Pores within this lattice-like network are filled with marrow and are normally approximately 1mm in diameter (Keaveny, Morgan and Yeh, 2004). The thickness of individual trabeculae is an order of magnitude lower.

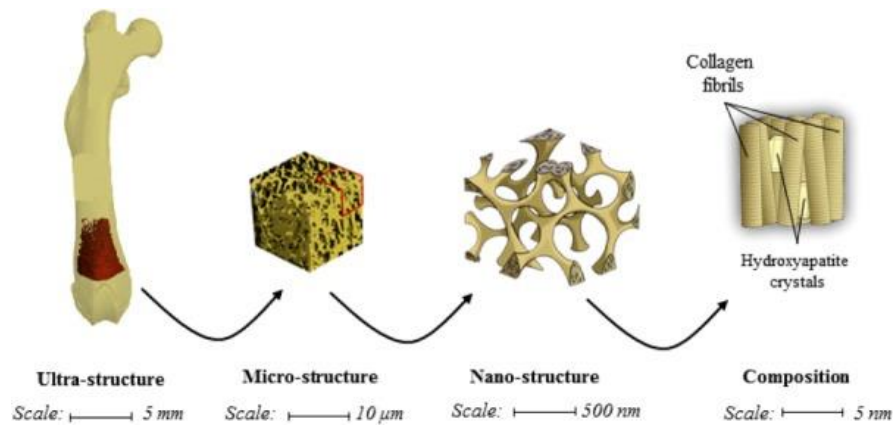


Figure 2.1 Hierarchical structure of trabecular bone (adapted from Oftadeh *et al.*, [2015]).

#### 2.1.4 Cortical Bone

Hamed, Lee and Jasiuk (2010) have identified various hierarchical levels of cortical bone (figure 2.2).

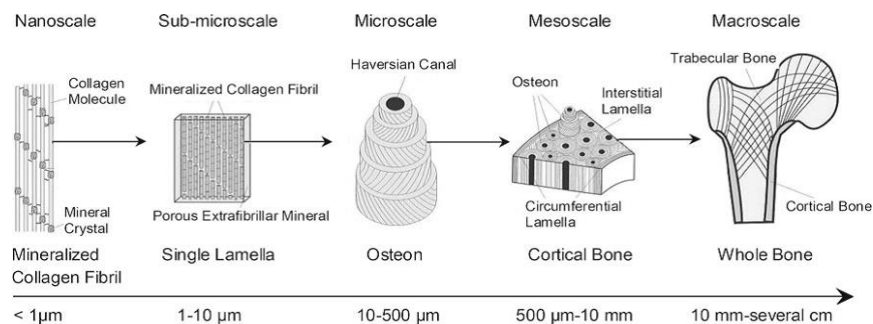


Figure 2.2 Hierarchical structure of cortical bone (adapted from Hamed, Lee and Jasiuk, [2010]).

At the sub-microstructural level, cortical bone is comprised of single lamella. Mineralised collagen fibrils are orientated in preferential directions to form lamellae that are approximately three to seven microns thick (Rho, Kuhn-Spearing and Zioupos, 1998). At the microstructural level cortical bone is comprised of osteons and interstitial lamellae. Osteons are long cylinders made of concentric rings of lamellae and surround a hollow Haversian canal.

Osteons are several millimetres long and 200-300 microns in width (Rho, Kuhn-Spearing and Zioupos, 1998). In the femur, they are aligned in its longitudinal direction. At the macrostructural level, cortical bone exists as a distinct continuum material that is distinguishable from trabecular bone.

## 2.2 BIOMECHANICS OF TRABECULAR AND CORTICAL

### 2.3 BONE

Bone material properties are generally defined at the apparent level and are often described using elastic constants. The elastic constants of bone help determine its mechanical behaviour and are thus related to bone's strength under loading (Goldstein *et al.*, 1983; Ciarelli *et al.*, 1991; Morgan and Keaveny, 2001) and by extension, risk of fracture. Because calculating the elastic constants of bone rests on an understanding of the concepts of stress, strain and the interaction between the two, these will be described in the following sections first.

#### 2.3.1 Stress

Internal forces within an object are produced at the same time the object experiences strain *i.e.* deformation under load. The internal forces an object experiences under loading are called stresses ( $\sigma$ ). Stress contains information about magnitude, direction and the plane on which it acts (Currey 1984). It is represented by a symmetric matrix of tensor components (Cowin and Telega, 2003), the elements of which denote normal and shear stresses (equation 2.1).

$$\sigma = \begin{bmatrix} \sigma_{11} & \sigma_{12} & \sigma_{13} \\ \sigma_{21} & \sigma_{22} & \sigma_{23} \\ \sigma_{31} & \sigma_{32} & \sigma_{33} \end{bmatrix} \quad 2.1$$

Stress is defined as force per unit area and is calculated by dividing the magnitude of the force by the area over which it acts and is quantified using Pascals (Pa).

### 2.3.2 Strain

When a load is applied to any solid object, it deforms from its original shape and dimensions. The deformation experienced is called strain ( $\epsilon$ ). Strain is represented by a symmetric matrix of tensor components (Cowin and Telega, 2003) as in equation 2.2:

$$\epsilon = \begin{bmatrix} \epsilon_{11} & \epsilon_{12} & \epsilon_{13} \\ \epsilon_{21} & \epsilon_{22} & \epsilon_{23} \\ \epsilon_{31} & \epsilon_{31} & \epsilon_{33} \end{bmatrix} \quad 2.2$$

The elements on the diagonal of the strain matrix,  $\epsilon_{11}$ ,  $\epsilon_{22}$ ,  $\epsilon_{33}$ , are the normal strains and all others are the shearing strains. Strain is a dimensionless ratio of geometric change and therefore has no units. It is calculated by dividing the change in length of an object under loading by the original length.

### 2.3.3 Bone Elastic Constants

#### 2.3.3.1 *Young's Modulus*

It is possible to use stress and strain to define a material's Young's modulus,  $E$ . The Young's modulus of a material indicates its stiffness. Thus, the higher the Young's modulus a material has, the stiffer it is. Young's modulus can be calculated by plotting a stress-strain curve from mechanical tests which bring about axial deformation of an object. For any such test, it is possible to calculate structural properties of individual specimens by plotting the axial force vs. the length change of the specimen. Doing so produces different force-deflection curves for different specimens of the same material (figure 2.3).

However, it is often more useful to calculate material properties. By plotting the axial force divided by the area on which it acts vs. the length change of the material the force is acting on divided by the original length, a stress-strain curve is produced instead (figure 2.3). Instead of producing different curves for different specimens of the same material, a single curve can be produced for all specimens, which approximates the average elastic behaviour of the material from which all tested specimens are made, as opposed to the mechanical behaviour of individual specimens.

The gradient of the linear region of the slope of the stress-strain curve denotes the Young's modulus (*i.e.* stiffness) of the material and represents the ratio of normal stress to normal strain in the direction of the force. Because it is calculated from a stress-strain curve, Young's

modulus is considered a material property. In bone, Young's modulus varies as a function of bone density (see section 1.2.11).

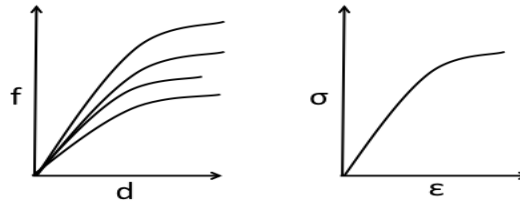


**Figure 2.3 Force-Deformation vs. Stress-Strain curves.** **Left:** Differently sized specimens of the same material produce different curves when the magnitude of the applied force is plotted against the magnitude of deformation. This provides information about the structural (size-dependant) as opposed to material properties of the specimens. **Right:** However, if these parameters are normalised and stress is plotted against strain, a single curve is produced instead. This curve provides information about the mechanical behaviour of the material as opposed to the specimens. This information is independent of specimen size.

The linear region of the stress-strain curve is governed by Hooke's law and represents elastic deformation in which the material is still able to return to its original dimensions once the load is removed. At the end of the linear region of a stress-strain curve, a non-linear region is observable and this represents yielding of the bone where plastic (*i.e.* permanent) deformation begins. This is known as the elastic limit. If plastic deformation continues beyond this point, the bone will finally fail and fracture. This point on the curve is known as the ultimate stress,  $\sigma_{ult}$  (figure 2.4).

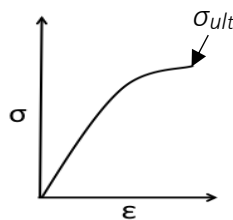


**Figure 2.4 The mechanical behaviour of bone under loading.** When a force is applied to bone, a stress-strain curve is produced with an initial linear region. The linear region characterises bone elastic behaviour which is governed by Hooke's law. If loading continues, bone's elastic limit will eventually be exceeded and the stress-strain curve becomes non-linear. Bone begins to yield at this point and if loading continues further, bone's ultimate stress,  $\sigma_{ult}$ , will be surpassed leading to failure and thus fracture.

Because strain is dimensionless,  $E$  adopts the units of stress and is therefore quantified using Pa. At the simplest level, stress, strain and Young's modulus are related to one another as in equation 2.3 and can be used to help model and understand the biomechanical behaviour of bone (Currey 1984):

$$E = \frac{\sigma}{\epsilon} \quad 2.3$$

### 2.3.3.2 *Poisson's ratio*

Poisson's ratio,  $\nu$ , is another elastic constant used to characterise the material behaviour of bone and characterises a solid material's tendency to retain its volume under deformation. If an object is subject to axial tensile load and subsequently elongates, there will be an associated contraction in the material's transverse directions. Poisson's ratio can therefore be defined as the ratio of transverse strain to longitudinal strain of an object under a state of stress.

### 2.3.3.3 *Shear Modulus*

The shear modulus,  $G$ , (also known as the modulus of rigidity) of a material is an elastic constant used to define the deformation which takes place when shear forces are applied to an object e.g. when parallel forces are applied to its opposite faces. The larger the value of  $G$  the more rigid a material is.

### 2.3.4 **Directional Dependence of Linear Elasticity**

A material's linear elastic behaviour is related to the number of planes of material symmetry it has. The number of planes of material symmetry relate to the directional dependence of a material's linear elastic properties. Thus, if a material has an infinite number of symmetry planes passing through every point within it, the material is classified as isotropic and there is no directional dependence characterising its linear elastic behaviour. In other words, its linear elastic material properties are the same in all directions. On the other hand, if a material has a small number of planes of symmetry passing through each point, or no symmetry planes at all, it is known as anisotropic and the linear elastic behaviour of such a material has a directional dependence. Directional dependence means planes of material symmetry have specific directions and, consequently, the material's linear elastic properties are direction dependant because they are aligned with these planes. Three types of material symmetry – orthotropy, transverse isotropy and isotropy – are described in the following sections.

#### 2.3.4.1 Orthotropic Materials

Orthotropy is a particular form of anisotropy. Orthotropic materials have three mutually orthogonal symmetry planes passing through each point. Therefore, the material's linear elastic behaviour is direction dependant. Orthotropic materials have nine elastic constants,

- Three Young's moduli,  $E_1, E_2$  and  $E_3$ , relating extensional strain in the direction of loading to stress in the direction of loading.
- Six Poisson's ratio,  $\nu_{23}, \nu_{32}, \nu_{13}, \nu_{31}, \nu_{12}$  and  $\nu_{21}$ , relating extensional strain in the loading direction to extensional strain in another direction.
- Three shear moduli,  $G_{12}, G_{13}$  and  $G_{23}$ , relating shear strain in the plane of shear loading to that shear stress.

Each of the elastic components is aligned with one of the axes of the orthotropic coordinate system. Although there are 12 elastic constants in the compliance matrix for an orthotropic material, only 9 are independent because:

$$-\frac{\nu_{12}}{E_1} = -\frac{\nu_{21}}{E_2}, \quad -\frac{\nu_{13}}{E_1} = -\frac{\nu_{31}}{E_3}, \quad -\frac{\nu_{21}}{E_2} = -\frac{\nu_{32}}{E_3} \quad 2.4$$

#### 2.3.4.2 Transversely Isotropic Materials

Transverse isotropy is a subclass of orthotropy. Transversely isotropic materials have a plane of isotropy at every point in the material. A plane of isotropy has the effect of reducing the nine elastic components of an orthotropic material to just five. This is because the in-plane elastic constants are equal to each other but different to those that are transverse to the plane of isotropy (Currey 1984). As a result, there are only five elastic constants:

$$E_p, E_t, \nu_p, \nu_t, G_t \quad 2.5$$

#### 2.3.4.3 Isotropic Materials

Isotropic materials are the least complex linear elastic materials to model due to the fact they have the highest possible type of symmetry. Isotropic materials have an infinite number of symmetry planes passing through each point and therefore their linear elastic properties are not direction dependant. In other words, every material direction is the same. For isotropic materials there is:

- A single Young's modulus,  $E$ , relating extensional strain in the direction of loading to stress in the direction of loading.
- A single Poisson's ratio,  $\nu$ , relating extensional strain in the loading direction to extensional strain in another direction.
- A single shear modulus,  $G$ , relating shear strain in the plane of shear loading to that shear stress.

Because  $G$  can be expressed in terms of  $E$  and  $\nu$ , there are only two independent elastic constants and the linear elastic behaviour of the material can be fully described by  $E$  and  $\nu$ .

### 2.3.5 The Material Complexity of Bone

The material properties of cortical and trabecular bone are considered anisotropic. Specifically, it has been shown that the material properties of cortical and cancellous bone can be described as orthotropic (Ashman *et al.*, 1984; Yang *et al.*, 1998; Turner *et al.*, 1999; Cuppone *et al.*, 2004). The anisotropic properties of cortical bone primarily arise from variations in its Haversian organisation (Martin and Ishida, 1989) while the anisotropic properties of trabecular bone primarily arise from the architectural organisation of trabeculae (Maquer *et al.*, 2015). Therefore, the directions of the planes of material symmetry for each bone type are closely related to their respective structural organisations.

### 2.3.6 The Relationship between Trabecular Bone Structural and Linear Elastic Properties

The spatial structure of trabecular bone is both complex and highly heterogeneous. Nonetheless, it frequently exhibits recognisable architectural patterns. Indeed, trabecular bone often has a 'grain' with groups of individual trabeculae orientated in similar directions within and across certain anatomical regions. This preferential arrangement of trabecular bone means is termed its architectural anisotropy or fabric.

It is generally accepted that trabecular bone's structural anisotropy is orthotropic in nature due to the fact measurements taken using the mean intercept length (MIL) technique (a technique used to quantify the directionality and anisotropy of trabecular bone's structural arrangement) can be fitted to an ellipsoid-shaped second-rank fabric tensor (Harrigan and Mann, 1984) (see chapter 3 for a more detailed explanation). This indicates that three mutually orthogonal symmetry planes are sufficient to describe its structural organisation.

The orientations of the orthotropic structural symmetry planes defined by the fabric tensor describe the main directions of the trabecular bone network being analysed. Furthermore, it is assumed that the orthotropic material properties of trabecular bone are aligned with those of the fabric tensor (Cowin, 1985; Cowin and Mehrabadi, 1989). Therefore, trabecular bone architecture at the structural, as opposed to the tissue, level gives rise to its material anisotropy.

Thus, for example, each one of the three Young's moduli is aligned with each one of the orthogonal fabric directions, with the largest (*i.e.* the stiffest) being aligned with the main trabecular direction. Ultimately this relationship gives trabecular bone, when considered at the apparent level, greater stiffness and strength in its main direction relative to its other directions (Rice, Cowin and Bowman, 1988).

Thus, trabecular bone not only forms where it is needed most but does so in such a way as to maximise its strength under loading. This adaptive functionality reflects the general notions postulated in Wolff's law that trabecular bone remodels and orientates itself to align with the principal stress directions experienced from habitual loading (Ruff, Holt and Trinkaus, 2006). In human vertebral bodies, for example, the main trabecular direction is in the superior-inferior direction. Research has shown that mean values for strength and stiffness are higher in the superior-inferior vs transverse directions by factors of 2.8 and 3.4 respectively (Keaveny *et al.*, 2001).

### **2.3.7 The Relationship between Cortical Bone Structural and Linear Elastic Properties**

Unlike trabecular bone, cortical bone's anisotropic properties appear to be influenced mainly at the microstructural level. At the microstructural level of cortical bone, it has been reported that Haversian tissue displays transverse isotropy and it is this that dictates cortical bone material properties (Lawrence Katz *et al.*, 1984; Martin and Ishida, 1989). Sevostianov and Kachanov (2000) and Yeni, Vashishth and Fyhrie (2001) have hypothesised that cortical microstructures such as Haversian canals, Volkman's canals, canaliculi and osteocyte lacunae can help explain the pattern of cortical bone orthotropy. They postulated that cortical bone is dominated by longitudinally orientated osteons and that, in agreement with other research (Lawrence Katz *et al.*, 1984; Martin and Ishida, 1989; Salguero, Saadat and Sevostianov, 2014), the principal material axis was aligned with their predominant direction.

This microstructural arrangement manifests itself mechanically and cortical bone has been shown to be stronger and stiffer under loading in the longitudinal direction, (*i.e.* in the axial direction of the bone), compared to loading in its circumferential or radial directions (Ashman *et al.*, 1984; Bensamoun *et al.*, 2004). In the circumferential and radial directions, the elastic constants strength of cortical bone are much more similar to each other, thus implying that cortical bone is transversely isotropic.

### 2.3.8 Other Properties of Cortical and Trabecular Bone

The mechanical properties of trabecular bone are primarily influenced firstly by its bone volume fraction (BV/TV), a measure of the ratio of bone per total unit volume of a specimen, and secondly by its structural arrangement (Maquer *et al.*, 2015; Musy *et al.*, 2017) *i.e.* its fabric; indeed, trabecular bone's bone volume fraction explains a significant proportion of its strength while, taken together, bone volume fraction and trabecular architectural anisotropy explain nearly all of its observed strength.

The mechanical properties of cortical bone at the macrostructural level are influenced by multiple factors including porosity, the degree of mineralisation and the organization of the ECM. Microstructural features like porosity can lead to considerable heterogeneity in mechanical properties and it may sometimes be necessary to take account of these (Martin and Ishida, 1989). For example, ultimate stress and modulus can halve in value when porosity increases from 5% to 30% (Schaffler and Burr, 1988; McCalden *et al.*, 1993). Similarly, small increases in levels of mineralization can lead to marked increases in strength and modulus (Currey, 1988).

The mode of loading also influences the strength of trabecular and cortical bone, with both being stronger under compression than in tension and shear (Reilly and Burstein, 1975; Keaveny *et al.*, 1994; Ford and Keaveny, 1996). However, under longitudinal loading, although ultimate stresses and therefore strength are higher in compression, ultimate strains in cortical bone are higher in tension with ultimate tensile strains reaching as high as five percent in adults. Ultimate tensile strains are generally lower (approximately one percent) in older people (McCalden *et al.*, 1993) indicating ageing bone is more brittle. Trabecular bone is weakest under shear loading but cortical bone is weakest when undergoing tensile loading in the transverse direction (Reilly and Burstein, 1975).

### 2.3.9 The Relationship between Bone Elastic Constants and Bone Density

At the structural level, bone's elastic constants vary as a function of density (Helgason, Perilli, *et al.*, 2008). A plethora of studies have explored the relationship between elastic constants and bone density using the same general protocol of experimentally measuring mechanical and density parameters and then constructing a statistical model to correlate results (Lotz, Gerhart and Hayes, 1990; Ciarelli *et al.*, 1991; Snyder and Schneider, 1991; Hodgskinson and Currey, 1992; Keyak, Lee and Skinner, 1994; Li and Aspden, 1997; Wirtz *et al.*, 2000; Morgan, Bayraktar and Keaveny, 2003; Kaneko *et al.*, 2004; Helgason, Perilli, *et al.*, 2008). Generally, the relationship between bone elastic constants and density is defined using power-law (usually cubic or square) relationships which take the general form:

$$E = ap^b \quad 2.6$$

Where  $E$  is the elastic constant of interest,  $a$  is a constant,  $p$  is density and  $b$  is the power. A single equation of the form in equation 2.6 can be used to model the mechanical properties of bone if it assumed that cortical and cancellous bone represent just one material. Alternatively, separate equations can be used to model the elastic properties of cortical and cancellous bone. In the isotropic case, only a single equation of the form in equation 2.6 is needed to approximate Young's modulus. In the orthotropic case, one such equation is needed for each of the orthotropic directions associated with each elastic constant.

## 2.4 HUMAN SKELETAL MUSCLE

Skeletal muscle functions primarily under conscious control to produce movement by exerting force on tendons which in turn pull on bones. Because muscles usually cross at least one joint, they produce movement of a bone about a joint. Like bone, muscle also has a hierarchical structure that displays different types of structural organization at different length scales (figure 2.5).

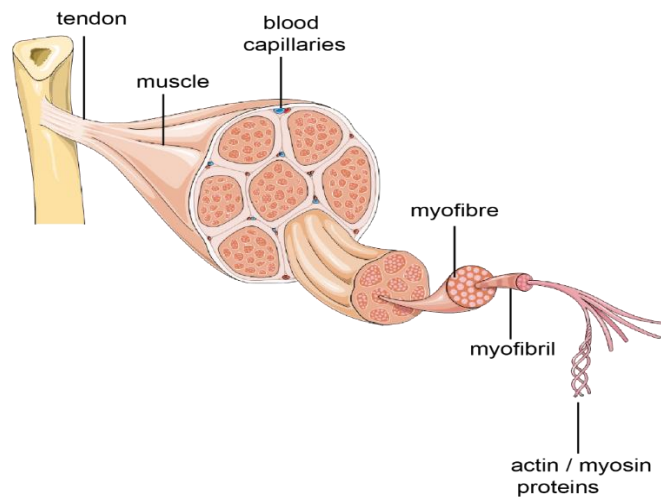


**Figure 2.5 The structure of human skeletal muscle.** A simplified illustration of the hierarchical structure of muscle which consists of bundles of myofibres. Each myofibre is comprised of myofibrils which in turn contains sarcomeres. Sarcomeres contain actin and myosin filaments. The interaction between actin and myosin facilitates muscle contraction. (Image adapted from optistem.org).

## 2.4.1 The Hierarchical Structure of Skeletal Muscle

Skeletal muscle is comprised of muscle fibres. Muscle fibres are arranged in bundles called fasciculi which are joined together by connective tissue. Skeletal muscle fibres are elongated, multinucleated, cylindrical cells with a small diameter of 10-60 $\mu\text{m}$  and a length of several mm to cm (although they can be much longer than this).

The muscle fibres themselves are composed of smaller units of longitudinal filaments called myofibrils which are approximately 1 $\mu\text{m}$  in length. Myofibrils, in turn, can be subdivided further into sarcomeres which are the structural and functional unit of skeletal muscle and in which there are two types of myofilaments. One type, composed of actin molecules, is thinner than the other being approximately 5nm in diameter. The other, thicker type composed of myosin molecules is approximately 12nm in diameter. It is the interaction between actin and myosin filaments that facilitates contraction of muscle. This interaction is best explained by the sliding filament theory.

### 2.4.1.1 Types of Muscle Contraction

#### 2.4.1.1.1 Eccentric

Eccentric contractions occur while muscle fibres are lengthening due to some strong opposing working against the force the muscle is generating. Often eccentric contractions happen

because the resistance trying to be overcome is greater than the force being generated by the muscle.

#### 2.4.1.1.2 Concentric

Concentric contractions occur when the fibres of a muscle are being shortened. In concentric contractions the force generated by a muscle is always less than the maximum force it can produce but greater than the resistance trying to be overcome.

#### 2.4.1.1.3 Isometric

Isometric contractions occur when muscle fibres are activated and contract but do so at a constant length. There is no lengthening or shortening of fibres in this type of contraction. The force generated during an isometric contraction is strongly dependant on the length of the muscle while it is contracting. Isometric contractions are often used to maintain posture.

### 2.4.2 Muscle Strength

Muscle strength can be quantified in several ways. The basic function of muscle is to produce a contractile and subsequent tensile force in order to move the skeleton. The ability to produce force within the muscle as well as the muscle's ability to create a moment about a joint both contribute to and describe the muscle's strength. They are related by equation 2.7:

$$M = r \times f \quad 2.7$$

Where **M** is the moment generated by muscle tensile force, **f**, at a distance from the joint axis (i.e. the centre of rotation), **r** (the muscle moment arm).

#### 2.4.2.1 Muscle Moment Arms

moment arms are defined as the perpendicular distance between a muscle's line of action and an axis of rotation (i.e. the joint centre about which movement is occurring) (Herzog and Read, 1993). Muscle with shorter moment arms will produce much more angular movement

than muscles longer moment arms, even if their shortening capacity is similar (Koh and Herzog, 1998).

#### **2.4.2.2 Muscle Force Production**

Muscle forces are produced by the stimulation and subsequent contraction of muscle fibres. This is termed muscle activation. Muscle activation is achieved via nervous, electrical or chemical impulses and produces a twitch of the muscle fibre. Successive twitches at a high enough frequency can produce stronger contraction forces because a previous twitch has not terminated before a new one begins. This is known as wave summation (Fung, 1993). If the frequency is high enough, it is not possible to distinguish between twitches. This is termed the tetanized state of a muscle (Fung, 1993).

#### **2.4.2.3 Factors Affecting the Degree of Muscle Force Production**

##### **2.4.2.3.1 Physiological Cross-Sectional Area (PCSA)**

The force a muscle can produce is a function of its size, also known as its physiological cross-sectional area (PCSA) (Raty *et al.*, 1999). A muscle's PCSA is a cross-sectional area within a muscle that takes account of all muscle fibres (Brand, Beach and Thompson, 1981). The larger the PCSA of a muscle, the larger a force it can produce. This is because a muscle with a larger PCSA tends to have more muscle fibres. This in turn means there is more actin and myosin present and therefore a greater number of potential cross-links that can be made between actin and myosin chains. Because the strength of contraction is dependent on the number of cross-links made, muscles with larger PCSA's therefore are generally able to produce larger forces (Fitts, McDonald and Schluter, 1991).

PCSA is influenced the angle of pennation (*i.e.* the angle at which muscle fibres insert into a tendon) exhibited by muscle fibres (Ichinose *et al.*, 1998). Although larger angles of pennation decrease contraction force, they tend to increase the PCSA of a muscle which in turn increases its force production ability (Aagaard *et al.*, 2001).

#### 2.4.2.3.2 Length-Tension Relationship

The length-tension relationship relates to the amount of force a muscle can produce at various discrete lengths (Marshall, Mazur and Taylor, 1990; Murphy *et al.*, 1995). The amount of force is essentially a function of the total amount of overlap between actin and myosin filaments. The resting length of the muscle usually provides the optimum length at which muscle can produce a maximum isometric force because there is maximum contact between actin and myosin filaments (Rassier, Dilson E.; MacIntosh, B. R.; Herzog, 1999; Rassier, 2004). Shortening muscle fibres maintains cross-linking but causes actin strands to interfere with each other. Lengthening muscle fibres leads to decreased contact between actin and myosin filaments. Therefore muscle fibre lengths that are shorter or longer than this optimal, resting length tend to produce forces below the maximum possible force (Gandevia and McKenzie, 1988; Gareis *et al.*, 1992).

#### 2.4.2.3.3 Force-Velocity Relationship

The force generated by a muscle is also a function of its velocity of contraction which can be defined as the muscle's change in length over time (Fenn and Marsh, 1935; Kanehisa, Ikegawa and Fukunaga, 1997; Cramer *et al.*, 2004). Force and velocity are inversely related (Knapik *et al.*, 1983). Thus, the faster the velocity of contraction the less force a muscle is able to produce because there is less time for cross-links to form between actin and myosin filaments (Aagard and Andersen, 1998). Conversely, slowing the velocity of contraction allows a muscle to produce more force because more cross-links are able to form. As a result, maximum force production is achieved at zero contraction velocities for isometric and concentric contractions.

Eccentric contractions differ to isometric and concentric contractions with respect to the influence of contraction velocity on force production. Studies have shown that, for the same contraction velocity, an eccentric contraction will produce more force than isometric or concentric contractions (Cress *et al.*, 1996; Evetovich *et al.*, 1998)

#### 2.4.2.3.4 Motor Units

The strength of a muscular contraction is also dependent on the total amount of muscle fibres stimulated (Fung, 1993). This is, in turn, determined by the number of active motor units and

thus by the frequency and intensity of the stimulation producing motor unit activity (Sandercock, 2005). A motor unit is defined as the number of muscle fibres innervated by a single nerve known as a motoneuron.

Increasing the intensity of the stimulus from motoneurons results in more motor units being recruited to produce twitch contractions and as the number of motor neurons being recruited increases so does the strength of contraction (Clamann, 1993). In this way, i.e. by modifying the frequency and intensity of the stimulus from the motor nerve, it becomes possible to produce maximal and submaximal contractions. Maximal contractions involve the recruitment of all available motor units (Miller *et al.*, 2006) while in sub-maximal contractions, only a proportion of motor units are recruited to produce the required force.(Rich and Cafarelli, 2000).

#### 2.4.2.3.5 Electromyography (EMG)

Electromyography measures muscle activity (Konrad, 2005). Usually there is a strong association between the electrical activity of a muscle and the force of contraction. As the contraction force increases so does a muscle's activity i.e. so does its EMG (Komi, 1973). EMG is ultimately only a measure of the number of active fibres in the muscle (Basmajian and De Luca, 1985) and it cannot directly inform about muscle force of contraction. Therefore, if the same number of fibres are recruited within the same muscle for an eccentric and concentric contraction, EMG will show similar levels of muscle activity, despite the fact the force of contraction will be larger in the eccentric contraction due to the different effects of contractile velocity of these differing modes of contraction. Additionally, EMG may not be able to distinguish between levels of activity produced by individual muscles (Farina, 2004).

### 2.4.3 Tendons

Tendons insert into bone at end and the periosteum of a bone at the other and thus connect and transmit forces from muscle to bone. They are cords of dense connective tissue with a structural arrangement that is hierarchical like that of bone and muscle (figure 2.6). The collagen fibres of tendons are assembled into primary bundles (fascicles) which are in turn enclosed by a sheath called the fascicular membrane to form the tendon. Tendon collagen

fibres are generally arranged in parallel; this reflects the fact that they are primarily loaded axially in tension.

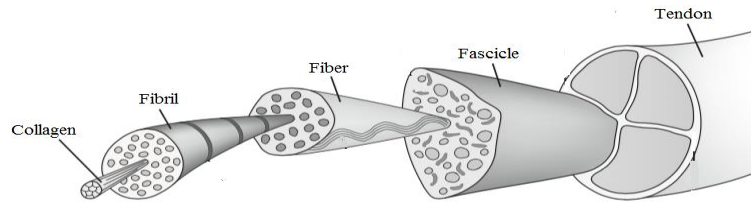


**Figure 2.6 The structure of human tendon.** Diagram illustrating the hierarchical structural organisation of human tendon. The tendon is comprised of fascicles which in turn are made from multiple, individual fibres generally arranged in parallel with each other. (Image adapted from (Adapted from Wilson, 2015)).

Although tendons display are non-linearly elastic behaviour, the middle of their stress-strain curves nonetheless display an approximately linear-elastic region (figure 2.7).

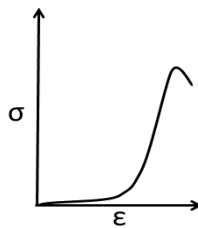


**Figure 2.7 Tendon stress-strain curve.** Although tendons display non-linear behaviour, the middle portion of their stress-strain curves is nonetheless characterised by a linear region (adapted from Fung, (1993)).

## 2.5 MUSCULOSKELETAL ANATOMY OF THE HIP JOINT

The hip joint is a ball-and-socket joint formed by the articulation between the head of the femur and the acetabulum of the pelvis (figure 2.8). The hip joint allows flexion, extension, abduction, adduction, circumduction, medial rotation and lateral rotation of the thigh.



**Figure 2.8 Hip joint.** The hip joint consists of the head of the femur inserting into the acetabulum of the pelvis bone. Together they form a ball and socket joint (adapted from Drake, Vogl and Mitchell, [2005]).

## 2.5.1 Hip Bones

### 2.5.1.1 Pelvis

Each side of the pelvis is comprised of three bones; the ilium, the ischium and the pubis (figure 2.9). The ilium is the largest and most superior bone in the pelvis and acts as an attachment site for a number of hip muscles. The ischium forms the inferior, posterior portion of the pelvis while the pubis forms the inferior, anterior portion. The acetabulum is a deep fossa formed by the ilium, ischium and pubis. The head of the femur sits inside the acetabulum to form the hip joint.

### 2.5.1.2 Proximal Femur

The femur is the longest, heaviest and strongest bone in the human body (figure 2.9). The femur's distal end articulates with the tibia and patella to form the knee joint while its most proximal end, the femoral head, articulates with the acetabulum to form the hip joint. The neck of the femur is a constricted region distal to the head and the shape of which can be roughly approximated as a beam. Hip fractures are often associated a fracture of the femoral neck.

The greater and lesser trochanter are projections of bone that form at the junction between the femoral neck and shaft. They act as attachment sites for the tendons of some of the hip musculature. The greater trochanter is located on the lateral aspect of the proximal femur and can be palpated through skin. The lesser trochanter is inferior and medial to the greater

trochanter. The intertrochanteric line forms along the anterior surface between the two, while the intertrochanteric crest is formed along the posterior surface between the two.

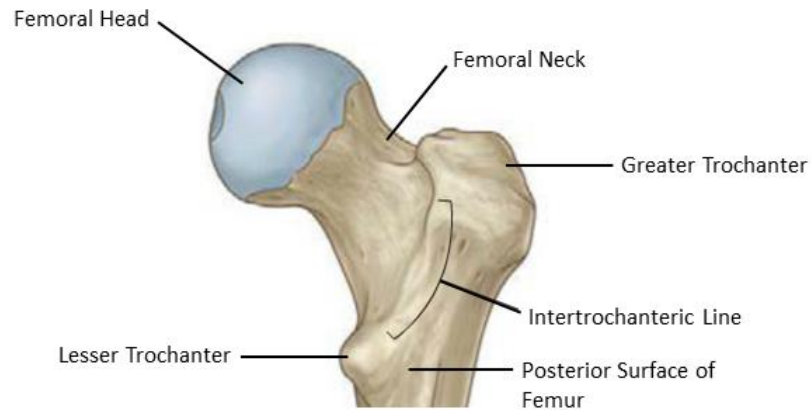


**Figure 2.9 Anatomy of the proximal femur.** The proximal femur consists of the femoral head at its most proximal portion to a region just below the lesser trochanter. It is defined by a number of bony landmarks and its surface has a number of hip muscle insertion points (adapted from Drake, Vogl and Mitchell, [2005]).

## 2.5.2 Hip Musculature

There are multiple muscles associated with the hip joint which have various functions including aiding bipedal locomotion, stability and maintaining posture. Most of the muscles of the hip originate from the pelvis and insert at various locations on the femur. They can be categorised into several groups.

### 2.5.2.1 Iliopsoas

The iliopsoas muscle is comprised of two separate muscle bellies – iliacus and psoas major – that share a common insertion site on the femur. Iliopsoas acts to flex the thigh at the hip joint and rotate the thigh laterally.

### 2.5.2.2 Gluteal Group

The gluteal group is comprised of gluteus maximus, gluteus medius and gluteus minimus. Gluteus maximus is the largest of the gluteal group and one of the largest in the human body and mainly acts as an extensor of the femur. Gluteus medius is deep to gluteus maximus and

is a strong abductor of the femur at the hip joint. Gluteus minimus is the smallest of the gluteal group and is an abductor and medial rotator of the femur at the hip joint.

### **2.5.2.3 Adductor Group**

Adductor brevis, adductor longus and adductor magnus are the muscles of the adductor group at the hip. They each act to adduct the femur at the hip joint but can also medially and laterally rotate the thigh

### **2.5.2.4 Lateral Rotators**

The lateral rotators laterally rotate the thigh at the hip joint. There are a number of lateral rotators and they all lie deep to gluteus maximus. They include piriformis, obturator externus, obturator internus, inferior gemellus, superior gemellus and quadratus femoris.

### **2.5.2.5 Knee Extensors**

The knee extensors have origins on the pelvis or proximal femur and femoral shaft. They insert distally at various points on the patella and also onto the tibial tuberosity. They include vastus intermedius, vastus medialis and vastus lateralis which all act to extend the shank about the knee joint.

## **2.5.3 Hip Musculature – Biomechanical Significance**

Of particular importance for this thesis, are the hip abductors and the hip flexor, iliopsoas. The hip abductors are considered the most important hip muscles due to their strength and function as pelvic stabilisers during gait (Widler *et al.*, 2009). Iliopsoas is also considered to be important and is implicated in stability of the femoral head (Lewis, Sahrman and Moran, 2007). Reflecting their functional importance for the hip joint is the fact that adverse changes to their strength, size and/or force contributions can lead to a number of hip joint related problem including acetabular labral tears, acetabular gliding and increased hip joint loading (Lewis, Sahrman and Moran, 2007; Mendis *et al.*, 2014). Studies using EMG to study muscle

function have shown abductor muscles to display high levels of muscle activity during and therefore contribute most to bipedal gait (Bogey & Barnes 2017).

In terms of fracture it is thought abnormal contraction of the hip musculature can lead to spontaneous hip fracture (Yang *et al.*, 1996; Gomez-Benito, Garcia-Aznar and Doblare, 2005). Conversely, the powerful abductors have been hypothesised as having a protective role against femoral neck fracture during bipedal gait by reducing tensile forces in the superior femoral neck (Matheson *et al.*, 1971; Dalla Pria Bankoff, 2012). Although studies utilising EMG show decreases in hip abductor and flexor muscle strength and function with increasing age (Morcelli *et al.*, 2014) which may, it is interesting that it has also been found that the hip abductors muscle strength is strongest in a side-lying posture (Widler *et al.*, 2009). Such a posture, at least qualitatively, appears to share similar characteristics to those of a sideways fall and therefore the relationship between hip abductor contractile activity and body posture may also be relevant for fracture.

## 3 LITERATURE REVIEW

---

### 3.1 $\mu$ CT

The architectural orientation of trabecular bone, also known as trabecular fabric (Cowin, 1985) is thought to be particularly important in biomechanical terms because there is robust evidence of a strong relationship between trabecular bone fabric, trabecular bone elastic constants and trabecular bone biomechanical behaviour (Kabel *et al.*, 1999). This is exemplified well by the synergy between trabecular bone's principal fabric and material directions (Odgaard *et al.*, 1997).

As a result, it is reasonable to assume that trabecular architectural arrangement may have an important role to play in determining and predicting bone strength and bone mechanical behaviour. Being able to accurately quantify bone strength and bone biomechanical behaviour is especially important in the prediction and prevention of hip fracture where accurate assessment of *in vivo* bone strength is essential (Kersh *et al.*, 2013).

CT scans allow subject-specific assessment of bone density (and therefore implied strength) and are thus widely used in both clinical and research contexts (Iwamoto *et al.*, 1998; Lochmüller *et al.*, 2003; Hudelmaier *et al.*, 2004; Turkyilmaz *et al.*, 2006). However, the resolutions associated with CT scans are insufficient to image individual trabeculae and delineate the structural properties of trabecular bone. Yet nearly all micro-architectural parameters associated with trabecular bone analysis are dependent on being able to do this. Therefore, any analysis of trabecular bone done using CT scanners is normally limited to measurements of BMD which as described in section 1.4.1 is an insufficient surrogate for quantifying bone strength and fracture risk (Milovanovic, Djonic, *et al.*, 2012).

Analysis and prediction of bone strength via  $\mu$ CT scanning thus represents an improvement upon assessments of bone strength via DEXA where only two-dimensional areal projections of bone and measures of BMD are possible, leading to incomplete predictions of bone strength and thus fracture risk.

With the development of  $\mu$ CT scanning and its' inherently high scan resolutions, measurements and subsequent analysis of multiple bone parameters including bone density and three-dimensional structural parameters (e.g. architectural orientation) that contribute to bone strength. With  $\mu$ CT it is now possible to image individual trabeculae and trabecular architecture with good clarity and accuracy. While  $\mu$ CT has limited application in clinical settings due to its high radiation doses, for research purposes  $\mu$ CT takes analyses of trabecular bone beyond measures of BMD and instead facilitates the derivation and detailed study of a plethora of trabecular bone parameters that are dependent on knowledge and quantification of (*i.e.* being able to properly image) trabecular architecture (Wegrzyn *et al.*, 2010; Yeni *et al.*, 2011).

A comprehensive picture of bone strength can therefore be obtained and, as a result, bone strength and biomechanical behaviour can be more accurately predicted.  $\mu$ CT scanning therefore represents an improvement upon assessments of bone strength via DEXA where only two-dimensional areal projections of bone and measures of BMD are possible, leading to incomplete predictions of bone strength and thus fracture risk.

BV/TV forms the most important of trabecular bone parameters that can be quantified with  $\mu$ CT because it is highly correlated with trabecular bone strength; it accounts for 89% and 75% of the variance in trabecular stiffness and yield strength respectively (Musy *et al.*, 2017). Trabecular bone principal fabric directions, due to their strong affinity with trabecular bone elastic constants, forms the other most important of these parameters and can explain up to 20% of the variation observed in bone strength (Hosseini, Maquer and Zysset, 2017). Together, although independent of each other, BV/TV and trabecular fabric therefore explain up to 97% of the elastic and yield properties of trabecular bone and can thus be considered the two most important determinants of the elastic properties of trabecular bone.

Trabecular fabric can be studied and quantified using a variety of mathematically independent techniques (e.g. mean intercept length (MIL) (Harrigan and Mann, 1984), mean surface length (MSL) (Hosseini, Maquer and Zysset, 2017), gradient structure tensor (GST) (Larsson *et al.*, 2014)), that make use of fabric tensors to quantify trabecular architectural, orthotropic orientations and the degree to which those trabecular structures are preferentially orientated (the degree of anisotropy or 'DA') (Moreno, Borga and O. Smedby, 2012). However, for scan resolutions of 100 microns or less, the MIL method is considered the gold standard for deriving architectural anisotropic information (Larsson *et al.*, 2014).

$\mu$ CT has an inherent link with FEA because FE models of the femur can be constructed directly from CT or  $\mu$ CT images. Due to the high resolutions associated with  $\mu$ CT and increasing recognition of the importance of bone anisotropy for predictions of bone strength and biomechanical behaviour, FEA studies have, in recent years, started to take account of and include aspects of femoral bone anisotropy by incorporating trabecular orthotropy into FE femoral models. As a result, several studies have shown that incorporating anisotropic properties can improve FE model predictions of bone mechanical properties.

Some studies have utilised first generation high resolution peripheral quantitative computed tomography (HR-pQCT) to determine trabecular fabric, usually at a voxel resolution of approximately 80-82 microns (Joshua A. MacNeil and Boyd, 2007; Enns-Bray *et al.*, 2014; Synek *et al.*, 2015) which is sufficient for determining trabecular architectural anisotropic properties using the MIL technique. The MIL technique is considered the gold-standard for assessment of trabecular structural anisotropy when scan voxel sizes are at or below 100 microns.

It has been noted that voxel size affects the accuracy of results describing a number of trabecular (and cortical) based micro-structural parameters including those describing bone anisotropy and BV/TV (Kim, Christopherson, Dong, Fyhrie, & Yeni, 2004; Yener N Yeni, Christopherson, Dong, Kim, & Fyhrie, 2005; Larsson *et al.*, 2014). Isaksson *et al.*, (2011) have recognised that increases and decreases in  $\mu$ CT scan resolution leads can significantly affect the ability to accurately measure trabecular and cortical microstructural parameters. Measures of BV/TV and anisotropy appear particularly sensitive to changes in voxel size. Values for BV/TV have been shown to decrease with increasing voxel sizes while measures of anisotropy display a non-linear relationship with voxel size. The relationships between voxel size and these parameters holds true for resolutions above and below voxel sizes of approximately 80 microns i.e. HR-pQCT resolutions.

Because more accurate measures of bone microstructural parameters are generally obtainable with decreasing voxel sizes (e.g. to approximately 15 microns (Tjong *et al.*, (2012)) and values for BV/TV and measures of anisotropy continue to change with decreasing voxel size below 80 microns (Isaksson *et al.*, 2011), this suggests that any attempts at mapping these parameters throughout the proximal femur with increased resolutions compared to those previously used (approximately 80 microns) may help to improve the quality of data. And because these parameters together explain such a large proportion of bone strength, the performance of FE femoral models built using this data may be improved too.

Typically, trabecular anisotropy is incorporated into FE models by initially calculating trabecular fabric throughout proximal femoral specimens and then incorporating this data into FE models of the same proximal femora. However, the calculated eigenvector data – vector data that describes trabecular orientation in three-dimensional space – is used only to map trabecular orthotropy in FE models (Hazrati Marangalou *et al.*, 2013; Larsson *et al.*, 2014) and no further analysis is done to analyse and explore variation in trabecular fabric.

Given the wealth of information that could be elucidated by analysing trabecular fabric throughout whole proximal femoral and its relevance for determining bone strength, biomechanical behaviour and fracture risk in the ageing femur, this is perhaps wasteful. It has been postulated that there is poor alignment between fall-related principal stress trajectories and principal trabecular orientations in the proximal femur and that because trabecular bone is strongest in these principal directions and weaker in other it is thought that this might be an important factor in determining fracture risk (Homminga *et al.*, 2002).

Therefore, being able to first quantify and discuss specific trabecular orientations in the proximal femur and secondly understand differences in FEA-predicted orientations of principal stress trajectories arising from fall-related impacts and MIL-derived trabecular fabric orientations may help explain to confirm this hypothesis and also help shed light on why certain regions of the proximal femur may be more susceptible to fracture.

Similarly, in studies where trabecular fabric has been analysed, it has been done so using DA. DA gives information on the degree to which trabecular bone is orientated in its primary direction compared to its tertiary direction but it is a dimensionless, scalar entity that gives no implicit directional information. While quantifying DA is useful because it is related to bone strength (Homminga *et al.*, 2002), it nonetheless provides a superficial analysis of the true directionality of trabecular bone for a given bone specimen.

DA has been utilised to show heterogeneity in trabecular architecture in the femur (Tanck *et al.*, 2009). However, although it is assumed that trends in DA will be reflected by trends in actual principal trabecular orientations, no work has been done to test this and it remains unclear what DA means for differences/heterogeneity in actual trabecular orientations. It is therefore important to quantify and understand heterogeneity in principal trabecular architectural orientations to test this relationship and aid understanding of how each of these parameters contributes to bone strength.

A single study has sought to go beyond DA and specify trabecular orientations in the proximal femur (Chiba *et al.*, 2013). Although such an approach is welcome, this study was restricted to femoral head samples which although important for load bearing and associated with fracture, are not a critical region for femoral fracture. Additionally, angular orientations were calculated relative to the coordinate system axes used for scanning. Therefore, it is unclear how comparisons made between specimens in this study were affected by differences in positioning during scanning. This approach also makes it difficult to compare data obtained in Chiba *et al.*, (2013) with new studies taking a similar approach for the exact same reason.

While the analysis conducted by Chiba *et al.*, (2013) of heterogeneity in principal trabecular directions within femoral head was highly detailed, data across subjects was pooled with between-subject comparisons being made which might mask inter-subject variability in trabecular microstructural arrangement. Thus, while variance within the femoral head was analysed, it is unclear to what degree variance exists between individuals for principal trabecular orientations.

Finally, multiple studies analysing trabecular anisotropy have taken advantage of high resolution  $\mu$ CT to image trabecular bone but analyses have been restricted to a small number of sub-regions taken from larger anatomical regions (Milovanovic, Djonic, *et al.*, 2012; Saers *et al.*, 2016). Sampling from and analysing a small number of sub-regions has some practical advantages but also some limitations.

The implicit assumption when taking this approach is that trabecular fabric data obtained from a small number of sub-regions will be representative of trabecular fabric throughout the whole specimen from which samples are taken or of larger anatomical regions within that specimen. The proximal femur is considered to display great heterogeneity in trabecular architectural organisation and material properties, even within anatomical regions such as the femoral head (Chiba *et al.*, 2013).

It is therefore conceivable that data from just two trabecular sampling regions which are in close proximity to each other may vary greatly in values for the same trabecular bone parameter(s). This might be especially true for ageing bone where it has been shown that degradation of bone quality can lead to differences within and between regions (Tanck *et al.*, 2009).

Taking all this into account, chapter 4 of this thesis attempts to address the issues outlined in this review. Its specific aims and objectives are outlined below.

### 3.1.1 Aims:

1. To quantify trabecular fabric and bone volume fraction (BV/TV) throughout five ageing proximal femora at resolutions below 80 microns.
2. To validate and map trabecular fabric throughout the trabecular region of the ageing proximal femora to facilitate construction of subsequent orthotropic FE models (chapter 6).
3. To specify principal trabecular fabric directions and use this data to investigate and test for variation in the principal trabecular fabric directions within and between the ageing proximal femora for the femoral head, superior femoral neck and inferior femoral neck regions.

### 3.1.2 Objectives:

- $\mu$ CT scan five ageing proximal femora at 68 – 72.9 microns.
- Develop custom-written MATLAB code to virtually split scans into discrete cubic regions to facilitate mapping and analysis of trabecular fabric and BV/TV throughout the trabecular compartments of proximal femora.
- Conduct MIL and BV/TV analysis using BoneJ to derive principal trabecular architectural fabric.
- Develop further custom-written MATLAB code to permit selection of trabecular orientations in the femoral head, superior femoral neck and inferior femoral neck.
- Develop further custom-written MATLAB code to convert selected eigenvector data into three-dimensional angle and ratios for analysis and discussion.
- Statistically analyse trabecular orientations in the femoral head, superior femoral neck and inferior femoral neck within and between femora.
- Use orthotropic data as input parameters in subsequent FEA simulations (chapter 6).

## 3.2 MDA

Despite their proportionately small incidence rate amongst fallers, hip fractures are one of the most serious fall-related injuries; they have a mortality of 10% at one month and 30% at

one year (NICE, 2011) and cost UK hospital an estimated at £1.1 billion annually (Leal *et al.*, 2016). While changes in bone structural and material properties with increasing age have a significant effect on fracture risk, nearly all hip fractures are caused by falls (Grisso *et al.*, 1991).

Therefore, understanding the ways in which falls contribute to hip fracture risk is essential in formulating preventative strategies and understanding its aetiology. Research delineating the relationship between falls and hip fracture has illustrated that fall-type as well as the magnitude and direction of loading on the proximal femur from a fall, contribute to hip fracture risk.

For example, it has been shown that people who fall during turning are at greater risk of fracturing their hip (Thigpen *et al.*, 2000a). Others have shown that the direction of the impact load relative to the proximal femur, which is largely determined by the characteristics of a fall, has an effect on ultimate bone strength and thus likelihood of fracture (Keyak, Skinner and Fleming, 2001; Bessho *et al.*, 2009; Wakao *et al.*, 2009).

Sideways falls in particular appear to confer a high risk of hip fracture (Kannus *et al.*, 2006). Thus, while only 1 – 2% of falls are thought to result in hip fracture, the risk of hip fracture associated specifically with a sideways fall is estimated to be 20 times higher (Parkkari *et al.*, 1999).

The differences in fracture risk attributed to fall types and fall-related loading directions hints that there are factors intrinsic to each fall-type that influences fracture risk. Multiple parameters are associated with both falling and hip fracture risk including impact velocities, force magnitudes and fall kinematics and it is likely that the variation that occurs in parameters like these during differing fall types may influence the likelihood of hip fracture. MDA offers a methodological platform in which to predict and study this variation.

MDA has been used in a variety of contexts including modelling running economy in extinct and living taxa (Sellers and Manning, 2007; Sellers *et al.*, 2010), how surgical procedures might affect muscle moment arms (Delp, Ringwelski and Carroll, 1994), human gait (Sellers *et al.*, 2004; Piazza, 2006; Ren, Howard and Kenney, 2006; Ren, Jones and Howard, 2007a; Ren, Richard K. Jones and Howard, 2008) and traumatic injury and falls (Doorly and Gilchrist, 2006, 2009; Forero Rueda and Gilchrist, 2009).

Although often based on real-world kinematics collected in laboratory settings, MDA computer simulations of human movement allow for the prediction of parameters with repeatability and precision, which can be difficult to achieve experimentally. This is especially true for the prediction muscle forces where methodological approaches such as EMG cannot specify and attribute forces to specific muscles but MDA can. Additionally, MDA facilitates collection of data, e.g. impact forces, which would otherwise be difficult to obtain physically and/or repeatedly due to ethical and safety concerns.

This makes MDA an obvious candidate and potentially very useful tool for the study of falls and as an indirect way to investigate hip fracture. This is particularly true given that there is a noticeable lack of EMG data on muscle activity during sideways falls. Bisdorff *et al.*, (1999) investigated EMG muscle activity in falling subjects. However, subjects fell from a couch and it is isn't clear how well hip muscle activity during the fall correlates to that which occurs during a sideways fall from standing height. Additionally, EMG data for the leg was taken for the quadriceps only. Quadriceps muscles however insert only on to the very distal part of the proximal femur and their effect on stress patterns in critical regions for femoral fracture are likely to be small. Finally, EMG data was taken only at the onset of falling and not at the moment of impact which is when hip fracture usually occurs. Wicke and Oman (1982) also used EMG to study muscle activity during a fall but their study only recorded EMG activity during the fall rather than at impact and was restricted to muscles which, as with Bisdorff *et al.*, (1999), are likely have only minor effects on stresses in critical regions of the proximal femur for fracture. More recently Phinyomark *et al.*, (2012) investigated muscle activity during fall prevention exercises and while other have applied EMG to fall detection (Leone *et al.*, 2015) which is more concerned with fall initiation than fall termination.

Therefore, although MDA suffers from many practical shortcomings in relation to its ease-of-use and application in clinical contexts, it can account for factors (e.g. impact force magnitudes and muscle forces etc.) related to fracture risk that more traditional assessment tools like DEXA, FRAX and EMG alone cannot. MDA represents an attractive methodological approach that can be seen as complimentary to  $\mu$ CT, EMG, FEA, DEXA and/or FRAX.

MDA has been used to study falls but much of this research has focused on the relationships between falls and traumatic head injuries or other contexts outside of hip fracture. For example Doorly and Gilchrist, (2006) & (2009) have used MDA to examine fall-related brain injury and Forero Rueda and Gilchrist, (2009) have investigated falls from climbing apparatus in children. In any of those studies, only impact forces are quantified and the conclusions have

limited value for the study of hip fracture in older people given their focus on other anatomical regions and younger demographics.

Currently, only a limited number of studies have employed MDA as a tool with which to analyse fall-related hip fracture. Kłodowski, Valkeapää and Mikkola (2012) demonstrated how flexibility could be introduced into the usually rigid bodies of MDA musculoskeletal models to predict strain in the femur. Similarly, (Hirabayashi *et al.*, 2013) combined MDA and FE models to predict impact forces acting on the hip joint due to a backwards fall. More recently, Luo *et al.*, (2013) & Sarvi *et al.*, (2014) elucidated that by using subject specific MDA models of sideways fall, impact forces could be more accurately predicted.

Experimental research into falls (i.e. outside of MDA and other *in silico* work) has illustrated general trends and relationships between fall orientation and fracture risk but a detailed picture of nuances in the relative contribution of the components of impact forces attributed to specific fall types and their potential effect on hip fracture has not yet been studied. But there is little research delineating the pattern of (and variation in) loading at the hip associated with a specific fall type.

Given sideways falls confer a great risk of fracture, there is perhaps something specific to the resultant impact force associated with them that modifies femoral stresses in such a way as to increase fracture risk. MDA could help to address this issue because it is possible to model impact forces across multiple simulations and construct a detailed picture of the contributions of the individual X, Y and Z impact force components to each resultant force. Understanding how they relate to stress patterns within the proximal femur, e.g. through FEA, could in turn help inform about femoral fracture.

Viceonti *et al.*, (2012) used MDA to investigate spontaneous hip fracture and demonstrated that, for individuals with low (e.g. osteoporotic) bone quality and reduced neuromuscular control, muscle forces could be sufficient to cause fracture of the proximal femur. To this author's knowledge this study represents one of only several attempts at elucidating the relationship between hip muscle forces and femoral fracture. However, spontaneous hip fracture is a specific and unusual type of femoral fracture that is thought to occur during gait. It is therefore unclear how relevant this study is for hip fractures resulting from falls.

More recently, it has been demonstrated that hip musculature could have a protective role against fall-related fracture risk in the proximal femur by reducing stresses and strains in the femoral neck (Choi, Cripton and Robinovitch, 2014) but arbitrarily chosen muscle forces were

utilised and only a small number of muscles modelled in this study. It is therefore unclear whether the forces applied to the synthetic femur used were accurate and elicited an appropriate biomechanical response.

Given that muscle force magnitudes alone are thought sufficient to cause spontaneous fracture of the proximal femur during bipedal gait (Viceconti *et al.*, 2012), their contractile activity could have a significant influence on stresses experienced in the proximal femur from a fall-related impact. Choi's study demonstrates this point well but further work is clearly needed to understand what this influence might be.

Given the limitations associated with EMG and other experimental approaches in quantifying muscle forces during human movement, MDA offers an alternative approach for accomplishing this. MDA could help to address this issue because it allows for the prediction of internal (e.g. muscle) mechanical loads. Being able to quantify these forces is a first step towards understanding how they might modify fall-related stress patterns within the proximal femur, e.g. through FEA, and ultimately offer new perspectives on the process of femoral fracture.

Taking all this into account, it is thought that quantifying both sideways fall-related impacts and muscle forces may be important for understanding fall-related stresses in the proximal femur and more generally, increase understanding about the mechanisms and risk of femoral fracture. MDA provides an excellent tool by which this can be achieved. By utilising a human musculoskeletal model that approximates skeletal geometry, body mass, joints, muscle-tendon properties and interactions between the musculoskeletal model and external environment, it will be possible to predict sideways falls, such as muscle and impact forces, for a given kinematic sequence e.g. a fall.

Chapter 5 of this thesis therefore attempts to address these issues and its specific aims and objectives are outlined below:

### **3.2.1 Aims:**

1. To simulate five real-world sideways falls onto the hip using MDA.
2. To quantify MDA-predicted impact and hip muscle forces that occur at impact during these simulated sideways falls for use in subsequent FE simulations (chapter 6).

3. To investigate variation in impact and hip muscle forces across simulated falls to explore the potential relationship between these parameters and sideways fall specifically.

### 3.2.2 Objectives:

- Conduct five separate kinematic recordings of a single, young, healthy subject falling sideways onto their hip.
- Use and modify an existing musculoskeletal model with appropriate musculoskeletal and interaction parameters.
- Combine a genetic algorithm (GA) optimisation routine and a forwards dynamics approach to match model kinematics to recorded real-world fall kinematics.
- Derive and perform statistical analyses of impact and muscle force parameters.
- Use impact and muscle force data as input parameters in subsequent FEA simulations (chapter 6).

## 3.3 FEA

FEA reduces complex geometries like that seen in the femur, into a finite number of small, discrete but interconnected elements. The elements are constrained in three-dimensional space by the geometry of the structure they represent and can incorporate representative material and micro-structural properties.

When modelling bone, computed tomography (CT) scans are usually used to define the geometry of the finite element (FE) model and the material properties of its constituent elements. After simulating applied forces to the model, it becomes possible to analyse the deformations and stresses it experiences and place these findings within the context of bone strength and likelihood of fracture.

FEA currently lacks the speed and practicality of DEXA scans within a clinical setting. Some attempts have been made to automate the construction of FE models of the femur (Viceconti *et al.*, 2004) and recent advances in computing power have aided the speed with which patient specific FEA models of the hip can be constructed. Nonetheless, compared to the time

and effort required to conduct and analyse DEXA scans, the process of FE model construction and analysis is still time consuming and its feasibility for use in a clinical setting is therefore somewhat compromised and yet to be fully realised.

Despite this, FEA's ability to incorporate three-dimensional biomechanical characteristics of the femur as well as quantify the effect applied forces have in terms of fracture risk means it generally predicts fracture more accurately than do assessments of BMD and lifestyle factors via DEXA and FRAX (Engelke *et al.*, 2013; Zysset *et al.*, 2013, 2015; Kopperdahl *et al.*, 2014; van Rietbergen and Ito, 2015; Engelke, van Rietbergen and Zysset, 2016). In turn, this makes it an attractive alternative to DEXA and FRAX, that with further efforts to increase its efficiency and efficacy, could become a powerful clinical assessment tool.

FEA has been used to improve understanding of a number of bone related topics including fracture behaviour, bone remodelling, bone and orthopaedic implant interactions, bone material properties and more generally, the relationship between whole bone geometry, material properties and mechanical loading (Taghizadeh *et al.*, 2016). FEA has proved to be especially useful in aiding the understanding and prediction of the process of hip fracture. Given the grave socioeconomic impact of hip fracture, continued efforts have been made to improve the power of the FE method to predict and ultimately prevent its occurrence.

CT-based finite element models have been shown to perform better in the prediction of bone strength and fracture risk compared to DXA; the clinical gold standard for assessing bone strength and fracture risk (Cody *et al.*, 1999; Dall'Ara *et al.*, 2012; Janne E M Koivumäki *et al.*, 2012; Edwards, Schnitzer and Troy, 2013) with results from FEA simulations of hip fracture generally demonstrating good agreement with experimental results (Dall'Ara *et al.*, 2013a).

Nonetheless, further efforts are required to improve FEA's predictive ability because discrepancies still exist between FEA and experimental results. These discrepancies, in part, reflect the choice of material properties used by researchers to model femoral bone and in part reflect the choice of boundary conditions (e.g. simulated loads and model constraints) chosen by researchers to model the loading conditions to which the femur is subjected to during a sideways fall.

In terms of material property assignment, many studies have constructed isotropic FE models of the femur (Helgason, Taddei, *et al.*, 2008; Langton, Pisharody and Keyak, 2009; Janne E.M. Koivumäki *et al.*, 2012; Dall'Ara *et al.*, 2013b; Nawathe *et al.*, 2014; Nishiyama *et al.*, 2014; Liebl *et al.*, 2015). One of the advantages of this approach is the simplicity in which isotropic

properties can be assigned to FE models (because no prior knowledge of bone architectural arrangement is required) using well known power-law relationships between bone density and elastic constants (Helgason, Perilli, *et al.*, 2008). Despite the fact that, generally speaking, there is good agreement between results obtained from isotropic FE models and experimental results (Dall'Ara *et al.*, 2013a), there is still a need to improve the accuracy with which bone material properties are modelled in order to properly capture bone biomechanical behaviour and thus better predict fracture risk.

More recently, a number of studies have looked to the inclusion of anisotropic parameters in FE femoral models to achieve this and to explore differences in the performance of anisotropic and isotropic models (Trabelsi and Yosibash, 2011). San Antonio *et al.*, (2012) elucidated differences in strain of up to 14% between anisotropic and isotropic FE models of the femur under loading. Some studies have shown that including anisotropic properties can improve how well FE femoral models predict femoral bone stiffness (Hazrati Marangalou, Ito and van Rietbergen, 2012). Luisier, Dall'Ara and Pahr, (2014) found that including anisotropic parameters improves prediction of the ultimate strength of the proximal femur during stance (7%) and sideways falls (1.2%) although the latter improvement was not statistically significant. Nawathe *et al.*, (2014) incorporated trabecular anisotropy into their finite element models to explore microstructural failure mechanisms in the ageing femur during a sideways fall and showed that, particularly for weaker bones with less structural redundancy, structural failure began in trabecular bone before propagating out to the cortical shell.

Differences and improvements in the prediction of indices such as these and the processes governing fracture initiation are unsurprising given that there exists a close relationship between bone's architectural and material axes (Cowin, 1985) and the contribution of trabecular fabric to bone strength (Hosseini, Maquer and Zysset, 2017). These studies therefore suggest that incorporating anisotropic data into FE simulations can improve femoral FE model performance. As such, there is a valid argument that anisotropy should be included within FE models whenever the biomechanical response of bone to loading is being modelled and a number of studies have sought to do just this.

These studies have made important contributions but there are a number of issues associated with these studies. Peng *et al.*, (2006) used global axes as a surrogate for defining a homogenous orthotropic fabric scheme throughout a FE model of the femur but this bears little resemblance to the biological reality of trabecular architectural arrangement in the femur and results, perhaps as a consequence of this, showed little difference to those from

isotropic FE models. Other studies have utilised principal stress trajectories from FE simulations to define a varying trabecular fabric throughout the FE model (San Antonio *et al.*, 2012). There are well-established practical and theoretical arguments for doing this but as yet there has been no rigorous validation of the technique.

A number of other studies have incorporated trabecular anisotropic data obtained directly from HR-pQCT scans of whole proximal femoral specimens into FE models (Hazrati Marangalou, Ito and van Rietbergen, 2012; Hazrati Marangalou *et al.*, 2013; Synek *et al.*, 2015; Enns-Bray *et al.*, 2016; Sornay-Rendu *et al.*, 2017). But HR-pQCT derived eigenvector data might lose some accuracy due to HR-pQCT voxel resolutions and it is uncertain how well proposed calibration equations (e.g. (Varga *et al.*, 2011; Luisier, Dall'Ara and Pahr, 2014)) address this issue. More certain, is that increasing scan resolution will generally improve the prediction of both femoral structural anisotropy and ultimate strength (Luisier, Dall'Ara and Pahr, 2014).

Two studies have used  $\mu$ CT scans to build FE models of the proximal femur (Verhulp, van Rietbergen and Huiskes, 2008; Nawathe *et al.*, 2012). However, the study sample from (Verhulp, van Rietbergen and Huiskes, 2008) was limited to only two specimens which were modelled as having isotropic, homogenous and single bone material properties and the voxel resolution of 80 microns represents only a very slight improvement on that obtained with HR-pQCT. Nawathe *et al.*, (2012) addressed these limitations to some extent by increasing both the sample size and voxel resolution. However bone was again treated as a homogenous and single isotropic material and how accurate these properties are and what effect they have on results remains unclear.

(Luisier, Dall'Ara and Pahr, 2014) suggested that anisotropic models of the femur did not significantly improve predictions of femoral ultimate strength during a sideways fall. However, it is difficult to assess how accurate this conclusion is because the material parameters assigned to trabecular bone in the femoral models were taken from human vertebral studies, cortical bone was modelled as isotropic and the fall loading configuration tested was relatively simple and did not consider loading from hip musculature or differences in loading direction.

Some have recognised how different loading directions might influence femoral fracture risk (Keyak, Skinner and Fleming, 2001; Bessho *et al.*, 2009; Wakao *et al.*, 2009). As a result, these studies have looked beyond bone material properties, instead using FEA to focus on the loading directions the femur is subject to during a fall as a way of improving the predictive ability of FEA for hip fracture and indicated that the femur might be weakest and at the

greatest risk of fracture due to impacts arising from falls in the poster-lateral direction (Keyak, Skinner and Fleming, 2001; Bessho *et al.*, 2009; Wakao *et al.*, 2009).

Despite the findings of Keyak, Skinner and Fleming, (2001), Bessho *et al.*, (2009) and Wakao *et al.*, (2009) much of the current literature tends not to address this potentially important issue and there is a tendency to model just a single impact load in FE simulations representing an impact from a fall with the ground. Yet, as has been demonstrated in chapter 4 of this thesis, kinematically similar sideways fall sequences can result in a variety of loading configurations acting on the proximal femur and these in turn may change the stress distributions in the proximal femur and may therefore relate to an increase or decrease in hip fracture risk.

The loading conditions defined in FE simulations in a number of studies have been determined by an experimental set-up destructively testing cadaveric specimens against which the FE femur model is validated (e.g. Luisier, Dall'Ara and Pahr, 2014). This can elucidate very important information about how accurately FE models represent real world outcomes e.g. the experimental set-up. But even if the FE model shows good affinity (e.g. Yosibash, Tal and Trabelsi, 2010; Schileo *et al.*, 2007, 2008; Nawathe *et al.*, 2014), this does not mean it will predict fracture outside of an experimentally controlled environment. This is because the experimentally controlled (*i.e.* loading) environment does not necessarily reflect the loading conditions to which a femur is subjected to during a fall because it does not account for differences in the direction of the impact load nor the numerous other forces (e.g. from hip muscles) acting on the femur.

In this respect, a handful of studies have modelled more complex loading scenarios by applying relevant muscle forces to femoral FE models (e.g. San Antonio *et al.*, 2012). Nonetheless, the number of muscles modelled has been limited with only rare exceptions (e.g. A. T.M. Phillips, 2009). Furthermore, studies that have included loading from hip musculature in FE simulations only model forces that occur during stance or certain other locomotive patterns such as standing or stair climbing (Lotz, Cheal and Hayes, 1995; Duda *et al.*, 1998; Speirs *et al.*, 2007; A. T.M. Phillips, 2009).

However, a large number of muscles act on the proximal femur at any given time, have varying lines of action and some (e.g. gluteus maximus) are amongst the strongest in the human body. Given the role attributed to hip musculature in both helping to safeguard against hip fracture (Matheson *et al.*, 1971; Dalla Pria Bankoff, 2012; Choi, Cripton and Robinovitch, 2014) and causing it in cases of spontaneous hip fracture (Horiuchi *et al.*, 1988; Cristofolini *et al.*, 2007;

Viceconti *et al.*, 2012), hip musculature could have a significant influence on the loading patterns witnessed in the proximal femur during a sideways fall and may help negate against or contribute to fracture risk.

Choi, Cripton and Robinovitch, (2014) represents the only study, through the use of mechanical as opposed to computer simulation experiments, attempting to explore the role of hip musculature at the moment of impact from a fall on to the hip. The results hint that hip musculature plays an important role in hip fracture risk but their use of a synthetic femur, a limited number of muscles and arbitrary muscle forces make it unclear how applicable the conclusions drawn from this study are for hip fracture.

Taking these findings on the potential significance of the hip musculature for fracture risk into consideration, it is perhaps surprising that no FE study to date has considered how a broad range of hip muscle forces coincident with an impact force resulting from a sideways fall might relate to both the aetiology and likelihood of femoral fracture.

Chapter 6 of this thesis attempts to address these issues and its specific aims and objectives are outlined below:

### **3.3.1 Aims:**

1. To construct subject-specific, orthotropic FE models of five ageing proximal femora.
2. To investigate how hip muscle forces concurrent with an impact force (both predicted by MDA in chapter 4) can affect observed stress patterns in the femoral neck region in FE simulations.

### **3.3.2 Objectives:**

- Segment  $\mu$ CT scans of proximal femoral specimens used in chapter 4 to define FE model geometry and cortical/trabecular bone compartments.
- Create fully orthotropic models by:
  - Developing custom-written MATLAB code and a protocol to incorporate orthotropic trabecular fabric data obtained in chapter 4 into FE models.
  - Defining cortical orthotropic directions based on femoral surface geometry.

- Construct simplified hip musculature within FE simulations and apply impact and hip muscle forces, derived in chapter 5, to FE models.
- Run multiple FE simulations and quantify von Mises and principal stresses in the femoral neck region to determine how hip muscle forces concurrent with an impact force modify femoral neck stress patterns compared to simulations that model impact forces only.

## 4 DETERMINING THE ANISOTROPY AND BONE VOLUME FRACTION OF TRABECULAR BONE IN THE AGEING PROXIMAL FEMUR USING MICRO-COMPUTED TOMOGRAPHY

---

### 4.1 INTRODUCTION

Femoral bone strength is influenced by bone density and three-dimensional structural parameters. Assessing and predicting fracture risk in the femur is therefore dependent not only on quantifying bone density but also upon quantification of trabecular microstructural features. Together, both density and fabric parameters are thought to explain nearly all the observed variation in bone strength (Musy *et al.*, 2017). As a result, recent work has sought to include trabecular orthotropic properties into biomechanical models and explanations of femoral bone strength and fracture risk.  $\mu$ CT is a three-dimensional imaging modality that, due to its high scan resolutions, can be used to quantify trabecular microstructural parameters including bone density (BV/TV) and trabecular fabric.

Because of their relevance for bone strength and fracture risk, a number of studies have sought to map trabecular fabric and BV/TV throughout proximal femora and then incorporate both these parameters into FE femoral models (e.g. Baca *et al.*, 2008; Schneider *et al.*, 2009; Hambli, Bettamer and Allaoui, 2012; San Antonio *et al.*, 2012a; Synek *et al.*, 2015). However, in these studies no quantification or analysis of trabecular orientation was conducted. Others have described trabecular anisotropy using DA which offers no information on actual trabecular orientations (Homminga *et al.*, 2002). Furthermore, while a single study has explored variation in trabecular orientation for the femoral head (Chiba *et al.*, 2013), there are no studies that have analysed this parameter in other femoral regions or investigated inter-specimen variation between regions. But being able to quantify trabecular orientations is important because the relationship between trabecular orientation and fall-related principal stresses is thought to contribute to fracture risk (Tanck *et al.*, 2009).

Most studies using  $\mu$ CT to map trabecular fabric throughout whole proximal femora have been limited to voxel sizes of 80 microns or more (Joshua A. MacNeil and Boyd, 2007; Enns-Bray *et al.*, 2014; Synek *et al.*, 2015). While this is sufficient to describe trabecular bone parameters, it has been shown that decreasing voxel sizes below this size, even by small increments (e.g. 14 microns), improves the accuracy of trabecular bone parameter data

(Isaksson *et al.*, 2011). Any improvements in voxel size should therefore be welcomed; more accurate data be derived and this in turn can be used to improve FE model performance.

Other studies looking at femoral trabecular fabric have relied on sampling only a limited number of or small anatomical regions in the proximal femur to describe trabecular structure throughout the proximal femur (Milovanovic, Djonic, *et al.*, 2012; Saers *et al.*, 2016). Due to heterogeneity in trabecular architecture in the proximal femur, this approach might mask gross trends in trabecular fabric and BV/TV, somewhat limit the extrapolation of these findings to specific femoral regions.

Therefore, there is currently a lack of knowledge about the specific directions trabecular architecture takes within and between proximal femoral regions as well as the variation that exists in trabecular fabric between ageing femora is lacking. The current chapter aims to address these issues.

Specifically, it aims to use  $\mu$ CT to map trabecular fabric throughout whole, multiple ageing proximal femur so this data can be used to construct orthotropic FEA models of the proximal femur (chapter 6). This chapter also aims to develop a method of analysis for quantifying and describing principal trabecular orientations to explore variation in principal trabecular orientations for the femoral head and neck and, in chapter 6, investigate the relationship between fall-related principal stresses and principal trabecular orientations.

This will be achieved using with smaller voxel sizes and a larger number of sampling regions compared to studies conducted previously to that which has been used previously. It is hoped that both these factors will help to capture and quantify trabecular architectural arrangement more accurately and ultimately improve FE model performance in chapter 6.

## 4.2 METHODS

### 4.2.1 Study Sample

In total, five cadaveric proximal femora were obtained for the purposes of this study. The five proximal femora were formalin fixed, were all from the right leg and were from old individuals (67-95 years of age, 3 female, 2 male) (table 4-1). All specimens were cut just below the lesser trochanter and therefore comprised only the most proximal part of the femoral bone.

**Table 4-1 Donor information.** Age, sex and cause of death of donors from which proximal femoral specimens came.

| Donor | Died Date  | Age at Death | Sex | Cause of Death                |
|-------|------------|--------------|-----|-------------------------------|
| 152J  | 18/01/2010 | 90           | F   | OLD AGE                       |
| 186K  | 22/11/2011 | 95           | F   | PNEUMONIA                     |
| 187K  | 25/11/2011 | 67           | F   | PULSELESS ELECTRICAL ACTIVITY |
| 190L  | 12/02/2012 | 84           | M   | SEPTICIAEMIA                  |
| 210M  | 06/05/2013 | 93           | M   | BRONCHOPNEUMONIA              |

#### 4.2.2 $\mu$ CT Scanning

All femurs were packed in heat sealed, clear plastic bags prior to scanning. For scanning, the femoral specimens, inside the sealed bags, were placed in the chamber of a Nikon XTH225ST  $\mu$ CT scanner at the National Composites Centre (NCC), Bristol, UK. Specimens were clamped at their distal ends, just below the lesser trochanter, to constrain movement in rotational and translational directions. All specimens were orientated in the same way with respect to the scan chamber. The specimens were scanned at 75kV and with an isotropic voxel size of either 68 microns (one specimen) or 72.9 microns (four specimens). The resulting images were exported as .TIFF files and each image stack consisted of between 1218 – 1834 slices in the transverse plane, with the total number depending on the physical dimensions of the femur and voxel resolution.

#### 4.2.3 Splitting of $\mu$ CT Scans into Cubes

Femoral  $\mu$ CT scans were split, computationally, into multiple, discrete cubic regions for subsequent analysis of bone volume fraction and trabecular architectural anisotropy. Cube shaped regions were picked to discretise the scans into sub-regions for several reasons. Firstly, they ensure all cube regions and their associated bone parameters are separate from one another because the faces belonging to each cube can be exactly aligned with those surrounding it. Secondly because all cubes can be exactly aligned with each other, the sampling space for deriving parameters, *i.e.* the trabecular core, can be maximised in terms of filling it with as many sampling regions as possible. Both features make sense in terms of subsequent mapping and analysis of bone parameters because these parameters will be specific to the region from which they were sampled, due to a lack of overlap between cubes but also continuous throughout the trabecular core due to the exact alignment of each cube with respect to others.

A custom-written MATLAB script (Appendix B, 'cube\_generation' function) (The Mathworks Inc., 2016) was developed (Jafar Alsayednoor personal communication 2015) to split scans into three-dimensional cubes of 5mm<sup>3</sup>. This size was chosen because it has been shown as sufficient to properly capture architectural anisotropy in bone (Cowin and Telega, 2003).

The script split femoral specimens into bone cubes (figure 4.1) using a grey value threshold of 100. This value was picked because trials using this value qualitatively demonstrated a good level accuracy in selecting bone and non-bone regions. A total of between 529 and 1105 cubes were created *per* femur depending on the original specimen dimensions. Resulting image stacks for each cube contained either 73 or 69 images with the number of slices dependant on the original scan resolution.

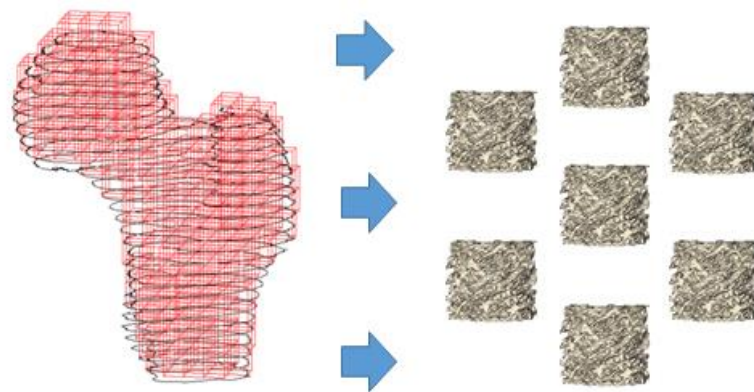


**Figure 4.1 Virtual splitting of  $\mu$ CT scans into cubes.** Representation of how femoral scans were split into discrete but interconnected, three-dimensional, 5mm<sup>3</sup> bone cubes using custom written MATLAB scripts.

All bone cube image stacks for all specimens (3590 cubes in total) were then manually inspected so that any image stacks containing image slices with empty space outside of the femoral bone geometry and/or areas of cortical bone could be excluded (figure 4.2); including areas of cortical bone or regions of space outside the femoral geometry would adversely affect the quality of the data describing the chosen bone parameters.

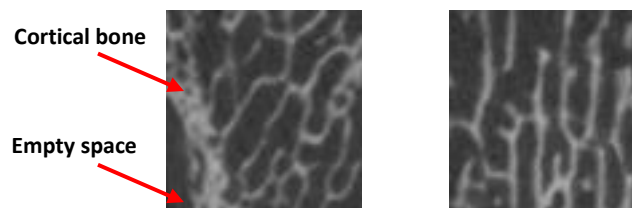


**Figure 4.2 Bone boundaries.** **Left:** Image slice from bone cube image stack showing cortical and empty regions. Bone cubes that contained images like this were excluded from analysis. **Right:** Image slice from bone cube image stack containing only trabecular bone. Only bone cube image stacks fulfilling this criteria were used for analysis.

#### 4.2.4 Trabecular Bone Parameters

BV/TV and trabecular principal architectural directions were calculated for all bones cubes from each femoral specimen. The principal trabecular fabric direction was then calculated and statistically analysed for the femoral head and neck regions due to the susceptibility of the femoral neck for fracture. Results for BV/TV were obtained for FE model construction in chapter 6 and not analysed in the present chapter.

#### 4.2.5 Calculating Trabecular Architectural Anisotropy Using the MIL Method

BoneJ (Doube *et al.*, 2010) was used to conduct the MIL analysis on all bone cubes using a custom-written java script to automate the process (appendix A). The MIL method uses the boundaries between the 'phases' (e.g. bone and marrow) of a material to estimate its architectural anisotropic properties. The traditional formulation of the MIL is to use a grid of parallel lines whose direction and magnitude are defined by the vector,  $\theta$  (figure 4.3).

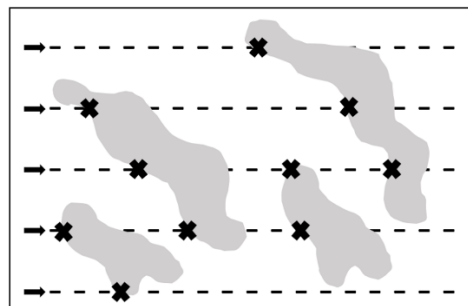


**Figure 4.3 MIL method.** Grid of parallel line vectors passing through material phase interfaces. Each time a line vector hits a new interface between phases, a new intercept is counted for that vector. Here, 10 intercepts are counted (indicated by crosses) (adapted from Moreno, Borga and Ö. Smedby [2012b]).

The total number of intersections  $I(\theta)$  between these lines and the interface between both phases of the material is counted. The MIL with respect to  $\theta$ ,  $MIL(\theta)$  can then be calculated as:

$$MIL(\theta) = \frac{L}{I(\theta)} \quad 4.1$$

Where L is the summation of the length of all lines used. In other words, the MIL is the average distance between two bone/marrow interfaces measured along a test line and its value is a

function of the slope of the line,  $\theta$  (*i.e.* its angle), along which that measurement is taken (Cowin and Mehrabadi, 1989)

Because the MIL method relies directly on the detection and counting of boundaries between bone-marrow phases, it was necessary to convert imaged specimens into binary form. Doing this has the effect that the image distinguishes only these two phases because image voxels belonging to each phase are assigned as either black or white. As such, all bone cube image stacks were converted to 8bit grey scale images. Images were then binarised using the Otsu thresholding method (figure 4.4). This thresholding method was chosen based on a qualitative assessment of its accuracy in binarizing trabecular cube images. Out of all available methods, this qualitatively appeared to binarise images most accurately. Once completed, bone cubes were then analysed for their main orthotropic orientations using the MIL method.

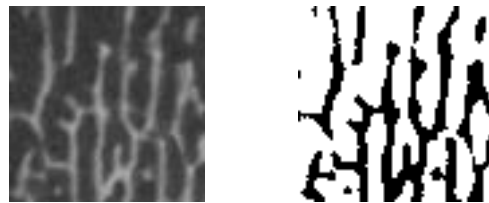


**Figure 4.4 Binarisation of trabecular cubes.** **Left:** Image slice from a bone cube stack showing trabecular (lighter structures) and marrow (darker spaces) phases in original image format **Right:** The same image slice as in left-hand figure but showing trabecular (darker structures) and marrow (white spaces) phases after binarisation.

For two-dimensional problems, Whitehouse (1974) has shown that ellipses are produced on polar diagrams when values of MIL vs  $\theta$  are plotted. Indeed, when test lines are rotated through multiple values of  $\theta$ , and values of  $MIL(\theta)$  are taken, the data fits the general equation for an ellipse closely.

Harrigan and Mann (1984) generalised this result to three-dimensions. They noted that structures like trabecular networks could be represented by an ellipsoid and could therefore be thought of as a quadratic form of a positive definite second rank tensor. A positive definite second rank tensor is represented by a symmetrical matrix,  $M$ , with nine components and which has positive eigenvalues (this latter feature being an essential requisite for quadratic equations that produce ellipsoids). Where  $n$  is a unit vector describing the directions of test lines, Harrigan and Mann (1984) defined a material anisotropy tensor by:

$$\frac{1}{MIL^2(n)} = n \cdot M \cdot n \quad 4.2$$

Cowin (1985) went on to describe a fabric tensor as ‘any symmetric second rank tensor that characterizes the local geometric arrangement of solid material or microstructure of a porous material’. More specifically, Cowin defined a MIL fabric tensor,  $H$ , as the inverse square root of  $M$  by:

$$H = M^{-1/2} \quad 4.3$$

Inverting  $M$  has the consequence that a material’s structural anisotropy and elastic constants can be easily related to one another because increasing values of  $H$  are accompanied by increasing values of Young’s modulus in that direction.

However, it should be noted that BoneJ’s computation of trabecular anisotropy does not go as far as Cowin’s mathematical definition (equation 4.3) and instead uses Harrigan and Mann’s fabric tensor definition (equation 4.2). Nonetheless, by creating and using the second rank tensor  $M$  to calculate trabecular orientations, this approach does fall within the remit of Cowin’s general postulation that a fabric tensor characterizes the architectural arrangement of a material and as such, for the purposes of this study the distinction does not appear to be crucial.

The method implemented in BoneJ also differs slightly from the more traditional ‘line grid’ formulation of the MIL method in that multiple vectors of the same length were constructed within the bone cube samples that originated from the same randomly seeded point and were drawn outwardly from this central point through the sample. Thus, instead of sampling with grids, sampling occurred using sampling ‘spheres’ from which the MIL for that particular region was constructed. For each sampling sphere, every time a vector (50,000 were used per sphere) hit a bone boundary, an intercept was counted for that vector. The MIL for that vector was then the length of the vector divided by number of boundary hits as in equation 4.1.

It was decided to use multiple sampling spheres per bone cube specimen (as opposed to a single sampling sphere) to determine the trabecular orientations of each trabecular cube. This approach helped to remove any bias associated with sampling from a single location as would occur with a single sphere, where regional structure may influence results. Sampling from multiple points helps to (but does not completely) negate this issue because a convergence routine can be adopted; that is, sampling spheres are continually and randomly seeded throughout the bone specimen until results converge and the coefficient of variation falls below 0.005 for the final 100 sampling spheres. Because results from multiple spheres

converge, there can be a degree of certainty that results are representative of the entirety of the structure from which they are derived. The fact that it normally takes several hundred sampling spheres before results stabilise suggests this approach is important. For this reason, a value of 200 sampling spheres per specimen was selected as the minimum number of spheres that could be used to construct the MIL fabric tensor.

Other important factors that might influence the reliability of results include the size of the sampling spheres as defined by the vector line lengths (*i.e.* sphere radius) from the sphere centre and the vector sampling size, which is the distance between sampling points along vector lines. Concerning vector line length, if the sampling sphere is too small with respect to the spatial frequency of features (e.g. bone-marrow boundaries), then the number of counted intercepts may be insufficient for results to be meaningful. For this reason, a vector length of 1.2mm was chosen. This value represented a compromise between ensuring vector lines were of sufficient length compared to phase spatial frequency and ensuring that significant portions of the outer borders of bone specimens were not excluded from analysis; a distance equal to the sampling sphere radius is used between the image border and the sampling point so that nothing outside of the image bounds is used during analysis.

With regards to the vector sampling size, as already discussed, the MIL method relies directly on the detection and counting of boundaries between phases. A boundary is counted when adjacent sample points belong to different phases. If the sampling size was too large, it is conceivable that multiple boundaries would not be counted and any results would be inaccurate. Taking this into account, a conservative vector sampling size was chosen that was approximately half the size of the image pixel spacing. This made certain that sampling points would fall within and therefore capture the presence of different phases across entire bone specimens.

Utilising the data produced from multiple sampling spheres, a three-dimensional cloud of points was constructed for each specimen with each of these points representing the value resulting from multiplying the vector line length by its MIL (figure 4.5). This cloud of points was then fitted to an ellipsoid.

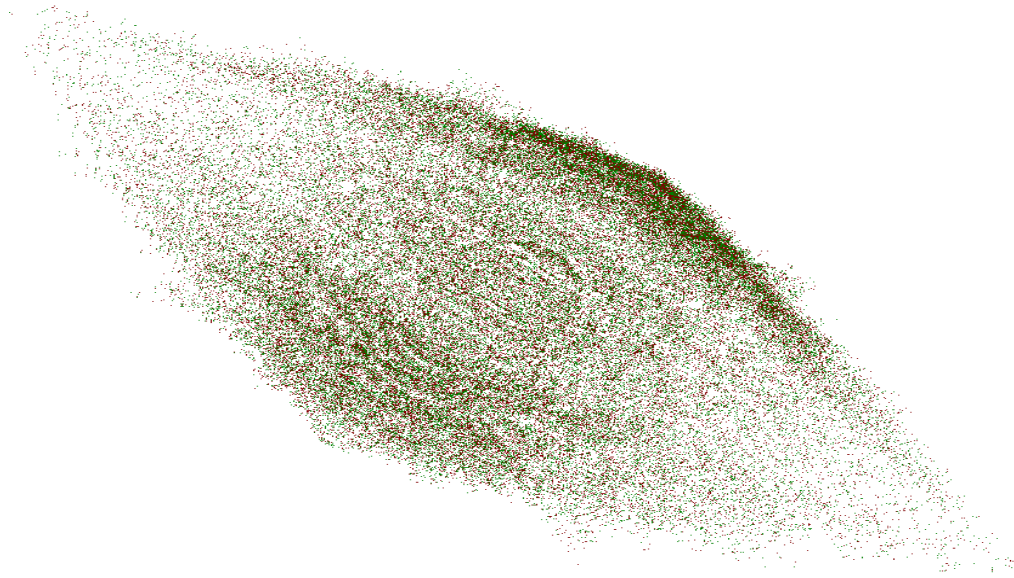


**Figure 4.5 MIL point cloud.** A three-dimensional visualisation of the MIL vector point cloud from a single bone cube. This cube displayed a high degree of anisotropy and therefore the cloud has a long primary axis relative to the two remaining axes orthogonal to it. It is easy to see how an ellipse can be fitted to an MIL point cloud.

For each cube, BoneJ then applied an eigendecomposition to  $M$ , and this resulted in three eigenvalues that indicated the length of the bone cube's ellipsoid's axes and three eigenvectors (essentially unit vectors comprised of X, Y and Z Cartesian coordinates describing direction in three-dimensional space) that denoted the orientations of these axes. The largest eigenvalue indicates the shortest axis, the intermediate eigenvalue indicates the intermediate axis, while the smallest eigenvalue indicates the primary material axis because the radius of each of the ellipsoid's three orthogonal axes is related to mean spacing in that direction and each eigenvalue,  $\lambda$ , is related to the radius of the ellipsoid,  $r$ , by:

$$r = \frac{1}{\sqrt{\lambda}} \quad 4.4$$

By determining the principal fabric directions in trabecular bone structures, it is possible to assign to them specific values for Young's modulus based on an orthotropic material definition and the assumed relationship between bone's principal elastic and fabric orientations (Cowin, 1985). The largest or primary axis is assigned the largest of value of Young's modulus. The intermediate axis is assigned an intermediate value for Young's modulus. And the smallest axis is assigned the smallest value of Young's modulus.

#### 4.2.6 Calculating Bone Volume Fraction

Bone volume fraction can simply be defined as the volume of mineralised bone per unit volume of the reference specimen. A voxel based approach was taken to calculate BV/TV in BoneJ. This approach required prior conversion of all bone cube image stacks into binary form so that the trabecular network and marrow spaces were represented only by black and white voxels respectively. Therefore, the bone cube image stacks that had already been converted to 8bit grey scale images and binarised using the Otsu thresholding method (figure 4.4) were used, based on the prior qualitative assessment of this method's accuracy in binarizing trabecular cube images. BV/TV was then calculated as the total number of bone voxels divided by the total number of voxels in the image stack.

#### 4.2.7 Plotting Trabecular Orientations

Trabecular orientations throughout each proximal femur were plotted in order to a) validate the accuracy of the MIL method used by allowing a direct comparison between these orientation plots and the original  $\mu$ CT scan images and b) facilitate subsequent statistical analysis within and between specimens to explore variation associated with this parameter. Custom-written MATLAB scripts were used to achieve this and semi-automate the process.

Because there was incongruence between the  $\mu$ CT scanner coordinate system and the coordinate system used in BoneJ to calculate trabecular anisotropy, it was necessary to rotate all eigenvectors 90 degrees about the Y-axis so all eigenvectors were orientated in the correct directions relative to the bone cube positions.

Once completed, eigenvector values were associated with the origin coordinates denoting the bone cube from which each eigenvector was derived. Both the cube position together with its eigenvectors were then plotted together in three-dimensional space. However, due to the complexity of the resulting plot (e.g. each plot contained all cube coordinates from each femur plus each cube's three principal directions), and the fact it covered multiple anatomical sites and therefore contained great heterogeneity in terms of trabecular orientations (figure 4.6), further refinement was needed for subsequent analysis and to assess the accuracy of the data could be better evaluated.

As such further MATLAB functions were developed and implemented to split the femoral plots (and by proxy, the femur itself) into distinct anatomical and therefore more manageable regions. This was done in two ways. The first automated the splitting of the femur into coronal, sagittal and transverse 'slices' and associating them with each of the three main directions separately (figure 4.7).

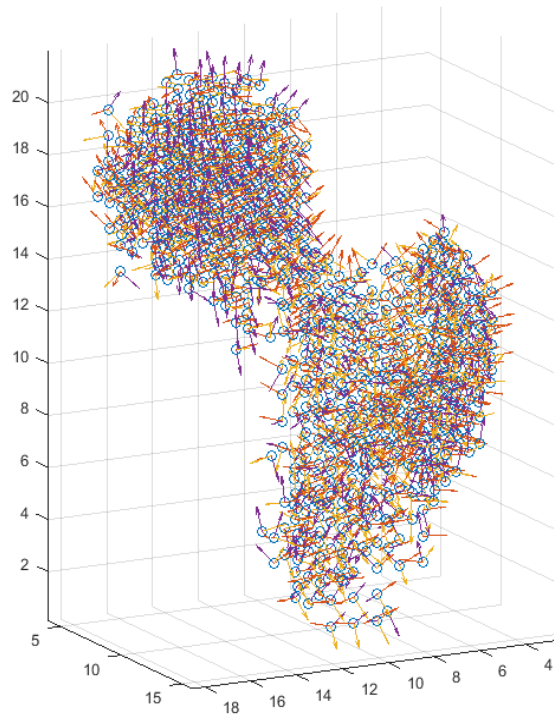


**Figure 4.6 3D plot of trabecular orthotropic directions.** Initial 3D plot of all three principal trabecular directions throughout the proximal femur. Blue circles denote the origin coordinates for each cube, while the coloured arrows show the main trabecular directions calculated for each cube.

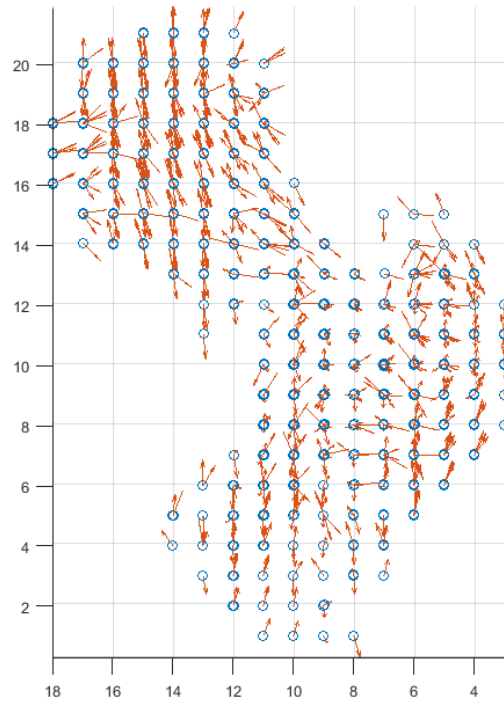


**Figure 4.7** *Slice plot of trabecular directions.* 3D plot of the same femur as in figure. 3.6. Plot has been simplified for analysis such that it represents just a single 'slice' of cubes in the same sagittal plane and with only the main trabecular direction plotted (red arrows) at each cube's origin coordinates (blue circles).

The second function allowed the user to select specific bone cubes (through selection of their origin coordinates) together with their associated eigenvectors. This permitted the user to focus on particular regions of interest (ROI's) for analysis e.g. the femoral head or smaller sub-regions.

#### 4.2.8 Analysis of Trabecular Orientations

Trabecular architectural anisotropy was analysed in two ways using MATLAB with the aim of combining the results from both approaches to help better describe trabecular orientation throughout the proximal femur.

The first analysis method ranked and converted to ratios the values of the Cartesian components of each bone cube's eigenvectors. Where  $v_n$  represents an eigenvector's component, each component was expressed as a ratio,  $v_{rat}$ , of the sum of all components.

The rationale behind taking this approach was the assumption that the component with the largest magnitude would have a greater effect on an eigenvector's orientation relative to one or both of the other components. Thus, if the X component was greatest, that eigenvector

orientation would be more aligned with the X axis than either the Y or Z axes. Each component's ratio was related back to its original magnitude to help quantify to what extent each component contributed to the eigenvector's direction and ultimately help qualitatively explain in what general direction the trabecular network contained within that particular bone cube region was orientated.

The second type of analysis quantified the three-dimensional angle between eigenvectors and the femoral neck axis (FNA), defined as a vector, to enhance the specificity of the analysis and discussion of architectural anisotropy in the proximal femur. The angle of the main trabecular directions relative to the FNA was chosen for several reasons. First, to remove the influence of differences in femoral positions across specimens on quantifying trabecular angles. Second, it permitted the relationship (if any existed) between the FNA and main trabecular orientations to be explored.

The first step in determining the three-dimensional angles between the FNA and eigenvectors representing trabecular orientations was to take the cross-product of an eigenvector and the FNA. The norm of the cross-product, was obtained to assign the cross-product a magnitude (*i.e.* its Euclidean distance). The dot-product of the FNA vector and eigenvector was then calculated and the angle between these was then found using their magnitudes and the arctangent function.

The four-quadrant inverse tangent was chosen due to its increased accuracy (compared to  $\cos^{-1}$ ) in dealing with angles near to 0 or  $\pi$  because it includes both the norm of the vector cross product and scalar dot product in its calculations. Because the cross product must be positive, resulting values were given in the range of 0 to  $\pi$ . Thus, the final step was to convert results in radians into degrees.

#### **4.2.9 Defining Femoral Neck Axis**

The femoral neck axis was idealised as a straight line passing through the centre of the femoral head and the centre of the middle portion of the neck. The femoral head and neck centres were calculated in MATLAB using the readily available Sphere Fit function (Jennings, 2010). Briefly, both functions work by using surface coordinate data and computing the centre point of these coordinates using a least squared fitting method.

Once both centre points were computed by using femoral head and neck surface coordinate data from the femoral  $\mu$ CT scans and the Shere Fit function, a custom written MATLAB script utilised their coordinates to create a three-dimensional vector between the two points before converting it into its unit vector equivalent. Where  $x$  is a p-by-m matrix and  $x_p$  therefore represents matrix rows, the vector,  $v$ , was calculated as the difference in magnitude between the Cartesian coordinates of the two centre points.

#### 4.2.10 Combining Approaches

The results from both of these approaches were taken together for each bone cube to map and quantify the orientation of the trabecular architecture at each cubic region. And by considering all bone cubes it became possible to map and quantify this architectural parameter throughout the entire proximal femur. Quantification of eigenvector component magnitudes and ratios helped explain the general orientation of trabecular architecture while the angular values (relative to the femoral neck axis) gave some specificity and clarity as to the exact direction trabecular bone took.

#### 4.2.11 Statistical Analysis

Statistical analyses were conducted in MATLAB. Brown-Forsythe tests for homoscedasticity were used to delineate differences in homoscedasticity of angular data between femurs, for each of the three analysed regions. Kruskal-Wallis one-way analysis of variance was used to explore statistical relationships in angle medians. Box's M test was used to define statistical relationships in homoscedasticity for covariate eigenvector data for all femoral specimens for each of the three femoral regions analysed. One-way multivariate analysis of variance (MANOVA), canonical analysis and principal components analysis (PCA) were also used to explore the strength of statistical relationships in eigenvector data for the three regions of interest between all femoral specimens.

## 4.3 RESULTS

### 4.3.1 Validation

Main trabecular architectural anisotropic directions were successfully mapped and quantified for multiple ageing proximal femora based on  $\mu$ CT resolution data (68 – 72.9 microns). Good agreement was found between actual trabecular principal directions in all femoral specimens and trabecular principal directions modelled and plotted in this study (e.g. figures 4.8 and 4.9). These observations help validate the methods used and results obtained in this study.

Nonetheless, the qualitative assessment of the thresholding method used for subsequent analyses may have affected the quality of derived trabecular data. In particular, this may have affected BV/TV results because particularly small or thin trabecular structures, that are often present in ageing trabecular bone, may have been unintentionally excluded from analysis. In the absence of a sensitivity analysis demonstrating the effects of different approaches to thresholding it is difficult to quantify the extent to which results may have been affected. However, the method has been demonstrated as an effective tool for thresholding gray-level images previously (Otsu, 1979) and as showing strong correlations with histomorphometrically derived parameters such as BV/TV (Chang *et al.*, 2013). Taking these factors into account and the fact that qualitative assessment of thresholded images appeared to show good results, it is thought that the quality of trabecular parameters is sufficient for the purposes of this study.

All MATLAB code used for this chapter is outlined in appendix B of this thesis.

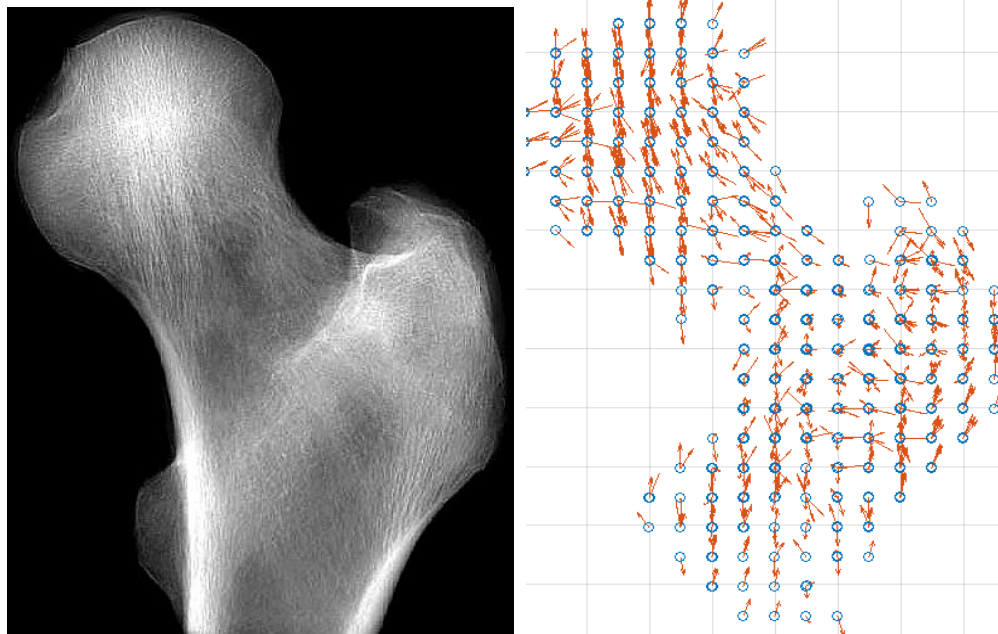


**Figure 4.8 Comparison of actual and modelled trabecular directions.** **Left:** Radiograph in the sagittal view of a proximal femoral specimen used in this study. The radiograph was made using custom MATLAB scripts. **Right:** The full set of principal eigenvectors (red arrows) and their corresponding cubes (blue circles) for the radiographed femur. There is good agreement between principal trabecular directions observed in the actual femur and those modelled using eigenvector analysis throughout the entire trabecular region.

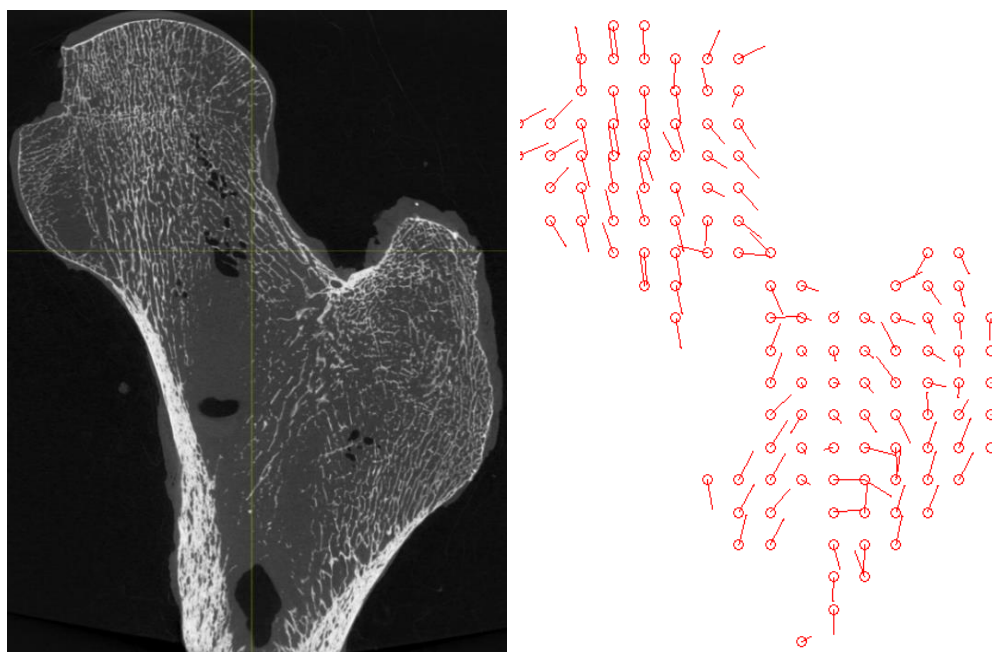


**Figure 4.9 Slice plot comparison of actual and modelled trabecular directions.** **Left** Sagittal slice through the same proximal femoral specimen as in figure 3.8. **Right:** A corresponding sagittal slice of approximately the same region constructed with principal eigenvectors (red lines) and their corresponding cubes (red circles) shown. There is good agreement between principal trabecular directions observed in the actual femur and those modelled using eigenvector analysis throughout this region.

## 4.3.2 Trabecular Orientations in the Femoral Head

### 4.3.2.1 Angles

Principal trabecular angular orientations relative to the femoral neck axis showed a good degree of similarity across specimens (table 4-2). Median three-dimensional angular values for principal trabecular orientations relative to the specimen's femoral neck axis varied by as little as 9.6 degrees for specimens one to four and by 33.5 degrees when specimen five is included. Median angular values are outlined table 4-2.

**Table 4-2 Median 3D angles – femoral head.** Median 3D angles of trabecular structures throughout the femoral head relative to the femoral neck axis.

| Femoral Specimen | Median Angle (degrees) |
|------------------|------------------------|
| Specimen 1       | 33.9                   |
| Specimen 2       | 35.4                   |
| Specimen 3       | 25.8                   |
| Specimen 4       | 32.7                   |
| Specimen 5       | 56.0                   |

#### 4.3.2.1.1 Statistical Analysis – Angles

Brown-Forsythe tests for homoscedasticity determined that femoral specimens three and five showed a statistically significant difference in homoscedasticity ( $p < 0.05$ ). Kruskal-Wallis' one-way analysis of variance elucidated significant differences between specimens three and five too. Statistical results showed that while no significant differences existed between specimens one, two and four, specimens three and five were significantly different with respect to each other and to the other three femurs ( $p < 0.05$ ) (figure 4.10).

### 4.3.2.2 Eigenvectors

In terms of the specific orientations trabecular structures took within the femoral head, an analysis of the individual X,Y and Z components of the eigenvector data shows that for all specimens, the principal trabecular orientation occurred primarily in the superior-inferior direction, secondly in the anteroposterior direction and lastly in the mediolateral direction.

Consequently, trabecular structures within the femoral head of these specimens can generally be described as being primarily orientated superior-inferiorly with additional tendencies to be orientated slightly forwards and posteriorly towards the superior and posterior portions of the femoral head.

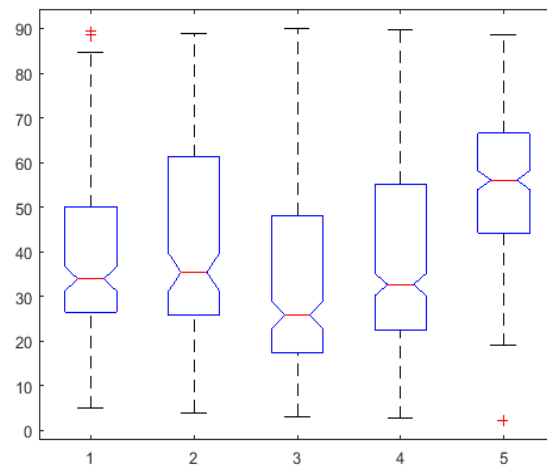


**Figure 4.10 Kruskal-Wallis box plot for femoral head angular data.** Kruskal-Wallis box plot elucidating differences in the mean ranks of angular data in the femoral head relative to the femoral neck axis for femoral specimens 3 and 5. Y-axis = angular data. X-axis = femoral specimen.

It should be noted however, that around the periphery of the femoral head, trabecular structures tended to deviate from this pattern and instead displayed a tendency to be arranged more evenly in the superior-inferior and mediolateral directions. This is demonstrated by an increase in the magnitudes of the X component of each principal eigenvector and an increased frequency in the similarity of magnitudes between the X and Z component of each eigenvector in these regions.

#### 4.3.2.2.1 Statistical Analysis - Eigenvectors

Subsequent analysis of the eigenvector components, using MANOVA and PCA, illustrates why differences in angular data might exist. Due to the large sample sizes ( $n > 20$ ), any violations to normality were negated as a result of the multivariate central limit theorem. Box's M test for homoscedasticity between covariance matrices showed significant differences ( $p < 0.05$ ) between femoral specimens. Although MANOVA is relatively robust to departures from homogeneity of variance, there were unequal sample sizes for the dependant variables which can affect the reliability of subsequent results. Therefore, all dependant variable sample sizes

were reduced to the same number of data points as the smallest dependant variable, using a random number generator to determine which data points were to be omitted.

Results from MANOVA indicate several features exist within the eigenvector data. Firstly, group means were significantly different ( $p < 0.05$ ) but were nonetheless closely related, existing along a line within one-dimensional space. Secondly, an analysis and plot of the first two canonical variables illustrates which linear combinations of the original eigenvector components create the largest separation between femoral specimens. Compared to pairs of eigenvector components (figure 4.11), it is clear from figure 4.12 that the canonical variables do not display any significant increase in separation between eigenvector components. This suggests that combinations of the original dependent variables already explain much of the observed separation between groups.

Therefore, when taking either the canonical or the original variables into account, the trends remain much the same and it is therefore apparent which linear combinations of the original variables the canonical variables are comprised. It appears that canonical variable 1 (C1) is comprised mainly of linear combinations of the X and Y eigenvector components, and much like those patterns seen for the combined effects of these variables there is a reasonably distinct clustering between femoral specimens three, four and five and to a much lesser extent femoral specimen two (figure 4.12). C2 appears to be comprised of linear combinations of the X and Z components, with the same separation seen between groups as C1 but to a slightly lesser extent. This implies that differences, although moderate, in the orientation of trabecular structures between femoral specimens occur primarily in the mediolateral direction.

PCA coefficients indicate the Z eigenvector component describing trabecular orientations as being most strongly correlated with principal component one (0.937) whilst being weakly correlated with principal component two (0.197). The X eigenvector component is positively but weakly correlated with component one (0.339) but strongly correlated with principal component three (0.884). The Y eigenvector component was negatively correlated with principal component one, strongly correlated with principal component two (0.926) and weakly correlated with principal component three (0.367).

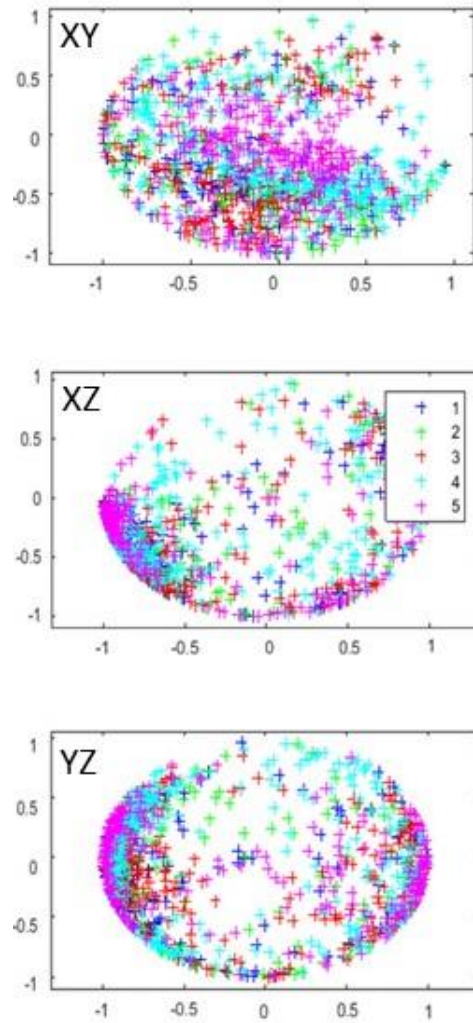


**Figure 4.111 Eigenvector paired plots.** Plotted pairs of eigenvector components that define principal trabecular orientations in the femoral head for each femur. The colour of each symbol denotes which femoral specimen the eigenvector belongs to (legend in middle plot). Axes describe the value of each eigenvector component.

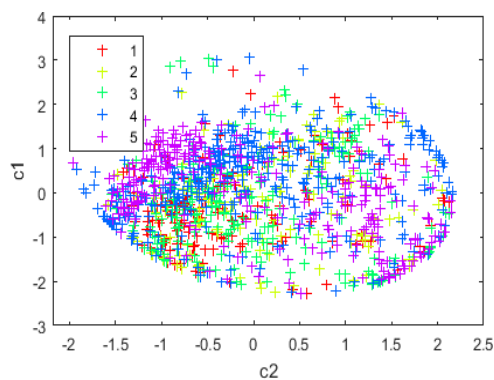


**Figure 4.122 Canonical analysis of eigenvectors.** The first two canonical variables are plotted against each other in the plot to the left. As can be seen the canonical variables show little improvement in clustering (*i.e.* separation) between femoral specimens when compared with the X vs Y subplots above (middle left and middle top). This suggests the original paired variables already best explain any observed differences and that any such differences are weak to moderate in nature.

These results suggest that the Z component contributes much to the variation seen in the main directions trabecular structures take because principal components one and two explain up to 86.7% of the variation seen in principal trabecular orientations. Conversely, the Y component appears to contribute the least because of its strong correlation with principal component two and weak correlation with principal component three which explains only 13.3% of the observed variation. This makes sense when one considers the qualitative observation in the eigenvector component magnitudes.

### 4.3.3 Trabecular Orientations in the Inferior Femoral Neck

#### 4.3.3.1 Angles

Principal trabecular orientations relative to the femoral neck axis showed a good degree of similarity across specimens. Median three-dimensional angular values for principal trabecular orientations (as defined by eigenvector data for each cube) relative to the specimen’s femoral neck axis varied by as little as 14.7 degrees for all five specimens. Median angular values are outlined in table 4-3.

**Table 4-3 Median 3D angles – inferior neck.** Median 3D angles of trabecular structures throughout the inferior femoral neck relative to the femoral neck axis.

| Femoral Specimen | Median Angle (degrees) |
|------------------|------------------------|
| Specimen 1       | 44.0                   |
| Specimen 2       | 52.3                   |
| Specimen 3       | 53.6                   |
| Specimen 4       | 43.1                   |
| Specimen 5       | 57.8                   |

#### 4.3.3.1.1 Statistical Analysis - Angles

Brown-Forsythe tests for homoscedasticity determined that significant differences existed between femoral specimens for homoscedasticity ( $p < 0.05$ ). However, Kruskal-Wallis’ one-way analysis of variance and Scheffe’s procedure indicated that no statistically significant differences in angular data existed for all femoral specimens ( $p = 0.07$ ) (figure 4.13).

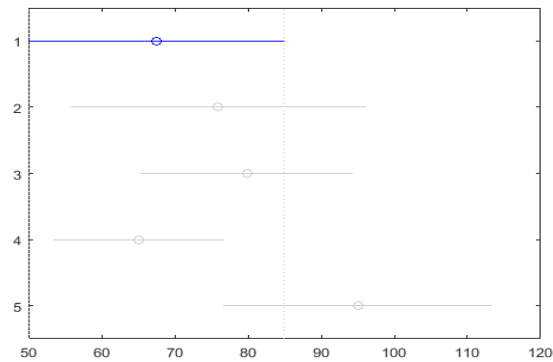


**Figure 4.13 Scheffe's procedure - inferior femoral neck.** Scheffe's procedure for multiple pairwise comparisons elucidating no significant differences existed between specimens one to five (all overlap). Y-axis = femoral specimen. X-axis = average group ranks.

### 4.3.3.2 Eigenvectors

In terms of the specific orientations of principal direction trabecular structures within the inferior portion of the femoral neck, the individual X, Y and Z components of the eigenvector data show that, generally speaking, for specimens one and three to five, the principal trabecular orientation occurred primarily in the superior-inferior direction, secondly in the anteroposterior direction and lastly in the mediolateral direction. For femoral specimen two, the principal trabecular orientation occurred primarily in the anteroposterior direction, secondly in the mediolateral direction and lastly in the superior-inferior direction.

Consequently, trabecular structures within the femoral specimens can generally be described as being primarily orientated superior-inferiorly with additional tendencies to be orientated anteriorly and medially towards the anterior medial compartments of the femoral neck.

#### 4.3.3.2.1 Statistical Analysis - Eigenvectors

Due to the large sample sizes ( $n > 20$ ), any violations to normality were negated as a result of the multivariate central limit theorem. Box's M test for homoscedasticity between covariance matrices showed significant differences ( $p < 0.05$ ) between femoral specimens. Although MANOVA is relatively robust to departures from homogeneity of variance, there were unequal sample sizes for the dependant variables which can affect the reliability of subsequent results. Therefore, all dependant variable sample sizes were reduced to the same number of data

points as the smallest dependant variable, using a random number generator to determine which data points were to be omitted.

Results from MANOVA indicate several features exist within the eigenvector data. Firstly, group means were significantly different ( $p < 0.05$ ) and existed in a two-dimensional space indicating that for the inferior femoral neck, grouped means were not as well clustered as they were for the femoral head region. A subsequent cluster plot reveals why this is the case and confirms qualitative observations for eigenvector data that specimen two differs in eigenvector distributions for this anatomical region (figure 4.14). It is likely these differences exist because of the predominant anteroposterior, as opposed to superior-inferior, orientation of trabecular structures in the inferior femoral neck for specimen two.

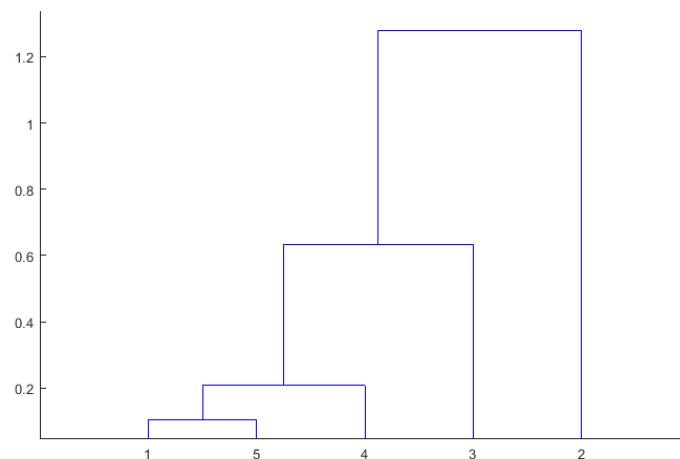


**Figure 4.134 MANOVA dendrogram plot - eigenvectors, inferior femoral neck.** MANOVA cluster plot indicating the separation of femur 2 from all others in the sample likely reflecting the fact specimen 2's trabecular structures were primarily orientated in the anteroposterior as opposed to the superior-inferior direction observed in all other specimens.

PCA results mirrors those found for the femoral head to a good degree. The Z eigenvector component was most strongly correlated with principal component one (0.758) and moderately correlated with principal component two (0.567). The X eigenvector component is positively but weakly correlated with component one (0.328) but strongly correlated with principal component three (0.944). The Y eigenvector component is strongly correlated with principal component two (0.823) and weakly correlated with principal component three (0.215). These results suggest that the Z component contributes much to the variation seen in the direction trabecular structures take because principal components one and two explain

up to 92.8% of the observed variation while the X component appears to explain the least because principal component three explains only 7.2%.

#### 4.3.4 Trabecular Orientations in the Superior Femoral Neck

##### 4.3.4.1 Angles

Principal trabecular orientations relative to the femoral neck axis again showed a good degree of similarity across specimens. Median three-dimensional angular values for principal trabecular orientations (as defined by eigenvector data for each cube) relative to the specimen's femoral neck axis varied by as little as 14.3 degrees for specimens one to four and by 21 degrees when specimen five is included. Median angular values are outlined in table 4-4.

**Table 4-4 Median 3D angles – superior neck.** Median 3D angles of trabecular structures throughout the superior femoral neck relative to the femoral neck axis.

| Femoral Specimen | Median Angle (degrees) |
|------------------|------------------------|
| Specimen 1       | 54.8                   |
| Specimen 2       | 41.9                   |
| Specimen 3       | 41.3                   |
| Specimen 4       | 40.5                   |
| Specimen 5       | 61.5                   |

##### 4.3.4.1.1 Statistical Analysis - Angles

Brown-Forsythe tests for homoscedasticity determined that no significant differences existed between femoral specimens for homoscedasticity ( $p = 0.15$ ). However, Kruskal-Wallis' one-way analysis of variance indicated that statistically significant differences in angular data existed between femoral specimens four and five ( $p < 0.05$ ) but that there were no statistically significant differences between all other specimens (figure 4.15).

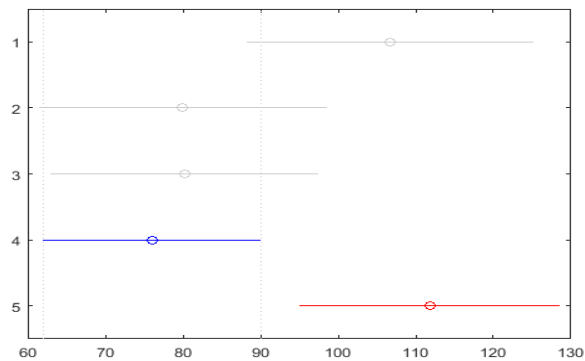


**Figure 4.145 Scheffe's procedure - superior femoral neck.** Scheffe's procedure for multiple pairwise comparisons elucidating significant differences existed between specimens four and five (blue & red respectively). Y-axis = femoral specimen. X-axis = average group ranks.

#### 4.3.4.2 Eigenvectors

In terms of the specific orientations of principal direction trabecular structures within the superior femoral neck, an analysis of the individual X, Y and Z components of the eigenvector data shows that for all specimens, the principal trabecular orientation occurred primarily in the anteroposterior direction, secondly in the mediolateral direction and lastly in the superior-inferior direction. It should be noted however that the preferential anteroposterior direction of trabecular bone over a mediolateral direction was much less pronounced than those differences found between the X, Y and Z components of eigenvectors in the other regions. This is in contrast to those principal trabecular directions found for the inferior femoral neck and head.

Consequently, trabecular structures within the superior portion of the femoral neck could be described as being primarily orientated anteroposteriorly with a tendency to be orientated mediolaterally to a noticeable extent and superior-inferiorly to a lesser extent.

##### 4.3.4.2.1 Statistical Analysis - Eigenvectors

Once again, due to the large sample sizes ( $n > 20$ ), any violations to normality were negated as a result of the multivariate central limit theorem. Because Box's M test for homoscedasticity between covariance matrices showed significant differences ( $p < 0.05$ ) between femoral specimens and dependant variables had unequal sample sizes, a random

number generator was again used to reduce the dependant variable sample sizes to the same number of data points as the smallest dependant variable.

Results from MANOVA indicated no significant differences exist between group means in collective eigenvector data for the superior portion of the femoral neck ( $p = 0.2$ ). Given the non-significant differences between femoral eigenvector data, a canonical analysis was not conducted. A cluster diagram does show however that, despite the fact no significant differences were found, specimen four was most separated from all others (figure 4.16). This supports prior qualitative observations in eigenvector data whereby specimen 4 showed differences in the contribution of the Y eigenvector component to trabecular directionality, compared to all other specimens.

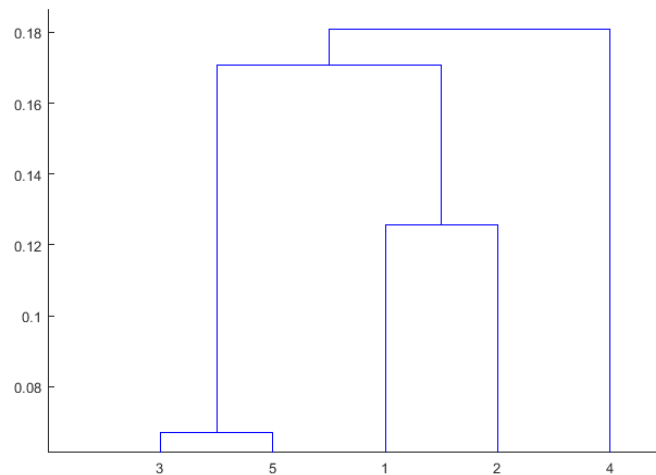


**Figure 4.156 MANOVA dendrogram plot - eigenvectors, superior femoral neck.** MANOVA cluster plot indicating the (non-significant) separation of femur 4 from all others in the sample likely reflecting the fact this specimen's principal trabecular directions differed very slightly (absolute distances as indicated by height of braches) between all specimens are small) from the others in terms of their anteroposterior direction.

PCA coefficients show the Y component of each eigenvector as being most strongly positively correlated with principal component one (0.726). X and Z eigenvector components are negatively correlated with principal component one. All eigenvector components contribute fairly evenly to principal component two ( $X = 0.573$ ,  $Y = 0.688$ ,  $Z = 0.446$ ) while, in contrast to those trends seen for the femoral head and inferior femoral neck, the Z eigenvector component is most strongly correlated with principal component three (0.781) while contributing least to principal component two.

Thus, when considering the entire group of femoral specimens collectively, the Y component of each principal eigenvector appears to contribute to a significant proportion of the observed variation in principal trabecular architectural orientations while the Z component contributes the least.

#### 4.4 DISCUSSION

This study has mapped, quantified and analysed principal trabecular architectural orthotropic orientations for multiple, whole ageing proximal femora scanned at resolutions below 80 microns (figure 4.8 & 4.9). A suite of novel functions, developed in MATLAB and used in combination with functions available in the BoneJ open source software, have been utilised to achieve this. Their semi-automated and inexpensive nature means they are relatively time- and cost-effective, particularly when considered in the context of the large amount of data that can be gleaned through their use. A number of these functions are being integrated into an intuitive MATLAB program with a simple, easy-to-use GUI that interested researches could use with minimal effort to conduct similar work. Further development of this program is needed but its implementation could be beneficial for future studies looking at the quantification of trabecular architectural anisotropy.

Mapping trabecular orthotropic orientations with increased resolutions relative to those used previously builds upon that work which has been done. It has been shown in a number of studies that increasing voxel resolution improves the prediction and quantification of trabecular parameters (Kim *et al.*, 2004; Yeni *et al.*, 2005; Joshua A MacNeil and Boyd, 2007; Sode *et al.*, 2008; Wolfram *et al.*, 2009; Kersh *et al.*, 2013; Krause *et al.*, 2014; Larsson *et al.*, 2014; Zhou *et al.*, 2016).

More specifically, it has been noted that decreasing values of BV/TV are associated with increases in voxel size and that measures of trabecular anisotropy have been shown to be highly dependent on and display a non-linear relationship with voxel size (Isaksson *et al.*, 2011). But in contrast to BV/TV, measures of trabecular anisotropy decrease with decreasing voxel sizes below 100 microns. These trends are true for small differences in voxel sizes (e.g. 14 micron intervals) and have been shown to exist between voxel sizes of 84 and 70 microns.

Given these findings and due to the small size of individual trabeculae (approximately 100 microns thick), it is conceivable that decreases in voxel resolution at or below this size, will

enhance the clarity with which the trabecular network is imaged. Since trabecular architectural parameters are derived directly from scan images, their prediction and/or quantification is also improved. As a result, the increase in voxel resolution compared to the approximate size of individual trabeculae, there can be some degree of certainty that the data obtained in this study is of good quality and potentially more accurate than that derived previously. In terms of its application for FE model construction in chapter 6, it is anticipated that the increased accuracy of BV/TV and trabecular fabric data will lead to improved model performance.

One of main advantages of this work was that trabecular orthotropic orientations were mapped and analysed throughout the proximal femur (figure 4.8 & 4.9). This was possible by virtually splitting the femur into discrete regions. This approach represents an improvement on a number of previous studies which have relied on a small number of sub-samples, physically cut out in a laboratory setting, to define architectural parameters for entire regions (Milovanovic, Djonic, *et al.*, 2012; Saers *et al.*, 2016).

Taking the virtual approach adopted in this study has the potential to capture and properly define the full range of variation within and between regions in the proximal femur which may otherwise be missed or masked when using only a limited number of sub-samples. However, the compromise in taking this approach relates is the modest improvement in scan resolution. Voxel resolutions were restricted in size due to the large specimen dimensions. Given the desire to map trabecular orientations throughout entire proximal femora (for subsequent incorporation into FE models constructed in chapter 6), as well as the benefits of being able to study trabecular orientations in a continuous sense through each femur, scanning whole specimens with reduced resolution (compared to what would be possible when scanning small, sub-samples) was judged preferable.

A multitude of studies have sought to analyse trabecular architectural parameters within the proximal femur. However, these analyses provide only a cursory or superficial overview of trabecular architectural orientations because they focus on the degree of anisotropy which as a dimensionless parameter, as other researchers have noted (Hosseini, Maquer and Zysset, 2017), ultimately tells us nothing about the directionality of trabecular bone.

It has been shown in this study, that across multiple, ageing proximal femora, for the femoral head and inferior femoral neck, while main trabecular directions primarily took a superior-inferior trajectory, anteroposterior alignment was more dominant than mediolateral. And in the superior femoral neck, trabecular orientations were primarily anteroposterior. This is not

readily discernible from more traditional (*i.e.* sagittal) views of the femur that are frequently used to discuss trabecular arrangement in the proximal femur. This finding highlights the need to continue to formulate new approaches to the study of trabecular architectural organisation, particularly approaches that allow us to properly quantify and standardise trabecular directionality for femoral specimens because of its biomechanical significance for hip fracture (Cowin, 1985; Odgaard *et al.*, 1997).

The similarity in angular values for each analysed region (tables 4.1 – 4.3) suggested that trabecular networks take a similar direction but could not, in and of themselves, confirm this; the methods used found the angle merely by calculating the shortest circle path between the vectors of interest. The eigenvector distribution analysis provided directionality and specificity to observed angular patterns and has shown that similarity in angle data is likely due to similarity in directionality.

Although not exhaustive, the novel approach taken here to define trabecular architectural orientation through the combined use of three-dimensional angles and eigenvector analysis therefore appears to be a relatively good solution for approximating the specific directions of trabecular networks and has extended current knowledge about trabecular arrangement in the ageing proximal femur. Additionally, by defining trabecular orientations relative to the femoral neck, angular data is standardised and permits repeatable measurements between specimens in future work. This represents an improvement on the more subjective approach used by Chiba *et al.*, (2013) where differences in positioning of specimens might mask or artificially create differences in orientation data.

Trabecular networks between specimens generally followed similar trajectories although the exact trajectory appears to be region specific. The principal direction of trabecular bone in the femoral head and inferior femoral neck was very similar as shown by the relative contributions of the X, Y and Z components of eigenvectors and relatively small difference in their angular deviations from the femoral neck axis (tables 4.1 – 4.3). Nevertheless, the angular data indicated that trabecular bone in the femoral head was more closely aligned with the femoral neck axis (table 3-1) than was trabecular bone in the inferior (table 4-2) or superior femoral neck (table 3-3).

It has been hypothesised that during bipedal gait the femur is loaded approximately collinearly with the femoral neck axis (Kalmey and Lovejoy, 2002), and this leads to a significantly thicker cortex in the inferior femoral neck because a greater proportion of the load is borne by this portion of the neck (Carter, Orr and Fyhrie, 1989). The femoral specimens in this study have

a visibly thicker cortex in this region (figure 4.9) and moderate angular deviations in main trabecular directions relative to the femoral neck axis for the femoral head and inferior neck, with these regions of trabecular appearing to be better aligned with the inferior femoral neck border. This suggests that habitual loads are approximately collinear with the inferior femoral neck rather than the femoral neck axis itself and therefore seem to support a slightly modified form of Kalmey and Lovejoy's (2002) hypothesis.

Underpinning any theory of trabecular architectural organisation is the general principle underlying Wolff's law that bone adapts its structure to mechanical stimulus (Wolff, 1986). This adaptation allows trabecular bone to align its principal directions with those in which principal stresses occur due to mechanical loading. This is advantageous because trabecular bone is strongest in its principal direction due to the well-known relationship between trabecular bone's elastic and architectural properties (Cowin, 1985; Odgaard *et al.*, 1997). Consequently, this remodelling capacity of trabecular bone allows it to be strongest in the same direction as that in which principal stresses from habitual loading occurs.

For the human proximal femur, the main mechanical stimulus arises from habitual loading due to bipedal gait. Given that these habitual loads could be considered generally collinear with the inferior neck, it is unsurprising that trabecular bone in the femoral head and inferior neck is highly orientated in a very similar direction to that of the inferior femoral neck borders (figure 4.9 & tables 4-1 & 4-2). The additional tendency for an anteroposterior orientation however has not been recognised previously and challenges simple assumptions made about the complex structural arrangement of trabecular bone as well the dynamic nature of joint loading during gait. Further work is needed to explain the observed trabecular architectural arrangement in this region but the additional tendency for an anteroposterior trabecular orientation may relate to the dynamic muscle and joint reaction forces experienced during gait.

Assuming that trabecular structures reflect principal stress trajectories arising from habitual loading, the principally anteroposterior and mediolateral orientation of the principal direction of trabecular bone in the superior femoral neck provides insight into the direction principal stresses take in this region. Traditionally, stresses in the femoral neck are described as compressive or tensile. This distinction is important for understanding the aetiology of hip fracture. Adding a directional component to further distinguish the types of stresses that occur in the femoral neck undoubtedly aids this understanding because of the orthotropic nature of bone; if the principal stresses from a sideways fall follow markedly different

trajectories to those that occur routinely (and which ultimately define trabecular principal direction) then bone is likely to be weaker in this direction and more susceptible to fracture.

It is difficult to place the predominant anteroposterior organisation of trabeculae in the superior femoral neck within the context of habitual loading due to bipedal gait. Some have postulated that the powerful abductor group can significantly modify the stress distributions and patterns experienced in the femoral neck (Carter, Orr and Fyhrie, 1989; Owen Lovejoy *et al.*, 2002; Lovejoy, 2005). This being the case, it might be that the combined effect of loading from bipedal locomotion and the accompanying action of hip muscle groups could be a sufficient influence to drive the trabecular orientations observed in this region.

An alternative explanation for the main trabecular direction observed in the superior femoral neck is that these directions do not reflect architectural adaptation to habitual loading. It has been noted that the superior femoral neck experiences only modest stresses and strains during habitual loading (Kalmey and Lovejoy, 2002) and is subject to significant micro-architectural deterioration (Kawashima and Uthoff, 1991; Lundeen, Vajda and Bloebaum, 2000; Djuric *et al.*, 2010; H Chen *et al.*, 2013). A lack of mechanical stimulus accompanied by age-related deterioration in bone quality may lead to a less well organised, more random network of trabeculae that do not align optimally with principal stress trajectories. However, the general good agreement (as illustrated by non-significant differences and close statistical clustering (e.g. figures 4.13 & 4.16)) in patterns of main trabecular orientation observed between specimens suggests they are not random and are therefore not driven by low mechanical stimulus and age-related deterioration.

The congruence in the principal trabecular direction for all three regions between femoral specimens suggests that principal trabecular directions may be maintained with increasing age and in both sexes. This is true even for the superior femoral neck, which as aforementioned, undergoes significant micro-structural deterioration with ageing and is subject to only modest habitual loading. These observations are in agreement with previous research that found as bone mass decreases, trabecular elements parallel to the principal stress trajectories are preserved while trabecular elements transverse to the principal stress trajectories are resorbed (Ciarelli *et al.*, 2000).

Mechanical loading therefore provides a likely candidate for explaining the high degree of similarity between specimens found in this study and increases confidence in the hypothesis that the trabecular organisation within the superior femoral neck is a result of mechanical loading. Nonetheless, a genetic component/influence to trabecular organisation and change

in the ageing proximal femur should be considered alongside or as an alternative to mechanical explanations (Judex *et al.*, 2004; Lazenby *et al.*, 2008).

Future work exploring whether the main trabecular direction in the ageing superior femoral neck is in fact a direct result of habitual (muscle and joint) loading regimes or rather the result of micro-architectural deterioration would be an essential first step in properly understanding trabecular organisation in the proximal femur. Similarly, understanding exactly how principal trabecular orientations in the superior femoral neck might relate to the likelihood of fracture by comparing the differences or similarities between the principal stress directions arising from a sideways fall impact with the principal direction of the trabeculae in that region could help to explain more fully how that trabecular organisation relates to hip fracture and more specifically, why the superior femoral neck is a particularly critical (*i.e.* susceptible) region for hip fracture (de Bakker *et al.*, 2009).

FEA could be used to address any number of these issues because it would be possible to compare the principal stress trajectories caused within FE models by specific loading regimes to principal trabecular orientations as determined by studies like this one. Ultimately, this could shed light on what processes drive trabecular organisation at various ages, help quantify the relative contributions of each of these processes to trabecular organisation and help elucidate the relationship between principal stresses experienced the femur during a fall and trabecular organisation might contribute to hip fracture.

It would also possible to validate orthotropic FEA models based on principal stresses determined from FE simulations (e.g. (San Antonio *et al.*, 2012)) or evaluate the performance of a general orthotropic FE model that approximated the principal trabecular orthotropic directions of all five femoral specimens against the performance of orthotropic FE models of the individual femoral specimens for a given lading scenario. By doing this, it would be possible to assess how valuable such general orthotropic FE models of the ageing femur might be for the study of hip fracture.

However, given the overarching aims of this thesis, the data gleaned in this chapter will be incorporated into FE models (in chapter 6) in several alternative ways. Firstly, the eigenvector and BV/TV will be incorporated into FE models representing each of the proximal femora analysed in this chapter. In doing so, fully orthotropic models with appropriate orthotropic material properties can be constructed. Secondly, because it has been possible to describe the main trabecular orientations for the femoral neck, these can be compared to the principal stress directions occurring in the femoral neck due to muscle and impact loads resulting from

a sideways fall. Ultimately, this will facilitate discussion about how habitual loading might influence trabecular arrangement in the proximal femur as well as about the underlying mechanisms of hip fracture and the susceptibility of the superior femoral neck to fracture.

#### 4.5 LIMITATIONS

The strength of these findings and conclusions are limited by a number of factors. While there were strong and reasonably consistent relationships between specimens, the small sample size limits the ability to extrapolate these findings out to a wider, ageing population. Due to the small sample size, sex differences were also not explored. It is likely that with a larger sample size differences might be found but in the present study, there were no readily identifiable differences between sexes for the parameters studied.

Only three regions were analysed for directionality in this study resulting in the exclusion of the trochanteric and inter-trochanteric regions from the analyses. Like the femoral neck, these regions are important for hip fracture and their inclusion in this type of analysis should be an area for future investigation. Essential to their inclusion is the formulation of a protocol that would permit an efficient and standard way in which these regions could be split into sub-regions for analysis. This is very important given that they contain trabecular networks that are highly heterogeneous in terms of directionality. Similarly, further compartmentalisation of the three anatomical regions analysed in the present study may have also been beneficial and better captured variation in principal trabecular directions that existed throughout the proximal femoral specimens.

Only the main trabecular direction was statistically analysed between specimens. This was done due to its biomechanical importance and the ease with which the eigenvector data for the principal direction could be validated against the observed trabecular orientations in the  $\mu$ CT scans. However, to fully understand variation in trabecular architectural anisotropy and its relevance for bone strength and biomechanical behaviour, the remaining orthotropic directions should be included in future analyses.

Finally, the accuracy of the data obtained in this study is wholly dependent on the scan resolution used. The resolution used in the current study may have led to an underestimation of BV/TV and the accuracy of the eigenvector data because smaller trabecular elements (*i.e.* those smaller than the voxel resolution) may have been omitted from scan images. However,

given the normal range of trabecular dimensions, it is assumed the majority of trabeculae were in fact captured in scan images.

Of those that were too small to image, it was assumed that such thin trabecular would confer minor biomechanical significance and that their omission would have little effect on the statistical relationships defined and conclusions arrived at in this study. Nonetheless, it would be good to validate the current study and these assumptions by scanning a subsection from one of the femoral specimens at a greater resolution than used here and comparing the new results with those of the current study.

Other trabecular parameters were not considered and it is not known how the inter-subject similarities in trabecular orientations is related to and reflected in other trabecular parameters such as trabecular connectivity. However, other trabecular parameters are not usually incorporated into orthotropic FE models of the femur and BV/TV is considered an indicator of and reflection for certain microstructural parameters such as trabecular connectivity (Kazama *et al.*, 2010).

## 4.6 CONCLUSIONS

This study has developed novel, semi-automated methodologies to accurately map, quantify and statistically analyse orthotropic principal trabecular directions throughout the multiple proximal femora in conjunction with the open source BoneJ software. Both angular and eigenvector data for the main trabecular direction between specimens is remarkably similar but region specific. The results suggest that habitual loading due to bipedal gait explains and contributes towards much of the observed congruence between specimens and is responsible for the preservation of principal trabecular directions in old age and between sexes.

## 5 USING MULTIBODY DYNAMIC ANALYSIS TO MODEL AND PREDICT SIDEWAYS FALL-RELATED HIP MUSCLE AND IMPACT FORCES

---

### 5.1 INTRODUCTION

Excluding spontaneous hip fracture, nearly all hip fractures are a result of falls (Greenspan *et al.*, 1994; Hayes *et al.*, 1996; Jarvinen *et al.*, 2008). Sideways falls are associated with a high risk of hip fracture (Parkkari *et al.*, 1999; Kannus *et al.*, 2006) and it is still not well understood why they confer a greater risk. Understanding the dynamic processes associated with sideways falls may therefore help in the prediction and prevention of hip fracture.

Fall-related impacts with the ground create large stresses within the femur that contribute to femoral fracture and in models of femoral fracture it is often only these impact forces (and resultant stresses) that are considered (e.g. Luisier, Dall'Ara and Pahr, 2014). While the relationship between fall types and fracture risks have been studied (Keyak, Skinner and Fleming, 2001; Bessho *et al.*, 2009; Wakao *et al.*, 2009), the effect of variation in impact forces associated with specific fall types, including sideways falls, on the risk of hip fracture is not well defined.

The proximal femur has multiple muscles inserting onto its surface, some of which are considered to exert significant forces; during gait, it is thought that hip muscle forces are sufficient to modify stresses experienced by the femur and mitigate against fracture risk and conversely to cause spontaneous femoral fracture (Dalla Pria Bankoff, 2012; Viceconti *et al.*, 2012a). Given this, it is plausible that hip muscle contractile activity during a sideways fall impact may be sufficient to modify femoral stresses caused by a sideways fall impact.

Such modifications may contribute to or help mitigate against fracture risk (as occurs during gait) but there is a dearth of research in this area. Only several studies have used MDA to investigate fall-related impact forces at the hip (Hirabayashi *et al.*, 2013; Luo *et al.*, 2013; Sarvi *et al.*, 2014) and only one has modelled muscle forces at the moment of impact (Choi, Cripton and Robinovitch, 2014). Consequently, the influence of hip musculature on fall-related femoral stress patterns is still relatively unknown but determining if/how hip musculature might affect these stresses may help inform methodological approaches towards predictive models of femoral fracture and elucidate why sideways fall might confer a high risk of fracture.

Taking these factors into consideration, quantifying and exploring variation in sideways-fall related impact and hip muscle forces may shed light on sideways falls have a high likelihood of fracture. The quantification and evaluation of these two parameters therefore forms the primary aim of this study. A first step in achieving this is to quantify a range of potentially plausible impact and hip muscle forces that might occur at impact during a sideways fall. MDA is a methodological approach where this can be achieved because, although it often depends on biological assumptions and approximations, it allows the prediction and quantification of individual muscle forces which would otherwise be unattainable using other methods such as EMG or because of ethical concerns regarding experimental designs

To this author's knowledge there are no studies that have specifically attempted to predict combined sideways fall-related hip muscle and impact forces through the use of MDA (or other methodological approaches such as EMG). The current chapter aims to conduct an initial exploratory analysis and investigation into impact and hip muscles force that might occur during sideways falls by using MDA. MDA will be used to simulate kinematically recorded real-world falls to predict concurrent hip muscle and impact forces. Variation in these forces between falls will also be explored. The data obtained in this study will be used to suggest why sideways falls might confer greater risk of femoral fracture and used as input for subsequent FEA simulations to explore the effect of hip muscle activity during a sideways fall on stress patterns in the ageing proximal femur (chapter 6).

## 5.2 METHODS

MDA is a modelling technique where a movement system, e.g. the human body, is treated as being composed of a set of rigid links (e.g. limbs) which are constrained by the joints between them and acted upon by a variety of forces (Sellers, Dennis and Crompton, 2003). To successfully simulate sideways falls using MDA for the present study, certain elements were required. Because a forwards dynamics approach was taken, the required elements were:

- A computer simulation package to derive and integrate the equations of motion, solve constrained non-linear optimisation problems and monitor and quantify a number of internal human variables (e.g. muscle forces, joint forces etc).
- An optimisation algorithm to drive model behaviour according to kinematic data.

- Real-world kinematic data of a sideways fall, to aid in the optimisation of model performance and ultimately muscle force prediction.
- A musculoskeletal model that incorporates many internal anatomical and biomechanical human parameters so details about the physiology of a sideways fall can be understood at the muscle level.

The specifics of each of these elements and the relationship between them are described in more detail in the following sections.

### 5.2.1 Simulations

*Simulator:* All simulations were carried out in the open dynamics engine (ODE; <http://www.ode.org>) version of the GaitSym (Sellers and Manning, 2007) simulator with a forwards dynamics global optimization system where random muscle activation patterns are generated by a genetic algorithm (GA) to produce optimised movement throughout the musculoskeletal model.

GaitSym uses the equations of motion to derive and quantify values for a number of parameters (e.g. muscle forces). For a given movement system (e.g. a musculoskeletal model) with  $n$  degrees of freedom, the equations governing motion can be written as:

$$[M(\theta)]\ddot{\theta} = C(\theta, \dot{\theta}) + G(\theta) + F_m(\theta) \quad 5.1$$

Where  $\theta$ ,  $\dot{\theta}$ ,  $\ddot{\theta}$  are  $n \times 1$  vectors of displacement, velocity and acceleration,  $[M(\theta)]$  is the  $n \times n$  inertia matrix,  $C(\theta, \dot{\theta})$  is an  $n \times 1$  vector of Coriolis and centrifugal terms,  $G(\theta)$  is an  $n \times 1$  vector of gravitational terms and  $F_m(\theta)$  is an  $n \times 1$  vector of applied forces and moments.

### 5.2.2 Forwards Dynamics

A forwards dynamics approach was adopted in this study. The forwards dynamics approach enforces the equations of motion by calculating the movement of a system for a specified time period as a result of prescribed forces and initial simulation conditions. As in the biological world, forwards dynamics results in the movement of body segments of a

musculoskeletal model, due to applied muscle forces and joint torques. Forwards dynamics is therefore ‘forwards’ in the sense that forces produce motions (Piazza, 2006).

The system inertial matrix,  $[M(\theta)]$ , is a function only of joint positions,  $\theta$ , is non-diagonal and is positive-definite which means its inverse,  $[M(\theta)]^{-1}$ , always exists (Pandy & Andriacchi, 2010.). This means that equation 4.1 can be used in forwards dynamics to solve for joint accelerations by rewriting it as:

$$\ddot{\theta} = [M(\theta)]^{-1} \left( C(\theta, \dot{\theta}) + G(\theta) + F_m(\theta) \right) \quad 5.2$$

Because the inverse matrix is non-diagonal this also means the biomechanical system is coupled and all sources of applied force,  $F_m(\theta)$ , contribute to joint accelerations as in equation 5.2.

One of the disadvantages to the forwards dynamics approach is the fact that it is very computationally expensive (Ren, Jones and Howard, 2007b) because equations of motion need to be integrated into each time step (Alamdari and Krovi, 2016). Additionally, in musculoskeletal models more muscles exist than are necessary to produce the degrees of freedom present in the model (Ren, Howard and Kenney, 2006). This problem is termed ‘redundancy’. In other words, because each joint is spanned by several muscles, joint moments can be produced by a large variety of different muscle force combinations (Pandy & Andriacchi, 2010). This is particularly true for the hip joint where more than 15 muscles control only three degrees of freedom.

It can be argued that the forwards dynamics approach takes advantage of this redundancy problem to an extent because of its predictive nature. Similar to that which occurs biologically, forwards dynamics predicts and uses neural excitation signals as inputs to produce motion in the model. Due to redundancy, forwards dynamics can predict any number of solutions for a given kinematic sequence and thus it is able to capture the variation that likely exists biologically in the muscle activations and forces that produce the same or similar movements. This predictive ability of forwards dynamics is one of its main advantages, makes it a powerful modelling tool for the study and prediction of human movement and is the main motivation for adopting it in the present study.

### 5.2.3 Genetic Algorithm Optimisation

Nonetheless, while forwards dynamics can exploit redundancy to find a whole range of biologically feasible solutions to a kinematic sequence, redundancy also means there are an unquantifiable number of solutions for the same observed motion, some of which will be sub-optimal and have no real grounding biologically. Therefore, without some optimisation criteria to guide simulations, solving and identifying optimal solutions with the forwards dynamics approach can be particularly difficult and inefficient. Given the large number of muscles spanning the hip joint relative to its degrees of freedom, this could be especially true in the present study.

Optimisation refers to the process of minimising some objective function of movement e.g. metabolic cost. The optimisation criteria chosen for this study was minimising the aggregate deviation between the simulated kinematics of the musculoskeletal model and real-world kinematic data of sideways falls. A GA was employed to achieve this.

The GA was designed to optimize the muscle activation pattern that yielded the best fit between model and experimental markers across the full sequence of falling. It achieved this in the following way:

1. The GA generated a 'population' of random muscle activation patterns. The population size was always 100. Each activation pattern was then applied to the musculoskeletal model in dynamic simulations.
2. The 'fitness' of the activation patterns was evaluated. Better fitness scores corresponded to activation patterns that yielded better fits between data target (see section 5.2.5.6) positions and model reporter (see section 5.2.5.7) positions from real-world kinematic recordings.
3. Activation patterns from the population were then chosen to 'reproduce'. The chance of being selected for reproduction was based on fitness scores, such that activation patterns with higher fitness scores had a higher chance of selection and producing more 'offspring'.
4. Reproduction was achieved by copying selected activation patterns and altering them through a combination of mutation (defined by a Gaussian mutation rate of 0.1) and merging values (defined by a crossover rate of 0.1).
5. The new population therefore contained activation patterns that tended to improve model performance relative to the real-world kinematics with a tendency to continue

to lose those that did not. Additionally, mutation and cross over may have further increased overall fitness of offspring in the new population.

6. The new 'fitter' population was returned to stage 2 and stages 2, 3 and 4 were repeated multiple times until no improvements were made or until a maximum specified time or number of simulations was reached.

#### **5.2.4 Kinematic Data Collection**

##### **5.2.4.1 Subject**

A single healthy human subject (male, 31 years old, 1.7m, 73kg) without any limb abnormalities or injuries was used to collect kinematic data for a sideways fall. Although fall-related hip fracture occurs mainly in older people, it was not possible to collect fall-related data from this demographic due to safety concerns and ethical issues. As such a young, healthy subject was chosen for fall experiments.

##### **5.2.4.2 Protocol**

The subject was asked to walk in a straight line at a self-selected speed from a prescribed starting point until they were adjacent with a crash mat that had been placed on the floor to the right of their path of walking. Once adjacent with the crash mat the subject fell sideways on to the crash mat with their right hand outstretched but without using it to break the fall (figure 5.1). This strategy for falling is in line with previous research where, as in this experiment, volunteers self-initiated the fall (Van Den Kroonenberg, Hayes and McMahon, 1996). This strategy however conflicts other studies where participants outstretched hands impacted the floor first (Feldman and Robinovitch, 2007). But unlike Van Den Kroonenberg, Hayes and McMahon's (1996) study, participants in Feldman and Robinovitch's (2007) study did not self-initiate the fall and this might explain the observed differences in fall strategies.

Regardless, in Feldman and Robinovitch's (2007) study participants were young volunteers and it is unclear whether breaking the fall with an outstretched hand would be an adopted fall strategy in older people. Because using an outstretched arm reduced hip impact velocity, it was suggested by Feldman and Robinovitch (2007) that its potential absence as a fall

strategy in older people might help explain why older people are more susceptible to injurious falls. Additionally, Feldman and Robinovitch's (2007) subjects were engaged in only a very simple motor task, i.e. standing, while the subject in Van Den Kroonenberg, Hayes and McMahon's (1996) study was engaged in the more complex task of walking prior to fall initiation. The difference between these two pre-fall scenarios in terms of cognitive demands and body kinematics may therefore influence the fall strategy an individual adopts during a fall. Taking these factors into account, although it would have been beneficial to capture a range of fall strategies, the fall strategy adopted by the subject in the present study was deemed acceptable.

The subject was asked to repeat the fall protocol a total of five times in order to capture some of the kinematic variation that might occur during a sideways fall in individuals. The subject had an array of 16 spherical retroreflective markers attached to repeatable bony landmarks located at the head, sternum, and bilaterally at the acromion process (shoulder), distal end of the radius (hand), anterior–superior–iliac spine (ASIS), greater trochanter (hip), lateral epicondyle of the femur (knee), patella (kneecap), lateral malleolus (ankle), medial malleolus (ankle), posterior surface of the calcaneus (heel) and hallux (toe) (appendix C).

#### **5.2.4.3 Data Collection**

Before kinematic data collection was undertaken, the motion capture camera system was calibrated. The Qualisys calibration frame was orientated such that the X axis was parallel with the long axis of the walkway (*i.e.* the walking direction), the Y axis defined the left and right directions perpendicular to the walkway and the Z axis defining up and down. Once calibrated, kinematic data was recorded using an integrated 12-camera Qualisys ProReflex motion capture system which actively record the three-dimensional positions of the retroreflective markers during the entirety of the kinematic sequence and then collected using Qualisys Track Manager. All kinematic data was recorded at a sampling frequency of 100Hz for the time-period that allowed the entirety of the kinematic sequence (*i.e.* just prior to the start of walking to a point in time just after completion of a sideways fall).



**Figure 5.1 Kinematic data collection.** The subject falling sideways on to the crash mat. It is possible to see one of the kinematic markers located on the subject's lateral malleolus. This marker corresponds to a green dot on the left-hand side figure.

#### 5.2.4.4 Data Processing

Marker trajectory data collected for each kinematic trial was manually gap-filled where necessary and then filtered in QTM to smooth it. It was then stored in a .tsv file which contained the full three-dimensional coordinate data, relative to the global reference frame, describing the trajectory of each marker. All coordinate data was transformed from cm into m. Using custom-written MATLAB scripts, each of the x, y and z components of the marker coordinate data was analysed to calculate the linear velocity of each marker during the fall.

However, the linear velocities of the centre of mass (CoM) of each body segment, as opposed to each marker, was required for the musculoskeletal model definition for subsequent dynamic simulations. Therefore, to approximate the linear velocities of the CoM of each body segment, the velocities of each segment's proximal and distal ends (as defined by the relevant markers) were taken and then averaged. The mean value was assumed to represent the segment's CoM linear velocity. Thus, for example the mean of the linear velocities of markers representing the greater trochanter and the lateral knee was taken to represent the linear velocity of the thigh and the mean of the linear velocities of markers representing the lateral knee and lateral ankle was taken to represent the linear velocity of the shank. For the trunk

however, only the linear velocity of the sternum marker was used because the position of this marker was very close to the trunk's CoM. Additionally, the linear velocities of markers representing the hallux and the posterior calcaneus was taken to represent the linear velocity of the foot. Linear velocities were then taken and used to define the linear velocity starting conditions of each segment for subsequent dynamic simulations of sideways falls.

Angular velocities for all body segments were calculated in GaitSym. Using GaitSym, simulations were run in which the musculoskeletal model could fall for just several time increments from its prescribed starting position. The obtained angular velocities, which approximated the motion of each body segment about its centre of rotation, were then taken and used to define the angular velocity starting conditions for subsequent final and full dynamic simulations of sideways falls.

## 5.2.5 Musculoskeletal Model

### 5.2.5.1 Overview

The musculoskeletal model utilized in this study represents a modified form of that used in a previous study by Sellers and colleagues (Sellers *et al.*, 2010) (figure 5.2). The model was the Leg3D model, taken from Model Repository 6.1 of the AnyBody Research Project ([www.anybody.aau.dk](http://www.anybody.aau.dk)). The musculoskeletal model definition is contained within an .xml file (appendix D) and its main components are described in the sections below.



**Figure 5.2** *The musculoskeletal model.* The musculoskeletal model used in the current study with the muscles used (red lines) displayed.

#### **5.2.5.2 Body**

The model consisted of a rigid head-arms-torso (HAT) segment, right and left thighs, right and left shank and three foot segments (rear-, mid-foot, metatarsals and toes) and a number of associated lower extremity muscles.

#### **5.2.5.3 Joints**

The hip joints were modelled as ball joints, the knees as hinge joints, the ankles as hinge joints, while the joints between foot segments were fixed. Modelling foot segments with fixed joints had the effect of creating a single rigid body. Because the purpose of this study was to use the musculoskeletal model to simulate sideways falls (as opposed to gait), fixing the joints between foot segments was assumed to have little effect on overall model performance but had the benefit of reducing unnecessary complexity within the model and reducing CPU time. Joint ranges of motion were kept the same as in Sellers et al., (2010) and were originally taken from (Silder *et al.*, 2007).

#### **5.2.5.4 Muscles and Tendons**

A total of 72 lower extremity muscles and associated tendons were included within the musculoskeletal model with 36 present on each leg. All muscle-tendon units (MTU's) were represented using GaitSym's custom implementation of a Hill-type muscle model (Figure 5.3). The Hill-type muscle model contains 3 elements:

1. Contractile element (CE): A contractile element (muscle) which has zero tension when at rest.
2. Series elastic element (SEE): An elastic element (tendon) arranged in series with the contractile element.
3. Parallel elastic element (PEE): An elastic element that is parallel with the contractile element that accounts for the inherent elasticity of muscle.

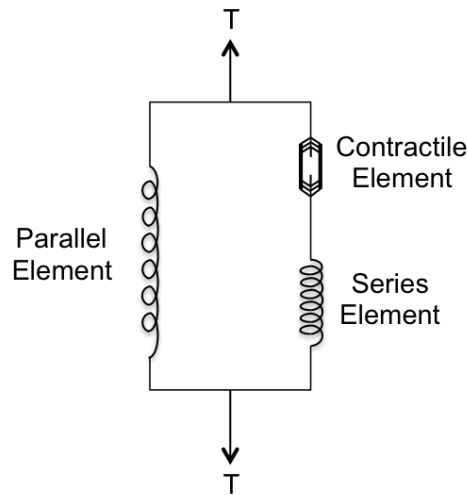


**Figure 5.3 Hill-type muscle model.** Schematic representation of the Hill-type muscle model illustrating the relationship between each of the three necessary elements. Adapted from Fung (1993).

Modelling muscles in this way had the advantage of being able to account for elastic energy storage during simulations.

All muscles were defined as having a specific tension of 0.3MPa and a strain of 60% at maximum isometric force. Activation rates – the time it takes for a muscle to reach full activation from a state of zero activation – for all muscles were set to 500ms. The maximum contractile speed was set to 8.4 lengths per second. Values for physiological cross-sectional areas (PCSA's), fibre lengths and tendon lengths were specific to each muscle-tendon unit. A proportion of 50% slow twitch to 50% fast twitch fibres was assigned to all muscles. These values appear to be a reasonable approximation of those that occur in older (and younger) individuals where there seems to be only slight deviations from a 1:1 ratio of type I and type II fibres (St-Jean-Pelletier *et al.*, 2017). All tendons were modelled as having 6% strain at maximum isometric contraction of the muscle component of the MTU.

#### 5.2.5.5 Geoms

Modifications were made to the model used in Sellers *et al.*, (2010) with respect to model-environment interactions through the addition of cylindrical 'geoms' to the right shank, thigh and hip (figure 5.4). By attaching geoms to regions of interest in the model, these parts of the model are able to interact with the simulated floor. The nature of the contact between geom and floor is governed by stiffness and damping values.

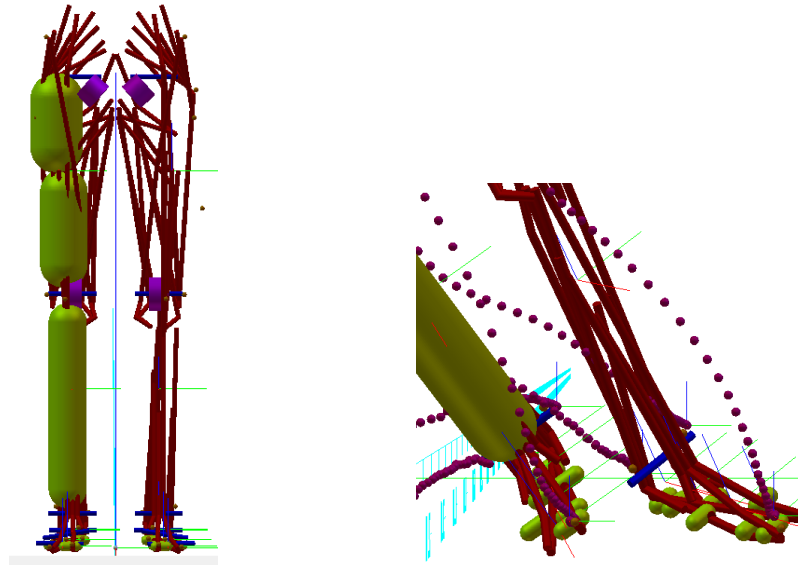


**Figure 5.4 Geoms.** **Left:** The musculoskeletal model with geoms (yellow cylinders) attached to the right leg. The geoms allow the leg to interact with the simulated floor during a sideways fall. **Right:** Zoomed in section of the feet belonging to the musculoskeletal model showing attached geoms. These allow the feet to interact with the simulated floor.

Cylindrically shaped ('capped cylinders') geoms were chosen because out of all available options these represented the most realistic shape for the anatomical structures they were representing (the shank, thigh and hip). The spring constant for the hip and thigh geoms was set to 68.9kN/m, the damping coefficient set to 1.0kN s/m and the coefficient of friction set to 0.5 because these have been identified as appropriate values for the upper leg region (Majumder, Roychowdhury and Pal, 2007). Similarly, the spring constant for the shank geom was set to 130.5kN/m, the damping coefficient set to 1.0kN s/m and the coefficient of friction set to 0.5 (Majumder, Roychowdhury and Pal, 2007).

Geoms were also modelled across several anatomical regions within the feet to model contact between the musculoskeletal and the simulation environment 'floor' (figure 5.4). Although quantifying loads during the hip-floor interaction at the end of each simulation was one of the ultimate aims of this study, each fall simulation started with the model in a semi-upright position and with the feet contacting the simulated ground. If the spring and damping values selected to model contact between the model feet and simulation floor were unrealistic (e.g. by being too high or too low), model behaviour and, consequently, the reliability of results could be adversely affected. For example, if the modelled contact interaction was too stiff, the model could spring upwards before falling to the side. This would affect the kinematics of the simulated fall which would in turn affect both impact and muscle forces. As such foot

geoms were modelled with the same spring and damping values used in Sellers *et al.*, (2010) because these had been deemed appropriate values for studies analysing human gait.

#### **5.2.5.6 Data Targets**

Data targets were included in the musculoskeletal model definition so that the model, via the optimisation procedure outlined, had the potential to match the recorded kinematic data of sideways falls in subsequent dynamic simulations to a reasonable degree of accuracy. Each data target corresponded to a retro-reflective marker used during kinematic data collection and contained coordinate information about each marker's three-dimensional trajectory for the time period of interest. Data targets thus represented the optimal trajectories for the model to match in subsequent dynamic simulations of sideways falls due to applied muscle activations and forces. The Euclidean distance between the data target (*i.e.* marker coordinate data) and the positions of model markers (that corresponded to those attached to the subject during kinematic data collection), also known as reporters (see below), was then calculated and used to judge how well each simulation matched the kinematic data. Data targets on the left leg of the model were given a lesser importance, relative to those on the right leg, in terms of how optimally reporters were required to match data target trajectories. This was done to allow improved optimisation of the right (*i.e.* impact) leg.

#### **5.2.5.7 Reporters**

As noted above, reporters were incorporated into the musculoskeletal model (figure 6). Reporters were attached to model body segments and corresponded to the markers attached to the subject for kinematic data collection. During subsequent dynamic simulations, the reporters output their position, orientations and velocities. The parameter of interest (position, in this case) was then compared to that of the data targets and as already discussed, used to assess how closely the model simulation matched the recorded kinematic sequence.

#### **5.2.5.8 Drivers**

Drivers were used in the musculoskeletal model to actuate muscles in the model. Drivers specify the stimulation patterns that are sent to muscles to create time dependant change in a number of muscle associated parameters. Without drivers, muscles in the model would act

as passive elements with zero activation. Specifically, stacked boxcar drivers were used in the present study. These allow multiple boxcar functions to produce the desired activation waveforms. Boxcar functions are functions whose values are zero except for a finite part of their arguments where they have a constant non-zero value.

The height of the non-zero value in each boxcar function represents the prescribed muscle activation level and its width represents the prescribed duration of that activation. Stacked boxcar drivers are cyclic in nature, applying the necessary activation levels for a specified time and at various frequencies. The cyclic frequencies, heights and widths of each boxcar function were specific to each muscle. Generic to all muscles however was the use of two boxcar functions to define the muscle's activation waveform. Two boxcar functions were chosen because it has been found previously that this improves the ability of the model to match a given kinematic sequence (William Sellers personal communication 2016).

#### ***5.2.5.9 Global and Environmental Parameters***

Global and environmental parameters that exist outside of the musculoskeletal model definition but that affect its behaviour were also defined. These parameters control the overall simulation environment. Acceleration due to gravity was given a standard value of  $-9.81\text{m/s}^2$ . The amount of interpenetration between contacts was set to 0.001 to aid simulation stability. The simulation integration step size was set to  $1\text{e-}4\text{s}$ . The integration step size advances the simulation by the value assigned to it. For each new step, adjustments are made to the state of the model.

The error reduction parameter (ERP) was set to 0.2. The ERP reduces errors associated with joints that violate prescribed joint constraints. These errors can occur at each integration step. The value assigned to ERP controls what proportion of the joint error will be fixed during the next integration step with a value of 0 signifying that no joint error will be corrected. Constraint force mixing (CFM) was assigned a value of  $1\text{e-}10$ . Non-zero values for CFM allow joint constraints to be violated to an extent by creating a 'soft' constraint. This essentially allows the bodies about the joint to come together and interact with each other more 'softly' than would otherwise be the case. Together, ERP and CFM can be used to define the spring and damping constants present at joints in the model and therefore control how body

segments interact with each other. They relate to the spring constant,  $k_s$ , and damping constant,  $k_d$ , as in equations 5.3a and 5.3b:

$$ERP = \frac{hk_s}{hk_s + k_d} \quad 5.3a$$

$$CFM = \frac{1}{hk_s + k_d} \quad 5.4b$$

Where  $h$  is the integration step size.

#### **5.2.5.10 *Scaling the Musculoskeletal Model***

Finally, the body segments of the musculoskeletal model were scaled so that the respective distances between reporters defined in the model matched the distances between retro-reflective markers used in the kinematic data collection. Scaling was achieved with a custom written MATLAB script. Individual scaling factors were determined for all lower extremity and HAT segments by comparing the distance between experimental markers and reporters on the musculoskeletal model. Using these scaling factors, the musculoskeletal model geometry was scaled. Joint locations, centre of masses and muscle attachment points were scaled according to the specific scaling factors of the body segment to which they belonged.

### **5.2.6 Simulation Protocol**

#### **5.2.6.1 *Defining the Starting Position of the Musculoskeletal Model for Forwards Dynamic Simulations***

Before dynamic simulations of sideways falls could be undertaken, it was first necessary to define the starting position of the model for each fall sequence (figure 5.6). The model's starting position is defined such that the positions of the reporters on the model reach an optimal match to the positions of the subject's markers at a particular point in time from each kinematic recording. Matching the model to the kinematic data in this way is called a static match.

The static match was carried out using a GA optimisation technique to randomly generate and test different combinations of body segment positions and orientations, with the match to kinematic marker positions judged by a least square fit across the full set of markers. In total, five static matches were made – one for each of the five sideways fall sequences – essentially resulting in the use of five musculoskeletal models. Each musculoskeletal model shared the same properties but differed in their starting positions (and data target values).

Trial simulations showed that it was not possible to perform a full dynamic match for the full kinematic sequence from the initiation of gait to the termination of a sideways fall. The sharp transition in the position, orientation and velocities of model body segments between gait and the initiation of a sideways fall presented difficulties during simulations that led to poor quality results. As such, it was decided to define the starting point for the static match and subsequent dynamic simulations just after the initiation of the sideways fall for each kinematic trial. This resulted in much better model performance.

The initiation of the sideways fall for each kinematic trial was identified in two ways. First, the linear velocity of the sternum marker was tracked in the x-direction. At the moment of initiation of a sideways fall, there was a sharp and rapid decrease in linear velocity. The point in time associated with this sharp transition was assumed to be the initiation of the sideways fall. Secondly, this point of time was corroborated by checking the kinematic recordings. A point in time immediately after this was then taken as the starting point for all static matches and dynamic simulations of the model. Linear velocities were used instead of the kinematic recordings because tracking linear velocities allowed more specificity and objectivity in identifying sideways fall initiation.

Because the purpose of this study was to quantify muscle and impact forces resulting from a sideways fall impact with the ground, modelling the fall only was deemed an acceptable approach. It was assumed that omission of the gait sequence preceding the fall will have had a significant effect on the final muscle and impact forces. Additionally, because it was possible to model the full fall sequence this increased confidence in the accuracy of the simulation with respect to the kinematics of a sideways fall and thus confidence in the reliability of results.

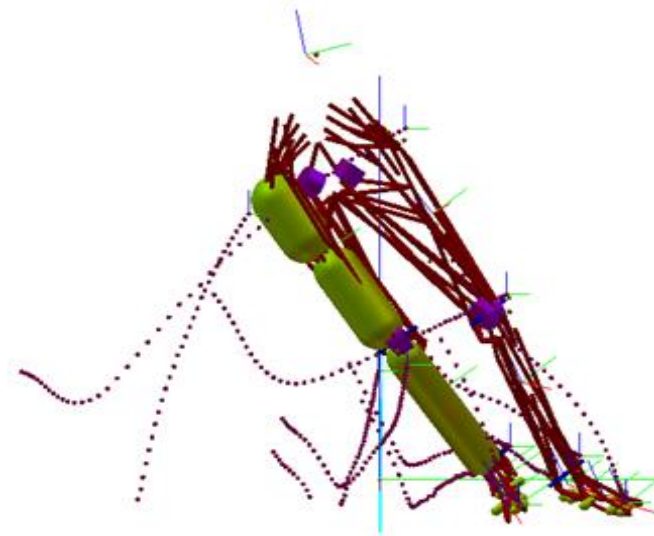


**Figure 5.5 Static match.** The ‘static match’ of the model corresponding to point in time from the kinematic data where a sideways fall has initiated. The static match formed the starting point for dynamic simulations. The purple dotted trajectory lines represent the data targets (*i.e.* the most optimal kinematic sequence) for the model to match. The single brown dots (e.g. at the shoulders) illustrate the reporters. These correspond to the markers from the kinematic data collection and are used to optimise the kinematics of the model through time through comparison of their positions with those of the data targets.

### 5.2.6.2 Forwards Dynamic Simulations of Sideways Falls

Once successful static matches had been achieved with the musculoskeletal model, it was possible to begin forwards dynamic simulations for each of the five sideways falls sequences. In contrast to the static matches where the model must match kinematic data for only a fixed instant in time, the full set of marker positions (as defined by data targets) for the entire duration of the chosen time-period from each kinematic recording represented the optimal solution for the forwards dynamic simulation. But like the static matches and as already discussed, dynamic simulations employed a GA optimisation technique to randomly generate and test different muscle activation patterns to find optimal solutions. The GA was designed to optimize the muscle activation pattern that yielded the best fit between model and experimental markers across the full sequence of walking as described in earlier sections.

Prior to commencement of forwards dynamic simulations, some minor and final modifications were made to each of the five musculoskeletal models used for each fall sequence. The linear and angular velocities calculated from the three-dimensional coordinate positions of retro-reflective markers as described in earlier sections were added to the musculoskeletal model body definitions to help describe the initial conditions for all body segments.

Each modelled fall was subject to 20 independent optimisation procedures, resulting in a total of 100 optimisation simulations for the full five fall sequences. Each fall sequence was subject to multiple optimisation simulations due to the issue of redundancy. Some of these solutions would work well in minimising the objective function of minimising the aggregate deviation between the simulated kinematics of the musculoskeletal model and real-world kinematic data of sideways falls whilst some would not. Being able to derive data from multiple simulations with good fitness means that the inherent and multifaceted variation in muscle activation sequences for a given kinematic sequence can, in part, be accounted for. If only a small number of optimisation procedures were run, the ability to capture this variation would be limited. Furthermore, running only a small number of optimisation procedures would increase the chance of obtaining only solutions with poor fitness and thus model behaviour might have little grounding in biological reality.

For each fall, each GA optimisation procedure was applied to the model until no further improvements in model performance were made or until the maximum number of optimisation repeats (20,000,000) or the maximum simulation time allowed (24 hours on 256 cores) was reached. Following this, each of the 100 optimised models was evaluated qualitatively within the GaitSym simulator for fitness. Simulations were judged qualitatively for fitness. Simulations in which the model displayed a poor-quality match to the kinematic data were disregarded whilst simulations with a good match to the kinematic data (based on how well the right leg and torso matched kinematic data) were retained and subjected to a final GA optimisation procedure.

The final GA optimisation differed slightly in approach because the starting population of muscle activation patterns for each simulation was not random. Instead the starting population contained muscle activation patterns of the fittest population taken from the relevant, initial GA optimisation routine. This starting population was then optimised further through additional exposure to the optimisation routine previously described. Starting the final optimisation with the 'fit' population meant the optimisation procedure could potentially provide more directed solutions that better minimised the objective function. It has been found previously that negating this step can lead to the optimisation routine continuing to explore a sparsely populated search space that would likely produce poor quality results (Sellers, Dennis and Crompton, 2003).

## 5.2.7 Parameters Quantified

### 5.2.7.1 *Kinematic Data*

X, Y and Z Linear velocities for the subject's sternum marker from each of the five recorded falls were analysed for differences. Being able to identify differences or similarities in linear velocities during the falls was used as a surrogate for identifying differences in the kinematics of each recorded fall. The rationale behind this approach was that doing so would help to explain and account for any variability in model behaviour between falls. Without first checking for variability in the kinematic data, it would be difficult to ascertain whether differences in model behaviour was a result of the inherent variability associated with the optimisation routine adopted in this study or the model retaining, at least qualitatively, the kinematics specific to each fall.

### 5.2.7.2 *Musculoskeletal Model*

Impact force magnitudes, muscle force (i.e. contractile force) magnitudes and tendon length changes were quantified from all successful simulations of sideways falls in GaitSym. These parameters were specifically chosen because they were needed as essential input into subsequent FEA simulations in chapter 5 to implement and realise the overarching aims of this thesis.

All parameters were calculated by averaging values from a 20ms time-period that began at the moment of impact. The moment of impact was defined as the point in time in which one or more parts of right hip geom contacted the simulated floor. A time-period of 20ms was chosen because (Majumder, Roychowdhury and Pal, 2008) demonstrated that this is approximately the time-period it takes for a peak force magnitude resulting from an impact with the floor to be applied to the hip when soft tissues are taken into account. Averaging the impact force values that occurred during this time period while the hip geom interacted with the environment floor therefore provided a reasonable way to approximate this process and assign appropriate values for impact forces in subsequent FE simulations. This method also had the added benefit of 'smoothing' out any unrealistically high impact forces that occurred at the initial moment of impact that would otherwise adversely affect results.

The X, Y and Z components and the resultant magnitude of each impact force were calculated. The relative contributions of each of these components to the overall force magnitude was of particular interest. Given that it is not possible to validate the accuracy of the absolute forces within the context of a human impacting the floor due to ethical and safety reasons (one of the main motivations for using MDA modelling), measuring differences in the relative contributions of each of these components to overall impact forces still permits meaningful discussion because these differences can be applied in FE simulations to explore their effects on stress/strain distributions in the femur.

Contractile muscle force magnitudes and tendon length changes were taken and averaged for the same 20ms period used to define impact forces for the following muscles:

- Gluteus maximus (3 muscle bellies)
- Gluteus medius (3 muscle bellies)
- Gluteus minimus (3 muscle bellies)
- Iliopsoas
- Piriformis
- Vastus lateralis
- Vastus intermedius

Gluteus maximum, gluteus medius and gluteus minimus are represented by three muscle bellies to better capture the large areas of attachment these muscles have to bone. Because of the overarching aims of this thesis it was decided to focus on these muscles because of their potential relevance for fracture of the proximal femur; their insertion sites are situated across various locations throughout the proximal femur and as such, their contractile behaviour could affect stress patterns and distributions and thus the likelihood of fracture.

### **5.2.8 Statistical Analysis**

All statistical analyses were carried out in MATLAB. The Kolmogorov-Smirnov test, QQ plots and kernel density estimates were used to check all data for departures from normality. The Kendall tau rank correlation coefficient was used to define how well correlated muscle forces were between simulations. The Brown-Forsythe test for homoscedasticity was used to identify statistically significant differences in homoscedasticity for muscle and impact force magnitudes. Kruskal-Wallis' one-way analysis of variance was used to test for statistically

significant differences in impact forces and Scheffe's procedure was used as a post-hoc test for Kruskal-Wallis to conduct multiple pairwise comparisons and locate exactly where significant differences lay. One-way multivariate analysis of variance (MANOVA) was used to test for statistically significant relationships between the components of linear velocities associated with each fall as well as between the components of impact forces associated with each fall.

## 5.3 RESULTS

### 5.3.1 Kinematic Data

#### 5.3.1.1 *Fall type*

For each of the five sideways falls, the subject can be described as falling in an anterolateral direction, without use of the forelimbs to modify the impact at the hip.

#### 5.3.1.2 *Linear velocities*

Qualitatively exploring the data with a matrix plot (figure 5.7) of each pair of the X, Y and Z components for the sternum marker shows a discernible difference between the linear velocities of fall five and the other four falls. This is particularly true for the linear velocities in the Z direction where values appear to be higher in magnitude.

Generally, the other four falls show a good degree of overlap for linear velocity in each of the X, Y and Z directions. Specifically, falls one, three and four show a high degree of overlap in all directions. Fall two appears to show more variability in values relative to falls one, three and four, especially in the X and Z directions.

Generally, the other four falls show a good degree of overlap for linear velocity in each of the X, Y and Z directions. Specifically, falls one, three and four show a high degree of overlap in all directions. Fall two appears to show more variability in values relative to falls one, three and four, especially in the X and Z directions.

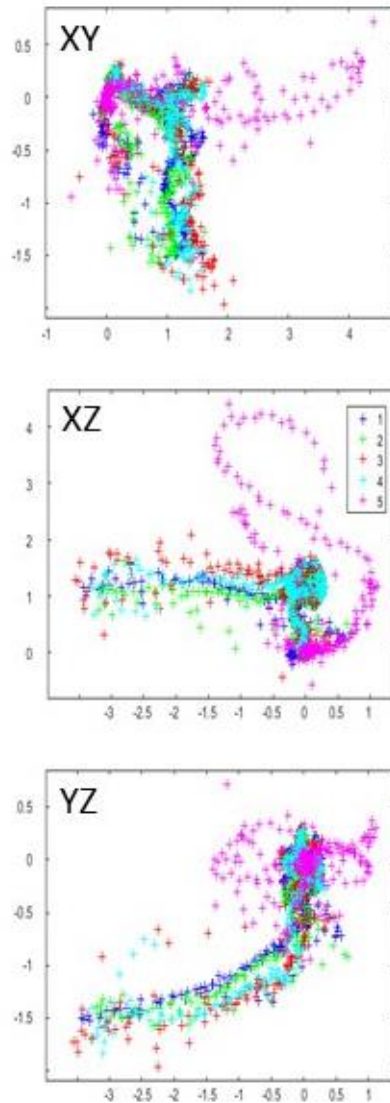


**Figure 5.6 Paired plots of linear velocity components.** Each pair of the X, Y and Z linear velocity components plotted together and belonging to each fall. The colour of each data point corresponds to the fall from which it is derived as delineated in the symbol legend in the middle plot. Axes values correspond to linear velocities. Purple data points belong to fall 5 and it is clear that these do not cluster as closely together as other falls do with each other. Fall 5 displays much larger values and more variation for linear velocities, particularly in the Z (inferior-superior) direction. Velocities for X, Y and Z components for the other 4 falls cluster much more closely together.

MANOVA results for the combined X, Y and Z linear velocities of the sternum marker support these qualitative observations. Significant differences ( $p < 0.05$ ) were found between the five falls with all group means existing in a two-dimensional space (*i.e.* within a plane). However, if data for fall five was excluded from MANOVA, the group means existed within a one-dimensional space (*i.e.* along a line). This indicates that falls one to four clustered more closely to each other than any did to fall five. A MANOVA cluster plot (figure 5.8) supports these conclusions by delineating the proximity (in terms of their degree of similarity) of each fall to the others.

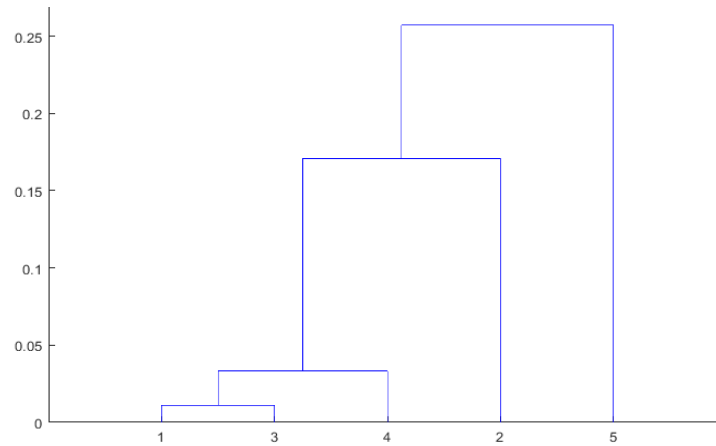


**Figure 5.7** MANOVA dendrogram plot for linear velocities of real-world falls. MANOVA cluster plot highlighting the statistical strength of relationships between the linear velocities of falls 1 to 5. The cluster plot shows falls 1 to 4 to have a closer relationships with each other than fall 5 has with any of falls 1 to 4. Additionally, falls 1 and 3 and falls 2 and 4 respectively closer relationships than they do with any other falls.

### 5.3.2 Musculoskeletal Model

#### 5.3.2.1 Successful Simulations

In total, 35 out of a possible 100 forwards dynamic simulations of sideways falls were judged to be successful based primarily on how well the right leg and trunk matched kinematic data (e.g. figure 5.9). Judging was guided by fitness scores and a qualitative assessment of model kinematics. The simulations represented data from four out of five recorded real-world fall sequences; 19 simulated falls from fall one, three from fall two, 10 from fall three, three from fall four and none from fall five. For each successfully simulated fall, the number of optimisation iterations before no improvements were seen in model fitness ranged between approximately 2,000,000 and 10,000,000.

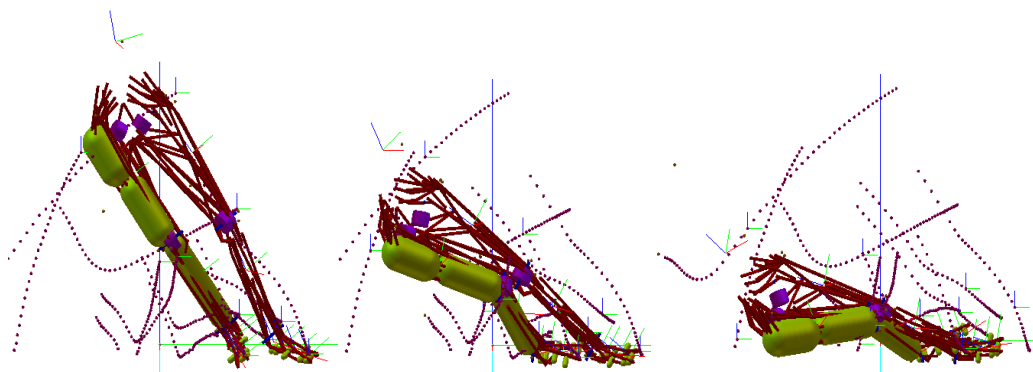


**Figure 5.8 Successful falls.** Example of a successful forward dynamics simulation of a sideways fall. The left hand side picture shows the model's start position as determined by the static match. Moving from left to right maps the model's trajectory through time from the initiation of a sideways fall until the model impacts the ground with the right hip.

For some of the falls judged to be successful, the left limb behaved unrealistically at the hip joint, displaying a greater range of motion than would occur during human movement. This was probably due in part to the fact that data targets on the left limb were deliberately given a lesser weighting compared to those on the right lower limb in terms of the importance assigned to them during GA optimisation procedures. Allowing unrealistic behaviour at the left hip when judging falls to be successful was deemed an acceptable compromise because it was thought to have minimal influence on the fitness of the right leg and torso with respect to the kinematic data.

### 5.3.3 Impact Forces

The range of absolute impact force magnitudes of all successfully simulated falls was 2753 to 14,804N (figure 3.11). The range of impact force magnitudes for the components of the simulated falls was X = 26 to 4414N; Y = 7 to 5734N; Z = 2406 to 13,561N (figure 5.10).

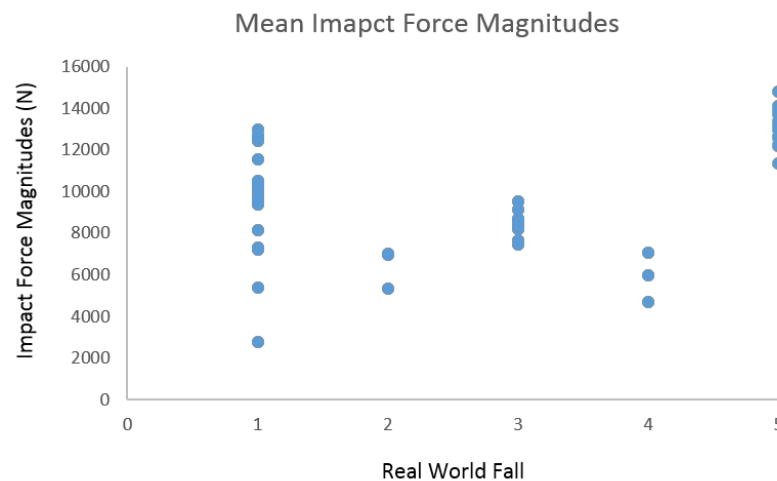


**Figure 5.9 Mean impact forces (N).** Average simulated impact force magnitudes. Falls were grouped by the real-world fall they were simulating and the mean calculated by using relevant impact data. Impact forces were determined through the modelled contact interaction between the simulated floor and the model hip geom.

The average impact force magnitude of all simulated falls was 8696N. The range of average impact force magnitudes of simulated falls with respect to each of the recorded real-world falls was 5996 to 13,151N. The range of average impact force magnitudes for the components of simulated falls with respect to each of the recorded real-world falls was X = 367 to 2674N; Y = 817 to 4816N; Z = 5477 to 11,919N (figures 5.11 & 5.12). The range of absolute component contributions are illustrated in figure 5.13.

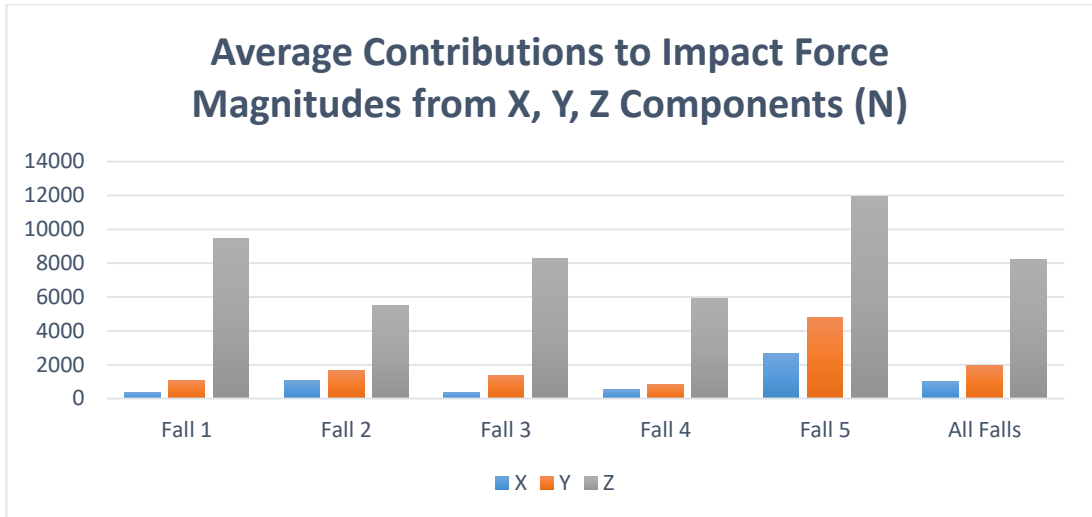


**Figure 5.10 Average impact force component contributions (N).** Average contributions of individual X, Y & Z force components to average simulated impact force magnitudes. Falls were grouped by the real-world fall they were simulating and the mean calculated by using relevant impact data. Impact forces were determined through the modelled contact interaction between the simulated floor and the model hip geom.

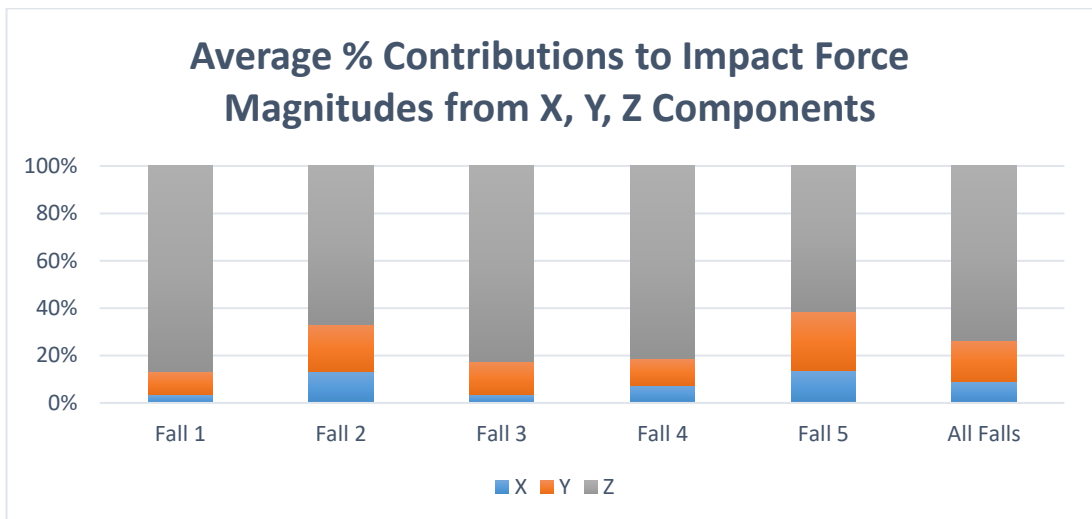


**Figure 5.11 Average percentage impact force component contributions.** Average contributions of individual X, Y & Z force components to average simulated impact force magnitudes, expressed as percentages.

## Contributions to Impact Force Magnitudes from X, Y, Z Components

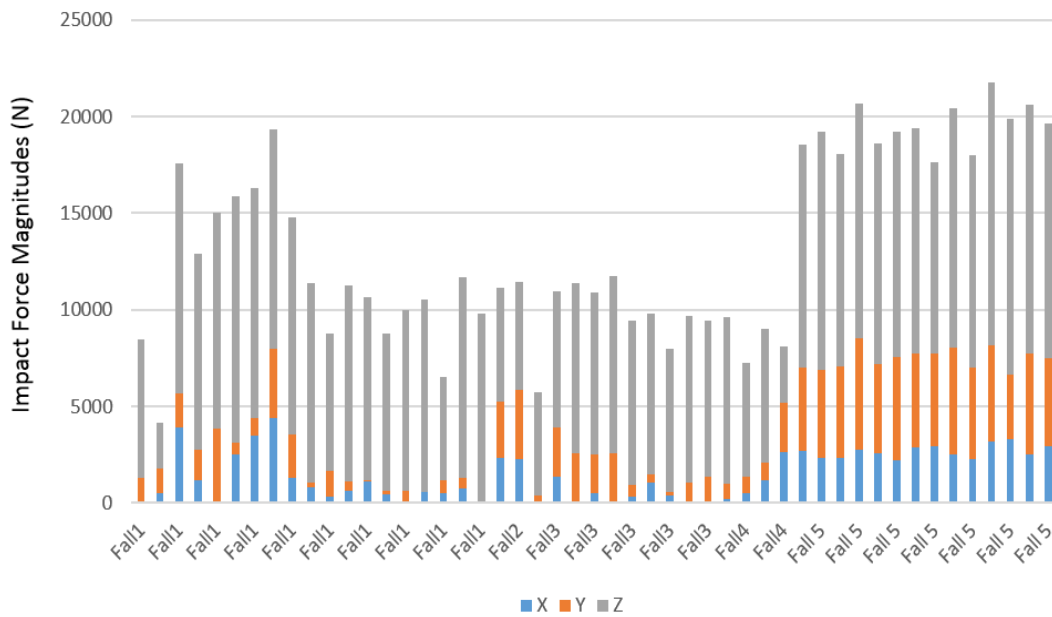


**Figure 5.12 Absolute component contributions (N).** Absolute X, Y & Z force component contributions to overall impact force magnitudes for all successful simulations, grouped by the real-world fall each simulation represented.

### 5.3.3.1 Determining normality of impact force data

Simulation impact force data was initially tested for normality using the one-sample Kolmogorov-Smirnov test. This test showed data to be non-normally distributed ( $p < 0.01$ ).

### 5.3.3.2 Statistical Analysis of Impact Forces

#### 5.3.3.2.1 Impact Force Magnitudes

On the basis data was non-normally distributed, the Brown-Forsythe test for homoscedasticity was used to test for differences in sample variances. Results demonstrated that simulated impact force magnitudes between simulations belonging to each of the five modelled falls had unequal variance ( $p < 0.01$ ) (figure 5.14).

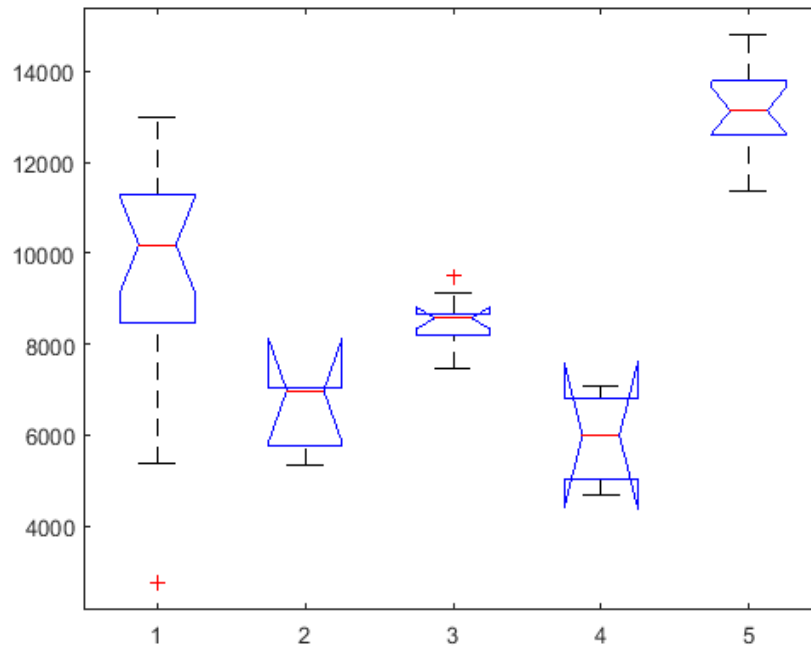


**Figure 5.13 Brown-Forsythe - impact force magnitudes.** Brown-Forsythe box plots of collective impact force data for each simulated real-world fall. The incongruence between box plots demonstrates statistically significant differences in variance of impact data between falls. Y-axis = impact force (N). X-axis = real-world fall.

The non-parametric Kruskal-Wallis one-way analysis of variance was therefore used to compare impact force magnitudes between each group of simulations modelling each real-world fall to test for statistically significant differences. Kruskal-Wallis one-way analysis of variance indicated that significant differences existed between the five modelled falls.

Post hoc pairwise comparisons were then computed using Scheffe's procedure to explore exactly which groups of simulations showed statistically significant differences for impact force magnitudes. Pairwise comparisons elucidated statistically significant differences between simulations belonging to fall 5 and all others ( $p < 0.05$ ). All other impact force magnitudes across falls one to four showed no statistically significant differences (figure 5.15).

#### 5.3.3.2.2 Impact Force Components

Tests to find statistically significant differences in the combined, relative contributions of X, Y and Z components of impact forces between simulated falls were also performed. QQ-plots and kernel density estimates were used to explore the normality of force component residuals and these demonstrated residuals for the X and Y components had conservative bimodal distributions. Residuals for the Z component showed a normal distribution.

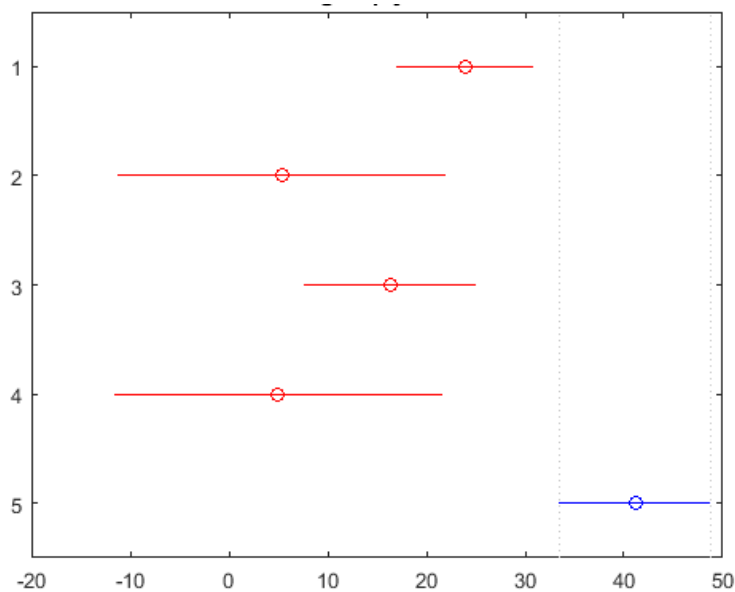


**Figure 5.14 Scheffe's procedure - impact force magnitudes.** A plot resulting from Scheffe's procedure for multiple pairwise comparisons illustrating that impact forces for fall 5 (blue) were significantly different from impact forces for falls 1 to 4 (red). However, the plot also shows that impact forces for falls 1 to 4 were not significantly different from each other. Y-axis = real-world fall. X-axis = average group ranks.

There were clear reasons for these residual distribution patterns; the magnitudes of the X and Y components for simulations belonging to fall five were much higher than compared to any other simulations while there was much greater overlap between all simulations in Z component magnitudes. A pairs plot (figure 5.16), with XY, XZ and YZ components plotted together highlight these patterns well with the XY plots showing a clear separation between simulations belonging to fall five and remaining simulations belonging to all other falls.

MANOVA was performed to explore collective differences in X, Y and Z components between fall simulation groups. MANOVA results (figure 5.17) supported observations previous observations in residual distributions and found component data for fall five to be significantly different from component data for all other falls. Component data between falls one and three was more related than with any other falls. Component data between falls two and four was more related than with any other falls.

When component data for fall five was excluded from the MANOVA analysis (and thus residuals more normally distributed), the multivariate means existed only along a one-dimensional line vector, as opposed to existing along two-dimensional plane when fall five component data was included. In other words, the collective component data was more closely related between falls one to five than for all five falls.

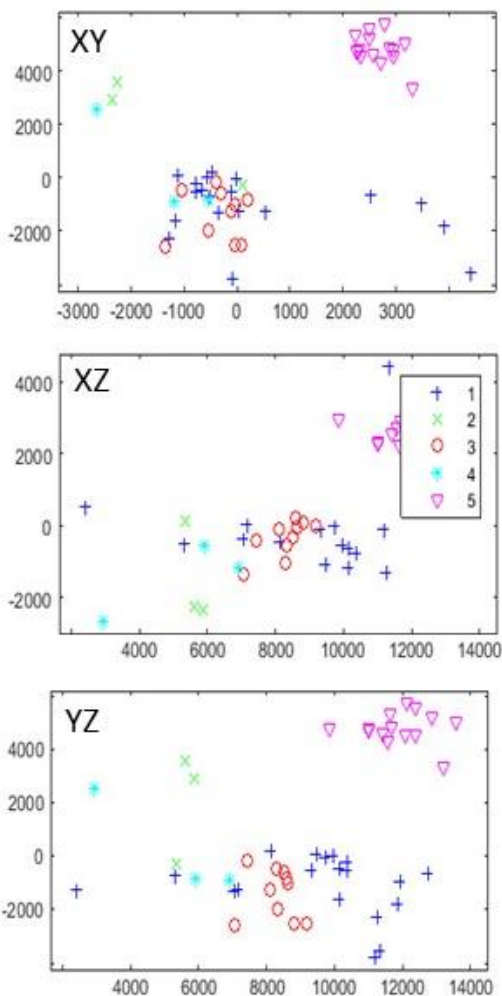


**Figure 5.15 Paired plots of impact force components.** Each pair of the X, Y and Z force components plotted together and belonging to each fall. The colour of each data point corresponds to the fall from which it is derived as delineated in the symbol legend in the middle plot. Axes values correspond to force magnitudes in newtons. Purple data points belong to fall 5 and it is clear that these do not cluster as closely together as other falls do with each other. Fall 5 displays larger values for impact force components, particularly in the Z (inferior-superior) direction. Force components the other 4 falls generally cluster more closely together.

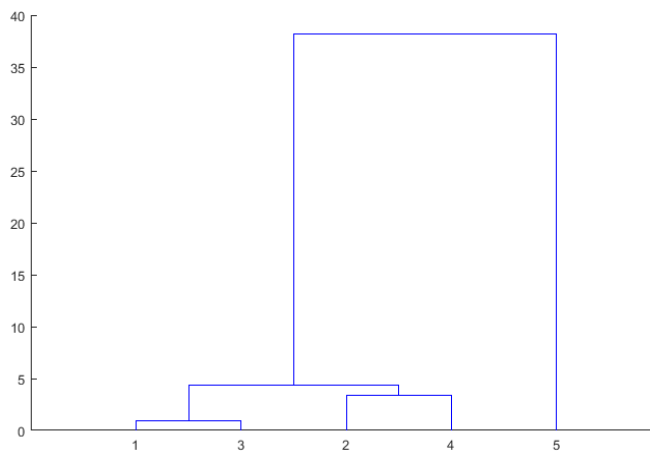


**Figure 5.16 MANOVA dendrogram - impact force components.** MANOVA dendrogram highlighting the statistical strength of relationships between simulated impact forces of falls 1 to 5. The dendrogram clearly shows that falls 1 to 4 to have closer relationships with each other than fall 5 has with any of falls 1 to 4. Additionally, falls 1 and 3 and falls 2 and 4 respectively closer relationships than they do with any other falls.

### 5.3.4 Muscle Forces

The range of values for each muscle across all simulated falls were as follows: Gluteus maximus 0.7 to 909.3N, gluteus medius 0 to 1450.2N, gluteus minimus 0 to 334.9N, iliopsoas 0 to 1314.8N, piriformis 0.3 to 175.8N, vastus intermedius 0.1 to 1128.3, and vastus lateralis 1.4 to 1627.7N.

Mean force values for each muscle during the moment of impact for all simulated falls were as follows: Gluteus maximus 200.5N, gluteus medius 286.2N, gluteus minimus 92.2N, iliopsoas 345N, piriformis 42N, vastus intermedius 521.4N, and vastus lateralis 849.9N. Simulations that modelled real-world fall five displayed poor-quality muscle data and were therefore excluded from subsequent analyses.

Mean force values for each muscle at the moment of impact across all simulated falls excluding fall five were as follows: Gluteus maximus 246.5N, gluteus medius 357.7N, gluteus minimus 116.4N, iliopsoas 394.9N, piriformis 52.5N, vastus intermedius 594.4N, and vastus lateralis 994N.

However, as the range of muscle force values suggests, mean values derived from the entirety of simulation data mask the considerable variation in muscle force magnitudes that occurred within and between groups of simulations belonging to each fall (e.g. appendices E1 & E2). Reflecting this, muscle force magnitudes for the same muscle across simulations modelling the same real-world fall varied by several orders of magnitudes (appendix E2).

Despite the heterogeneity witnessed for muscle forces, vastus intermedius and vastus lateralis consistently produced higher forces than other muscles in nearly all simulations. To a lesser extent, iliopsoas, Gluteus maximus and Gluteus medius also tended to do this. Appendices E1 and E2 highlight these trends well with these muscles represented by near continuous red/dark red rows elucidating higher force production relative to other muscles.

#### 5.3.4.1 *Statistical Analysis of Muscle Forces*

Each muscle from each simulation belonging to the same real-world fall – e.g. gluteus maximus for simulations 1-19 modelling real-world fall one – was analysed for correlations

with itself using Kendall's Tau rank correlation coefficients. It was generally found that each muscle was positively correlated with itself e.g. Gluteus maximus tended to be positively correlated with itself across simulations 1-19 belonging to real-world fall one and so on.

The positive correlations suggest a general trend for increasing muscle force during impact (e.g. figure 5.18). Correlation coefficients were consistently larger for some muscles compared to others, with iliopsoas in particular showing strong, positive correlations with itself across the majority simulations for all real-world falls (e.g. figure 5.19).

Although there was a general trend for positive correlations (and therefore increasing muscle forces) during impact, there was nonetheless a broad spectrum of weak to strong correlation coefficient values ( $R=0.01$  to  $R = 1$ ) and ultimately, there is no readily clear, discernible pattern of correlation between simulations for each fall for each muscle with itself.

Gluteus maximus provides a good example of this inconsistency. Across simulations 1-19 which simulated real-world fall one, gluteus maximus was sometimes positively correlated with itself and the gradient of the slope defining this positive correlative relationship was also positive. This suggests that gluteus maximus tended to show an increase in muscle force production for the 20ms period defining the fall impact. For other simulations belonging to real-world fall one (*i.e.* simulations 1-19) gluteus maximus was sometimes negatively correlated with itself and on occasion, positively correlated with itself but with a negative gradient to the correlations slope, suggesting conversely, gluteus maximus demonstrated decreasing muscle force production during the 20ms period defining impact.

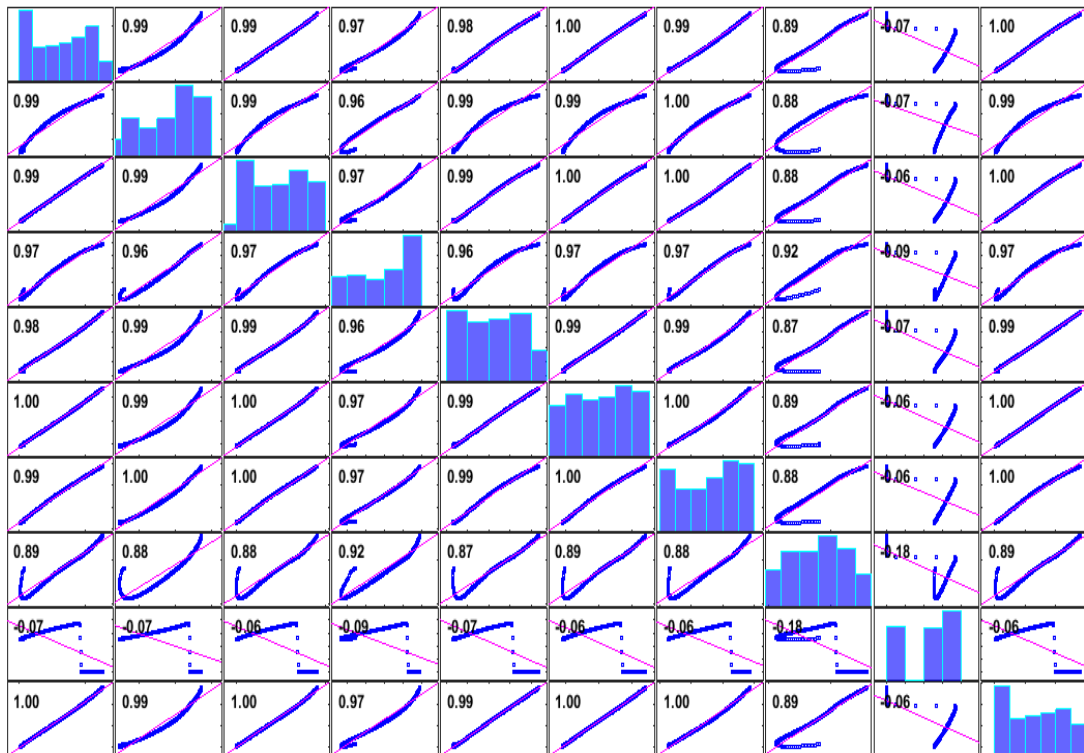


**Figure 5.18 Kendall tau matrix plot - gluteus maximus** Matrix plot providing an example of the positive correlations between forces belonging to the same muscle across the majority of simulations modelling real-world fall 3. Gluteus maximus is shown here. The positive gradient of the slope describing each relationship suggests muscle forces increase during the 20ms time frame used here to define impact with the ground. Rows (left to right) and columns (top to bottom) signify simulations 1-10. The matrix plot is symmetrical about the diagonal and each row and column corresponds to a specific simulation. The histograms on the diagonal are histogram plots of the raw data from which the correlations have been inferred. Numbers in the top left of each plot are the correlation coefficients.

Brown-Forsythe tests for homoscedasticity revealed statistically significant differences in the variance of muscle force data ( $p < 0.05$ ). Kruskal-Wallis' one-way analysis of variance was used to determine whether there were statistically significant differences in force magnitudes for each muscle between simulations modelling each real-world fall e.g. in force magnitudes for gluteus maximus between simulations modelling fall one. Statistically significant differences were found for every muscle across all falls ( $p < 0.05$ ).

However, it was generally difficult to discern clear or consistent patterns as to when these statistically significant differences would occur. Post-hoc pairwise comparisons computed using Scheffe's procedure helped to elucidate some statistical relationships, but they should still be considered inconsistent. Iliopsoas force magnitudes showed the least number of significant differences across simulations (e.g. figure 5.20) with some clustering of muscle force mean ranks. To a lesser extent, vastus intermedius and vastus lateralis displayed some clustering too.

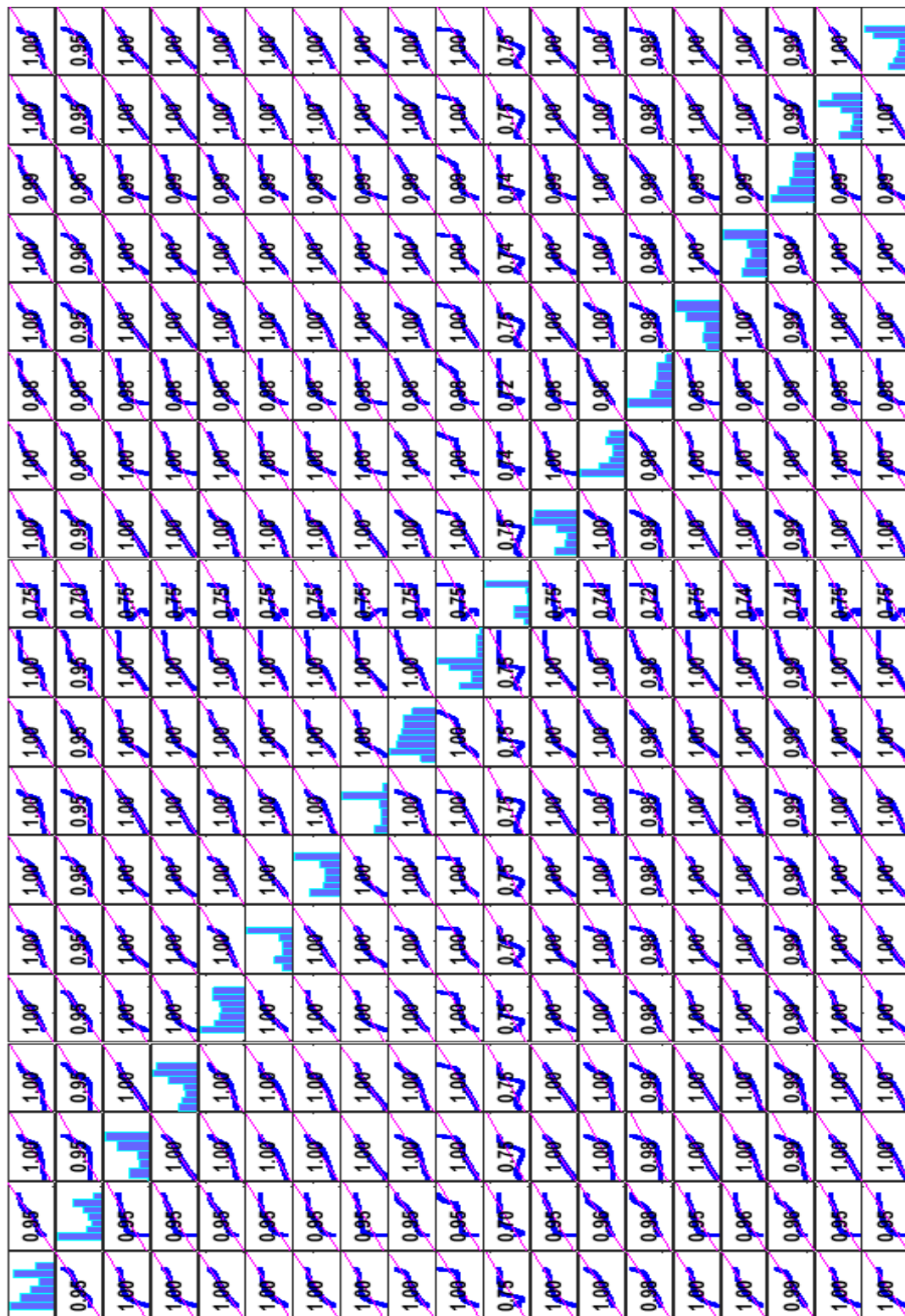
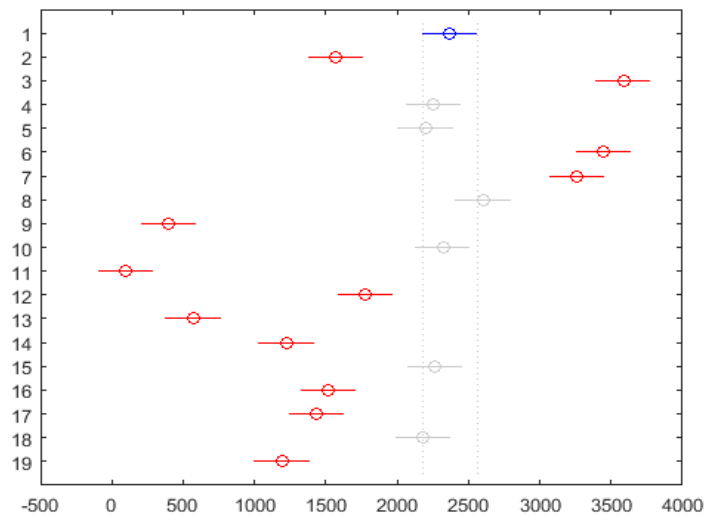


Figure 5.19 Kendall tau matrix plot - iliopsoas. Matrix plot of Kendall tau correlation coefficients for iliopsoas across all simulations modelling real-world fall 1. The plots show the strong positive correlation for iliopsoas force data across all of these simulations. Rows (left to right) and columns (top to bottom) signify simulations 1-19. The matrix plot is symmetrical about the diagonal and each row and column corresponds to a specific simulation. The histograms on the diagonal are histogram plots of the raw data from which the correlations have been inferred. Numbers in the top left of each plot are the correlation coefficients.



**Figure 5.20 Scheffe's procedure - iliopsoas.** Multiple pairwise comparisons for iliopsoas muscle forces across all simulations belonging to fall 1 (y-axis). Some moderate clustering between mean ranks (x-axis) is shown (blue and grey). Clustering demonstrates samples come from the same population. Additional clustering can be seen between mean rank samples to the immediate left of those shown in blue and grey.

When Kendall tau was used to search for correlations for force magnitudes between all 13 muscles during a single simulation, several patterns were discernible. For each simulation belonging to falls one, two and four, all 13 muscles were positively correlated with one another, except for iliopsoas, vastus intermedius and vastus lateralis, which were positively correlated with each other but negatively correlated with all other muscles (e.g. figure 5.21).

For simulations modelling fall three, vastus intermedius and vastus lateralis tended to be positively correlated with other muscles, while iliopsoas tended to remain negatively correlated with all others. Given the lack of congruency for within fall muscle data, statistical comparisons were not conducted for between fall data.



**Figure 5.21 Kendall tau matrix plot - all muscles.** Matrix plot of Kendall tau correlation coefficients for lengths all 13 muscles of interest in from a single simulation. The matrix plot shows positive correlations between all muscles except iliopsoas, vastus intermedius and vastus lateralis which have negative correlations to all other muscles but positive correlations to each other. The matrix plot is symmetrical about the diagonal and each row and column corresponds to a specific simulation. The histograms on the diagonal are histogram plots of the raw data from which the correlations have been inferred. Numbers in the top left of each plot are the correlation coefficients.

### 5.3.5 Tendon Length Changes

Tendon length changes were quantified at the moment of impact. They were quantified for use as inputs into subsequent FE simulations (chapter 6). Median length changes of tendons at the moment of impact from simulations grouped by the real-world fall they modelled – e.g. the median length change value for gluteus maximus from simulations 1-19 representing real-world fall 1 – are described in appendix F.

## 5.4 DISCUSSION

At a very general level this work has demonstrated that MDA can be used to model real-world sideways falls to explore the potential impact forces, muscle forces and tendon length changes that might occur at the moment of impact during a sideways fall. For falls one to four, nearly all simulated impact forces are within or close to the range of values previously reported in experimental and modelling studies (Robinovitch, Hayes and McMahon, 1991; Robinovitch, McMahon and Hayes, 1995; van den Kroonenberg, Hayes and McMahon, 1995; Groen, Weerdesteyn and Duysens, 2007a, 2008; Hirabayashi *et al.*, 2013) and intimates the musculoskeletal model, in a kinematic sense, behaves reasonably when considering the relationship between kinematic and impact force data found in this study (figure 5.10). All simulations modelling fall five produced impact forces well above those reported previously (figure 5.10) and may be indicative of the general poor performance of the model and the fact that the GA optimisation procedure can converge on sub-optimal solutions.

It is harder to validate muscle forces due to the inadequacies of EMG in quantifying the force production of individual muscles (Pandy and Andriacchi, 2010) and due to a lack of experimental and modelling research quantifying or predicting muscle forces during falls of any type; often the focus has been on quantification or prediction of muscle forces during other biomechanical activities such as walking or running (Sasaki and Neptune, 2006; Barrett, Besier and Lloyd, 2007; Ren, Richard K Jones and Howard, 2008; Rajagopal *et al.*, 2016). It is possible however, to use the range of forces from those studies as a guide and the muscle force magnitudes from this study fall within those predicted ranges. For example, the force magnitudes at impact of gluteus medius, gluteus maximus and vastus muscles generally agree with those found with Pandy and Andriacchi (2010) for walking and running activities. This suggests that, as with the kinematics, the musculoskeletal model performed to an acceptable

level when simulating muscle behaviour.

This study has established that impact (to a lesser extent) and muscle force magnitudes (to a greater extent) can vary significantly during a sideways fall, even for very similar kinematic sequences. This variation can be thought of as being inherently linked to three factors:

1. The kinematics specific to each fall.
2. The inherent randomness of the genetic algorithm used for model optimisation.
3. The issue of abundance/redundancy.

There can be a certain level of confidence in the fact that the variation seen in impact force magnitudes arises, in part, due to the idiosyncratic kinematics of each fall and not solely due to the randomness associated with the optimisation procedure and thus random differences in how well the model matched kinematic data.

This proposition is supported by previous research that has found the kinematics associated with specific fall-types and falling strategies have a direct impact on the magnitudes of impact forces and velocities (Robinovitch *et al.*, 2000; Robinovitch, Brumer and Maurer, 2004; Nankaku *et al.*, 2005; Tan *et al.*, 2006; Feldman and Robinovitch, 2007; Groen, Weerdesteyn and Duysens, 2007b, 2008). Further support for the effect of model kinematics on simulated impact forces comes from the fact that there is strong agreement between the statistical clustering of fall linear velocities (used as a qualitative surrogate to differentiate between the kinematics specific to each fall) and impact forces (figure 5.8). A strong positive correlation between linear velocity and impact force has been demonstrated (Luo *et al.*, 2014) and it should therefore be unsurprising that those statistical relationships seen between the linear velocities of each fall (figure 5.7) are reflected in the statistical relationships observed for impact forces.

For this strong positive correlative relationship to hold true, the model must preserve at least qualitatively, some of the specifics of the kinematics of each fall. Importantly then, the fact that this relationship exists in the present study implies that the forwards dynamics approach generally and the musculoskeletal model specifically have been able to capture both kinematic idiosyncrasies and the effects these have on resultant parameters such as impact forces.

Despite this, it is likely that some part of the observed variation in model behaviour and thus impact forces is due to the randomness associated with the optimisation procedure which directly affects how well the model is able to match the experimentally measured kinematics.

This is demonstrated by multiple simulations modelling the same fall (e.g. the 19 simulations modelling fall one) displaying measurable differences for impact force magnitudes.

Across most simulations, there were inconsistent patterns for muscle force magnitudes at impact (e.g. appendices E1 & E2). There were several exceptions to this rule; the relative consistency in force production of vastus intermedius, vastus lateralis, and iliopsoas and the general tendency for muscle contractile force to increase during the 20ms following impact (figures 5.18 & 5.19). While absolute muscle force magnitudes reflect the properties assigned to muscles, the relative consistency in force production between simulations for these three muscles, suggests that fall kinematics may also be influential, at least for these muscles.

That vastus intermedius, vastus lateralis and iliopsoas are most consistent in force production might make sense when we place their contractile behaviour within the contextual framework of the qualitative kinematics. During each sideways fall, the position of the right thigh and shank are relatively static. For vastus intermedius and vastus lateralis (both of which are major contributors to movement at the knee joint), the relatively static nature of the right thigh and shank combined with the fact that degrees of freedom are constrained at the knee because it is a hinge joint, may explain why there is more consistency observed in their force magnitudes. The relatively static nature of the interaction between the trunk and right thigh may help to explain why there is also a reasonable level of consistency seen for iliopsoas which contributes to flexion of the hip.

However, the hip joint is able to move through several DoF's. As a consequence of relatively high mobility at the hip, the thigh may be more prone to small variations in internal and external rotation than the knee, which have minimal effect on overall model performance. Such rotational movements are controlled by other hip musculature such as gluteus maximus, gluteus medius and gluteus minimus and this might explain, in part, why there is much variability observed for these muscles.

Although the fall kinematics may be influential, it appears that the kinematics specific to an anterolateral fall may have less of an effect on muscle force magnitudes than they do on impact forces. It is likely that randomness associated with the genetic algorithm component of the optimisation process and the issue of abundance/redundancy contributes significantly towards the variability and inconsistency of muscle force magnitudes (Pandy and Andriacchi, 2010). It is perhaps unsurprising, given the large number of muscles controlling just three degrees of freedom at the hip joint (even with relatively the static positions of body segments during each sideways fall), that abundance/redundancy may be a source of the variation in

muscle force magnitudes found in the present study.

Additionally, the inability to detect and define consistent trends and statistical relationships for muscle force magnitudes may result from the small number of simulations used in this study, compared to the large number of possible muscle activation sequences. Given the vast number of possible muscle activations for the modelled movements, 20 initial optimisation runs may simply be insufficient to capture any underlying patterns in resultant muscle force magnitudes; it is plausible that optimal solutions centre about certain activation patterns/muscle force magnitudes. Indeed, recent work by Valero-Cuevas *et al.*, (2015) has demonstrated that muscle activations are constrained by specific kinematic sequences e.g. throwing a disc, to a higher degree than has previously been envisaged which would. This suggests that with a larger cohort of simulations, more consistent muscle activations and force magnitudes might be attainable.

Exploring this possibility would be an exciting prospect but is currently impractical due to the significant time and computational resources that would be required using the methods employed in this study. One way to bypass these potential constraints would be for future work to utilise Monte-Carlo or canonical analytical techniques, to explore potential activation sequences. A Monte-Carlo approach has previously been used successfully (Viceconti *et al.*, 2012). Monte-Carlo and canonical approaches could also be used to quantify which of the three factors identified here as the main drivers for variation in muscle force magnitudes (idiosyncratic kinematics, redundancy and the optimisation process) best explain this variation. For impact force data however, this study suggests that linear velocities specifically, and the kinematics of the fall more generally, best explain impact force magnitudes and the relative contributions of each of the X, Y and Z impact force components arising from an anterolateral fall.

Tendons for all MTU's at impact showed an increase in length relative to their original lengths (appendix F). The relationship between tendon length change and the contractile behaviour of a muscle of an MTU is not a straightforward one (Lichtwark and Wilson, 2006). An increase in tendon length for example, may or may not imply concentric contractile behaviour of the muscle (Ishikawa, 2005; Lichtwark and Wilson, 2006). Therefore, the fact that tendons show an increase in length relative to their original lengths at impact does not necessitate concentric contraction and shortening of muscle fibres in the right limb during a fall. Rather it could, for example, merely reflect alterations in limb position. To fully understand and characterise this facet of MTU behaviour additional analysis of the model would be needed or

experimental data would need to be collected during the kinematic recordings. Although such data could be useful in a number of contexts including proprioceptive abilities during gait (e.g. (Klint *et al.*, 2008)), the length change values from this study were quantified because they were deemed necessary input parameters for FE simulations in chapter 5 of this thesis.

Indeed, all data gleaned from this study can be incorporated into FE simulations in chapter 5. By incorporating impact force data it will be possible to explore how variations in impact force magnitudes and the relative contributions of the X, Y and Z force components associated specifically with sideways falls contribute to and drive changes in stress distributions observed in the proximal femur. And by including concurrent muscle force data in these simulations it will be possible to analyse whether hip muscle loading modifies the stress distributions associated with sideways falls impacts. Delineating such a relationship could help form predictive models of falls that, within the context of hip fracture, could be useful in aiding understanding of the aetiology of hip fracture and helping to form strategies to prevent its occurrence. The tendon length change data will be used so that the muscle forces quantified in this chapter can be applied to FE models.

## 5.5 LIMITATIONS

### 5.5.1 Falls

Due to ethical and safety considerations it is difficult to produce realistic falls in a laboratory setting. The subject was a young healthy volunteer and due to the experimental design, falls were self-initiated. The subject was therefore able to anticipate the fall. This combined with the young age, will have influenced the fall strategy. In turn, it is likely that this will have led to fall kinematics, velocities and ultimately the range of predicted muscle forces that are different to those that occur during genuine accidental falls.

Therefore, while the impact and muscle force data gleaned in this study has relevance for the study of sideways falls generally, it should be considered within the context of the fall strategy used by the fall subject. This is an important distinction to make because it has been shown that fall strategy can influence, for example, impact velocities and force magnitudes (e.g. Feldman and Robinovitch, 2007; Yamamoto *et al.*, 2009; Luo *et al.*, 2014; Sarvi & Luo 2017). Although not tested in the present study, it seems reasonable to assume that fall strategy may

also influence muscle force magnitudes, given differences in limb position and linear velocities.

The limited number of recorded falls used to drive MDA simulations is also an important consideration/limitation. Recording and collecting data from a) a greater number of falls and b) using a greater number of subjects would have had been beneficial. It would have better captured variation in kinematics associated with sideways falls, may have provided greater scope for delineating consistent trends in impact but particularly muscle force data and ultimately would have led to an increased level of confidence in results.

### 5.5.2 Musculoskeletal Model

The strength of the data and conclusions drawn rests heavily on the validity and accuracy of the musculoskeletal model utilised in this study. The Anybody musculoskeletal models ([www.anybody.aau.dk](http://www.anybody.aau.dk)) have been used widely and validated in a number of research contexts. The anatomical information included within them can therefore be considered reasonably accurate, if simplified.

Even so, it should be noted that the way the model performs in simulations is dictated and determined by user-defined parameters and starting conditions. These are ultimately only approximations and idealisations of that which occurs in biological and physical reality. This is particularly true for the current study where a general, albeit scaled, musculoskeletal model has been used. Given the age of the subject used for falls and the musculoskeletal properties of the model that were used, this limits the ability to extrapolate results out to older populations. Future work would benefit in this regard by including subject-specific musculoskeletal models that better characterise those physiological and biomechanical properties that occur in older people *i.e.* the demographic for which falling presents the most serious complications.

The contact properties given to model leg geoms have an obvious and direct impact on impact force results. Appropriate leg geom properties were taken from the literature and captured differences in interaction between the ground and the human hip and thigh. Impact forces for the hip from the current study generally fell within previously found ranges and there can be some confidence in the properties used here. Nonetheless, initial contact of the hip geom with the simulated floor was characterised by an initial unrealistically high impact force peak. By taking an average value for 20ms at impact, the effects of this were minimised but it is

likely that this will have had some effect on impact force results.

### 5.5.3 Simulation Protocol

The optimisation procedure used in this study does not allow for an exhaustive search of all possible solutions, particularly because only 20 initial iterations of the optimisation process were used for each fall. An increased number of optimisation iterations for each fall would allow a more exhaustive search of the solution space and potentially improve the ability to converge on similar solutions, particularly for muscle force data. Doing so could also permit a better understanding of how variations in model performance (e.g. as defined by fitness scores) affect output parameters such as impact and muscle force magnitudes acting on the hip.

Aside from increasing the number of optimisation iterations to find a greater number of (potentially good) solutions, an alternative (and perhaps more practical approach), would be to use EMG in an experimental setting to detect the timings of muscle activations for relevant muscle groups on the limb impacting the ground. These timings could then be incorporated into model simulations such that the optimisation procedure need only find a suitable range of muscle forces for the given kinematic sequence. This would in effect help to reduce to the solution space and refine predictions for muscle force magnitudes.

## 5.6 CONCLUSION

This study has demonstrated it is possible to model a sideways fall using MDA and quantify potential impact and muscle force magnitudes that might occur at impact. The musculoskeletal model was able to capture, at least qualitatively, the idiosyncratic kinematics of multiple real-world falls. Variation in impact force magnitudes reflect the variation seen in fall kinematics suggesting that a discernible relationship exists between these two parameters. However, variation in muscle force magnitudes is much more fragmented suggesting that either there is insufficient power to detect underlying patterns/relationships and/or that redundancy is a significant driver in creating the observed variation.

In order to investigate 1) how these hip muscle forces might modify stresses in the ageing proximal femur produced by fall-related impacts and 2) how variation in these parameters

modifies stress distributions in the ageing proximal femur this data (as well as MTU length change data) will be incorporated into FE models and FEA simulations in chapter 6.

## 6 THE EFFECT OF HIP MUSCULATURE AND FALL CONFIGURATION ON STRESS PATTERNS IN ORTHOTROPIC FINITE ELEMENT MODELS OF THE AGEING PROXIMAL FEMUR: IMPLICATIONS FOR RISK OF FEMORAL NECK FRACTURE

---

### 6.1 INTRODUCTION

Hip fracture is an increasing socioeconomic burden that confers great cost to national economies and the individual (Cooper *et al.*, 1993; Magaziner *et al.*, 1997; Leibson *et al.*, 2002; Haentjens *et al.*, 2010; Svedbom *et al.*, 2013). Patient specific FE models of the femur, constructed using patient CT scans, are a promising tool for predicting and preventing femoral fracture. Reflecting this is the recognition of FEA by the International Society of Clinical Densitometry (ISCD) as an assessment tool for bone strength (Zysset *et al.*, 2015).

Femoral fracture occurs when the stresses experienced by the femur due to loading (i.e. an impact) exceed the femur's ultimate strength. FEA is an excellent methodological tool for predicting stress magnitudes and/or patterns in the proximal femur but the accuracy of results depends on multiple factors, including the material properties used to model bone and the loading conditions FE models are subjected to in FE simulations.

Studies have tended to simulate and apply only impact loads to FE femoral models, without considering how hip muscle forces might modify stress patterns in the proximal femur (e.g. Luisier, Dall'Ara and Pahr, 2014). Where more complex loading regimes are modelled through the inclusion of muscle forces, they have been done so only within the context of locomotive activities as opposed to falling (Lotz, Cheal and Hayes, 1995; Duda *et al.*, 1998; Speirs *et al.*, 2007A; T.M. Phillips, 2009; San Antonio *et al.*, 2012). To this author's knowledge, no FEA study has yet modelled concurrent fall-related hip muscle and impact forces.

Loading of the femur with hip muscle and fall-related impact forces is multi-directional in nature due to the differences between muscle lines of action and impact force orientation. Therefore, modelling bone with orthotropic properties for such a loading regime may be important due to the directional dependence of bone orthotropic elastic properties (Cowin, 1985). Much of the literature has tended to model bone material properties as isotropic (e.g. Helgason, Taddei, *et al.*, 2008; Langton, Pisharody and Keyak, 2009; Janne E.M. Koivumäki *et*

*al.*, 2012; Dall'Ara *et al.*, 2013b; Nawathe *et al.*, 2014; Nishiyama *et al.*, 2014; Liebl *et al.*, 2015) which is a simplification. Both human trabecular and cortical bone are thought to display orthotropic properties, and as a result, isotropic FE models have been shown to produce less accurate results (San Antonio *et al.*, 2012a). For studies that have incorporated orthotropic properties into FE models, only trabecular bone has been modelled or single material has been used to represent both cortical and trabecular bone compartments (Verhulp, van Rietbergen and Huiskes, 2008; Nawathe *et al.*, 2012; Luisier, Dall'Ara and Pahr, 2014). Given that muscle and impact forces are applied directly onto the cortical surface of the femur this might adversely affect model performance.

Due to the high computational cost associated with the construction of voxel-based orthotropic FE models of the femur, orthotropic continuum FE models of the femur FE studies of hip fracture currently represent the most promising and practical way in which to model femoral microstructural properties. Studies that have used orthotropic, continuum models of the femur have been constructed with microstructural data obtained with  $\mu$ CT at or above voxel sizes of 80 microns. But as detailed in chapter 4, this can result in some loss of accuracy in the microstructural data used to model bone material properties (Isaksson *et al.*, 2011) which in turn may affect FE model performance.

Taking all this into account, this work aims to construct fully orthotropic FE models of the ageing proximal femur from  $\mu$ CT scans with voxel sizes below 80 microns and apply a range of fall-related impact and hip muscle forces to these FE femoral models. Orthotropic properties are included to aid the accuracy of FE femoral model biomechanical behaviour. However, the primary purpose of this chapter is to explore how inclusion of simulated, fall-related hip muscle forces concurrent with fall-related impact forces in FE simulations modify stress patterns within the proximal femur. The relevance of these findings for hip fracture will be discussed.

## 6.2 METHODS

### 6.2.1 Subject Specific FE Model Construction

FE models were constructed using the same  $\mu$ CT scans of the five proximal femora outlined in chapter 3 (table 3-1), resulting in the construction of five FE proximal femora models. The process of constructing the finite element models is outlined in the sections below.

### 6.2.2 Segmentation of $\mu$ CT Scans

In order to begin constructing the finite element models, the  $\mu$ CT scans were first segmented using Mimics (Materialise, Leuven, Belgium) to define the FE model geometry and delineate the each femur's cortical and trabecular bone compartments. Segmentation of CT or  $\mu$ CT scanned bone involves the creation of separate coloured 'masks', each of which defines the physical geometries of one or more anatomical regions or compartments of a bone. Therefore, the 'mask' refers to an area within and across slices of a CT or  $\mu$ CT scan that has been attributed a specific colour to it. This area can be defined by the user, by an algorithm or by using a combination of both. A completed mask or set of masks form the end-point of the segmentation process (figure 6.1).

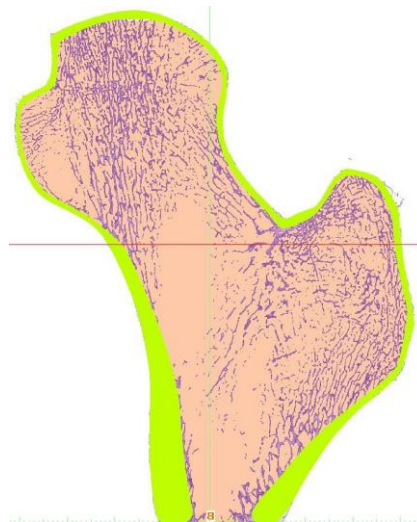


**Figure 6.1 Bone masks.** Sagittal slice showing a set of masks defining femoral regions/materials. The lime mask delineates cortical bone, the purple mask trabecular bone and the pink mask marrow spaces.

A variety of methods have been developed to segment CT scans (e.g (Pilgram *et al.*, 2008; Yokota *et al.*, 2009; Krčah, Székely and Blanc, 2011)). Automated methods that use algorithms to create bone masks based on pre-defined criteria (Yokota *et al.*, 2009; Krčah, Székely and

Blanc, 2011) (e.g. BMD thresholds) offer the quickest way in which to segment a bone and create its associated masks. These automated methods are also assumed to be less subjective than semi-automated or manual methods that rely more heavily on user input in that masks are created 'by eye'. However, the criteria these automated algorithms use to create segmented masks are nonetheless user-defined and based on a number of potentially unsatisfactory assumptions and over-simplifications. Thus, while automated algorithms might facilitate the quickest and most practical (in terms of time) form of mask segmentation, they do not necessarily represent the most reliable or efficient method.

Semi-automated and manual methods for mask generation also exist. Manual methods rely entirely on manual input from the researcher to create the mask(s). This offers unparalleled control over what is and isn't selected for inclusion in each mask but can be prone to user error and within and between-user (*i.e.* subjective) variability. Additionally, manual methods can be very time intensive which may not always be desirable where large data sets are used or speed is a priority.

Semi-automated methods combine computer-based algorithms and manual input to create masks. Semi-automated methods therefore offer a good compromise between speed and accuracy; large regions can be selected quickly using automatic algorithms and then refined by eye. For this study a semi-automated approach was taken in the creation of the femoral bone masks for several reasons. Given the large number of slices per  $\mu$ CT scanned femur (between 1218 – 1834 slices in the transverse plane), speed and efficiency were of importance. However, due to the nature of this study and its focus on incorporating bone material and architectural properties for both cortical and trabecular bone, it was important that both regions were defined to a good level of accuracy.

In numerous studies, cortical and trabecular bone are distinguished by employing pixel grey value (GV) or Hounsfield unit (HU) thresholds. This approach is suitable for CT scans with low resolution where the contrast between pixels belonging to cortical or trabecular bone is usually sufficient to make a distinction. However, in  $\mu$ CT scans this approach does not produce good results. The high spatial resolution of the scans means that many of the individual trabeculae and, more generally, the trabecular network are readily observable. Consequently, there is significant overlap in pixel GV/HU values between cortical and trabecular bone and

while it is easy to segment bone as a single material, it is significantly harder to distinguish between the two using a more traditional, threshold based method.

As a result, the cortical and trabecular compartments in this study were idealised as a cortical shell characterised by dense, non-porous bone and a trabecular core characterised by a porous network of trabeculae. This method had the advantage of allowing the creation of distinct masks for both bone types but had the obvious disadvantages that there was an element of subjectivity in defining the boundary between bone types and that it involved a considerable investment of time as each  $\mu$ CT scan slice had to be manually edited.

The first step in taking such a semi-automated approach involved using Mimics' own segmentation algorithm that, by allowing the user to set upper and lower limits for pixel GV's, exclusively identified and defined all bone material contained within each scan slice. In doing so, a single mask was created that contained all bone within each femur (figure 6.2).

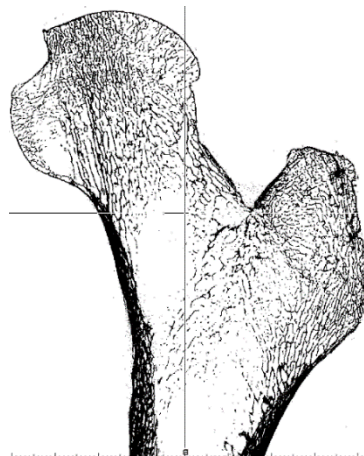


**Figure 6.2 Whole bone mask.** Sagittal slice showing the initial single mask used to define all femoral bone material (black).

#### **6.2.2.1 Creation of the initial cortical bone mask**

This mask, that treated all bone as a single material, was then edited manually, slice by slice, to separate the idealised cortical and trabecular compartments by deleting pixels from the mask along the user-defined boundary between the cortical and trabecular bone (figure 5.3). A region growing operation was performed to isolate the outer region of this mask and from this a new mask was created which solely defined the cortical shell of the femur bone (figure 6.3). The cortical mask was then smoothed using Mimics' own mask smoothing algorithm.

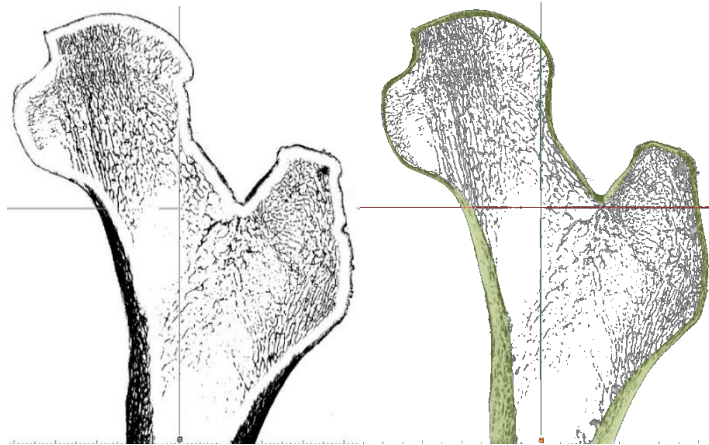


**Figure 6.3 Cortical mask creation.** Left Sagittal slice showing separation of bone along the border between cortical and trabecular bone as indicated by the red arrow. Right: Sagittal slice showing the resulting cortical mask (lime) following separation of bone compartments.

### 6.2.2.2 Creation of a three-dimensional cortical model

Upon completion of this initial smoothing, the cortical mask was converted into a three-dimensional model. The three-dimensional model consisted of a point cloud that defined the hollow outline of the mask's geometric boundaries in three-dimensional space and formed the template from which subsequent three-dimensional surface models could be made (figure 6.4).



**Figure 6.4 Three-dimensional cortical shell.** A three-dimensional point-cloud model of the cortical shell. This three-dimensional model is hollow inside and acts only to define the outer borders of the cortical geometry.

$\mu$ CT scans capture a large amount of anatomical detail because of inherently high scan resolutions. As a result, the initial masks and associated three-dimensional models created in this study retained a massive amount of anatomical detail which was unnecessary; capturing such detail allows for highly geometrically accurate three-dimensional reconstructions but it can make construction of finite element models highly impractical and perhaps more

importantly, lead to unreliable results from finite element simulations (e.g. due to numerical singularities).

Consequently, a number of modifications were made in order to simplify the surface meshes that defined model geometries. This ultimately led to the construction of finite element models that found a reasonable balance between biological detail, practicality and mathematical robustness - a necessary compromise for most finite element reconstructions of complex biological structures. The three-dimensional cortical model was simplified through multiple procedures.

A wrapping operation was first performed. This removed and simplified a number of surface features and closed any open holes in the surface. This resulted in a less detailed and completely closed surface mesh. After wrapping, a smoothing operation was applied to the surface mesh to smooth and remove remaining 'sharp' features that might lead to regions that cannot be meshed or unreliable results in subsequent finite element simulations.

### **6.2.2.3 *Creation of the final cortical bone mask***

A new cortical bone mask (*i.e.* a modified form of the original cortical mask) was then created from this wrapped and smoothed three-dimensional model. A consequence of using a wrapping operation is that cortical geometry is thickened slightly to protect particularly thin regions (e.g. cortical bone around the femoral head) from excessive erosion and the appearance of holes in the mesh. The new bone mask's geometry therefore differed to some extent when compared to the mask which was initially segmented. As a result, this new cortical mask was manually segmented a final time, using the original mask geometry as a guide. This allowed thinning of regions where excessive thickening of the cortical shell had occurred as a result of the wrapping operation so that both mask geometries matched as closely as possible.

In turn, this ensured that the final cortical mask followed the geometry of cortical bone to a good level of accuracy. In addition, it ensured that regions of noticeably thin cortical bone were captured and incorporated into finite element models. Previous studies utilising finite element models of the proximal femur assume a constant thickness throughout the cortical shell (usually 1mm). When working with CT scans of low/clinical resolution, it is very difficult

to determine cortical thickness and this assumption can be justified due to practical considerations.

However, it is clear from study of the  $\mu$ CT scans used in this study that the cortical shell is both thicker and thinner than 1mm across many regions of the proximal femur. Cortical bone is, for example, thinner than 1mm in areas such as the femoral head and superior femoral neck. Because the latter is considered a critical anatomical site for fracture of the femur (de Bakker *et al.*, 2009). It was therefore deemed important to create a mask that that better represented cortical thickness on the basis this would increase model accuracy and better predict bone biomechanical behaviour due to mechanical loading. The final step was to calculate a new and final three-dimensional point cloud model from this mask.

#### 6.2.2.4 Creation of the Trabecular Mask

The procedure to construct the trabecular mask and model was much simpler. The cavity of the final cortical shell was filled using a cavity filling operation in order to generate a new mask that defined the trabecular core of the femur (figure 6.5). The same smoothing operation used for the cortical mask, was applied to the trabecular mask and from this, the three-dimensional point cloud of the trabecular core was calculated. It was not necessary to make any further modifications to the trabecular model. The final cortical mask closely followed cortical geometry and was sufficiently simplified. Therefore, because the trabecular mask followed the boundaries of the cortical mask, the resulting three-dimensional model was also sufficiently simplified and geometrically accurate.

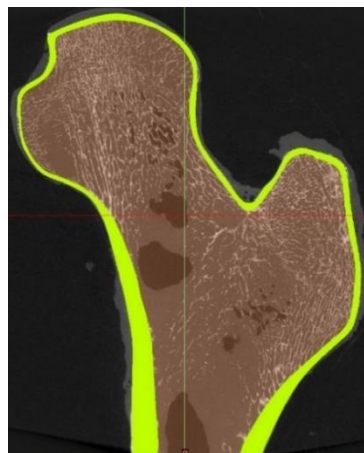


**Figure 6.5 Trabecular mask.** Sagittal slice showing the trabecular mask (pink) was created by filling the cavity bound by the cortical mask (lime).

### 6.2.3 Creation and Optimisation of Surface Meshes

A new three-dimensional surface mesh was generated from the final cortical and trabecular masks. Surface meshes are similar to point cloud models in that they define a model's geometric boundaries in three-dimensional space but differ in that they use a mesh made up of triangular elements to do this (figure 6.6). The surface mesh provides the template from which volumetric, finite element meshes are made.

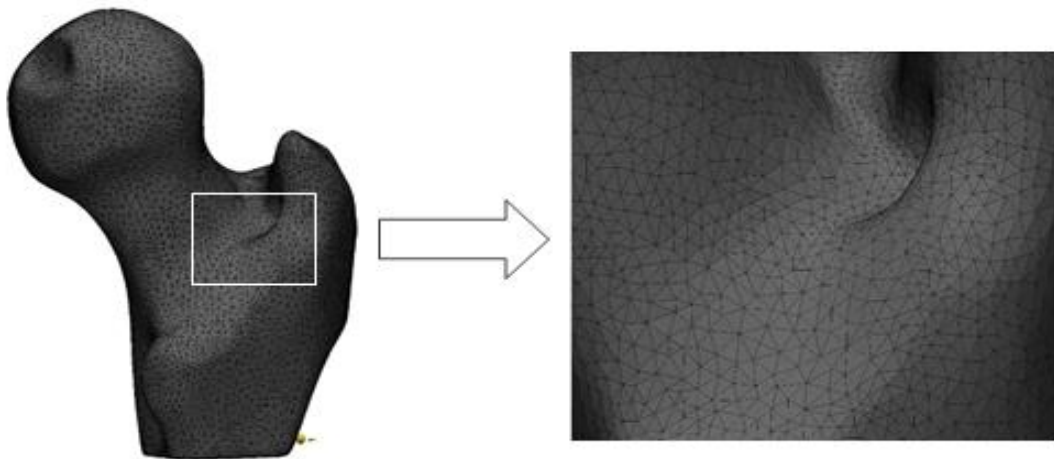


**Figure 6.6 Surface mesh.** The femoral surface mesh. This differs from the point cloud model because the mesh is a completely enclosed surface made from triangular elements as shown in the magnified portion of the femur.

However, before a volumetric, finite element mesh can be made, the surface mesh must first be optimised. Optimisation in this context, refers to the process of optimising the shape of triangular elements comprising the surface mesh so that all triangles can be considered as meeting or exceeding a certain minimum shape threshold. Meeting this threshold is often a prerequisite for creating a volumetric, finite element mesh in later stages. An equilateral triangle is considered the most optimal shape while triangles whose shape diverges from this are considered accordingly less optimal. When modelling complex biological structures like the proximal femur it is not possible, with current methods, to obtain a mesh that consists entirely of equilateral triangles – a ‘perfect’ mesh. However, a surface mesh can be optimised so that the minimum shape requirements for finite element mesh creation can be met and exceeded.

Triangular shape quality can be measured using a variety of methods but for this study, in order to optimise femoral surface meshes, a normalised height to base ratio was chosen. This parameter calculates the normalised ratio between the height of the triangle and the length of its base. A value of 1 is indicative of a perfectly equilateral triangle.

A ratio of 0.4 was used as the minimum threshold for determining acceptable ( $\geq 0.4$ ) vs. bad ( $< 0.4$ ) quality triangles as this threshold value generally needs to be met for the successful conversion of a surface mesh to a volumetric, finite element mesh. Triangle quality was improved iteratively with a maximum geometric error of 0.05mm per iteration until all surface triangles conformed to a shape quality of 0.4 or higher. 0.05mm was chosen as the maximum geometric error per iteration because this was the minimum level of geometric deviation that also allowed the minimum shape threshold for all triangles to be met. For all models only a very small proportion of triangles ( $< 0.01\%$ ) conformed to a height to base ratio threshold of less than 0.5. All triangles across all models surpassed the minimum threshold of 0.4.

After the last optimisation iteration, triangle edge length was adjusted and set to a maximum of 3mm. This resulted in a heterogeneous surface mesh comprised of differently sized triangles but where none exceeded the designated maximum edge length. Finally, a quality preserving triangle reduction procedure was applied. This reduced the total number of triangles in each surface mesh without compromising triangle shape quality or femoral geometry. The exact same optimisation routine was used to convert point cloud models to fully optimised but separate cortical and trabecular surface meshes (figure 6.7).

#### **6.2.4 Non-Manifold Assembly Creation**

Once separate trabecular and cortical surface meshes had been optimised, it was necessary to join these surface meshes together to make a complete, single femoral model. The process of combining both surface meshes into a single model generates a non-manifold assembly. The construction of a non-manifold assembly essentially involves creating a single common surface between separate entities that in reality, have irregular and difficult to define contacts; such as those that occur between cortical and trabecular bone.

Mimics own algorithm was used to create the non-manifold assembly, and this resulted in a single model that contained both cortical and trabecular surface meshes (figure 6.7). Triangular shape quality of the new surface model was checked and optimised where necessary using the procedures outlined above.

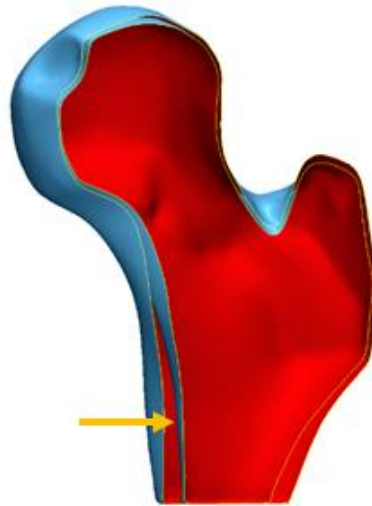


**Figure 6.7 Non-manifold assembly.** A cross section through the surface model of a femur to illustrate how the non-manifold assembly combined the inner trabecular compartment and outer cortical shell into a single model by creating a common surface between the two (indicated by the orange arrow).

### 6.2.5 Generation of the finite element models

Next, a finite element mesh (also known as a volumetric mesh) of the non-manifold assembly surface model was constructed using Mimic's own volumetric mesh generating algorithm. Creating a volumetric mesh represents the final stage in finite element model mesh generation and produces a mesh. The mesh captures the entirety of the three-dimensional volume of the femur (as opposed to only its geometric boundaries) and is comprised of a finite number of tetrahedral or hexahedral elements.

For this study, tetrahedral elements were chosen for construction of the finite element mesh due to various practical considerations. Of particular importance was the ability of tetrahedral meshes to create a constant, relatively smooth and curved outer model surface. Modelling the bone surface in this way is essential for modelling a surface based definition of cortical bone orthotropy so that cortical fabric direction and material properties could be aligned with cortical shell geometry throughout the model. By contrast, hexahedral elements only allow a globally orientated surface definition of orthotropy due to the fact the outer faces of all surface hexahedral elements are orientated in the same way and aligned with the global axes. Additionally, the mathematical accuracy of tetrahedral elements in determining solutions to finite element problems has greatly improved and consequently, choosing hexahedral over tetrahedral elements confers no significant advantage in this regard (Ramos and Simões,

2006).

Volumetric meshes were generated in the first instance using four-noded tetrahedral elements. All tetrahedral element edge lengths were set to a maximum of 3mm. Tetrahedral element shape quality was measured using an aspect ratio criterion to determine whether elements were of sufficient quality. The aspect ratio measure calculates the ratio of the maximal element edge length to the height of the volume unit. For FEA, an aspect ratio value below 100 is generally required. Without meeting this threshold, the volumetric mesh can be considered of insufficient quality to produce reliable results.

For all models, all mesh elements fell well below this threshold value. Once meshes of sufficient quality were generated, four-noded tetrahedral elements were converted to ten-noded tetrahedral elements. This conversion made certain that mesh elements were not too 'stiff' during finite element simulations and therefore less representative of bone biomechanical behaviour. For all models, the meshing procedure resulted in a single mesh with heterogeneous element sizes equal to or less than 3mm (figure 6.8). Mesh elements were grouped according to the cortical or trabecular region in which they were nested. The non-manifold edge from the surface model determined which elements belonged to which region.

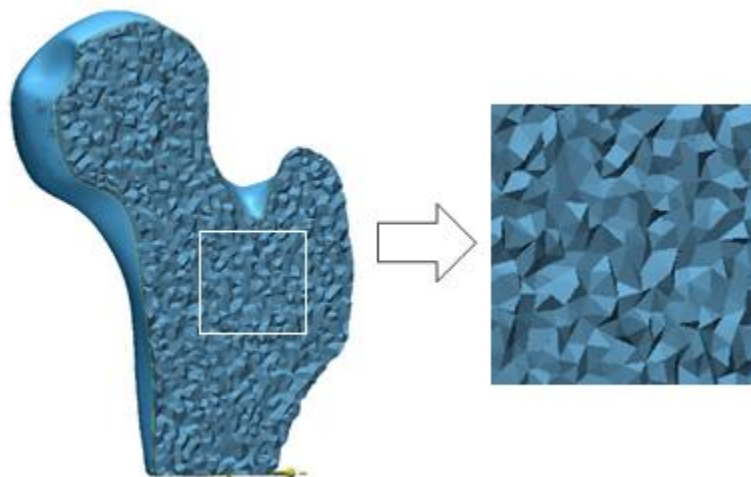


**Figure 6.8 Finite element mesh.** Completed finite element mesh. Unlike the surface mesh, this volumetric mesh is completely filled with 3D tetrahedral elements of various sizes but which all have edge lengths equal to or less than 3mm and meet or exceed minimum shape requirements.

## 6.2.6 Material Property Assignment

Elements belonging to cortical or trabecular regions in the finite element model needed to be assigned corresponding material properties. Given the nature of the multidirectional mode of loading the femoral bone specimens is subject to from muscle and impact forces in these finite element simulations, it was deemed important to incorporate the anisotropic properties of cortical and trabecular bone so the effects of such a loading scenario could be better understood and quantified. Material properties were calculated for and assigned to all elements using custom-written MATLAB (The Mathworks Inc., 2016) scripts (appendix G).

### 6.2.6.1 Cortical Bone Material Property Assignment

Cortical bone was modelled as a heterogeneous, transversely isotropic material by assigning individual values for density, Young's modulus, shear modulus and Poisson's ratio to each cortical element in the model. Hounsfield Unit (HU) values for each cortical element were converted into apparent density ( $\rho$ ) by assuming a linear relationship between these two parameters. The maximum HU value,  $HU_{max}$ , was taken from each femoral scan and an average of all maximums,  $HU_{avg}$ , was calculated.  $HU_{avg}$  was assumed to represent an apparent density of 1.85g/cm<sup>3</sup>. A value of 0 HU, the HU value for water (1g/cm<sup>3</sup>) was assumed to equate to an apparent density of 0g/cm<sup>3</sup>.

This approach differs very slightly from that taken previously (e.g. (Peng *et al.*, 2006)) in that  $HU_{avg}$  was assigned an apparent density of 1.85g/cm<sup>3</sup> compared to  $HU_{max}$  being assigned an apparent density of 2.0g/cm<sup>3</sup>. The approach taken here was preferred so as to capture the relative differences in bone density (and therefore material properties) across femoral specimens because they showed differences in HU values (and therefore bone density) upon visual inspection of HU histograms.  $HU_{avg}$  was assigned a lower value of 1.85g/cm<sup>3</sup> (as opposed to 2.0g/cm<sup>3</sup>) due to the age of the donors based on the fact that increasing age is associated with a decrease in cortical thickness and increase in cortical porosity (Chen *et al.*, 2010). This approach is similar to others (Ikhwan *et al.*, 2012). A specific value of 1.85g/cm<sup>3</sup> was chosen because it is considered the standard for cortical bone density as defined by the International Commission on Radiological Protection (ICRP, 2007).

100 separate materials were assigned between all cortical elements by taking the range of HU values for cortical elements and dividing this range into one hundred equal intervals ( $HU_{int}$ ). A total of 100 materials was chosen because, based on previous research, this number represents a good compromise between computational efficiency and convergence and accuracy of stress/strain results (Peng *et al.*, 2006) A constant,  $x$ , was defined as:

$$x = \frac{1.85}{HU_{avg}} \quad 6.1$$

The maximum value of apparent density ( $\rho_{max}$ ) for each femur was then calculated as:

$$\rho_{max}[g/cm^3] = xHU_{max} \quad 6.2$$

Apparent density was then assigned to each material interval ( $\rho_{int}$ ) using the assumed linear relationship between apparent density and HU:

$$\rho_{int}[g/cm^3] = \frac{HU_{int} \times \rho_{max}}{HU_{max}} \quad 6.3$$

Equation 6.3 is essentially a modified form of the equation 4.4 where this approach been used in previous studies (Weinans *et al.*, 2000; Hölzer *et al.*, 2013) that defines a linear relationship between HU's and apparent density:

$$\rho[g/cm^3] = \frac{2HU}{HU_{max}} \quad 6.4$$

Apparent density was limited to a lower threshold of  $0.5g/cm^3$  to help negate partial volume effects (due to a slight thickening of the cortical shell during segmentation) which would otherwise lead to an under estimation of some cortical elements. This threshold is lower than some used in the literature where lower limits for cortical bone apparent density have been set at  $0.9g/cm^3$  (San Antonio *et al.*, 2012). However, due to the old age of the cadaveric

specimens (resulting in decreased bone mineral density due to factors like increased porosity) this was deemed an acceptable threshold; previous studies have found cortical volumetric bone mineral density decreases to levels similar to or just below  $0.5\text{g/cm}^3$  by the time individuals reach ninety years of age (Riggs *et al.*, 2004; Nicks *et al.*, 2012).

Having calculated values for each  $\rho_{int}$  and assigned them across all cortical elements (figure 5.9), power law relationships were used to relate cortical bone apparent density to its' orthotropic material properties.

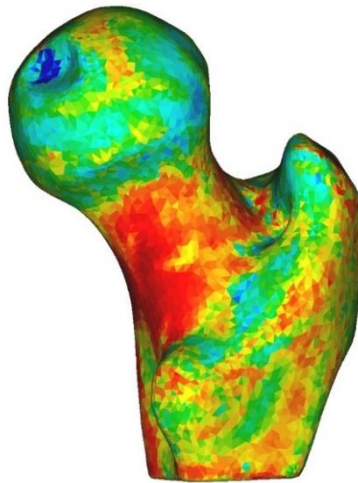


**Figure 6.9 Cortical bone material property assignment.** A finite element model illustrating the mapping and assignment of bone density values to individual cortical elements throughout. Red regions indicate areas of highest density and blue regions indicate areas of lowest density.

A number of material expressions exist to describe the relationship between cortical bone apparent density and its' orthotropic material properties. The relationships derived in Wirtz *et al.*, (2000), Taylor *et al.*, (2002) and Peng *et al.*, (2006) were used for the present study and are described in equations 6.5-6.6. Equations 6.5a, 6.5b and 6.5c were chosen to assign an orthotropic Young's modulus to each material:

$$CE_1[MPa] = 2314(\rho_{int})^{1.57} \quad 6.5a$$

$$CE_2[MPa] = 2314(\rho_{int})^{1.57} \quad 6.5b$$

$$CE_3[MPa] = 2065(\rho_{int})^{3.09} \quad 6.5c$$

Where  $CE_n$  is the Young's modulus and this property is labelled from 1 for the lowest to 3 for the highest. Equations 6.6a, 6.6b and 6.6c were chosen to assign an orthotropic shear modulus to each cortical material.

$$CG_{12}[MPa] = \frac{CG_{12max}(\rho_{int})^2}{(\rho_{int})^2} \quad 6.6a$$

$$CG_{23}[MPa] = \frac{CG_{23max}(\rho_{int})^2}{(\rho_{int})^2} \quad 6.6b$$

$$CG_{13}[MPa] = \frac{CG_{13max}(\rho_{int})^2}{(\rho_{int})^2} \quad 6.6c$$

Where  $CG_n$  is the shear modulus and the first subscript identifies the plane in which it acts, while the second subscript identifies the direction in which it acts. And where  $CG_{12max} = 5710$ ,  $CG_{23max} = 7110$ , and  $CG_{13max} = 6580$ .

Finally, since no experimentally determined relations between orthotropic Poisson's ratios and the  $\mu$ CT density values can be found in the literature, all cortical materials were assigned constant values as follows:

$$\nu_{12} = 0.4, \nu_{23} = 0.25, \nu_{13} = 0.25 \quad 6.6d$$

Where the first subscripts denote the direction of the applied load and the second subscripts the direction in which the Poisson's ratio acts as a result.

#### **6.2.6.2 Cortical Bone Material Fabric Assignment**

Because cortical bone was modelled with orthotropic material properties, it was necessary to assign each cortical element its orthotropic material axes. It was decided to define the orientation of cortical material axes based on femoral model surface geometry (figure 6.10). Consequently, the principal material direction of each element followed the in-plane

longitudinal direction, between the most distal and proximal portions of the femur. The radial material direction was defined in an out-of-plane direction that acted normal to the surface at any given point. Finally, the circumferential material direction acted in an in-plane direction that was orthogonal to both of these. Modelling cortical orthotropic orientations in this way was assumed to be a valid assumption due to the three-dimensional organisation of cortical bone at the tissue level and its relationship with cortical bone material properties.

To align each cortical element's material axes with the cortical surface geometry the outer surface of the cortical shell was first defined in ABAQUS 6.14-2 (SIMULIA, USA). A custom-written MATLAB script was developed to create a Python script and commands to loop through all cortical materials and their associated elements and define cortical material orientations using the process outlined below (appendix H).

Firstly, a normal axis,  $\hat{N}$ , for every cortical element was specified using the outer cortical surface. For each cortical element, the closest point on the outer surface was located and the surface normal at that point was used to define that element's normal (*i.e.* the radial) axis. Secondly, a primary material axis, defining the principal material direction, was specified for each cortical element. The primary axis,  $\hat{P}_1$ , was initially aligned with the global Z axis and, by taking into account the orientation of the radial axis, rotated at each element so that a 90-degree angle was formed between the normal and primary axes.

The secondary axis,  $\hat{S}$ , denoting the circumferential material direction, was then computed in ABAQUS 6.14-2 (SIMULIA, USA) by taking the cross product of the primary axis direction and the normal axis direction such that:

$$\hat{S} = \hat{P}_1 \times \hat{N} \quad 6.7a$$

Finally, the final primary axis direction,  $\hat{P}$ , was computed in ABAQUS 6.14-2 (SIMULIA, USA) by taking the cross product of the secondary and normal axis directions by:

$$\hat{P} = \hat{S} \times \hat{N} \quad 6.7b$$

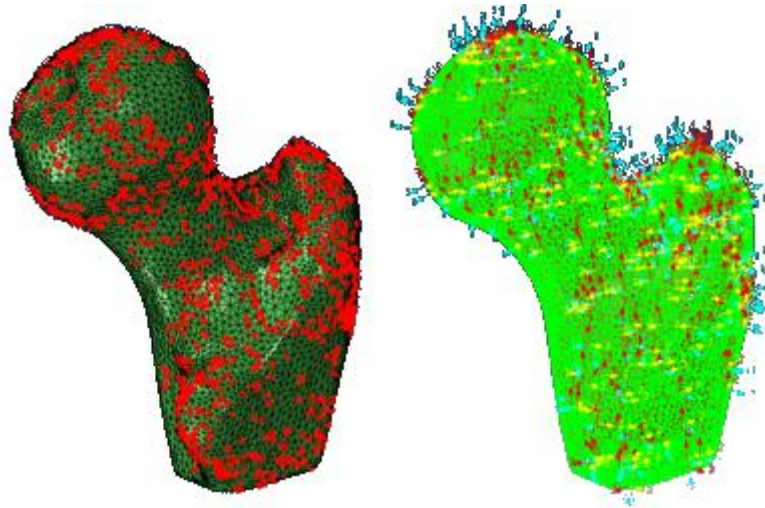


**Figure 6.10 FE model cortical bone orthotropy.** **Left** A finite element model of the proximal femur with elements belonging to one of the one hundred cortical materials assigned to the cortical compartment highlighted in red. **Right:** The same elements with their orthotropic orientations (coloured arrows). Orthotropic orientations closely follow the femoral surface geometry. Red arrows = primary material axis. Yellow arrows = circumferential material axis. Blue arrows = radial material axis.

### 6.2.6.3 Trabecular Bone Material Property Assignment

Trabecular bone was modelled as a heterogeneous, orthotropic material by assigning individual values for density, Young's modulus, shear modulus and Poisson's ratio to each trabecular element in the model as a function of BV/TV (figure 6.11). Custom-written MATLAB scripts were used to achieve this using an alternative method to that used for cortical elements. Because the trabecular core for each model had already been discretised into multiple cubic regions from chapter 3 and a BV/TV value had been obtained for each of these cubes, individual material properties were assigned to the elements that made up each cubic region in the finite element model. As such, the number of trabecular materials and associated material properties produced by this method, corresponded to the number of cubic regions each femur was split into in chapter 3.

The material properties of each trabecular cube were calculated using the direct relationship between BV/TV and trabecular orthotropic elastic constants derived by Yang *et al.*, (1998) in equations 6.8(a)-(i).

$$TE_1 = 1240E_t v_v (\text{bone})^{1.80} \quad 6.8a$$

$$TE_2 = 885E_t v_v(\text{bone})^{1.89} \quad 6.8b$$

$$TE_3 = 486.3E_t v_v(\text{bone})^{1.98} \quad 6.8c$$

$$TG_{23} = 266.65E_t v_v(\text{bone})^{2.04} \quad 6.8d$$

$$TG_{13} = 316.65E_t v_v(\text{bone})^{1.97} \quad 6.8e$$

$$TG_{12} = 486.3.E_t v_v(\text{bone})^{1.98} \quad 6.8f$$

$$v_{12} = v_{21} = \frac{1}{2}(0.176v_v(\text{bone})^{-0.25} + 0.125v_v(\text{bone})^{-0.16}) \quad 6.8g$$

$$v_{23} = v_{32} = \frac{1}{2}(0.256v_v(\text{bone})^{-0.09} + 0.153v_v(\text{bone})^{-0.05}) \quad 6.8h$$

$$v_{13} = v_{31} = \frac{1}{2}(0.316v_v(\text{bone})^{-0.19} + 0.135v_v(\text{bone})^{-0.07}) \quad 6.8i$$

Where  $TE_n$  is the Young's modulus (and this property is labelled from 1 for the lowest to 3 for the highest),  $TG_n$  is the shear modulus and  $v_n$  is the Poisson's ratio (where the first subscript identifies the plane in which it acts, while the second subscript identifies the direction in which it acts).

There was a good degree of contact and continuity between orthotropic cortical and trabecular elements due to unavoidable but slight increases in cortical thickness during the segmentation and model building process. However, due to the fact cubic regions were used to discretise trabecular cores into multiple regions, there was also an obvious incongruence between the complex topology of the cortical/trabecular boundary in the model and the three-dimensional cube shapes used. In addition to this, there were also some areas within the trabecular core where no cubes were created because there was no trabecular bone present in the scanned images.

Both these factors meant no architectural anisotropic information could be gleaned for these regions and that therefore, a small number of trabecular elements in each model were necessarily excluded from the process of an orthotropic material definition and required an alternative material definition. For these mesh elements, a heterogeneous, isotropic material

definition was chosen. Trabecular density was first defined according to equation 6.9 (Baca *et al.*, 2008):

$$\rho_{trab}(g/cm^3) = A.HU + 1 \quad 6.9$$

Where  $\rho_{trab}$  is trabecular effective density and  $A = 0.464 \cdot 10^{-4}(g/cm^3)$ . Isotropic material properties were then assigned to isotropic elements as a function of density, using equation 6.10a and 6.10b (Yang, Ma and Guo, 2010):

$$TE_{iso} = 1904\rho_{trab}^{1.64} \quad 6.10a$$

$$T\nu_{iso} = 0.33 \quad 6.10b$$

Where  $TE_{iso}$  is the isotropic Young's modulus,  $T\nu_{iso}$  is the isotropic Poisson's ratio. To ensure results using equation 6.9 were reasonable, values for  $TE_{iso}$  for isotropic trabecular elements were restricted to the same maximum value produced by equation 6.8a to calculate the orthotropic Young's modulus in the principal material direction.

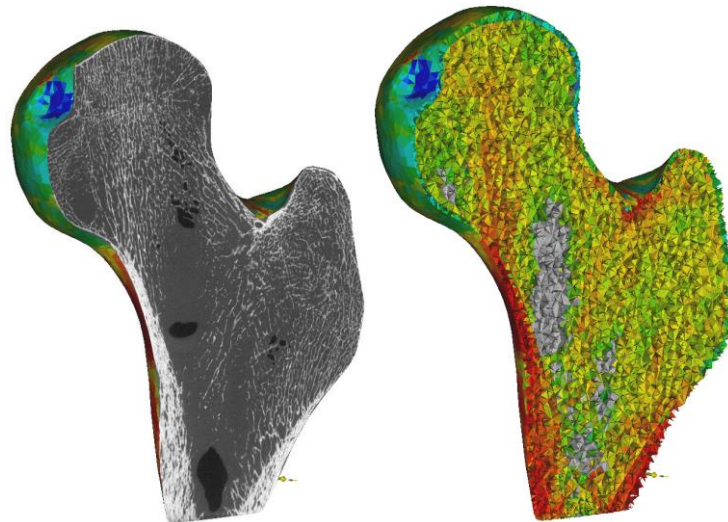


**Figure 6.11 Trabecular bone material property assignment.** Left  $\mu$ CT image elucidates the relationship between regions of higher/lower density and the presence/absence of trabecular bone. Right: A finite element model illustrating the mapping and assignment of bone density values to trabecular elements throughout. Red regions indicate areas of highest density and blue regions indicate areas of lowest density.

#### 6.2.6.4 Trabecular Bone Material Fabric Assignment

Instead of using a surface based definition to define orthotropic material orientations as was employed with cortical elements, eigenvector values as determined in chapter 3 were used

to map material orientations throughout the trabecular core. Custom-written MATLAB scripts were used to automate this process in a number of sequential steps (appendix I) which are outlined below.

The Cartesian coordinate for the single vertex defining each trabecular cube origin created in chapter 3, was converted into mm. Vertex origin coordinates were then adjusted so that the vertex origin was defined as being located at the bottom-right hand cube corner (instead of the top left) for subsequent plotting. Multiple  $5\text{mm}^3$  cubes were then plotted in three-dimensional space for each femur using the new vertex origin coordinates (figure 6.12). The number, positions and size of these cubes therefore corresponded exactly with those created and used in chapter 3. After plotting, the Cartesian coordinates, in mm, for all eight vertices belonging to each cube were obtained.

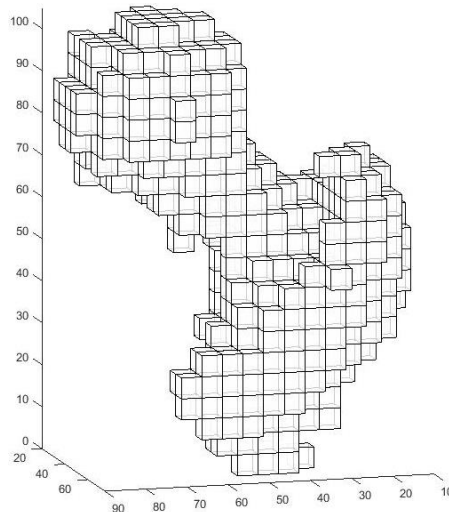


**Figure 6.12 Cube plot.** A plot of the created cubes belonging to the trabecular core of one of the scanned femoral specimens. Each cube corresponds exactly, in terms of size and position in three-dimensional space, with  $\mu\text{CT}$  scan bone cubes created for the same femoral specimen in chapter 4.

For the following step, it was assumed that straight lines connected the vertices belonging to each cube and that these lines bounded flat planes that defined all six cube faces as in figure 6.12. In this way, the cubes could be assumed to be completely enclosed and discrete entities. On the basis of this assumption, custom scripts then looped through all nodal coordinates contained within the trabecular core of the finite element model, related each node's Cartesian coordinates to its' individual nodal number and then identified which nodes (by their nodal number) were nested within the boundaries of each idealised cubic region. All nodes falling within a specific cube's boundaries were assigned to a set.

Individual node sets, and their corresponding nodal numbers, were then used to compute which tetrahedral elements were also nested within each idealised cubic region. This was possible because nodes form the vertices from which all mesh element geometries and positions are defined. After completion of this, discrete element sets were then created, and these sets were used to define and construct cubic regions within the finite element model itself. These element-based cubic regions corresponded to those created in chapter 3.

Therefore, each element set more or less formed a cubic shape of approximately  $5\text{mm}^3$  within the finite element model (figure 6.13) and the number of element sets corresponded to the original number of cubes analysed in chapter 3. Where an element crossed an idealised cube boundary (*i.e.* the element existed within two cube regions) that element was designated as belonging to the last cube in which that element was registered as being contained within.

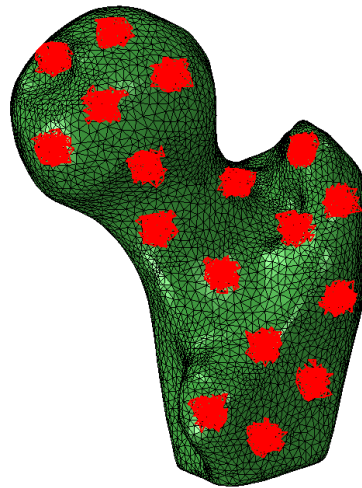


**Figure 6.13 FE cubic regions.** A finite element model with multiple trabecular cubic regions highlighted in red. The cube regions are constructed and defined using the finite elements themselves. Their positions and size correspond, in terms of size and position in three-dimensional space, with  $\mu\text{CT}$  scan bone cubes created for the same femoral specimen in chapter 4.

Finally, each finite element cube was assigned its correct orthotropic orientations using the eigenvector data gleaned from chapter 4 (figure 6.14). This final process of assignment was automated within ABAQUS 6.14-2 (SIMULIA, USA) using further custom-written Matlab scripts that created the Python script and commands necessary to achieve this (appendix H).

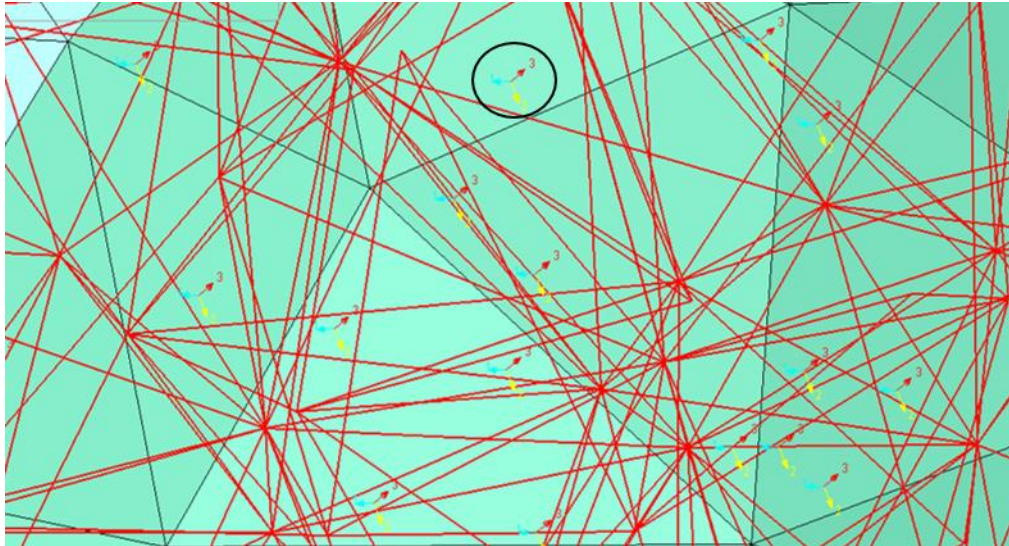


**Figure 6.14 Trabecular material orientations.** A zoomed in section of one of the cubic regions in the finite element model. The red lines delineate tetrahedral element edges. Each element within this element-based cubic region share the same orientation for their material axes. Orientations for each cubic region are based on eigenvectors from the MIL study. The group of arrows circled in black, which belong to a single element, provide an example of how each element's coordinate system is rotated to align with the eigenvector data. Red arrows = primary material axis. Yellow and blue arrows = the middle and minor material axes orthogonal to the primary axis.

### 6.2.7 Muscle-Tendon Units

The muscles chosen to be modelled in finite element simulations had to fulfil two criteria:

1. They were muscles for which data was obtained in chapter 5.
2. They had insertion sites on the proximal femur approximately at the level of or superior to the distal portion of the lesser trochanter, as this represented the most distal point of all femoral FE models.

Consequently, seven muscles that totalled eleven muscle bellies were modelled because gluteus minimus and gluteus medius were modelled with three separate muscle bellies each.

The modelled muscles were:

- Gluteus maximus
- Gluteus medius (3 muscle bellies)
- Gluteus minimus (3 muscle bellies)
- Iliopsoas
- Piriformis
- Vastus lateralis

- Vastus intermedius

### 6.2.7.1 Muscle Origins

Anatomical coordinates for muscle origins were based on those from Duda *et al.*, (1996) and Klein Horsman *et al.*, (2007) (figure 6.15).

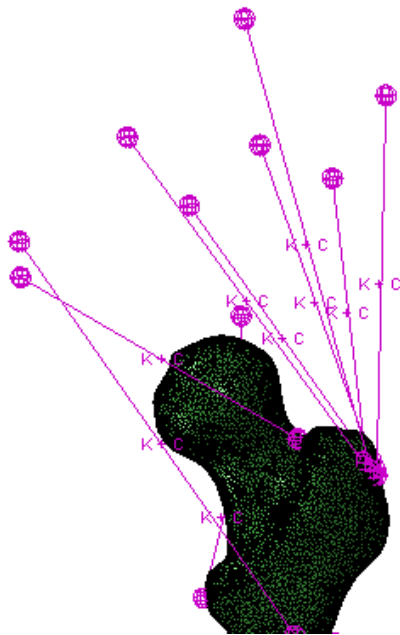


**Figure 6.15 Muscle-tendon unit origins.** A finite element model with muscle origin coordinates for various hip muscles highlighted by purple circles proximal to the femoral head. All muscle origin coordinates were defined using the hip joint centre (*i.e.* the femoral head centre) as the reference point.

These studies used the hip joint centre (HJC), defined as the femoral head centre, as the reference point by which all muscle origin coordinates were calculated. The HJC for all femoral specimens used in this study was computed by selecting multiple points from the femoral head, ascertaining their three-dimensional Cartesian coordinates and employing a least squares fitting method to calculate their centroid using the Sphere Fit function (Jennings, 2010) in MATLAB. This centroid was then implemented in all finite element models (figure 6.16).

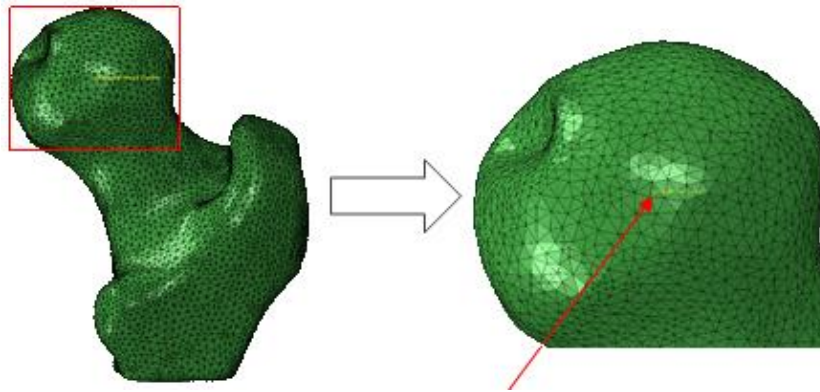


**Figure 6.16 Femoral head centre.** Zoomed in section of the femoral head elucidating the good level of accuracy achieved in locating the femoral head centre from which all relevant femoral muscle origins were modelled. The centre is indicated by the red arrow and the left-most margin of the yellow text.

### 6.2.7.2 Muscle-Tendon Insertion Sites

Muscle-tendon insertion sites based on coordinates from Duda *et al.*, (1996) and Klein Horsman *et al.*, (2007) were not used in this study. The wide variation in femoral geometry between specimens in this study and the original femur specimens used in these studies meant there was a high degree of incompatibility between the insertion defined in these studies and their positioning in the three-dimensional environment associated with each finite element model. On this basis, it was judged that using relevant anatomical landmarks and established descriptions (Susan Standring, PhD, 2009) allowed for more accurate modelling of muscle-tendon insertion sites across all specimens.

Muscle-tendon lines of action were checked to ensure the line of action between origin and insertion site was reasonable and would produce the correct femoral movement. All muscle-tendon insertion sites were defined as surfaces on the femoral mesh, with each muscle-tendon insertion surface designated a specific size ( $\text{mm}^2$ ) based on values from (A. T.M. Phillips, 2009) for predicted tendon cross sectional areas at the site of insertion (table 6-1) to ensure a reasonably standardized application of force between femoral specimens for a given load (figure 6.17).

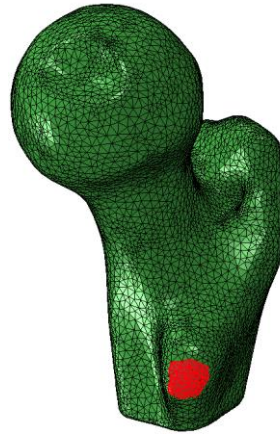


**Figure 6.17 Muscle insertion.** A finite element model exemplifying how element faces were used to define individual muscle insertion sites (iliopsoas in this instance). Their position and size were calculated using anatomical landmarks and values from the literature.

As already discussed, the femoral models utilised in this study comprise only the proximal portion of the femur (*i.e.* encompassing the femoral head through to a region just distal to the lesser trochanter). Some of the muscles modelled insert on the most distal regions of the finite element models at their most proximal points of insertion but would in reality have sites of insertion that continue distally along the femoral shaft. Amongst these muscles are gluteus maximus, vastus intermedius and vastus lateralis. For these muscles, only the most proximal part of their insertion sites was modelled (Table 6-1).

**Table 6-1 Muscle-tendon unit insertion areas.** Insertion areas used to define insertion surfaces on the finite element models. For gluteus maximus, vastus intermedius and vastus lateralis modified insertion areas were used due to the fact specimens were cut just below the greater trochanter and were based on anatomical descriptions of these sites and standardised across specimens

| Muscle-Tendon Unit | Insertion area (mm <sup>2</sup> ) |
|--------------------|-----------------------------------|
| Gluteus maximus    | 90                                |
| Gluteus medius     | 72                                |
| Gluteus minimus    | 53                                |
| Iliopsoas          | 93                                |
| Piriformis         | 17                                |
| Vastus intermedius | 100                               |
| Vastus lateralis   | 100                               |

### 6.2.7.3 Modelling muscle-tendon unit paths

Muscle-tendon units were modelled using single spring elements and dashpots in ABAQUS 6.14-2 (SIMULIA, USA) (figure 6.18). Using spring elements and dashpots to model muscle-tendon units had several advantages over more traditional load application approaches in finite element simulations such as instantaneously applying concentrated loads directly at mesh nodes. The latter approach not only creates unrealistically high stress concentrations around the point of application but also does not account in any way for muscle and tendon biomechanical behaviour during force production. Spring elements on the other hand permit modelling of stiffness and damping constants. Thus, by loading the femur indirectly by applying forces through these elements, as opposed to directly at nodes, the loading behaviour of muscles acting on the proximal femur is better approximated.

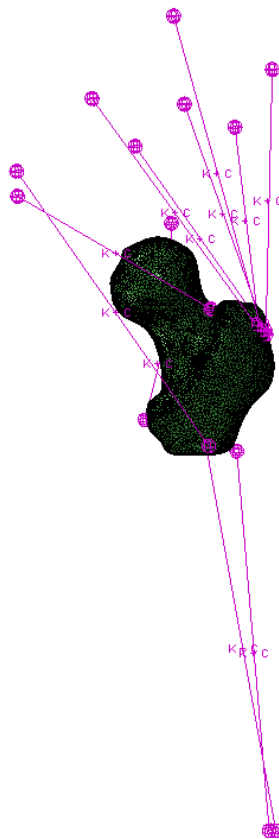


**Figure 6.18 Spring elements.** Muscle-tendon units were modelled using spring and dashpot elements (purple lines) that connected muscle origin and insertion sites and had relevant albeit simplified mechanical properties.

Generally, spring element and dashpot positions were delineated using two reference points; one that marked the muscle origin and one that marked the muscle insertion. In this way, these reference points formed each spring's start and end points. For each spring element

that was modelled in this way, a single reference point was specified so that it floated in three-dimensional space in close proximity to the insertion surface whilst still preserving the correct muscle line of action.

Iliopsoas and gluteus maximus provided two exceptions to this general rule. Iliopsoas has a curved path that wraps around the femoral bone from a point on the lesser trochanter on the posterior of the proximal femur to a more anterior position that is proximal to the femoral head. Given this, multiple reference points positioned close to the mesh surface were used to model this muscle wrapping (figure 6.19). Similarly, gluteus maximus also wraps around the femoral bone close to its point of insertion. Therefore, several reference points were used to approximate its curved path.

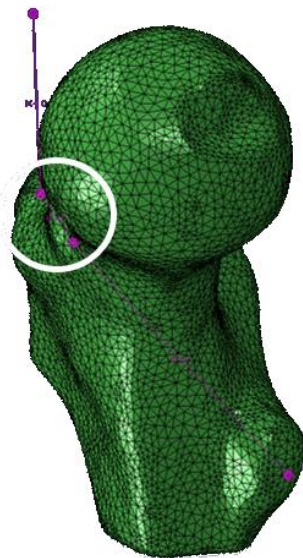


**Figure 6.19 Muscle-tendon unit lines of action.** Multiple reference points for spring/dashpot elements (highlighted by the white circle) were used to model the curved path of some muscles around femoral bone. This was done to help mimic each muscles line of action to a reasonable degree of accuracy.

#### **6.2.7.4 Modelling muscle-tendon unit material properties**

Springs were assigned stiffness and damping properties to approximate their biomechanical behaviour and transfer muscle forces to the surface of FE models. Stiffness values were calculated using MTU parameters defined for the musculoskeletal model used in chapter 4.

Specifically, resting tendon lengths were quantified and the maximum isometric contraction force,  $F_{max_{iso}}$ , of relevant muscles (table 6-1) from the musculoskeletal model was calculated as:

$$F_{max_{iso}} = PCSA \times FPUA \quad 6.11$$

Where  $PCSA$  is the physiological cross-sectional area of the muscle and  $FPUA$  is force per unit area ( $=300,000\text{KNm}^2$ ). Following (Sellers *et al.*, 2010) tendon stiffness,  $T_k$ , was then calculated assuming 60% tendon strain of initial resting length at the maximum isometric force of each muscle such that;

$$T_k = \frac{\Delta F_m}{\Delta L_t} \quad 6.12$$

Where  $\Delta F_m$  is change in muscle force and  $\Delta L_t$  is change in tendon length. A minor modification made to the properties assigned to all muscle-tendon units by A. T M Phillips (2009) included an additional damping coefficient of 0.1 (Millard, Kubica and McPhee, 2011). It was thought that by including this damping coefficient, muscle behaviour might be better represented.

#### 6.2.7.5 Muscle Force Vectors

Muscle force vectors were modelled in several ways depending on the complexity of a muscle's line of action. When muscle origin and insertion sites could be connected by a spring element whose longitudinal axis did not pass through the model's mesh, a single spring element was used to define the muscle tendon unit by connecting two reference points in a straight line. The muscle force vector was then defined as acting along the spring element's longitudinal axis and orientated so as to produce tension in the spring element.

Where a muscle followed a curved path, this path was modelled using multiple but connected spring elements. In such instances, multiple muscle vector definitions were used to replicate the changing direction in muscle force throughout the spring element's changing path. Therefore, moving from origin to insertion, at each new connection point, a new force vector

was defined for each element in the series that followed the longitudinal axis of the spring element proximal to it.

Additionally, in some instances the muscle insertion site was curved to a significant degree. Consequently, it was judged unsuitable to connect the spring element to the mesh surface using just a single reference point and using just a single force vector. Where this occurred, several reference points were used so that spring elements could connect to the curved surface without passing through the interior of the model (figure 6.20).

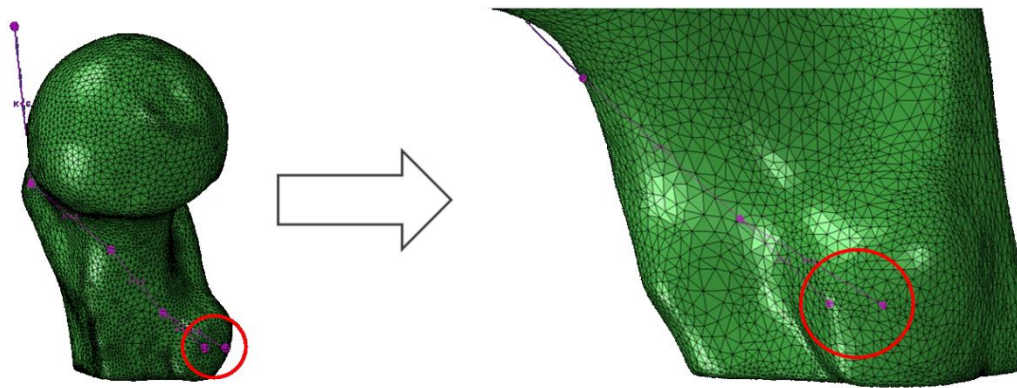


**Figure 6.20 Muscle force vectors.** Zoomed in section of the iliopsoas insertion site exemplifying how multiple reference points (highlighted by the red circle) were used to model muscles with curved insertion sites. Doing so helped to preserve the accuracy with which their line of action was modelled.

This ensured more realistic application of muscle forces to the FE model surfaces. For each of these points of insertion the force vectors were defined as acting approximately parallel to the tangent of the curved bone surface.

#### **6.2.7.6 Application of Muscle Forces**

Muscle forces were prescribed to the model using two differing techniques. Muscle force magnitudes derived from chapter 3 were applied to spring elements at the proximal ends for gluteus maximus, gluteus medius, gluteus minimus, iliopsoas and piriformis. Muscle force magnitudes were applied at the distal ends of spring elements representing vastus intermedius and vastus lateralis. Continuum distributing coupling constraints were then used to connect muscle insertion areas on the mesh surface with the insertion points of spring elements (figure 6.21).

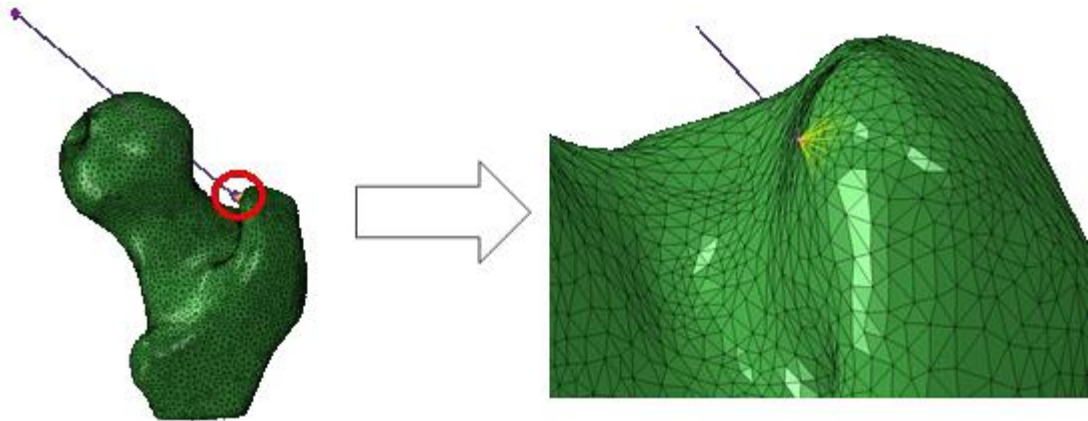


**Figure 6.21 Continuum distributing coupling constraints.** Zoomed in section of the piriformis insertion site illustrating how continuum distributing coupling constraints were used to model the interaction between muscle forces and the femoral surface. Utilising this type of coupling constraint helped to avoid unrealistically high stress concentrations resulting from the application of muscle forces on the model.

Continuum distributing coupling elements were utilised due to the way in which loads are applied using this technique. Instead of a ‘hard’, instantaneous load being applied at the surface as would be the case using concentrated loads or kinematic coupling constraints, continuum distributing coupling constraints apply the load in a ‘soft’ sense, averaging out the overall magnitude across the entire surface. This, coupled with relatively low stiffness properties, was deemed particularly suitable for application of loads that were meant to approximate those applied by muscle-tendon units.

### 6.2.8 Impact Forces

Impact forces were applied at the most lateral part of the greater trochanter in finite element models (figure 6.22). Impact areas were defined at the most lateral part of the greater trochanter. The impact area was limited to an approximate size of 1cm<sup>2</sup> for all models. Some studies apply hip joint reaction forces at the femoral head. However, it is difficult to know with certainty how these prescribed hip joint reaction forces would relate to the perceived, preceding impact on the greater trochanter, without first determining this relationship. As a result, the vectors defining such hip joint reaction forces are often assumed. By applying impact forces directly at the greater trochanter there is arguably more control over modelling predicted impact forces at the right location and ensuring they act in the right directions.

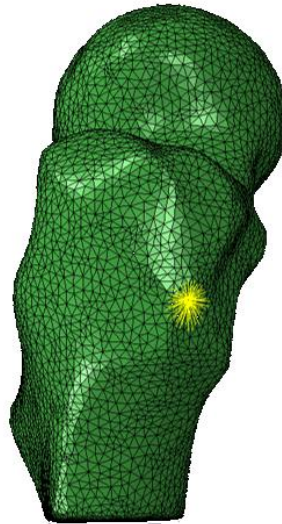


**Figure 6.22 Impact forces.** Impact forces were applied on the lateral most portion of the greater trochanter using continuum distributing coupling constraints as indicated by the yellow region.

In taking this approach, it also becomes possible to use fall impact data obtained from MDA simulations to model and apply proportionately the individual X, Y and Z force components contributing to overall impact force magnitudes, in order to see how their interaction might affect hip loading. Not only this, but such an approach also ensures that the resultant impact force vectors match exactly those derived from the relevant MDA fall sequence. This provides continuity between the kinematics of each fall sequence, the composition and effect of the resulting impact force and the associated muscle forces and activation patterns. In other words, this approach enables FE simulations to take account of the dynamic processes, from initial fall to a point in time immediately after impact, which occur during sideways falls onto the hip and place them into coherent, temporally linked frameworks that are specific to individual fall sequences.

Although contact forces between the acetabulum and femoral head were available from the MDA model, these were not applied to the femoral head. While their use might have been more physiologically representative, they would not have constrained the femoral head sufficiently for simulations to converge. Additionally, applying them alongside femoral head constraints would have led to unrealistically high stress magnitudes within the proximal femur. The femoral head constraints applied in simulations (as described in section 6.2.10) prevent translational movement that would otherwise occur after application of the impact force. In preventing translational movement, stresses are created around the constraints themselves but also within the proximal femur and therefore, although the interactions

between the constraints and femoral model are not physiologically accurate and may underestimate stresses, they could be viewed as approximating the contact forces that might occur between the femoral head and acetabulum. Typically, in FE studies of hip fracture, fall-related loads are applied at either the femoral head or greater trochanter (e.g. Yang *et al.*, 2009; Naylor *et al.*, 2012; Naylor *et al.*, 2013; San Antonio *et al.*, 2012). As such, the latter approach was deemed acceptable and taken here.

#### **6.2.8.1 Transforming X, Y and Z Components of Impact Forces**

The coordinate systems used for the finite element simulations and the MDA simulations from which the muscle force data was derived, differed relative to the femur. Therefore, a simple coordinate transformation was made so that X, Y and Z force components in the MDA simulation aligned with the Y, Z and X components respectively in subsequent finite element simulations.

#### **6.2.8.2 Application of Impact Force**

Similar to muscle loading, impact forces were applied using continuum distributing coupling constraints. The rationale was the same; using either concentrated loads or kinematic coupling constraints would have produced unrealistically and unnecessarily high stress concentrations around the area of application. While stress magnitudes might still be higher than expected using continuum distributing, it was assumed that their magnitudes would be more reasonable than would otherwise be the case when using concentrated loads or kinematic coupling constraints.

#### **6.2.9 Finite Element Simulations**

A variety of loading conditions were simulated for each femoral model leading to a total of 525 finite element simulations or 105 finite element simulations per model. All models were subject to the same sets of loading conditions, so comparisons could be made.

For each model, the following loading conditions were modelled:

- The impact force data associated with each successfully modelled fall from chapter 4 (35 in total).
- The muscle forces associated with each successfully modelled fall from chapter 4 (35 in total).
- The impact and muscle forces specific to each successfully modelled fall from chapter 4 (35 in total).

For all simulations, loads were applied in a single analysis step. Consequently, where simulations contained multiple applied loads, all loads were applied concurrently.

#### **6.2.10 Boundary Conditions – Femoral Models**

The femur was constrained at the femoral head from translational movement in all directions for all simulations. While these fixed conditions might not be physiologically accurate, the multi-directional nature of loading within the finite element simulations meant this was the most practical way to fix the femoral model in a standardised way across all simulations; without fully constraining the model, results could not converge.

#### **6.2.11 Boundary Conditions – Spring Elements**

Spring elements were also constrained from translational and rotational movement in all directions at their insertion points. At their origins, they were constrained from translational and rotational movement in all directions apart from in the direction of their longitudinal axis. Displacement along this axis was permitted in the direction that produced tension within the spring element. Displacement was modelled to reflect the average tendon length change that occurred in MDA simulations in chapter 4 at the moment of impact.

### 6.2.12 Analysis

All finite element simulations were simulated in ABAQUS 6.14-2 (SIMULIA, USA) and modelled as linear elastic, static problems. Linear elastic solutions were deemed appropriate due to the linear elastic behaviour of bone until failure and due to the linear elastic behaviour tendons display when loaded. Loads were applied incrementally with an initial step increment of 0.01.

Von Mises (VM) stresses and principal stresses were used to quantify the biomechanical response of femoral models to the various loading configurations. Although differences between FE models and between the magnitudes of stress were of interest, due to the limitations of working with uncalibrated  $\mu$ CT scans and limitations associated with the applicability of available analysis criteria in ABAQUS 6.14-2 (SIMULIA, USA) for orthotropic materials, rather than focus on absolute magnitudes of stress, this study chose to concentrate on the relative differences in proximal femur stress patterns produced by different loading configurations. Additionally, to aid clarity (which may be lost due to the large number of simulations and potential comparisons), there was also a focus on gross comparisons of the most consistent trends that this author considers to confer the most significant implications for hip fracture.

## 6.3 RESULTS

### 6.3.1 Creation of Fully Orthotropic FE models

Using the semi-automated, novel methods developed in this study it was possible to successfully incorporate principal trabecular orthotropic directions obtained from  $\mu$ CT scans in chapter 3, into each of the corresponding FE models. The resulting trabecular orientations in FE models therefore accurately represent those found in older peoples' femoral specimens (e.g. figures 3.8 & 3.9). Furthermore, by using a novel approach to define fully orthotropic orientations for the cortical shell of each FE model based on surface geometry, it was possible to assign transversely isotropic properties for cortical bone.

### 6.3.2 FE Simulations – General Remarks

For each simulation, the gross stress distribution patterns resulting from impact, muscle and impact plus muscle forces were qualitatively similar for all FE models, although differences in absolute magnitudes, as measured by VM stresses, varied considerably between specimens; by as much as approximately 300MPa for the largest impact force magnitude (13,002N) and approximately 80MPa for the smallest impact force magnitude (2,753N).

It should be noted that for all simulations high stresses were observed at the femoral head and greater trochanter (figure 6.24). These high stress areas were deemed unrealistic and a result of the overly harsh application of impact loads on the greater trochanter and imposition of boundary conditions on the femoral head during simulations. These regions were therefore ignored from all analyses. However, due to Saint-Venant's principle it was deemed that gross stress magnitudes/distributions throughout the FE models were not adversely affected by these areas of unrealistically high stresses and that, as a consequence, stresses occurring outside of these regions were permissible for analysis. This is not only a widely accepted approach within engineering, but it is clear from figure 6.24 that these localised but high stress magnitudes at the femoral head (due to boundary conditions) and greater trochanter (due to the impact force) will have had minimal influence on those analysed in the primary ROI, the femoral neck.

In the following sections, results are often considered in relation to the coordinate system adopted in this study for the application of impact force components to FE models. This system is summarised in figure 6.23.

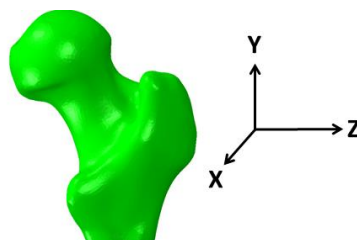


**Figure 6.23 Coordinate System.** The coordinate system used in this chapter for the application and interpretation of impact force components to FE models.

### 6.3.3 Impact-Only Simulations

#### 6.3.3.1 Von Mises Stresses

VM stresses for all femoral models and across all simulations displayed several noticeable trends. Overwhelmingly, impact forces created the largest stress magnitudes in the femoral neck region. Generally, high VM stress magnitudes occurred in the inferior and superior portions of the femoral neck with VM stress magnitudes tending to be higher in the superior portion of the femoral neck compared to the inferior portion (figure 6.24). This pattern of VM stress distributions was associated with much larger magnitudes of the Z component of each impact force relative to the X and Y components.

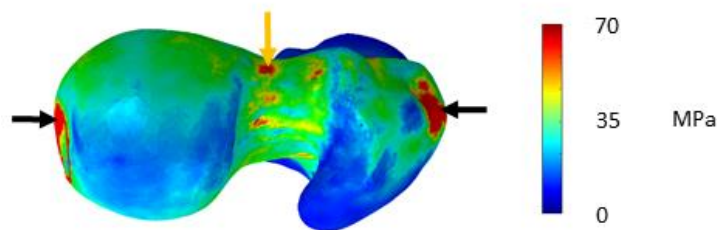


**Figure 6.24 VM stress plot – impact forces.** Superior view of a VM stress plot of a FE model of the largest femur subject to the smallest impact force (2,753N) from MDA simulations in chapter 4. VM stresses show the general trend for the occurrence of highest stress magnitudes (red areas & e.g. gold arrow) in the superior femoral neck due to impact forces derived in chapter 5. Lowest VM stresses are indicated by dark blue. Black arrows indicate the localised regions of unrealistically high stresses due to impact forces and boundary conditions which higher than the colour bar limits. However, due to Saint-Venant’s principle, they were assumed to have minimal influence on stress patterns/magnitudes in the femoral neck.

There was some deviation from this general trend. In a small number of simulations (4 per femur), high VM stress regions moved from superior and inferior regions of the femoral neck to ones that were more anteriorly or posteriorly positioned on the femoral neck. When this occurred, it was associated with increased magnitudes of the X component of each impact force relative to the other two components.

#### 6.3.3.2 Principal Stresses

Principal stresses generally reflected the same trends observed for VM stresses in that the largest tensile and compressive stresses coincided with the areas of the largest VM stresses. Therefore, for the majority of simulations, the superior and inferior portions of the femoral neck bore the largest compressive and tensile stresses. The superior neck tended to be subject

to large compressive stresses whilst the inferior portion of the femoral neck tended to undergo large tensile stresses (figure 6.25).

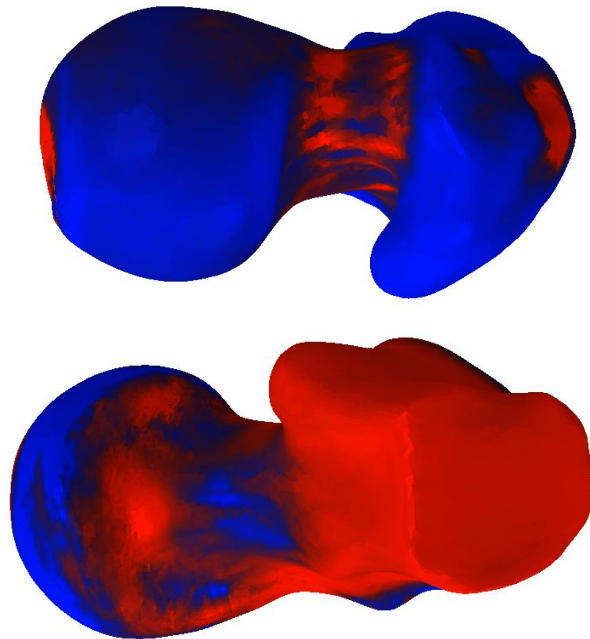


**Figure 6.25 Principal stress plots – impact forces.** **Top:** Principal stress plot illustrating the general trend for the prevalence of compressive stresses (red) in the superior femoral neck due to impact forces derived in chapter 4. **Bottom:** Principal stress plot illustrating the general trend for the prevalence of tensile stresses (blue) in the inferior femoral neck due to impact forces derived in chapter 5.

On occasion, regions of high stress magnitudes occurred in more anterior or posterior regions of the femoral neck although there was no predominant mode of loading (e.g. compression vs tension) associated with either region (figure 6.26). The prevalence of tensile stresses in the anterior or posterior neck was associated with the magnitude and direction of the X component of each impact force.

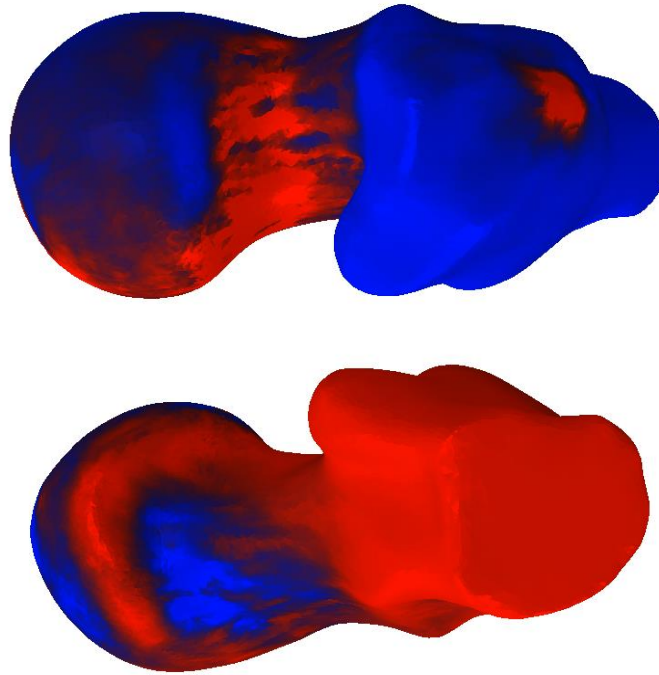


**Figure 6.26 Principal stress plots – impact forces.** **Top:** Superior view of principal stress plot illustrating compressive stresses (red) in the superior-posterior femoral neck due to impact forces. **Bottom:** Inferior view of principal stress plot illustrating tensile stresses (blue) in the inferior-anterior femoral neck due to impact forces derived in chapter 5.

In a small number of simulations (three per femur), the main patterns of stress observed in the majority of simulations (high compressive stresses in the superior portion of the femoral neck and high tensile stresses in the inferior portion of the femoral neck) were reversed. As a result, high tensile stresses occurred in the superior portion of the femoral neck while high compressive stresses occurred in the inferior portion of the femoral neck (figure 6.27).

This trend was associated with an increase in the contribution of the negative Y component of the simulated fall magnitude, particularly relative to the Z component. Typically, such stress distribution scenarios occurred when the Y value was approximately -2000N or greater and/or approximately 25% of the magnitude of the Z component.

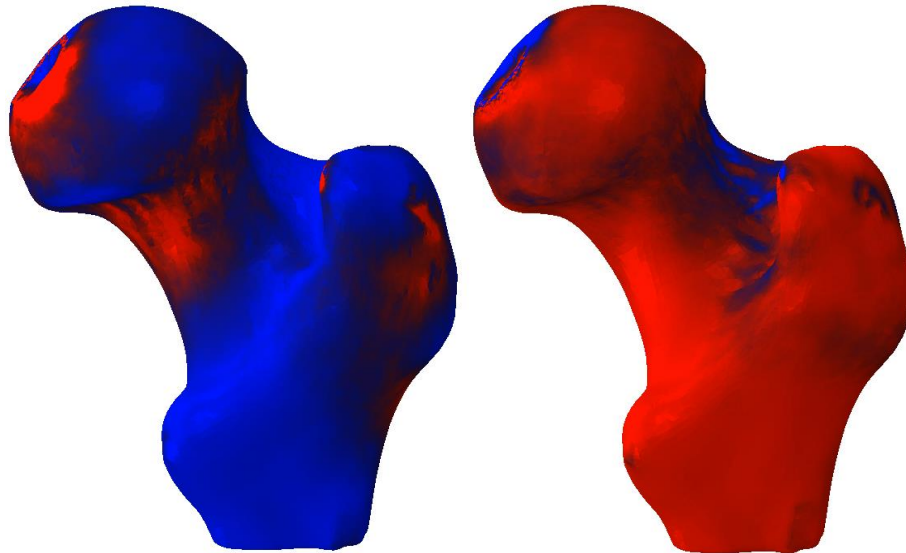


**Figure 6.27 Principal stress plots – impact forces.** Principal stress plot illustrating the reverse of the general trend that occurred in a small number of simulations for compressive stresses in the superior femoral neck and tensile stresses in the inferior neck due to impact forces. Instead compressive stresses (red) occurred in the inferior neck (left) and tensile stresses (blue) occurred in the superior neck (left).

### 6.3.3.3 Principal Stress Directions in the Femoral Neck

Compressive stress directions followed the axial (*i.e.* approximately mediolateral) direction of cortical bone throughout the superior femoral neck region (figure 6.28). For trabecular bone, compressive principal stress directions in the superior neck were more heterogeneous. In the medial portion of the superior neck, they were broadly similar to those seen in cortical bone (figure 6.28). However, towards the posterior portion of the superior femoral neck their orientation became more superior-inferiorly orientated. Tensile principal stresses followed the axial (*i.e.* approximately mediolateral) direction of cortical bone throughout the inferior femoral neck region. In trabecular bone, tensile principal stresses were also mediolateral in direction.

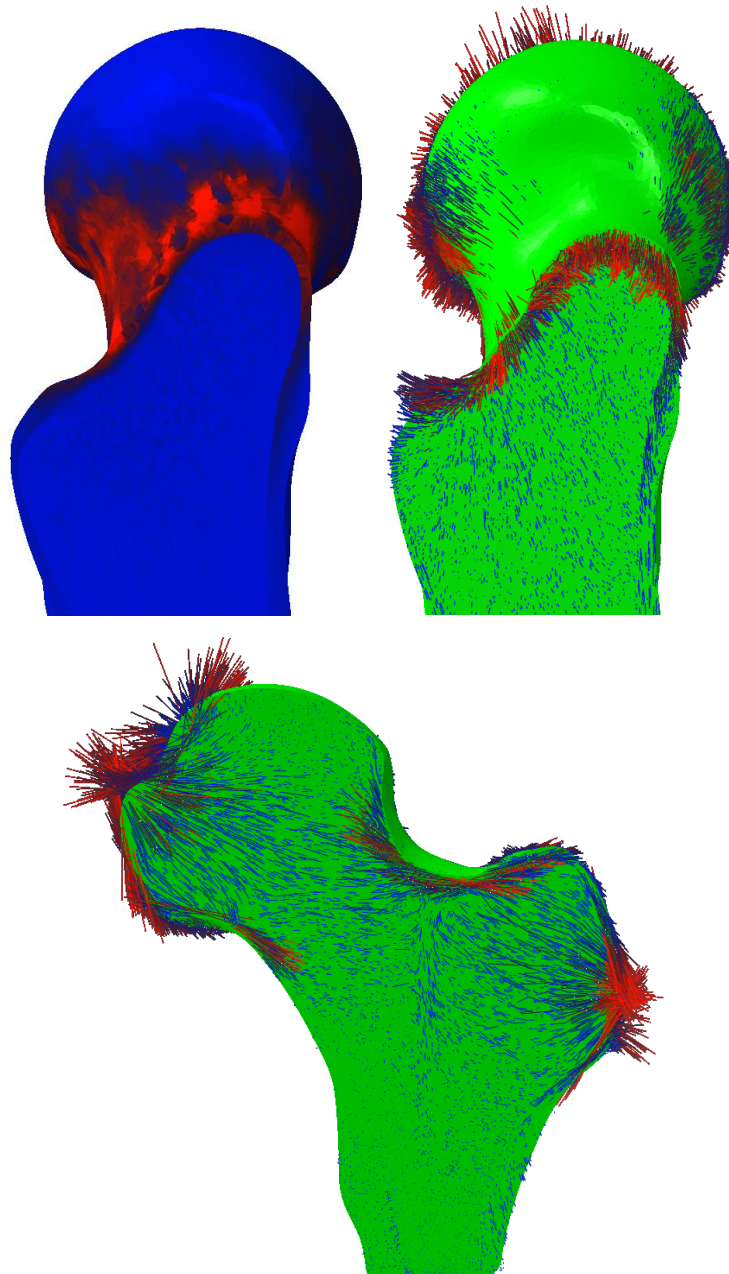


**Figure 6.28 Principal stress directions – impact forces.** **Top Left:** Coronal slice through principal stress plot of the proximal femur illustrating the general trend for the prevalence of compressive stresses (red) in the superior femoral neck due to impact forces. Provides a reference for the principal stress orientation plot (top right). **Top Right:** Coronal slice through the proximal femur showing the orientations of compressive principal stresses acting through the femoral neck. High magnitudes of compressive stresses are red, low magnitudes blue. **Bottom:** Sagittal slice through the proximal femur showing the orientations of compressive principal stresses throughout. High magnitudes of compressive stresses are red, low magnitudes blue.

#### 6.3.4 Muscle-Only Simulations

Despite the great heterogeneity of muscle force magnitudes and patterns observed in chapter 5, FE simulations modelling muscle-only forces illustrated that the combined effect of hip

musculature on the biomechanical behaviour of the femur was surprisingly consistent across simulations.

#### 6.3.4.1 Displacement

It appears that the combined effect of the hip muscle-only forces at the moment of impact was to abduct and medially rotate as well as flex the proximal femur (figure 6.29). Maximum displacement occurred in each model's most distal end and was consistently within the range of approximately 5-6mm.

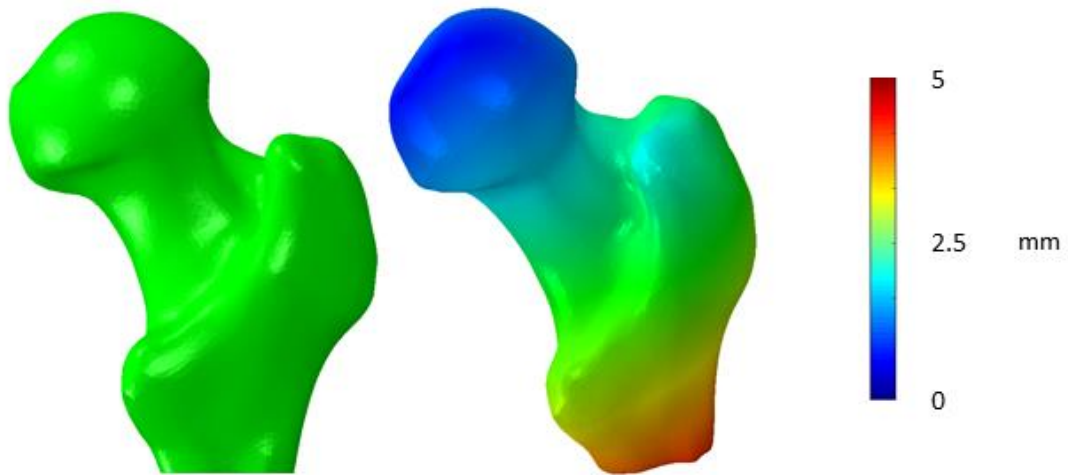


**Figure 6.30 Displacement plot – muscle forces.** Plot illustrating the main trends in displacement of the proximal femur due to contractile activity of the hip musculature at hip impact. Red colours indicate the largest displacements, blue indicate the smallest displacements. Hip musculature generally acted to abduct and medially rotate the femur at the hip joint. The displacement plot here is scaled by a uniform factor of 10. The green FE model on the left represents the original non-deformed and non-displaced version before the application of loads.

#### 6.3.4.2 Von Mises Stresses

As with impact-only simulations the highest values for VM stresses were maintained in the femoral neck relative to other regions of the proximal femur. However, unlike impact-only simulations the superior-anterior surface, as opposed to the superior surface, of the femoral neck was subject to the largest VM stress magnitudes for all simulations (figure 6.30). For all FE models, the largest magnitudes of stress were in the range of 35-60MPa.

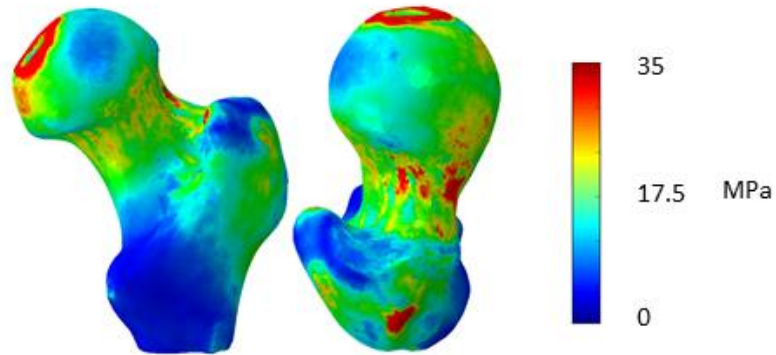


**Figure 6.29 VM stress plot – muscle forces.** **Left:** Posterior view of a VM stress plot of an FE model analysed in this study showing the general trend for the occurrence of high stress magnitudes (red) in the femoral neck region due to muscle forces. **Right:** Superior view of a VM stress plot of an FE model analysed in this study showing the general trend for the occurrence of highest stress magnitudes (red) in the superior femoral neck due to muscle forces. Lowest VM stresses are indicated by dark blue in both.

### 6.3.4.3 Principal Stresses

Compressive stress magnitudes consistently occurred in the superior-anterior femoral neck when simulations modelled muscle-only forces (figure 6.31). This was nearly always accompanied by the occurrence of tensile stresses in the inferior femoral neck (figure 6.31).

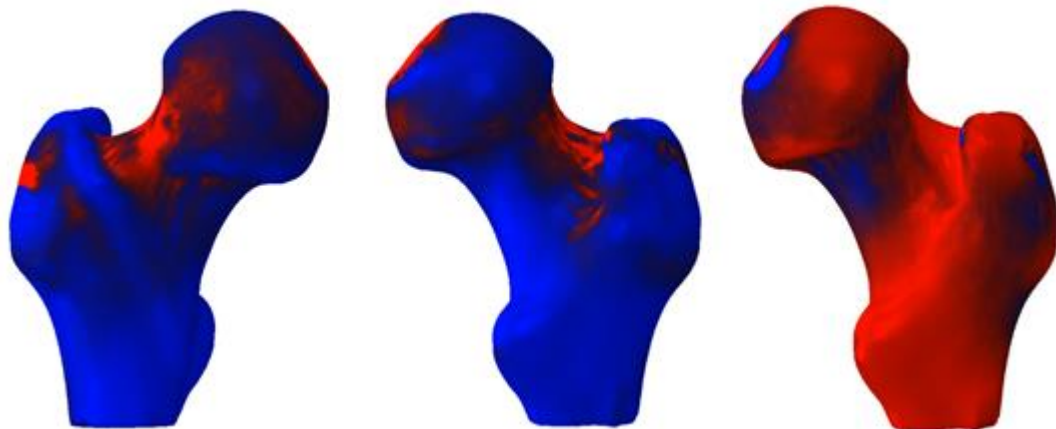


**Figure 6.30 Principal stress plots – muscle forces.** **Left and middle:** Principal stress plot illustrating the general trend for the prevalence of compressive stresses (red) in the superior-anterior femoral neck due to muscle forces. **Right:** Principal stress plot illustrating the general trend for the prevalence of tensile stresses (blue) in the inferior femoral neck due to muscle forces.

### 6.3.4.4 Principal Stress Directions in the Femoral Neck

Compressive stress directions in cortical bone in the superior femoral neck were more anteroposteriorly orientated relative to those observed for impact-only simulations (figure

6.32 & 6.40). For trabecular bone, compressive principal stress directions in the superior neck were slightly more superior-inferiorly and anteroposteriorly orientated relative to those seen in impact-only simulations, particularly in the most superior region (figure 6.32 & 6.40). Tensile principal stresses followed the axial (*i.e.* approximately mediolateral) direction of cortical bone throughout the inferior femoral neck region. In trabecular bone however, tensile principal stress orientations had strong affinity with the anteroposterior direction.

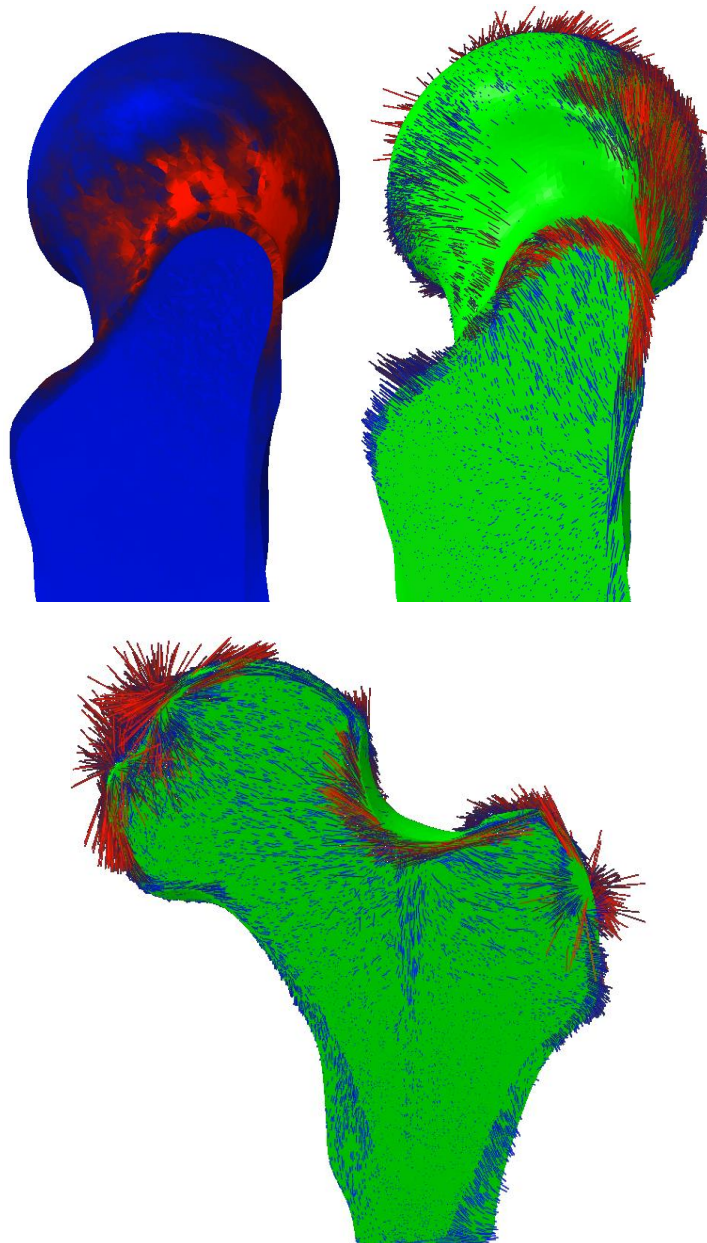


**Figure 6.31 Principal stress directions – muscle forces.** **Top Left:** Coronal slice through principal stress plot of the proximal femur illustrating the general trend for the prevalence of compressive stresses (red) in the superior femoral neck due to muscle forces. Provides a reference for the principal stress orientation plot (top right). **Top Right:** Coronal slice through the proximal femur showing the orientations of compressive principal stresses acting through the femoral neck. High magnitudes of compressive stresses are red, low magnitudes blue. **Bottom:** Sagittal slice through the proximal femur showing the orientations of compressive principal stresses throughout. High magnitudes of compressive stresses are red, low magnitudes blue.

### 6.3.5 Impact plus Muscle Force Simulations

The addition of muscle forces concurrent with an impact force noticeably modified both the stress magnitudes and distributions within the proximal femur relative to impact- and muscle-only simulations. As with muscle-only simulations, the combined effect of hip musculature on the biomechanical behaviour of the femur was consistent across simulations.

#### 6.3.5.1 Von Mises Stresses

Similar patterns of VM stresses were observed throughout the proximal femur when hip muscle forces were included in FE simulations. The highest values for VM stresses were maintained in the superior and inferior portions of the femoral neck but their magnitudes were generally increased compared to values observed in impact-only simulations (figure 6.33). Although the magnitudes of VM stresses were somewhat increased in both these regions, the superior surface of the femoral neck was subject to the largest increases in VM stress magnitudes. Increases in VM magnitudes were of the same order as those created in muscle-only simulations and therefore fell within the approximate range of 40-60MPa. This increase appeared to be independent from the overall magnitude of stress these regions of the proximal femur experienced due to the impact loads.

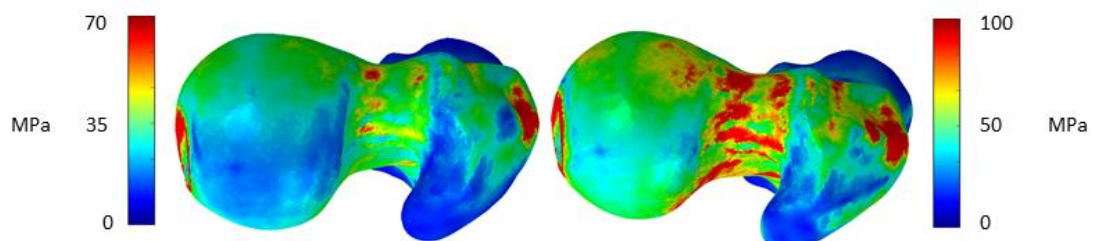


**Figure 6.32 VM stress plot – impact plus muscle.** **Left:** Superior view of a VM stress plot showing the general trend for the occurrence of highest stress magnitudes (red) in the superior femoral neck due to impact forces (same femur and impact as in figure 6.24). Lowest VM stresses are indicated by dark blue. **Right:** Superior view of a VM stress plot showing the general trend for an increase in VM stress magnitudes for the same femur and impact force when hip muscle forces are included in the simulation. The VM stresses (red) threshold is set at the same level as the left figure (e.g. 70MPa) for comparative purposes but the highest VM stress absolute magnitudes increase from approximately 70MPa to 100MPa and cover a larger area. Low VM stresses are indicated by dark blue.

Some slight variation in this pattern was observed for a small number of simulations. For these simulations the addition of muscle forces resulted in regions of high VM stress moving from

the superior portion of the femoral neck to its superior-posterior portion which may be related to the increased activity of specific muscles relative to others. Additionally, in some simulations, overall VM stress magnitudes were reduced.

Regions of the proximal femur that formed muscle insertion sites were necessarily subject to increased levels of VM stress. Unsurprisingly, muscles that produced large forces relative to the size of their insertion site produced the largest surface stress magnitudes. As a result, even though forces for vastus intermedius and vastus lateralis were consistently larger than any other muscles, the largest surface stresses were produced by muscles with smaller insertion sites despite their lesser magnitudes. Consequently, the greater trochanter was subject to a number of localised high VM stress magnitudes.

#### 6.3.5.2 *Principal Stresses*

Principal stress patterns for the majority of simulations mirrored the main trends observed in impact- and muscle-only simulations. Thus, compressive stresses occurred mainly in the superior portion of the femoral neck and tensile forces occurred in the inferior portion of the femoral neck (figure 6.34).

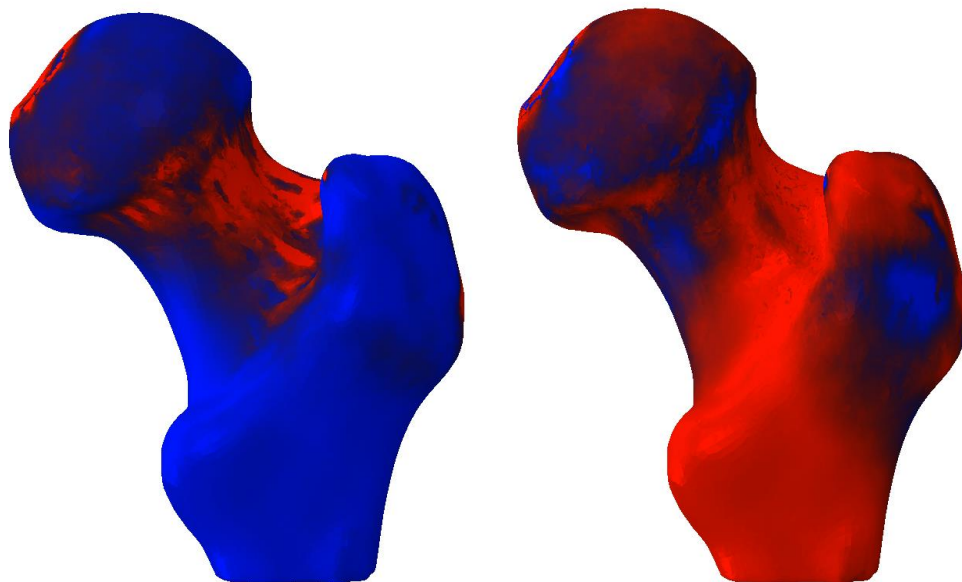


**Figure 6.33** *Principal stress plots – impact plus muscle.* **Left:** Principal stress plot illustrating the general trend for the prevalence of compressive stresses (red) in the superior femoral neck due to the combined action of impact and muscle forces. **Right:** Principal stress plot illustrating the general trend prevalence of tensile stresses (blue) in the inferior femoral neck due to the combined action of impact and muscle forces.

The main trend was for compressive stresses to consistently occur in the superior femoral neck when muscle forces were included in simulations (figure 6.35). This was accompanied by an increase in tensile stresses in the inferior femoral neck (figure 6.36). When an impact force caused compressive stress in the superior neck and tensile stress in the inferior neck, the effect of the musculature was to proliferate and exaggerate this pattern by increasing the overall magnitudes of these principal stresses within these regions (figure 6.35).

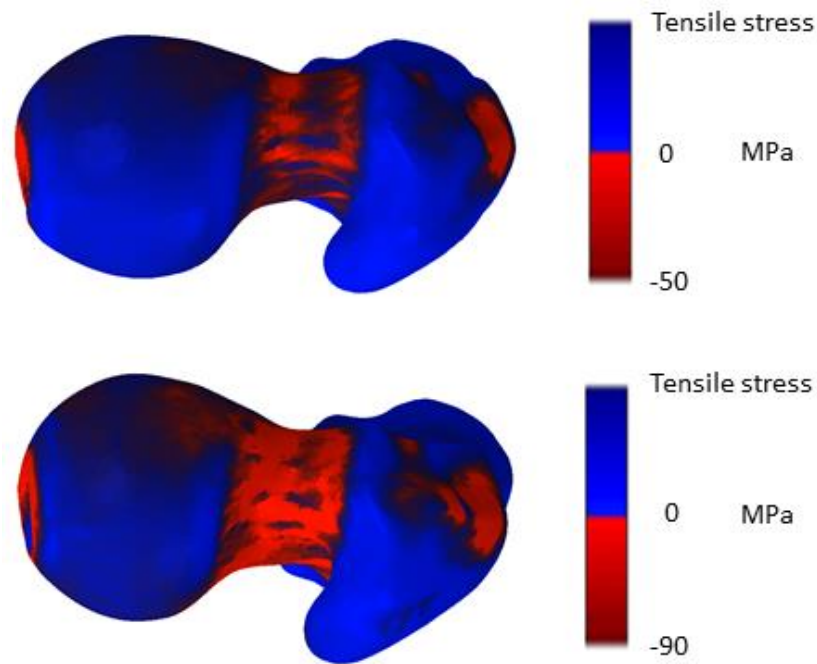


**Figure 6.34 Compressive principal stress increases - impact plus muscle.** **Top:** Superior view of a principal stress plot showing the general trend for the occurrence of compressive stresses (red) in the superior femoral neck due to impact forces. **Bottom:** Superior view of a principal stress plot showing the general trend for an increase in compressive stress magnitudes for the same impact force when hip muscle forces are also included in the simulation. Compressive stresses (red) increase in magnitude and cover a larger area.

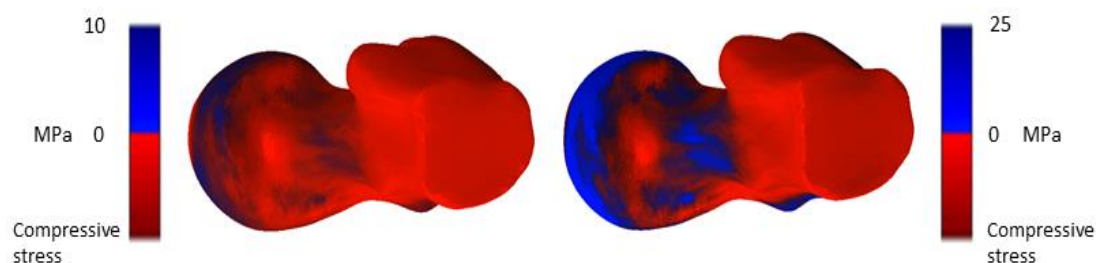


**Figure 6.35 Tensile principal stress increases - impact plus muscle.** **Left:** Inferior view of a principal stress plot showing the general trend for the occurrence of tensile stresses (red) in the superior femoral neck due to impact forces. **Right:** Inferior view of a principal stress plot showing the general trend for an increase in tensile stress magnitudes for the same impact force when hip muscle forces are also included in the simulation. Tensile stresses (red) increase in magnitude and cover a larger area.

Even when an impact force caused tensile stress in the superior neck and compressive stress in the inferior neck the addition of muscle forces always reversed this pattern, resulting in compressive stresses in the superior neck and tensile stresses in the inferior neck. However, the magnitudes of each of the principal stresses was less than those observed in the corresponding impact-only simulation. This in turn, appeared to reduce the VM stress magnitudes in this area.

When an impact force caused compressive stress in the superior-anterior neck and tensile stress in the inferior-posterior neck, the effect of the musculature was to proliferate and exaggerate this pattern by increasing the overall magnitudes of these principal stresses within these regions. This in turn increased the levels of VM stress in this area.

When an impact force caused tensile stress in the anterior neck and compressive stress in the inferior-posterior/posterior neck the addition of muscle forces tended to reverse this pattern, resulting in compressive stresses in the superior-anterior neck and compressive stresses in the inferior-posterior neck (figures 6.37 & 6.38). However, the magnitudes of each of the principal stresses was less than those observed in the corresponding impact-only simulation. This in turn, reduced the VM stress magnitudes in this area.

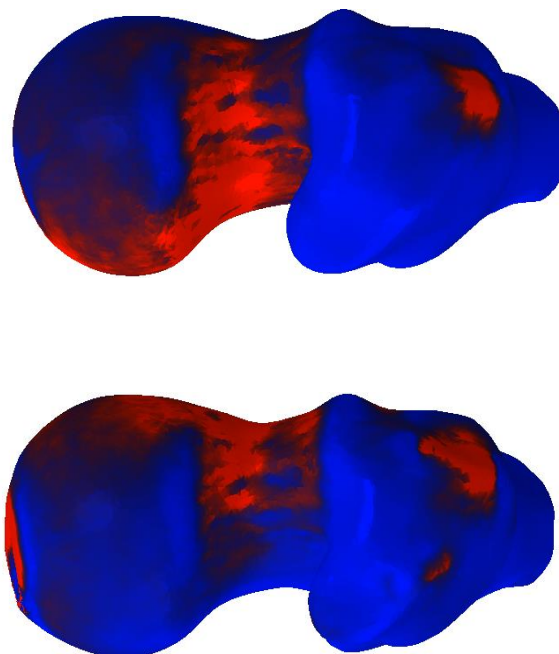


**Figure 6.36 Compressive stress distributions - impact plus muscle.** **Top:** Superior view of a principal stress plot showing compressive stresses (red) in the inferior-posterior femoral neck due to impact forces. **Bottom:** Superior view of a principal stress plot showing how the addition of hip muscle forces to the same impact force causes compressive stresses (red) to relocate to a more superior and anterior region on

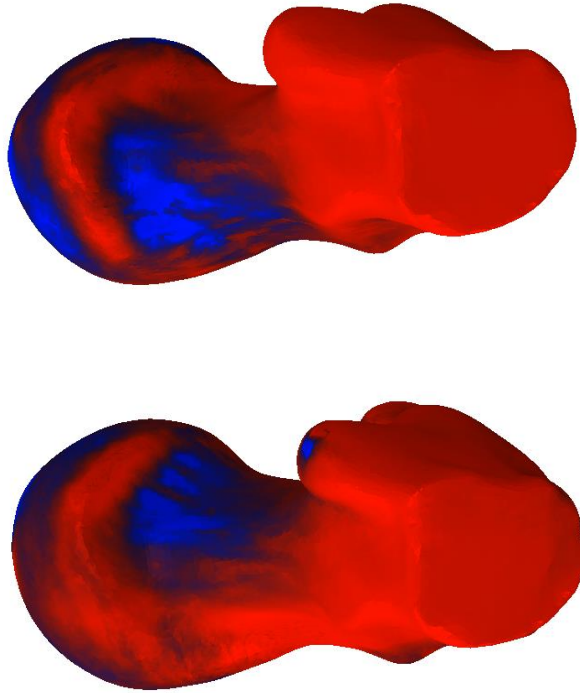


**Figure 6.37 Tensile stress distributions - impact plus muscle.** **Top:** Inferior view of a principal stress plot showing tensile stresses (blue) in the inferior-anterior femoral neck due to impact forces. **Bottom:** Inferior view of a principal stress plot showing how the addition of hip muscle forces to the same impact force causes tensile stresses (blue) to relocate to a more posterior region on the femoral neck.

### 6.3.5.3 Principal Stress Directions in the Femoral Neck

Compressive stress directions in cortical bone appeared to display similarities to both impact- and muscle-only simulations and followed the axial (*i.e.* approximately mediolateral) direction of cortical bone throughout the superior femoral neck region (figures 6.39 & 6.40) but with a slightly increased anteroposterior direction. For trabecular bone, compressive principal stress directions in the superior neck were more similar to those seen in muscle-only simulations being slightly more superior-inferiorly and anteroposteriorly orientated (figure 6.39 & 6.40). Tensile principal stresses were followed the axial (*i.e.* approximately mediolateral) direction of cortical bone throughout the inferior femoral neck region. In trabecular bone however, tensile principal stresses were generally absent from the most superior regions. In more inferior neck regions, orientations had strong affinity with the anteroposterior direction (figure 6.39).

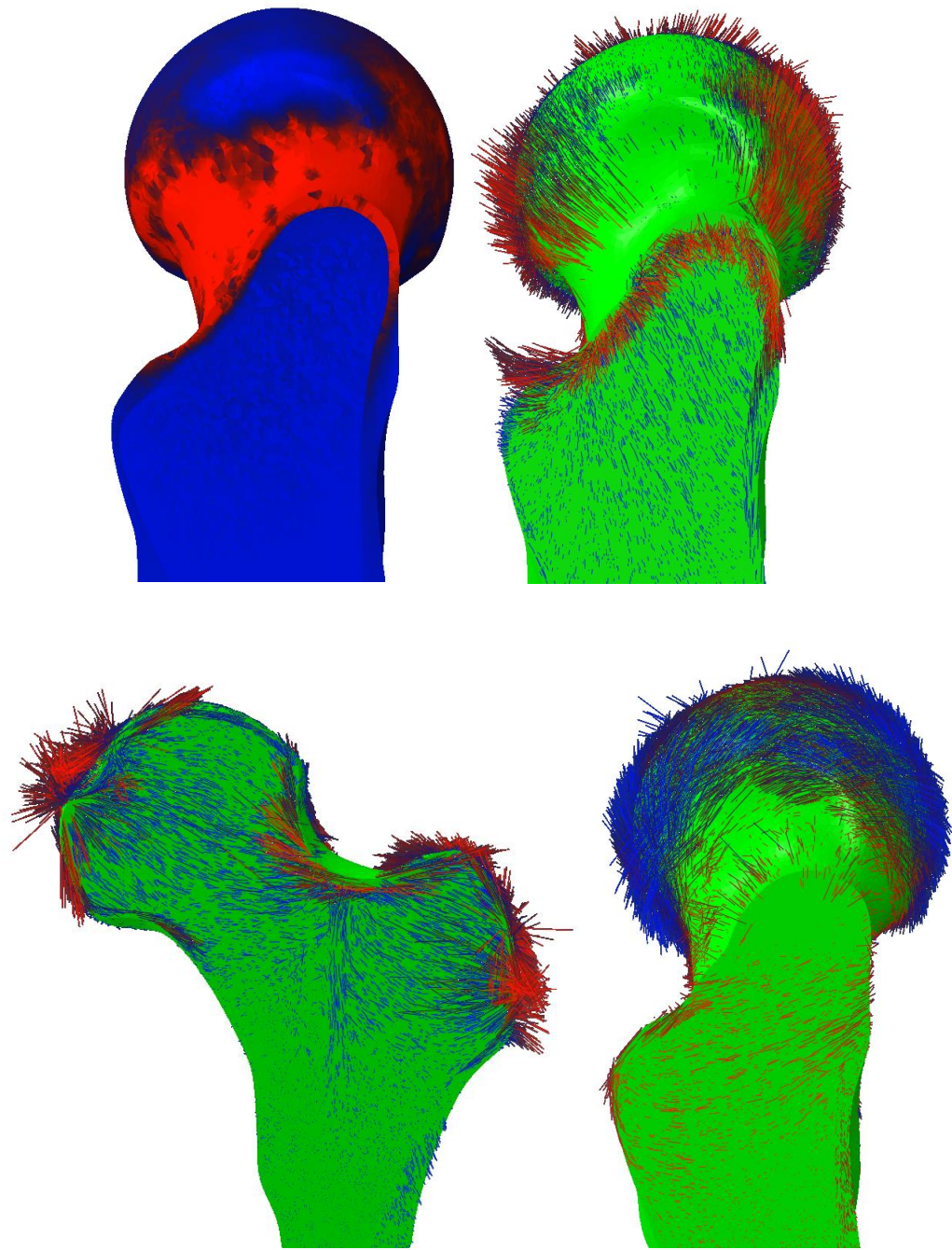


**Figure 6.38 Principal stress directions – impact plus muscle.** **Top Left:** Coronal slice through principal stress plot of the proximal femur illustrating the general trend for the prevalence of compressive stresses (red) in the superior femoral neck due to muscle and impact forces. Provides a reference for the principal stress orientation plots (top and bottom right). **Top Right:** Coronal slice through the proximal femur showing the orientations of compressive principal stresses acting through the femoral neck. High magnitudes of compressive stresses are red, low magnitudes blue. **Bottom Left:** Sagittal slice through the proximal femur showing the orientations of compressive principal stresses throughout. High magnitudes of compressive stresses are red, low magnitudes blue. **Bottom Right:** Coronal slice through the proximal femur showing the orientations of tensile principal stresses through the femoral neck. High magnitudes of tensile stresses are blue, low magnitudes red.

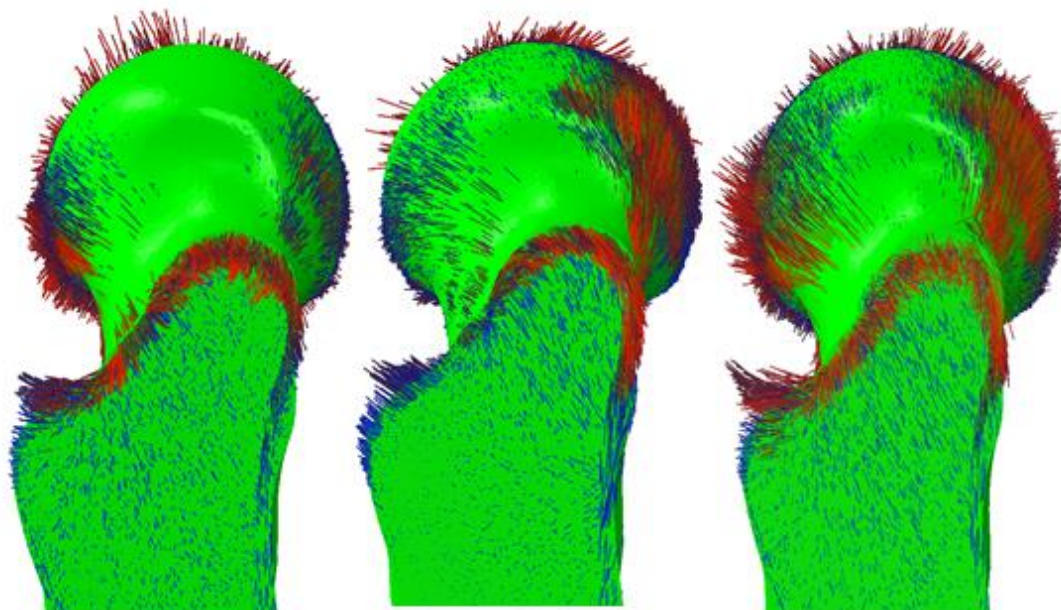


**Figure 6.39 Principal stress comparison - all.** Comparison of compressive stress (red lines) directions through the superior femoral neck of an impact-only simulation (left), the corresponding muscle-only simulation (centre) and an impact plus muscle force simulation using the same impact and muscle force data (right). Impact forces created primarily mediolaterally directed compressive stress trajectories through the superior femoral neck. Muscle forces created primarily anteroposteriorly directed compressive stress trajectories through the superior femoral neck. The addition of muscle forces to impact forces in simulations had the effect of modifying compressive stress trajectories so that they were more anteroposteriorly orientated through the superior femoral neck.

## 6.4 DISCUSSION

For the first time this study has created fully orthotropic, subject specific models of the ageing proximal femur and subjected them to the combined action of muscle and impact forces resulting from a sideways fall. A suite of novel scripts and functions have been developed in MATLAB to incorporate and map trabecular and cortical orthotropic orientations throughout FE models of the proximal femur. The semi-automated and inexpensive nature of the methods used means they are time- and cost-effective, particularly when considered in the context of the large amount of data that can be processed and incorporated into FE models through their use.

### 6.4.1 Material and Structural Properties

Previous FE studies have simplified the material and structural properties of the proximal femur (Helgason, Taddei, *et al.*, 2008; Langton, Pisharody and Keyak, 2009; Janne E.M.

Koivumäki *et al.*, 2012; Dall'Ara *et al.*, 2013b; Nawathe *et al.*, 2014; Nishiyama *et al.*, 2014; Liebl *et al.*, 2015). However, modelling bone in the proximal femur in a way that more accurately represents its material and structural properties, *i.e.* as orthotropic, is arguably one of the more important aspects in the creation of FE models of the proximal femur for the specific purposes of understanding and predicting hip fracture.

When modelling the proximal femur as an isotropic structure, the existence of infinite material symmetry planes means the imposition of and distinction between different loading directions and principal stress trajectories is less important because bone will have equal properties at every point and in every direction throughout the material.

However, the distinction is more critical for orthotropic models because bone has different properties in different directions and loading can occur in directions in which bone is less strong. As has been demonstrated in this study there likely exists a significant multidirectional loading scheme imposed on the proximal femur during a sideways fall. The multidirectional action of impact and muscle forces, results in increased stress magnitudes in a critical area for fracture (de Bakker *et al.*, 2009) (e.g. figure 6.33) and compressive principal stress trajectories in the femoral neck that are less well aligned with the principal material directions of cortical bone (figure 5.40). Thus, principal stress trajectories do not act in a direction in which cortical bone is strongest.

Similarly, while compressive principal stresses were more aligned with trabecular bone principal directions in the superior femoral neck for simulations combining impact and muscle forces, it was shown that tensile compressive stresses in the inferior femoral neck were not well aligned with principal trabecular material and structural directions (figure 6.39). Not accounting for these principal structural and stress trajectories through the use of inadequate (*i.e.* isotropic) material properties may result in inaccurate results and a subsequent loss of the predictive power of FE models for hip fracture.

On this basis, it was assumed in this study that using orthotropic properties would lead to more accurate FE models and subsequent results because they represented a more comprehensive representation of the complex biology of femoral bone. This is particularly so given the multidirectional nature of the loading schemes employed and because principal orthotropic directions for the trabecular core of all five FE models were mapped using data derived from  $\mu$ CT scans of multiple older peoples' proximal femora at resolutions below 80 microns. Although this represents a modest improvement in resolution compared to that used in previous studies, this may mean the principal orthotropic directions mapped in these

models are potentially more accurate than any developed previously, which may increase the quality of the models and subsequent results in this study.

A previous study by Luisier, Dall'Ara and Pahr, (2014) found that orthotropic models of the proximal femur do not improve the ability to predict fracture compared to equivalent isotropic models when loading in a sideways fall configuration. However, in this study cortical shells were modelled as isotropic and the loading scheme employed (*i.e.* a single impact load) was relatively simple. While it was not within the scope of this study to assess the performance of orthotropic FE models, it would be interesting to compare the performance of isotropic vs. orthotropic models of the proximal femur exposed to multidirectional loading such as those used in the present study to test the validity of the conclusions of Luisier, Dall'Ara and Pahr, (2014) and the assumption used in this study that orthotropic properties lead to improved model performance.

Although the focus of this study was on the qualitative differences and similarities in stress patterns between impact-only simulations and combined impact and muscle force simulations, there were appreciable differences in the stress magnitudes experienced in the femoral neck between FE models. It is not possible to delineate exactly how these differences relate to differences in bone density, geometry and trabecular fabric. However, it was shown in chapter 3 that the femoral specimens from which the FE models were constructed displayed similar principal trabecular directions in the femoral head and neck. This suggests that the differences in stress magnitudes experienced in these regions between models may primarily be a result of femoral bone density and geometry and that trabecular fabric in these regions plays a less important role in determining the biomechanical behaviour in this region of the ageing femur during a fall. More generally, this also implies that there might be region-specificity to the amount of trabecular fabric that contributes to overall trabecular strength. Future studies investigating the contribution of trabecular fabric to trabecular strength (Musy *et al.*, 2017) may want to explore this further.

#### **6.4.2 Impact-Only Simulations**

Impact forces consistently led to the largest VM and principal stress magnitudes occurring in the femoral neck (figure 6.24). More specifically, they led to compression in the superior neck and tensile stresses in the inferior neck with compressive stress magnitudes being larger than tensile ones (figure 6.25).

The presence of the high compressive stresses in superior neck due to impact forces makes sense biomechanically. The individual components of the impact forces in these simulations created a resultant force (figure 6.41) that will have caused the femur to pivot clockwise (when viewed from a posterior perspective) about an idealised point in the centre of the femoral neck. This pivoting results in a bending moment that causes compressive stresses in the superior neck and accompanying tensile stresses in the inferior neck.

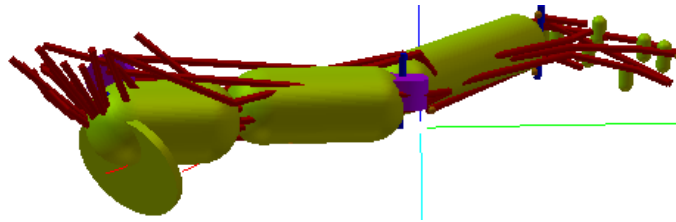


**Figure 6.40 Resultant impact forces at the hip.** Figure showing the right leg of the musculoskeletal model in an MDA simulation from chapter 4 at impact. The green disc located at the hip geom represents the direction of the impact force at the hip. Its orientation relative to the hip is such that it will cause a bending moment within the femoral neck that produces compressive stresses in the superior femoral neck and tensile stresses in the inferior femoral neck.

The fact that compressive stresses were consistently higher in magnitude than tensile stresses in the femoral neck is unsurprising given that all femoral specimens exhibited significantly less cortical bone in this region compared to the inferior femoral neck which displayed a relatively thick cortex (figure 6.42) which is typical of older peoples' femoral necks (Mayhew *et al.*, 2005; de Bakker *et al.*, 2009).

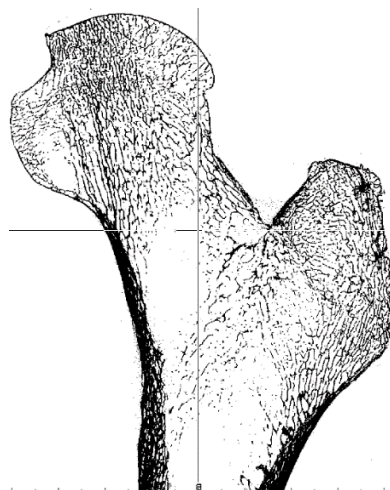


**Figure 6.41 Thin cortex at the superior femoral neck.** Image of a scan slice from a  $\mu$ CT scan of one of older peoples' femoral specimens used in this study. It is clear that the specimen exhibits especially thin cortical bone in the superior femoral neck while the inferior neck exhibits a much thicker cortex.

These findings suggest that impact forces from a sideways fall generally place the superior femoral neck at an increased risk of fracture relative to other regions. This is in agreement with a number of other experimental and numerical hip fracture studies that indicate the superior femoral neck experiences high compressive stresses during loading from a fall (Lotz *et al.*, 1995; Verhulp *et al.*, 2008) and is therefore a critical region for hip fracture (Mayhew *et al.*, 2005; de Bakker *et al.*, 2009). This to some extent validates the performance of the MDA model in chapter 4.

Unlike previous studies however, this study elucidated that, despite the general trend for areas of high compressive stress in the superior neck, kinematically similar sideways falls can cause a myriad of other stress distribution patterns in the proximal femur including a completely reversed scenario whereby tensile stresses occur in the superior neck and compressive stresses occur in the inferior neck (figure 5.27). Furthermore, it was shown that regions of high stress can also occur in the inferior or posterior portions of the neck too (figure 6.4).

While other studies have focused on the relationship between different fall directions and hip fracture risk (e.g. Nankaku *et al.*, 2005; Bessho *et al.*, 2009; Hirabayashi, Tsuchida and Tanaka, 2013), this study shows that important differences in impact force components can arise even for the same types of fall. Indeed, the reversed principal stress pattern (tensile stress in the superior neck and compressive stresses in the inferior neck (figure 6.27) could be significant in terms of hip fracture because fact bone is weaker in tension (Currey, 2005), cortical bone in the superior neck is preferentially lost with increasing age (Johannesdottir *et al.*, 2011) and impact loads from falls can be very large as shown in chapter 5. Therefore, subjecting this region to significant tensile loading could greatly enhance the chance of fracture.

It is possible to envisage how the small variations in the X component of each modelled impact might occur in real life due to rotation of the leg at the hip joint or small variations in the anterior or posterior trajectory of the fall and how they might lead to increased stresses in the anterior and inferior portion of the neck. It is less easy to envisage how real-world sideways falls might lead to the variations in the Y component observed in modelled impacts that caused tensile stresses in the superior femoral neck. For this to happen, it seems likely that the kinematics of a sideways fall would have to a greatly increased lateral translational component at impact that would be more indicative of a jump, rather than a fall, to the side. Nonetheless, it does provide insight into why other types of fall – such as those arising from slips on low friction surfaces or those that occur due to turning/obstacle negotiation – that

might be associated with increased variability and magnitude of the Y component might be related to increased hip fracture risk (Thigpen *et al.*, 2000b).

With respect to principal stress trajectories, in cortical bone generally and in the inferior and superior neck (*i.e.* regions of highest stress) specifically, the largest principal stress orientations followed cortical principal material and structural orientations (Lawrence Katz *et al.*, 1984; Martin and Ishida, 1989; Sevostianov and Kachanov, 2000; Yeni, Vashishth and Fyhrie, 2001). This is advantageous in that cortical bone is strongest in this direction. This implies that the likelihood of fracture due to a sideways fall in the cortical shell might be mitigated by its principal structural (and thus material) axes to a certain extent.

### 6.4.3 Muscle-Only Simulations

The gross action of hip musculature had similar effects on the displacement and stress patterns across the majority of simulations and for all FE models (figure 6.29 – 6.31). This lends confidence to the fact that, despite lacking a truly standardised methodology for defining muscle insertion sites on each of the FE models (e.g. by using a surface based registration approach), the use of proximal femoral anatomy to guide selection of appropriate insertion sites was an acceptable approach that produced broadly similar results.

The consistency in the effect of hip musculature on the displacement and stress patterns of the femur across simulations is in contrast to the statistically significant and heterogeneous differences in muscle force magnitudes found within and between many of the MDA simulations in chapter 5. This is likely attributable to the fact that regardless of the level of contractile activity, the function of many of these muscles is very similar. In other words, most of the muscles modelled act to either abduct, medially rotate and/or flex the hip femur at the hip joint. Therefore, even though absolute magnitudes differ, their collective action would nonetheless be similar.

Contraction of the hip abductors during stance provide lateral pelvic stabilisation (Krebs *et al.*, 1998) but they also act to reduce tensile stresses in superior neck (Dalla Pria Bankoff, 2012). This is a favourable outcome given bone is weaker in tension than compression and thus may be more likely to fracture in tension for the same given load. Supporting this notion is research reporting femoral neck fracture in runners due to fatigue of the hip abductors (Matheson *et al.*, 1971)

There were also some noticeable changes in compressive principal stress directions when the effects of muscle-only forces were modelled. Specifically, compressive principal stress directions in the superior neck for cortical bone and trabecular bone were much more aligned in the anteroposterior direction relative to impact-only simulations (figure 6.32 & 6.40). In chapter 4, it was found that trabecular structures in the superior femoral neck had a primarily anteroposterior direction.

Taking both of these factors into consideration, this suggests that (assuming the general concepts underlying Wolff's law (Ruff, Holt and Trinkaus, 2006)) hip muscle loading might be influential in defining principal trabecular directions in this region of the ageing proximal femur, or equivalently, that trabecular architecture in this region is arranged in such a way as to be strong in the principal direction of loading from muscle forces in this region. Perhaps with reduced mobility due to ageing (Shergold, Lyons and Hubers, 2015), although joint loading from gait remains the primary driver in the creation and maintenance of trabecular principal directions during bone remodelling, loading from musculature becomes a more significant factor. Future studies exploring the relationship between muscle and joint loading due to gait would help to shed light on whether compressive principal stress directions in this region were indeed a result muscle and joint loading or reflective of some other process such as age-related deterioration of trabecular bone.

#### **6.4.4 Combined Muscle and Impact Simulations**

It was apparent in this study that the addition of muscle forces to FE simulations of sideways falls noticeably altered the VM (figure 6.33) and principal stress distributions (figures 6.35 & 6.36) in the proximal femur compared to simulations that included impact-only forces. When an impact force resulted in the femoral necks of the FE models being subjected to tensile loading in the superior femoral neck and compressive loading in the inferior neck, the effect of muscle forces was to reduce VM and principal stress magnitudes in both the superior and inferior regions and reversed the regions in which compressive and tensile principal stresses occurred. This is likely a result of muscle forces reducing the bending moment caused by the impact force in the femoral neck and might help to mitigate fracture risk if the femoral neck is loaded in such a way during real-world falls (Matheson *et al.*, 1971).

However, such loading configurations were the exception. For most simulations, the femoral necks of all FE models were loaded in the opposite way with tensile stresses present in the

inferior neck and compressive stresses in the superior neck. Despite this, the action of the hip musculature remained the same. Thus, instead of reducing stresses in the femoral neck, muscles acted to increase VM stresses throughout the femoral neck, compressive stresses in the superior/superior-anterior neck and tensile stresses in the inferior neck by contributing to the bending moment caused by the larger impact force (figures 6.33, 6.35 & 6.36). The fact that hip musculature had this effect makes good sense when we consider the evolutionary and functional context of hip musculature (Vaughan, 2003) and the effect it had on the proximal femur in muscle-only simulations. Although bone is stronger in compression than tension (Currey, 2005), as already discussed, the ageing superior femoral neck is characterised by the presence of very thin cortical bone. Consequently, small to moderate increases in stress magnitudes in this area may have a disproportionate effect in increasing the likelihood of hip fracture in older individuals.

With regards to principal compressive stresses, as with muscle-only simulations, there were noticeable, albeit more moderate, changes in compressive principal stress directions when muscle forces were modelled alongside impact forces. Specifically, principal stress directions in the anterior portion of the superior neck for cortical bone and the superior portion of the neck for trabecular bone were more aligned with anteroposterior direction relative to impact-only simulations (figure 6.40).

Given the effect of muscle-only simulations on principal stress directions, this alteration is likely due to the effect of muscle forces. For cortical bone, this modification may enhance risk of fracture because the cortical shell is subject to stresses that are not aligned with its principal *i.e.* strongest direction. Conversely, the opposite may be true for trabecular and its ability to withstand compressive loads is enhanced due to muscle contractile activity during impact from a sideways fall.

Complicating the picture further however is that tensile principal stresses were not aligned with trabecular structures in the inferior femoral neck (figure 6.39). Chapter 4 demonstrated the principal structural trabecular direction as being mainly superior-inferior in direction. Yet tensile principal stresses in this region have a significant anteroposterior component to them. This is an undesirable outcome because trabecular bone is weak in tension (Currey, 2005) and this weakness will be exacerbated further by the poor alignment between principal stress trajectories and trabecular principal architectural directions.

This scenario highlights how the inferior neck could be another critical area for fracture. Supporting this notion are experimental studies showing that the inferior neck often fractures

after initial fracture at the superior surface (de Bakker *et al.*, 2009). It might be that the presence of tensile compressive stresses, acting in a direction different to principal trabecular structural directions contributes to the process of fracture initiation in this region.

One of the main findings in this study – that muscle forces act to increase impact-induced stresses in the superior femoral neck, a critical region for fracture, and thereby increase the likelihood of fracture – is in disagreement with the findings of a relatively recent paper by Choi, Cripton and Robinovitch (2014). Choi, Cripton and Robinovitch (2014) after loading a synthetic femur in mechanical experiments, postulated the hip abductors reduce stresses in the femoral neck and thus reduce the risk of hip fracture. While the present study has addressed some of the limitations of Choi, Cripton and Robinovitch's (2014) study (e.g. more muscles, non-arbitrary muscle forces more appropriate bone material properties were modelled/adopted), further work is clearly needed to understand whether hip musculature may negate or contribute to fracture risk of the femur.

On the basis of their findings, Choi, Cripton and Robinovitch (2014) advised that increased muscle strength would decrease risk of hip fracture and that this should inform future clinical screening, practice and/or decision-making. However, although the present author recognises that increased muscle strength likely leads to a decreased risk of falling and therefore hip fracture (Binda, Culham and Brouwer, 2003; Pijnappels *et al.*, 2008; Maciaszek, 2010; Trombetti *et al.*, 2016), on the basis of the findings in this study, fracture risk would be increased *at the moment of impact* with increased muscle strength. This is a critical distinction. Given the serious consequences of hip fracture to the individual, increased efforts should be made to better define the role of hip musculature in hip fracture risk.

Taken collectively, the findings in the present study on the effect of hip musculature coincident with an impact load from a sideways fall on the biomechanical response of the proximal femur demonstrate the potential importance of hip muscles in the aetiology and likelihood of hip fracture, specifically in relation to fracture of the femoral neck. Future research directed towards the prediction and prevention of hip fracture could therefore take account of this. More specifically, future FEA studies should not only seek to accurately model bone material properties in the proximal femur but should also work towards accurately modelling the loading conditions to which the proximal femur is subjected to during a sideways fall. It has been shown here that hip muscles may increase the likelihood of fracture at impact. Omission of muscle forces in FE research may therefore in part explain discrepancies between real world outcomes and predictive models of hip fracture based on

the finite element method. Their inclusion in future may improve the predictive power of the FE approach for hip fracture.

## **6.5 LIMITATIONS**

### **6.5.1 Experimental Validation**

Perhaps the biggest limitation to this study is the lack of experimental validation of results. Ultimately, FE models only approximate real-world properties and geometries. Yet the results obtained in this study are heavily dependent on the choice of such properties. Relatively complex material properties were incorporated into the FE models and care was taken to accurately represent femoral geometries. Thus, the models constructed in this study represent some of the more sophisticated femoral models developed within the field of FEA of hip fracture and there can be some confidence in the quality of the results obtained.

Additionally, the focus was very much on qualitative stress patterns as opposed to absolute stress magnitudes and outright prediction of bone failure. The issue of validation is therefore negated to some extent because it is more likely that these qualitative patterns would be preserved in an experimental set up than would the observed magnitudes of stress.

Validating the results with an experimental set up would be a worthwhile but considerable challenge. The investment of time and effort would be significant and experimental validation thus fell well outside of the scope of this study. It seems intuitive though that experimental validation of the results gleaned in this study would be a natural next step in exploring the role of hip musculature in fracture and in improving understanding about the underlying, fundamental mechanisms of hip fracture.

### **6.5.2 Cortical Bone Density**

Another important limitation was that it was not possible to calibrate the femoral  $\mu$ CT scans. User-defined values were instead used to define the bone density and thus elastic properties of the cortical shell. The calculated density values fell within density ranges measured experimentally in previous studies and therefore can be considered reasonably accurate. Nonetheless, this approach meant that the properties assigned to each FE model may have

not have accurately reflected the actual density properties of the specimen from which it was derived.

However, by assigning each model with its own distinct density properties based on the relative differences in HU values between the models, there was at least a qualitative representation of the density properties associated with each femur. And again, because the focus of this study was on qualitative patterns of stress, due to the linear elastic nature of these simulations and the linear relationship between density and elastic properties, the observed patterns of stress would likely be preserved, even if real density values had been used.

### **6.5.3 Muscle and Impact Loads**

Conclusions relating to the role of impact and muscle forces in hip fracture heavily depend on the quality of the data derived from MDA simulations. It is difficult to properly quantify the quality of such data and there should therefore be some caution when drawing conclusions from this work. However, the range of impact and muscle forces agree with values calculated in previous research, the action of the hip musculature in FE simulations makes good sense within its evolutionary and functional contexts and the stress patterns observed in the FE models sits well alongside other hip fracture research. Additionally, although a comprehensive set of hip muscles were modelled there were nonetheless still a number missing in FE simulations. Their addition may modify the stress patterns observed for the proximal femur in this chapter. However, given the similarity in the action both missing and modelled muscles have on the femur, perhaps any modifications would involve only changes to the magnitudes rather than to the actual patterns of the stresses observed in this study.

### **6.5.4 Insertion Sites**

There was no standardised protocol to define muscle insertion sites. This was beneficial to an extent because it meant that the individual anatomy of each femur was accounted for and that as a result appropriate insertion sites were defined for each model. This proved to be a better approach than using generalised coordinate data from the literature which invariably led to insertion sites floating somewhere in three-dimensional space as opposed to lying on the surface of the femoral models used.

Despite this, using femoral anatomy to define insertion sites was still a very general approach and clearly subject to user error and interpretation, particularly muscles with large insertion areas. Conversely, this approach may have allowed FE models to capture and account for the naturally variation found in muscle insertion sites between individuals. The fact that the hip musculature behaved similarly across simulations for all femoral models (*i.e.* by abducting and medially rotating the hip) suggests this approach was adequate for the current purposes. Being able to work with combined CT and magnetic resonance imaging (MRI) scans that incorporated subject-specific bone and soft tissue geometry and therefore, well defined insertion sites would provide an excellent solution to this problem.

### **6.5.5 MTU Properties**

Muscle forces were applied through tendons modelled as springs in the FE simulations. These springs were assigned relatively simple linear elastic properties tendons display significant non-linear behaviour. This approach was deemed acceptable due to the linear elastic region tendons display during loading and the relatively small deformations applied to each tendon in the FE simulations. Nonetheless, application of loads to the FE models could be improved in future work by better accounting for the non-linear behaviour of tendons.

## **6.6 CONCLUSION**

It has been possible to create fully orthotropic FEA models of the ageing proximal femur and simulate the combined effect of muscle and impact forces resulting from a sideways fall. This was achieved by developing novel functions and techniques that allowed the integration of data from a number of different methodological approaches.

It has been shown that sideways falls tend to produce the highest VM stress magnitudes in the superior femoral neck and that these stresses are mainly compressive in nature. This is in agreement with previous research and strengthens support for the notion that the superior femoral neck is a critical region for hip fracture during a sideways fall.

Nonetheless, this study has elucidated that there exists a reasonable amount of variation in the impact forces produced by a sideways fall and that opposite stress patterns are sometimes observed in the femur. The presence of tensile stresses in the femoral neck resulting from a

sideways fall may increase the risk of hip fracture as bone is weaker in tension than compression. However, it is unclear whether this reversed pattern of loading in the femoral neck is realistic or more a reflection of MDA simulations in chapter 4 performing poorly.

The addition of hip muscle forces to an impact force significantly alters the stress distributions the proximal femur experiences at the moment of impact. Despite great heterogeneity in hip muscle force production at the moment of impact, their collective action is still consistent in that they produce medial rotation and abduction of the hip. In doing so, they increase VM stress magnitudes and compressive stresses in superior neck, and produce sub-optimal principal stress trajectories. The effect of each and/or all of these is to increase fracture risk.

This effect of the hip musculature makes sense when it is considered within its evolutionary and functional adaptations for bipedal gait. Thus, while the action of the hip muscles is useful for mitigating fracture risk during gait, their cumulative action during a sideways fall may be to increase fracture risk.

FEA studies to date have not considered the potential role of hip musculature in mitigating or increasing hip fracture risk of hip fracture. Future work should either take account of or model hip muscle forces. It is anticipated that doing so would improve the predictive power of the FE method in predicting the incidence or risk of fracture.

## 7 CONCLUDING REMARKS

---

This thesis set out to use computer modelling approaches to explore and predict the effect of sideways fall-related impact and hip muscle forces on stresses in the ageing proximal femur, to aid understanding of why this type of fall confers a high risk of femoral fracture in older people. Essential to achieving this overall aim was being able to quantify trabecular orientations in the ageing proximal femur, sideways fall-related impact and hip muscle forces and femoral stresses due to loading from these impact and hip muscle forces. Three independent but complimentary computational methods were used to accomplish this.

First, trabecular orientations were mapped and defined in multiple ageing proximal femur (chapter 4) using  $\mu$ CT scanning (chapter 4). Second MDA was used to quantify a plausible and potential range of impact and hip muscle forces that occur during sideways falls (chapter 5). Finally, chapter 6 incorporated  $\mu$ CT data from chapter 4 to construct fully orthotropic models of the ageing proximal femur and data from chapter 5 to define appropriate boundary conditions, *i.e.* impact and muscle forces, for subsequent FE simulations of sideways falls.

In doing so, these chapters elucidated a number of trends:

Chapter 4:

- Trabecular orientations display a good degree of inter-subject variability for head and neck regions of the ageing proximal femur.

Chapter 5:

- Sideways falls may be associated with a heterogeneous range of impact and, in particular, hip muscle forces.

Chapter 6:

- That a sideways fall on to the hip generally subjects the superior femoral neck (subject to some variation in whether there was also an anterior or posterior component to this region) to high VM and compressive stresses relative to other regions of the proximal femur.
- That hip muscle forces occurring concurrently with a sideways fall impact force may exacerbate the risk of femoral neck fracture in three ways by:

- i) Increasing the (mainly compressive) stress magnitudes in the superior femoral neck caused by sideways fall impact forces and,
  - ii) Modifying compressive principal stress trajectories such that they are not optimally aligned with the assumed principal fabric directions of cortical bone.
  - iii) Modifying tensile principal stress trajectories such that they are not aligned with the assumed principal fabric directions of trabecular bone in the inferior femoral neck.
- 2) That fracture risk may be mitigated to some extent in the trabecular region of the superior femoral neck because hip muscle forces modify principal stress trajectories such that they are more aligned with the principal trabecular fabric direction.

However, the strength of these conclusions and, in particular, their relevance and implications for hip fracture rests on the strength of the data obtained in chapters 4 to 6. The  $\mu$ CT study of trabecular orientations is primarily limited by the small sample size used ( $n = 5$ ) and the voxel size used to derive microstructural data.

While there was a high degree of similarity found for principal trabecular orientations between ageing femoral specimens for the head and neck regions, the small sample size means that the trends found for principal trabecular orientation in this study may not be indicative of those that occur in older populations and more variation might exist in reality. This has significance for the conclusions drawn in chapter 6 whereby it was posited that principal stresses and principal trabecular orientations were sub-optimally aligned and this might contribute to a heightened risk of fracture. While this was true for most femoral specimens in this study, with a larger sample size, this trend might be less emphatically observed.

$\mu$ CT voxel sizes may have led to underestimation of BV/TV and affected anisotropy measures which will have impacted on FE model performance and comparisons made between principal stress trajectories and principal trabecular orientations in chapter 6. But given the focus was on analysing and modelling whole femoral specimens, the voxel size was at the limit of what was possible at the time and still represented an improvement previous work conducted with decreased resolutions (Joshua A. MacNeil and Boyd, 2007; Enns-Bray *et al.*, 2014; Synek *et al.*, 2015).

The MDA study of sideways falls in chapter 5 was limited by multiple factors including the use of a young subject for kinematic recordings, the subject's fall strategy, the fact the fall was self-initiated as opposed to accidental and that only a small number of falls and simulations

used. The presence of these will likely have had a pronounced effect on the validity of the MDA-derived impact and hip muscle force data which in turn decreases confidence in the results obtained using FEA in chapter and ultimately confidence in the answers provided in answering the over-arching questions of this thesis.

The use of a young subject and self-initiated falls likely influence both the fall strategy used by and fall kinematics of the subject and may not be indicative of either real-life falls and real-life falls in older people (Feldman and Robinovitch, 2007). Because the behaviour of the MDA model was essentially driven by the subject's real work falls, the impact and muscle forces predicted in MDA simulations to are likely to be influenced by the subjects age and the fact the fall was self-initiated. This, in combination with the fact that the model was not subject-specific and did not specifically approximate elderly musculoskeletal parameters, means it is possible that the impact and muscle forces obtained may not representative of those that occur in the elderly.

Additionally, the limited number of recorded real-world falls and simulations makes it unclear how representative the data derived in this study is of that which occurs in reality. Although the heterogeneous nature of data and inconsistent statistical relationships may in part reflect real-world biological redundancy in muscle activations (Valero-Cuevas *et al.*, 2015), it is also likely a consequence of the small number of simulations and falls modelled. The small number may have led to poor convergence on optimal solutions, i.e. solutions which are likely to occur in the real world, and this is reflected in the heterogeneous nature of the data. As a consequence, some of the force data might be a good approximation of biological reality, but further simulations are required to demonstrate increased convergence around these solutions and increase confidence in these results.

The limitations in chapter 5 combine to decrease overall confidence in MDA results and as a result, those derived in FEA simulations in chapter 6 too. This is especially true when considering the FEA methodology was also subject to some further limitations. Most significantly cortical density properties were essentially idealised but other limitations that affected the quality of results included simplified muscle properties and the exclusion of contact forces at the femoral head.

Despite these limitations and the heterogeneity of MDA data, results from FEA simulations were surprisingly consistent. In particular, muscle forces appeared to have largely the same effect on the femur across simulations which may be largely attributed to their similar lines of action and biomechanical action on the femur. The overall effect of the hip musculature in

FEA simulations was to abduct the femur and increase stresses in the superior femoral neck which is in agreement with previous findings (Matheson *et al.*, 1971; Krebs *et al.*, 1998; Dalla Pria Bankoff, 2012). Although it is not possible to say that the contractile activity of the hip musculature was accurate, perhaps this study was able to capture, at a very general level, the type of biomechanical effect hip muscles might be expected to have on the femur during a sideways fall impact.

As has been highlighted in this thesis, hip fractures are an increasing socioeconomic burden (Cooper, Campion and Melton, 1992; Cooper *et al.*, 1993; Gullberg, Johnell and Kanis, 1997; Magaziner *et al.*, 1997; Leibson *et al.*, 2002; Haentjens *et al.*, 2010; Svedbom *et al.*, 2013). Most hip fractures do not occur without an accompanying fall (Greenspan *et al.*, 1994; Hayes *et al.*, 1996; Jarvinen *et al.*, 2008), with sideways falls conferring a high risk of fracture (Kannus *et al.*, 2006). Therefore, this study set out to find out why and how sideways fall contribute to fracture risk in the hope of contributing to predictive models of femoral fracture. It shed light on this issue by elucidating how concurrent sideways fall impact forces and hip muscle contractile activity might lead to heightened risk at impact. The results from this study hint that a) hip muscles in FEA simulations of fall-related hip fracture should be included because they could improve its predictive capacity and b) hip musculature may have a role to play in fall-related fracture risk.

However, given the limitations associated with this study and especially those associated with chapter 5, the predictive capacity of this thesis is somewhat compromised. This problem is exacerbated by the inconsistency between FEA obtained here and those obtained in the only other paper exploring hip muscle forces concurrent with impact forces (Choi, Cripton and Robinovitch, 2014). More work is clearly needed in this area to improve the accuracy of fall-related forces (especially internal mechanical loads) and ultimately transform them from exploratory to predictive and clinically relevant.

The lack of confidence in the results of this study diminishes the strength of subsequent conclusions and clinical applications. Instead of being considered predictive in nature and showing, for example, that sideways falls internal and external mechanical loads increase fracture risk, the results in this thesis perhaps act as more of an exploratory analysis demonstrating instead, that sideways falls impact and hip muscle forces *might* cause an increased risk of fracture in the femoral neck.

Further work is needed to prove or disprove this proposition. In this way, although the work presented here falls short of initial expectations, its contribution can still be considered

important in the sense that it questions current hip fracture based FEA methodologies, contributes to current knowledge about the potential mechanisms of hip fracture and hopefully, will drive future interest and work in this area.

In this regard, it is recommended that future research, including but certainly not limited to FEA, seeking to understand and predict hip fracture should seek to take account of the potential role of hip musculature in contributing to hip fracture risk. First however, there should be a concerted effort to improve on the work done here and future studies should endeavour to quantify and more accurately predict the range of impact and hip muscle forces associated with sideways falls.

With improved understanding of these, it is anticipated that computer simulation approaches to hip fracture would demonstrate a greater clinical relevance and predictive capacity and eventually inform rehabilitative, preventative and other treatment programs designed to target hip fracture patients or at-risk individuals; something the current work fell short of.

More generally, this thesis developed a methodological framework that permitted the flow of data between independent computational approaches. For example, through the development of novel scripts, it was possible to incorporate orthotropic fabric directions of trabecular bone, determined using the MIL technique in chapter 3, into FE models in chapter 5. Furthermore, not only was it possible to model impact and muscle forces derived in chapter 4 in FE simulations in chapter 5, muscle forces were applied to FE models via 'tendons' (spring elements) whose mechanical behaviour was approximated utilising MTU parameters specific to the musculoskeletal model from which those forces were derived.

Multidisciplinary approaches in biomedical research, and science more generally, are increasingly recognised as important due to the wealth of data and alternative perspectives they provide. By establishing a methodology that facilitates the integration of data from independent computational methods this thesis has, to an extent, taken a multidisciplinary, multiscale modelling approach. This is perhaps one of the more appealing aspects of this thesis; not only has it demonstrated that broadening the traditional FEA methodology used to study hip fracture can yield new and potentially significant results but it has also established exact ways in which this can be achieved.

By employing a similar methodological framework to incorporate data from the computational approaches used in this study or by developing new and better methodological

frameworks that integrate data from other approaches not considered in this study, FEA's ability to predict hip fracture may be improved.

## REFERENCES

---

- Aagaard, P. *et al.* (2001) 'A mechanism for increased contractile strength of human pennate muscle in response to strength training: Changes in muscle architecture', *Journal of Physiology*, 534(2), pp. 613–623. doi: 10.1111/j.1469-7793.2001.t01-1-00613.x.
- Aagard, P. and Andersen, J. L. (1998) 'Correlation between contractile strength and myosin heavy chain isoform composition in human skeletal muscle', *Medicine & Science in Sports & Exercise*, 30, pp. 1217–1222. doi: 10.1097/00005768-199808000-00006.
- Alamdari, A. and Krovi, V. N. (2016) 'A Review of Computational Musculoskeletal Analysis of Human Lower Extremities', *Human Modeling for Bio-inspired Robotics: Mechanical Engineering in Assistive Technologies*, Elsevier, pp. 1–29. doi: <http://dx.doi.org/10.1016/B978-0-12-803137-7.00003-3>.
- Alamgir, H., Muazzam, S. and Nasrullah, M. (2012) 'Unintentional falls mortality among elderly in the United States: Time for action', *Injury*. Elsevier Ltd, 43(12), pp. 2065–2071. doi: 10.1016/j.injury.2011.12.001.
- Ammann, P. and Rizzoli, R. (2003) 'Bone strength and its determinants', *Osteoporosis International*, 14(S3), pp. 13–18. doi: 10.1007/s00198-002-1345-4.
- Ashman, R. B. *et al.* (1984) 'A continuous wave technique for the measurement of the elastic properties of cortical bone', *Journal of Biomechanics*, 17(5), pp. 349–361. doi: 10.1016/0021-9290(84)90029-0.
- Autier, P. *et al.* (2000) 'Costs induced by hip fractures: a prospective controlled study in Belgium. Belgian Hip Fracture Study Group.', *Osteoporosis International*, 11(5), pp. 373–80. Available at: <http://www.ncbi.nlm.nih.gov/pubmed/10912837>.
- Baca, V. *et al.* (2008) 'Comparison of an inhomogeneous orthotropic and isotropic material models used for FE analyses', *Medical Engineering and Physics*, 30(7), pp. 924–930. doi: 10.1016/j.medengphy.2007.12.009.
- de Bakker, P. M. *et al.* (2009) 'During sideways falls proximal femur fractures initiate in the superolateral cortex: Evidence from high-speed video of simulated fractures', *Journal of Biomechanics*. Elsevier, 42(12), pp. 1917–1925. doi: 10.1016/j.jbiomech.2009.05.001.
- Barrett, R. S., Besier, T. F. and Lloyd, D. G. (2007) 'Individual muscle contributions to the swing phase of gait: An EMG-based forward dynamics modelling approach', *Simulation Modelling Practice and Theory*, 15(9), pp. 1146–1155. doi: 10.1016/j.simpat.2007.07.005.
- Basmajian, J. V and De Luca, C. J. (1985) *Muscles alive*, Williams and Wilkins. Available at: <http://rheumatology.oxfordjournals.org/content/7/4/local/back-matter.pdf>.
- Becker, S. and Ogon, M. (2008) 'Epidemiology of osteoporosis', *Balloon Kyphoplasty*. Elsevier Ltd, 22(5), pp. 1–3. doi: 10.1007/978-3-211-74221-1\_1.
- Bensamoun, S. *et al.* (2004) 'Spatial distribution of acoustic and elastic properties of human femoral cortical bone.', *Journal of biomechanics*, 37(4), pp. 503–510. doi: 10.1016/j.jbiomech.2003.09.013.
- Bessho, M. *et al.* (2009) 'Prediction of proximal femur strength using a CT-based nonlinear finite element method: Differences in predicted fracture load and site with changing load and boundary conditions', *Bone*, 45(2), pp. 226–231. doi: 10.1016/j.bone.2009.04.241.

- Binda, S. M., Culham, E. G. and Brouwer, B. (2003) 'Balance, muscle strength, and fear of falling in older adults', *Experimental Aging Research*, 29(2), pp. 205–219. doi: 10.1080/03610730303711.
- Bisdorff, A. R. *et al.* (1999) 'EMG responses to free fall in elderly subjects and akinetic rigid patients.', *Journal of neurology, neurosurgery, and psychiatry*, 66(4), pp. 447–55. doi: 10.1136/jnnp.66.4.447.
- Bouxein, M. L. and Seeman, E. (2009) 'Quantifying the material and structural determinants of bone strength', *Best Practice and Research: Clinical Rheumatology*, pp. 741–753. doi: 10.1016/j.berh.2009.09.008.
- Brand, P. W., Beach, R. B. and Thompson, D. E. (1981) 'Relative tension and potential excursion of muscles in the forearm and hand', *Journal of Hand Surgery*, 6(3), pp. 209–219. doi: 10.1016/S0363-5023(81)80072-X.
- Carter, D. R., Orr, T. E. and Fyhrie, D. P. (1989) 'Relationships between loading history and femoral cancellous bone architecture', *Journal of Biomechanics*, 22(3), pp. 231–244. doi: 10.1016/0021-9290(89)90091-2.
- Cauley, J. A. *et al.* (2009) 'Risk factors for severity and type of the hip fracture.', *Journal of bone and mineral research : the official journal of the American Society for Bone and Mineral Research*, 24(5), pp. 943–55. doi: 10.1359/jbmr.081246.
- Center, J. R. *et al.* (1999) 'Mortality after all major types of osteoporotic fracture in men and women: An observational study', *Lancet*, 353(9156), pp. 878–882. doi: 10.1016/S0140-6736(98)09075-8.
- Center for Disease Control (2015) *Falls Among Older Adults: An Overview*, [www.cdc.gov](http://www.cdc.gov). Available at: <http://www.cdc.gov/homeandrecreationalsafety/falls/adultfalls.html>.
- Chang, P. C. *et al.* (2013) 'A comparison of the thresholding strategies of micro-CT for periodontal bone loss: A pilot study', *Dentomaxillofacial Radiology*, 42(2). doi: 10.1259/dmfr/66925194.
- Chen, H. *et al.* (2008) 'Regional variations of vertebral trabecular bone microstructure with age and gender', *Osteoporosis International*, 19(10), pp. 1473–1483. doi: 10.1007/s00198-008-0593-3.
- Chen, H. *et al.* (2010) 'Age- And gender-dependent changes in three-dimensional microstructure of cortical and trabecular bone at the human femoral neck', *Osteoporosis International*, 21(4), pp. 627–636. doi: 10.1007/s00198-009-0993-z.
- Chen, H. *et al.* (2013) 'Age-related changes in trabecular and cortical bone microstructure', *International Journal of Endocrinology*. doi: 10.1155/2013/213234.
- Chen, H. *et al.* (2013) 'Age-related changes in trabecular and cortical bone microstructure', *International Journal of Endocrinology*, 2013, p. 213234. doi: 10.1155/2013/213234.
- Chiba, K. *et al.* (2013) 'Heterogeneity of bone microstructure in the femoral head in patients with osteoporosis: An ex vivo HR-pQCT study', *Bone*, 56(1), pp. 139–146. doi: 10.1016/j.bone.2013.05.019.
- Choi, W. J., Cripton, P. A. and Robinovitch, S. N. (2014) 'Effects of hip abductor muscle forces and knee boundary conditions on femoral neck stresses during simulated falls', *Osteoporosis International*, 26(1), pp. 291–301. doi: 10.1007/s00198-014-2812-4.
- Ciarelli, M. J. *et al.* (1991) 'Evaluation of orthogonal mechanical properties and density of

- human trabecular bone from the major metaphyseal regions with materials testing and computed tomography', *Journal of Orthopaedic Research*, 9(5), pp. 674–682. doi: 10.1002/jor.1100090507.
- Ciarelli, T. E. *et al.* (2000) 'Variations in three-dimensional cancellous bone architecture of the proximal femur in female hip fractures and in controls.', *Journal of Bone and Mineral Research*, 15(1), pp. 32–40. doi: 10.1359/jbmr.2000.15.1.32.
- Clamann, H. P. (1993) 'Motor unit recruitment and the gradation of muscle force.', *Physical therapy*, 73(12), pp. 830–43. doi: 10.1073/pnas.0703993104.
- Cody, D. D. *et al.* (1999) 'Femoral strength is better predicted by finite element models than QCT and DXA', *Journal of Biomechanics*, 32(10), pp. 1013–1020. doi: 10.1016/S0021-9290(99)00099-8.
- Cooper, C. *et al.* (1993) 'Population-based study of survival after osteoporotic fractures.', *American journal of epidemiology*, 137(9), pp. 1001–1005. Available at: <http://aje.oxfordjournals.org/content/137/9/1001.short%5Cnpapers3://publication/uuid/4ADDE0D8-41BB-4C5C-A9CB-AC74E1CF0AD>.
- Cooper, C., Campion, G. and Melton, L. J. (1992) 'Hip fractures in the elderly: A world-wide projection', *Osteoporosis International*, 2(6), pp. 285–289. doi: 10.1007/BF01623184.
- Cowin, S. C. (1985) 'The relationship between the elasticity tensor and the fabric tensor', *Mechanics of Materials*, 4(2), pp. 137–147. doi: 10.1016/0167-6636(85)90012-2.
- Cowin, S. C. and Mehrabadi, M. M. (1989) 'Identification of the elastic symmetry of bone and other materials', *Journal of Biomechanics*, 22(6–7), pp. 503–515. doi: 10.1016/0021-9290(89)90001-8.
- Cowin, S. and Telega, J. (2003) 'Bone Mechanics Handbook, 2nd Edition. -', *Applied Mechanics Reviews*, 56(4), p. B61. doi: 10.1115/1.1579463.
- Cramer, J. T. *et al.* (2004) 'Gender, muscle, and velocity comparisons of mechanomyographic and electromyographic responses during isokinetic muscle actions', *Scandinavian Journal of Medicine and Science in Sports*, 14(2), pp. 116–127. doi: 10.1111/j.1600-0838.2003.00317.x.
- Cree, M. *et al.* (2000) 'Mortality and institutionalization following hip fracture.', *Journal of the American Geriatrics Society*, 48(3), pp. 283–8. doi: 10.1111/j.1532-5415.2000.tb02647.x.
- Cress, M. E. *et al.* (1996) 'Functional training: muscle structure, function, and performance in older women.', *The Journal of orthopaedic and sports physical therapy*, 24(1), pp. 4–10. doi: 10.2519/jospt.1996.24.1.4.
- Cristofolini, L. *et al.* (2007) 'In vitro replication of spontaneous fractures of the proximal human femur', *Journal of Biomechanics*, 40(13), pp. 2837–2845. doi: 10.1016/j.jbiomech.2007.03.015.
- Cui, W. Q. *et al.* (2008) 'Age-and region-dependent changes in three-dimensional microstructural properties of proximal femoral trabeculae', *Osteoporosis International*, 19(11), pp. 1579–1587. doi: 10.1007/s00198-008-0601-7.
- Cumming, R. G. (1997) 'Epidemiology of osteoporosis and osteoporotic fractures', in *Australian Prescriber*, pp. 13–17. doi: 10.3803/EnM.2013.28.2.90.
- Cummings, S. R., Bates, D. and Black, D. M. (2002) 'Clinical Use of Bone Densitometry', *JAMA*, 288(15), p. 1889. doi: 10.1001/jama.288.15.1889.

- Cummings, S. R. and Melton, L. J. (2002) 'Osteoporosis I: Epidemiology and outcomes of osteoporotic fractures', *Lancet*, pp. 1761–1767. doi: 10.1016/S0140-6736(02)08657-9.
- Cuppone, M. *et al.* (2004) 'The Longitudinal Young's Modulus of Cortical Bone in the Midshaft of Human Femur and its Correlation with CT Scanning Data', in *Calcified Tissue International*, pp. 302–309. doi: 10.1007/s00223-002-2123-1.
- Currey, J. (2005) 'Structural heterogeneity in bone: Good or bad?', *Journal of Musculoskeletal Neuronal Interactions*, 5(4), p. 317.
- Currey, J. D. (1988) 'The effect of porosity and mineral content on the Young's modulus of elasticity of compact bone', *Journal of Biomechanics*, 21(2), pp. 131–139. doi: 10.1016/0021-9290(88)90006-1.
- Dall'Ara, E. *et al.* (2012) 'QCT-based finite element models predict human vertebral strength in vitro significantly better than simulated DEXA', *Osteoporosis International*, 23(2), pp. 563–572. doi: 10.1007/s00198-011-1568-3.
- Dall'Ara, E. *et al.* (2013a) 'A nonlinear QCT-based finite element model validation study for the human femur tested in two configurations in vitro', *Bone*, 52(1), pp. 27–38. doi: 10.1016/j.bone.2012.09.006.
- Dall'Ara, E. *et al.* (2013b) 'A nonlinear QCT-based finite element model validation study for the human femur tested in two configurations in vitro', *Bone*. Elsevier Inc., 52(1), pp. 27–38. doi: 10.1016/j.bone.2012.09.006.
- Dall'Ara, E., Barber, D. and Viceconti, M. (2014) 'About the inevitable compromise between spatial resolution and accuracy of strain measurement for bone tissue: A 3D zero-strain study', *Journal of Biomechanics*. Elsevier, 47(12), pp. 2956–2963. doi: 10.1016/j.jbiomech.2014.07.019.
- Dalla Pria Bankoff, A. (2012) 'Biomechanical Characteristics of the Bone', *Human Musculoskeletal Biomechanics*, pp. 61–86. doi: 10.1016/S1067-2516(02)80064-3.
- Darnell, G., Mason, S. M. and Snooks, H. (2012) 'Elderly falls: a national survey of UK ambulance services', *Emergency Medicine Journal*, pp. 1009–1010. doi: 10.1136/emered-2011-200419.
- Delp, S. L., Ringwelski, D. A. and Carroll, N. C. (1994) 'Transfer of the rectus femoris: Effects of transfer site on moment arms about the knee and hip', *Journal of Biomechanics*, 27(10), pp. 1201–1211. doi: 10.1016/0021-9290(94)90274-7.
- Djuric, M. *et al.* (2010) 'Region-specific sex-dependent pattern of age-related changes of proximal femoral cancellous bone and its implications on differential bone fragility', *Calcified Tissue International*, 86(3), pp. 192–201. doi: 10.1007/s00223-009-9325-8.
- Doorly, M. C. and Gilchrist, M. D. (2006) 'The use of accident reconstruction for the analysis of traumatic brain injury due to head impacts arising from falls.', *Computer methods in biomechanics and biomedical engineering*, 9(6), pp. 371–377. doi: 10.1080/10255840601003551.
- Doorly, M. C. and Gilchrist, M. D. (2009) 'Three-dimensional multibody dynamics analysis of accidental falls resulting in traumatic brain injury', *International Journal of Crashworthiness*, 14(5), pp. 503–509. doi: 10.1080/13588260902826554.
- Doube, M. *et al.* (2010) 'BoneJ: Free and extensible bone image analysis in ImageJ', *Bone*, 47(6), pp. 1076–1079. doi: 10.1016/j.bone.2010.08.023.

- Drake, R., Vogl, W. and Mitchell, A. (2005) *Gray's Anatomy for Students, 3rd Edition*, Churchill Livingstone. doi: 10.1017/CBO9781107415324.004.
- Duda, G. N. *et al.* (1996) 'Variability of femoral muscle attachments', *Journal of Biomechanics*, 29(9), pp. 1185–1190. doi: 10.1016/0021-9290(96)00025-5.
- Duda, G. N. G. N. *et al.* (1998) 'Influence of muscle forces on femoral strain distribution', *Journal of Biomechanics*, 31(9), pp. 841–846. doi: 10.1016/S0021-9290(98)00080-3.
- Eckstein, F. *et al.* (2007) 'Sex differences of human trabecular bone microstructure in aging are site-dependent.', *Journal of bone and mineral research : the official journal of the American Society for Bone and Mineral Research*, 22(6), pp. 817–824. doi: 10.1359/jbmr.070301.
- Edwards, W. B., Schnitzer, T. J. and Troy, K. L. (2013) 'Torsional stiffness and strength of the proximal tibia are better predicted by finite element models than DXA or QCT', *Journal of Biomechanics*, 46(10), pp. 1655–1662. doi: 10.1016/j.jbiomech.2013.04.016.
- Engelke, K. *et al.* (2013) 'Advanced CT based in vivo methods for the assessment of bone density, structure, and strength', *Current Osteoporosis Reports*, 11(3), pp. 246–255. doi: 10.1007/s11914-013-0147-2.
- Engelke, K., van Rietbergen, B. and Zysset, P. (2016) 'FEA to Measure Bone Strength: A Review', *Clinical Reviews in Bone and Mineral Metabolism*, pp. 26–37. doi: 10.1007/s12018-015-9201-1.
- Enns-Bray, W. S. *et al.* (2014) 'Mapping anisotropy of the proximal femur for enhanced image based finite element analysis', *Journal of Biomechanics*, 47(13), pp. 3272–3278. doi: 10.1016/j.jbiomech.2014.08.020.
- Enns-Bray, W. S. *et al.* (2016) 'Morphology based anisotropic finite element models of the proximal femur validated with experimental data', *Medical Engineering and Physics*, 38(11), pp. 1339–1347. doi: 10.1016/j.medengphy.2016.08.010.
- Evetovich, T. K. *et al.* (1998) 'Gender comparisons of the mechanomyographic responses to maximal concentric and eccentric isokinetic muscle actions.', *Medicine and science in sports and exercise*, 30(12), pp. 1697–702. doi: 10.1097/00005768-199812000-00007.
- Farina, D. (2004) 'The extraction of neural strategies from the surface EMG', *Journal of Applied Physiology*, 96(4), pp. 1486–1495. doi: 10.1152/jappphysiol.01070.2003.
- Feldman, F. and Robinovitch, S. N. (2007) 'Reducing hip fracture risk during sideways falls: Evidence in young adults of the protective effects of impact to the hands and stepping', *Journal of Biomechanics*, 40(12), pp. 2612–2618. doi: 10.1016/j.jbiomech.2007.01.019.
- Fenn, W. O. and Marsh, B. S. (1935) 'Muscular force at different speeds of shortening.', *The Journal of physiology*, 85(3), pp. 277–297. doi: 10.1113/jphysiol.1935.sp003318.
- Fitts, R. H., McDonald, K. S. and Schluter, J. M. (1991) 'The determinants of skeletal muscle force and power: Their adaptability with changes in activity pattern', *Journal of Biomechanics*, pp. 111–122. doi: 10.1016/0021-9290(91)90382-W.
- Ford, C. M. and Keaveny, T. M. (1996) 'The dependence of shear failure properties of trabecular bone on apparent density and trabecular orientation', *Journal of Biomechanics*, 29(10), pp. 1309–1317. doi: 10.1016/0021-9290(96)00062-0.
- Forero Rueda, M. A. and Gilchrist, M. D. (2009) 'Comparative multibody dynamics analysis of falls from playground climbing frames', *Forensic Science International*, 191(1–3), pp. 52–57.

doi: 10.1016/j.forsciint.2009.06.007.

Fung, Y. C. (1993) 'Mechanical Properties of Living Tissues', in *Biomechanics*, p. 568. Available at: <http://www.springer.com/us/book/9780387979472>.

Gandevia, S. C. and McKenzie, D. K. (1988) 'Activation of human muscles at short muscle lengths during maximal static efforts', *Journal of Physiology*, 407, pp. 599–613. doi: 10.1113/jphysiol.1988.sp017434.

Gareis, H. *et al.* (1992) 'The isometric length-force models of nine different skeletal muscles', *Journal of Biomechanics*, 25(8), pp. 903–916. doi: 10.1016/0021-9290(92)90230-X.

Giangregorio, L. M. *et al.* (2012) 'FRAX underestimates fracture risk in patients with diabetes', *Journal of Bone and Mineral Research*, 27(2), pp. 301–308. doi: 10.1002/jbmr.556.

Gogate, Y. and Bhadada, S. K. (2012) 'FRAX: Facts and Fantasy.', *Indian journal of endocrinology and metabolism*, 16(Suppl 2), pp. S224-6. doi: 10.4103/2230-8210.104044.

Goldstein, S. A. *et al.* (1983) 'The mechanical properties of human tibial trabecular bone as a function of metaphyseal location', *Journal of Biomechanics*, 16(12), pp. 965–969. doi: 10.1016/0021-9290(83)90097-0.

Gomez-Benito, M. J., Garcia-Aznar, J. M. and Doblare, M. (2005) 'Finite element prediction of proximal femoral fracture patterns under different loads', *J Biomech Eng*, 127(1), pp. 9–14.

Gong, J. K., Arnold, J. S. and Cohn, S. H. (1964) 'Composition of trabecular and cortical bone', *The Anatomical Record*, 149(3), pp. 325–331. doi: 10.1002/ar.1091490303.

Greenspan, S. L. *et al.* (1994) 'Fall severity and bone mineral density as risk factors for hip fracture in ambulatory elderly.', *JAMA : the journal of the American Medical Association*, 271(2), pp. 128–133. doi: 10.1001/jama.271.2.128.

Grisso, J. A. *et al.* (1991) 'Risk Factors for Falls as a Cause of Hip Fracture in Women', *New England Journal of Medicine*, 324(19), pp. 1326–1331. doi: 10.1056/NEJM199105093241905.

Groen, B. E., Weerdesteyn, V. and Duysens, J. (2007a) 'Martial arts fall techniques decrease the impact forces at the hip during sideways falling', *Journal of Biomechanics*, 40(2), pp. 458–462. doi: 10.1016/j.jbiomech.2005.12.014.

Groen, B. E., Weerdesteyn, V. and Duysens, J. (2007b) 'Martial arts fall techniques decrease the impact forces at the hip during sideways falling', *Journal of Biomechanics*, 40(2), pp. 458–462. doi: 10.1016/j.jbiomech.2005.12.014.

Groen, B. E., Weerdesteyn, V. and Duysens, J. (2008) 'The relation between hip impact velocity and hip impact force differs between sideways fall techniques', *Journal of Electromyography and Kinesiology*, 18(2), pp. 228–234. doi: 10.1016/j.jelekin.2007.06.002.

Gullberg, B., Johnell, O. and Kanis, J. A. (1997) 'World-wide projections for hip fracture', *Osteoporosis International*, 7(5), pp. 407–413. doi: 10.1007/PL00004148.

Haentjens, P. *et al.* (2007) 'Survival and functional outcome according to hip fracture type: A one-year prospective cohort study in elderly women with an intertrochanteric or femoral neck fracture', *Bone*, 41(6), pp. 958–964. doi: 10.1016/j.bone.2007.08.026.

Haentjens, P. *et al.* (2010) 'Meta-analysis: excess mortality after hip fracture among older women and men.', *Annals of internal medicine*, 152(6), pp. 380–390. doi: 10.1059/0003-

4819-152-6-201003160-00008.Meta-analysis.

Hamed, E., Lee, Y. and Jasiuk, I. (2010) 'Multiscale modeling of elastic properties of cortical bone', *Acta Mechanica*, 213(1–2), pp. 131–154. doi: 10.1007/s00707-010-0326-5.

Harrigan, T. P. and Mann, R. W. (1984) 'Characterization of microstructural anisotropy in orthotropic materials using a second rank tensor', *Journal of Materials Science*, 19(3), pp. 761–767. doi: 10.1007/BF00540446.

Hayes, W. C. *et al.* (1996) 'Etiology and prevention of age-related hip fractures', *Bone*, 18(1), pp. S77–S86. doi: 10.1016/8756-3282(95)00383-5.

Hazrati Marangalou, J. *et al.* (2013) 'A novel approach to estimate trabecular bone anisotropy using a database approach', *Journal of Biomechanics*, 46(14), pp. 2356–2362. doi: 10.1016/j.jbiomech.2013.07.042.

Hazrati Marangalou, J., Ito, K. and van Rietbergen, B. (2012) 'A new approach to determine the accuracy of morphology-elasticity relationships in continuum FE analyses of human proximal femur', *Journal of Biomechanics*, 45(16), pp. 2884–2892. doi: 10.1016/j.jbiomech.2012.08.022.

Helgason, B., Taddei, F., *et al.* (2008) 'A modified method for assigning material properties to FE models of bones', *Medical Engineering and Physics*, 30(4), pp. 444–453. doi: 10.1016/j.medengphy.2007.05.006.

Helgason, B., Perilli, E., *et al.* (2008) 'Mathematical relationships between bone density and mechanical properties: A literature review', *Clinical Biomechanics*, pp. 135–146. doi: 10.1016/j.clinbiomech.2007.08.024.

Hernlund, E. *et al.* (2013) 'Osteoporosis in the European Union: medical management, epidemiology and economic burden', *Archives of osteoporosis*, 8(1–2), p. 136. doi: 10.1007/s11657-013-0136-1.

Herzog, W. and Read, L. J. (1993) 'Lines of action and moment arms of the major force-carrying structures crossing the human knee joint.', *Journal of anatomy*, 182 ( Pt 2, pp. 213–30.

Hirabayashi, S. *et al.* (2013) 'Simulation study on mechanisms of hip fractures in backward falls', *Journal of Biomechanical Science and Engineering*, 8(4), pp. 328–343. doi: 10.1299/jbse.8.328.

Hirabayashi, S., Tsuchida, T. and Tanaka, E. (2013) 'Simulation Study on Mechanisms of Hip Fractures in Backward Falls \*', 8(4), pp. 328–343. doi: 10.1299/jbse.8.328.

Hodgkinson, R. and Currey, J. D. (1992) 'Young's modulus, density and material properties in cancellous bone over a large density range', *Journal of Materials Science: Materials in Medicine*, 3(5), pp. 377–381. doi: 10.1007/BF00705371.

Hölzer, A. *et al.* (2013) 'Subject-specific finite element simulation of the human femur considering inhomogeneous material properties: A straightforward method and convergence study', *Computer Methods and Programs in Biomedicine*, 110(1), pp. 82–88. doi: 10.1016/j.cmpb.2012.09.010.

Homminga, J. *et al.* (2002) 'Cancellous bone mechanical properties from normals and patients with hip fractures differ on the structure level, not on the bone hard tissue level', *Bone*, 30(5), pp. 759–764. doi: 10.1016/S8756-3282(02)00693-2.

Horiuchi, T. *et al.* (1988) 'Spontaneous fractures of the hip in the elderly', *Orthopedics*, 11(9),

pp. 1277–1280. Available at:

[http://www.ncbi.nlm.nih.gov/entrez/query.fcgi?cmd=Retrieve&db=PubMed&dopt=Citation&list\\_uids=3174500](http://www.ncbi.nlm.nih.gov/entrez/query.fcgi?cmd=Retrieve&db=PubMed&dopt=Citation&list_uids=3174500).

Hosseini, H. S., Maquer, G. and Zysset, P. K. (2017) 'μCT-based trabecular anisotropy can be reproducibly computed from HR-pQCT scans using the triangulated bone surface', *Bone*, 97, pp. 114–120. doi: 10.1016/j.bone.2017.01.016.

Hudelmaier, M. *et al.* (2004) 'Can geometry-based parameters from pQCT and material parameters from quantitative ultrasound (QUS) improve the prediction of radial bone strength over that by bone mass (DXA)?', *Osteoporosis International*, 15(5), pp. 375–381. doi: 10.1007/s00198-003-1551-8.

Ichinose, Y. *et al.* (1998) 'Relationship between muscle fiber pennation and force generation capability in Olympic athletes.', *International journal of sports medicine*, 19(8), pp. 541–6. doi: 10.1055/s-2007-971957.

ICRP (2007) 'ICRP 103: The 2007 Recommendations of the International Commission on Radiological Protection', *Annals of the ICRP*, 37, p. 330. doi: 10.1016/j.icrp.2007.10.001.

Isaksson, H. *et al.* (2011) 'Structural parameters of normal and osteoporotic human trabecular bone are affected differently by microCT image resolution', *Osteoporosis International*, 22(1), pp. 167–177. doi: 10.1007/s00198-010-1219-0.

Ishikawa, M. (2005) 'Muscle-tendon interaction and elastic energy usage in human walking', *Journal of Applied Physiology*, 99(2), pp. 603–608. doi: 10.1152/jappphysiol.00189.2005.

Ito, M. *et al.* (2011) 'Age-related changes in bone density, geometry and biomechanical properties of the proximal femur: CT-based 3D hip structure analysis in normal postmenopausal women', *Bone*, 48(3), pp. 627–630. doi: 10.1016/j.bone.2010.11.007.

Iwamoto, K. *et al.* (1998) 'Correlation between the values of bone measurements using DXA, QCT and USD methods and the bone strength in calcanei in vivo', *Acta Anatomica Nipponica*, 73, pp. 509–515.

Jarvinen, T. L. N. *et al.* (2008) 'Shifting the focus in fracture prevention from osteoporosis to falls', *Bmj*, 336(7636), pp. 124–126. doi: 10.1136/bmj.39428.470752.AD.

Johannesdottir, F. *et al.* (2011) 'Distribution of cortical bone in the femoral neck and hip fracture: A prospective case-control analysis of 143 incident hip fractures; the AGES-REYKJAVIK Study', *Bone*, 48(6), pp. 1268–1276. doi: 10.1016/j.bone.2011.03.776.

Johnell, O. and Kanis, J. (2005) 'Epidemiology of osteoporotic fractures', in *Osteoporosis International*. doi: 10.1007/s00198-004-1702-6.

Johnell, O. and Kanis, J. A. (2006) 'An estimate of the worldwide prevalence and disability associated with osteoporotic fractures', *Osteoporosis International*, 17(12), pp. 1726–1733. doi: 10.1007/s00198-006-0172-4.

Jokinen, H. *et al.* (2010) 'Risk factors for cervical and trochanteric hip fractures in elderly women: A population-based 10-year follow-up study', *Calcified Tissue International*, 87(1), pp. 44–51. doi: 10.1007/s00223-010-9382-z.

Judex, S. *et al.* (2004) 'Genetically Based Influences on the Site-Specific Regulation of Trabecular and Cortical Bone Morphology', *Journal of Bone and Mineral Research*, 19(4), pp. 600–606. doi: 10.1359/JBMR.040101.

Kabel, J. *et al.* (1999) 'Constitutive relationships of fabric, density, and elastic properties in

- cancellous bone architecture', *Bone*, 25(4), pp. 481–486. doi: 10.1016/S8756-3282(99)00190-8.
- Kalmey, J. K. and Lovejoy, C. O. (2002) 'Collagen fiber orientation in the femoral necks of apes and humans: do their histological structures reflect differences in locomotor loading?', *Bone*, 31(2), pp. 327–332. doi: 10.1016/S8756-3282(02)00828-1.
- Kanehisa, H., Ikegawa, S. and Fukunaga, T. (1997) 'Force-velocity relationships and fatiguability of strength and endurance-trained subjects', *International Journal of Sports Medicine*, 18(2), pp. 106–112. doi: 10.1055/s-2007-972604.
- Kaneko, T. S. *et al.* (2004) 'Mechanical properties, density and quantitative CT scan data of trabecular bone with and without metastases', *Journal of Biomechanics*, 37(4), pp. 523–530. doi: 10.1016/j.jbiomech.2003.08.010.
- Kanis, J. A. *et al.* (2004) 'A meta-analysis of previous fracture and subsequent fracture risk', *Bone*, 35(2), pp. 375–382. doi: 10.1016/j.bone.2004.03.024.
- Kanis, J. A. *et al.* (2007) 'The use of clinical risk factors enhances the performance of BMD in the prediction of hip and osteoporotic fractures in men and women', *Osteoporosis International*, 18(8), pp. 1033–1046. doi: 10.1007/s00198-007-0343-y.
- Kanis, J. A. *et al.* (2008) 'FRAX™ and the assessment of fracture probability in men and women from the UK', *Osteoporosis International*, 19(4), pp. 385–397. doi: 10.1007/s00198-007-0543-5.
- Kanis, J. A. *et al.* (2012) 'FRAX?? with and without bone mineral density', *Calcified Tissue International*, pp. 1–13. doi: 10.1007/s00223-011-9544-7.
- Kanis JA on behalf of the World Health Organization Scientific Group (2007) *Assessment of osteoporosis at the primary health-care level., Technical Report. World Health Organization Collaborating Centre for Metabolic Bone Diseases.* Available at: [http://www.sheffield.ac.uk/FRAX/pdfs/WHO\\_Technical\\_Report.pdf](http://www.sheffield.ac.uk/FRAX/pdfs/WHO_Technical_Report.pdf).
- Kannus, P. *et al.* (2005) 'Secular trends in rates of unintentional injury deaths among adult Finns', *Injury*, 36(11), pp. 1273–1276. doi: 10.1016/j.injury.2005.07.011.
- Kannus, P. *et al.* (2006) 'A sideways fall and hip fracture', *Bone*, 39(2), pp. 383–384. doi: 10.1016/j.bone.2006.01.148.
- Kannus, P. and Parkkari, J. (2006) 'Prevention of hip fracture with hip protectors', in *Age and Ageing*. doi: 10.1093/ageing/afl087.
- Kawashima, T. and Uthoff, H. K. (1991) 'Pattern of bone loss of the proximal femur: A radiologic, densitometric, and histomorphometric study', *Journal of Orthopaedic Research*, 9(5), pp. 634–640. doi: 10.1002/jor.1100090503.
- Kazama, J. J. *et al.* (2010) 'Cancellous bone volume is an indicator for trabecular bone connectivity in dialysis patients', *Clinical Journal of the American Society of Nephrology*, 5(2), pp. 292–298. doi: 10.2215/CJN.04150609.
- Keaveny, T. M. *et al.* (1994) 'Differences between the tensile and compressive strengths of bovine tibial trabecular bone depend on modulus', *Journal of Biomechanics*, 27(9), pp. 1137–1146. doi: 10.1016/0021-9290(94)90054-X.
- Keaveny, T. M. *et al.* (2001) 'Biomechanics of Trabecular Bone', *Annual Review of Biomedical Engineering*, 3(1), pp. 307–333. doi: 10.1146/annurev.bioeng.3.1.307.

- Keaveny, T. M., Morgan, E. F. and Yeh, O. C. (2004) 'Bone Mechanics', *Standard Handbook of Biomedical Engineering and Design*, p. 8.1-8.23. doi: 10.1385/1-59259-366-6:369.
- Kersh, M. E. *et al.* (2013) 'Measurement of structural anisotropy in femoral trabecular bone using clinical-resolution CT images', *Journal of Biomechanics*, 46(15), pp. 2659–2666. doi: 10.1016/j.jbiomech.2013.07.047.
- Keyak, J. H., Lee, I. Y. and Skinner, H. B. (1994) 'Correlations between orthogonal mechanical properties and density of trabecular bone: Use of different densitometric measures', *Journal of Biomedical Materials Research*, 28(11), pp. 1329–1336. doi: 10.1002/jbm.820281111.
- Keyak, J. H., Skinner, H. B. and Fleming, J. A. (2001) 'Effect of force direction on femoral fracture load for two types of loading conditions', *Journal of Orthopaedic Research*, 19(4), pp. 539–544. doi: 10.1016/S0736-0266(00)00046-2.
- Kiebzak, G. M. *et al.* (2002) 'Undertreatment of Osteoporosis in Men With Hip Fracture', *Arch Intern Med*, 162(19), pp. 2217–2222. doi: 10.1001/archinte.162.19.2217.
- Kim, D. G. *et al.* (2004) 'The effect of microcomputed tomography scanning and reconstruction voxel size on the accuracy of stereological measurements in human cancellous bone', *Bone*, 35(6), pp. 1375–1382. doi: 10.1016/j.bone.2004.09.007.
- Klein Horsman, M. D. *et al.* (2007) 'Morphological muscle and joint parameters for musculoskeletal modelling of the lower extremity', *Clinical Biomechanics*, 22(2), pp. 239–247. doi: 10.1016/j.clinbiomech.2006.10.003.
- Klint, R. *et al.* (2008) 'Within-step modulation of leg muscle activity by afferent feedback in human walking', *The Journal of Physiology*, 586(19), pp. 4643–4648. doi: 10.1113/jphysiol.2008.155002.
- Kłodowski, A., Valkeapää, A. and Mikkola, A. (2012) 'Pilot study on proximal femur strains during locomotion and fall-down scenario', pp. 239–256. doi: 10.1007/s11044-012-9312-0.
- Knapik, J. J. *et al.* (1983) 'Isokinetic, isometric and isotonic strength relationships', *Archives of physical medicine and rehabilitation*, 64(2), pp. 77–80.
- Koh, T. J. and Herzog, W. (1998) 'Increasing the moment arm of the tibialis anterior induces structural and functional adaptation: Implications for tendon transfer', *Journal of Biomechanics*, 31(7), pp. 593–599. doi: 10.1016/S0021-9290(98)00052-9.
- Koivumäki, J. E. M. *et al.* (2012) 'Cortical bone finite element models in the estimation of experimentally measured failure loads in the proximal femur', *Bone*, 51(4), pp. 737–740. doi: 10.1016/j.bone.2012.06.026.
- Koivumäki, J. E. M. *et al.* (2012) 'Ct-based finite element models can be used to estimate experimentally measured failure loads in the proximal femur', *Bone*, 50(4), pp. 824–829. doi: 10.1016/j.bone.2012.01.012.
- Komi, P. . (1973) 'Relationship between muscle tension, EMG, and velocity of contraction under concentric and eccentric work', *New Developments in Electromyography and Clinical Neurophysiology*, 1, pp. 596–606. doi: 10.1017/CBO9781107415324.004.
- Konrad, P. (2005) 'The abc of emg', *A practical introduction to kinesiological ...*, (April), pp. 1–60. doi: 10.1016/j.jacc.2008.05.066.
- Kopperdahl, D. L. *et al.* (2014) 'Assessment of incident spine and hip fractures in women and men using finite element analysis of CT scans', *Journal of Bone and Mineral Research*, 29(3), pp. 570–580. doi: 10.1002/jbmr.2069.

- Krause, M. *et al.* (2014) 'Accuracy of trabecular structure by HR-pQCT compared to gold standard  $\mu$ CT in the radius and tibia of patients with osteoporosis and long-term bisphosphonate therapy', *Osteoporosis International*, 25(5), pp. 1595–1606. doi: 10.1007/s00198-014-2650-4.
- Krčah, M., Székely, G. and Blanc, R. (2011) 'Fully automatic and fast segmentation of the femur bone from 3D-CT images with no shape prior', in *Proceedings - International Symposium on Biomedical Imaging*, pp. 2087–2090. doi: 10.1109/ISBI.2011.5872823.
- Krebs, D. E. *et al.* (1998) 'Hip biomechanics during gait.', *The Journal of orthopaedic and sports physical therapy*, 28(1), pp. 51–59. doi: 10.2519/jospt.1998.28.1.51.
- van den Kroonenberg, A. J., Hayes, W. C. and McMahon, T. A. (1995) 'Dynamic models for sideways falls from standing height', *Journal of Biomechanical Engineering*, 117(3), pp. 309–318. doi: 10.1115/1.2794186.
- Van Den Kroonenberg, A. J., Hayes, W. C. and McMahon, T. A. (1996) 'Hip impact velocities and body configurations for voluntary falls from standing height', *Journal of Biomechanics*, 29(6), pp. 807–811. doi: 10.1016/0021-9290(95)00134-4.
- Langton, C. M., Pisharody, S. and Keyak, J. H. (2009) 'Comparison of 3D finite element analysis derived stiffness and BMD to determine the failure load of the excised proximal femur', *Medical Engineering and Physics*, 31(6), pp. 668–672. doi: 10.1016/j.medengphy.2008.12.007.
- Larsson, D. *et al.* (2014) 'Assessment of Transverse Isotropy in Clinical-Level CT Images of Trabecular Bone Using the Gradient Structure Tensor', *Annals of Biomedical Engineering*, 42(5), pp. 950–959. doi: 10.1007/s10439-014-0983-y.
- Lawrence Katz, J. *et al.* (1984) 'The effects of remodeling on the elastic properties of bone', *Calcified Tissue International*, 36(1 Supplement). doi: 10.1007/BF02406131.
- Lazenby, R. A. *et al.* (2008) 'A three-dimensional microcomputed tomographic study of site-specific variation in trabecular microarchitecture in the human second metacarpal', *Journal of Anatomy*, 213(6), pp. 698–705. doi: 10.1111/j.1469-7580.2008.00991.x.
- Leal, J. *et al.* (2016) 'Impact of hip fracture on hospital care costs: a population-based study.', *Osteoporosis international : a journal established as result of cooperation between the European Foundation for Osteoporosis and the National Osteoporosis Foundation of the USA*, 27(2), pp. 549–58. doi: 10.1007/s00198-015-3277-9.
- Lee, T. *et al.* (2012) 'The susceptibility of the femoral neck to fracture: An assessment incorporating the effects of age-remodeling and stress reduction', *Journal of Biomechanics*. Elsevier, 45(6), pp. 931–937. doi: 10.1016/j.jbiomech.2012.01.021.
- Leibson, C. L. *et al.* (2002) 'Mortality, disability, and nursing home use for persons with and without hip fracture: A population-based study', *Journal of the American Geriatrics Society*, 50(10), pp. 1644–1650. doi: 10.1046/j.1532-5415.2002.50455.x.
- Leone, A. *et al.* (2015) 'A wearable EMG-based system pre-fall detector', in *Procedia Engineering*, pp. 455–458. doi: 10.1016/j.proeng.2015.08.667.
- Lewis, C. L., Sahrman, S. A. and Moran, D. W. (2007) 'Anterior hip joint force increases with hip extension, decreased gluteal force, or decreased iliopsoas force', *Journal of Biomechanics*, 40(16), pp. 3725–3731. doi: 10.1016/j.jbiomech.2007.06.024.
- Li, B. and Aspden, R. M. (1997) 'Composition and mechanical properties of cancellous bone

from the femoral head of patients with osteoporosis or osteoarthritis.', *Journal of bone and mineral research : the official journal of the American Society for Bone and Mineral Research*, 12(4), pp. 641–51. doi: 10.1359/jbmr.1997.12.4.641.

Lichtwark, G. A. and Wilson, A. M. (2006) 'Interactions between the human gastrocnemius muscle and the Achilles tendon during incline, level and decline locomotion', *Journal of Experimental Biology*, 209(21), pp. 4379–4388. doi: 10.1242/jeb.02434.

Liebl, H. *et al.* (2015) 'In-vivo assessment of femoral bone strength using finite element analysis (FEA) based on routine MDCT imaging: A preliminary study on patients with vertebral fractures', *PLoS ONE*, 10(2). doi: 10.1371/journal.pone.0116907.

Lochmüller, E.-M. *et al.* (2003) 'Can Novel Clinical Densitometric Techniques Replace or Improve DXA in Predicting Bone Strength in Osteoporosis at the Hip and Other Skeletal Sites?', *Journal of Bone and Mineral Research*, 18(5), pp. 906–912. doi: 10.1359/jbmr.2003.18.5.906.

Lotz, J. C., Cheal, E. J. and Hayes, W. C. (1995) 'Stress distributions within the proximal femur during gait and falls: Implications for osteoporotic fracture', *Osteoporosis International*, 5(4), pp. 252–261. doi: 10.1007/BF01774015.

Lotz, J. C., Gerhart, T. N. and Hayes, W. C. (1990) 'Mechanical Properties of Trabecular Bone from the Proximal Femur: A Quantitative CT Study', *J Comp assist Tomog*, 14(1), p. 111. doi: 10.1097/00004728-199001000-00020.

Lovejoy, C. O. (2005) 'The natural history of human gait and posture. Part 2. Hip and thigh.', *Gait & posture*, 21(1), pp. 113–124. doi: 10.1016/j.gaitpost.2004.06.010.

Lowenstam, H. A. and Weiner, S. (1989) *On biomineralization*, Oxford University Press. Available at: [http://books.google.gr/books/about/On\\_Biomineralization.html?id=JbAgy0AAopsC&pgis=1](http://books.google.gr/books/about/On_Biomineralization.html?id=JbAgy0AAopsC&pgis=1).

Luisier, B., Dall'Ara, E. and Pahr, D. H. (2014) 'Orthotropic HR-pQCT-based FE models improve strength predictions for stance but not for side-way fall loading compared to isotropic QCT-based FE models of human femurs', *Journal of the Mechanical Behavior of Biomedical Materials*. Elsevier, 32, pp. 287–299. doi: 10.1016/j.jmbbm.2014.01.006.

Lundeen, G. A., Vajda, E. G. and Bloebaum, R. D. (2000) 'Age-related cancellous bone loss in the proximal femur of Caucasian females', *Osteoporosis International*, 11(6), pp. 505–511. doi: 10.1007/s001980070093.

Luo, Y. H. *et al.* (2013) 'A Subject-Specific Dynamics Model for Predicting Impact Force in Elderly Lateral Fall', *Applied Mechanics and Materials*, 446–447, pp. 339–343. doi: 10.4028/www.scientific.net/AMM.446-447.339.

Maciaszek, J. (2010) 'Muscle Strength and Aerobic Endurance as Factors Differentiating Falling and Non-Falling Men over 70 Years', *Journal of Human Kinetics*, 25(June), pp. 35–40. doi: 10.2478/v10078-010-0029-y.

MacNeil, J. A. and Boyd, S. K. (2007) 'Accuracy of high-resolution peripheral quantitative computed tomography for measurement of bone quality', *Medical Engineering & Physics*, 29(10), pp. 1096–1105. doi: 10.1016/j.medengphy.2006.11.002.

MacNeil, J. A. and Boyd, S. K. (2007) 'Accuracy of high-resolution peripheral quantitative computed tomography for measurement of bone quality.', *Medical engineering & physics*, 29(10), pp. 1096–1105. doi: 10.1016/j.medengphy.2006.11.002.

- Magaziner, J. *et al.* (1990) 'Predictors of functional recovery one year following hospital discharge for hip fracture: a prospective study.', *Journal of gerontology*, 45(3), pp. M101-7. doi: 10.1093/geronj/45.3.M101.
- Magaziner, J. *et al.* (1997) 'Excess mortality attributable to hip fracture in white women aged 70 years and older.', *American journal of public health*, 87(10), pp. 1630–6. doi: 10.2105/AJPH.87.10.1630.
- Majumder, S., Roychowdhury, A. and Pal, S. (2007) 'Simulation of hip fracture in sideways fall using a 3D finite element model of pelvis-femur-soft tissue complex with simplified representation of whole body', *Medical Engineering and Physics*, 29(10), pp. 1167–1178. doi: 10.1016/j.medengphy.2006.11.001.
- Majumder, S., Roychowdhury, A. and Pal, S. (2008) 'Effects of trochanteric soft tissue thickness and hip impact velocity on hip fracture in sideways fall through 3D finite element simulations', *Journal of Biomechanics*, 41(13), pp. 2834–2842. doi: 10.1016/j.jbiomech.2008.07.001.
- Malo, M. K. H. *et al.* (2013) 'Longitudinal elastic properties and porosity of cortical bone tissue vary with age in human proximal femur', *Bone*. Elsevier Inc., 53(2), pp. 451–458. doi: 10.1016/j.bone.2013.01.015.
- Maquer, G. *et al.* (2015) 'Bone volume fraction and fabric anisotropy are better determinants of trabecular bone stiffness than other morphological variables', *Journal of Bone and Mineral Research*, 30(6), pp. 1000–1008. doi: 10.1002/jbmr.2437.
- Marks, R. (2010) 'Hip fracture epidemiological trends, outcomes, and risk factors, 1970-2009', *International Journal of General Medicine*, pp. 1–17. doi: 10.2147/IJGM.S5906.
- Marshall, R. N., Mazur, S. M. and Taylor, N. A. S. (1990) 'Three-dimensional surfaces for human muscle kinetics', *European Journal of Applied Physiology and Occupational Physiology*, 61(3–4), pp. 263–270. doi: 10.1007/BF00357610.
- Martin, R. B. and Ishida, J. (1989) 'The relative effects of collagen fiber orientation, porosity, density, and mineralization on bone strength', *Journal of Biomechanics*, 22(5), pp. 419–426. doi: 10.1016/0021-9290(89)90202-9.
- Matheson, G. O. *et al.* (1971) 'Stress fractures in athletes. A study of 320 cases.', *The American journal of sports medicine*, 15(1), pp. 46–58. doi: 10.1177/036354658701500107.
- Mayhew, P. M. *et al.* (2005) 'Relation between age, femoral neck cortical stability, and hip fracture risk', *Lancet*, 366(9480), pp. 129–135. doi: 10.1016/S0140-6736(05)66870-5.
- McCalden, R. W. *et al.* (1993) 'Age-related changes in the tensile properties of cortical bone. The relative importance of changes in porosity, mineralization, and microstructure.', *The Journal of bone and joint surgery. American volume*, 75(8), pp. 1193–205. doi: 10.2106/JBJS.F.00001.
- McCloskey, E. V. *et al.* (2016) 'FRAX updates 2016', *Current Opinion in Rheumatology*, 28(4), pp. 433–441. doi: 10.1097/BOR.0000000000000304.
- Mendis, M. D. *et al.* (2014) 'Hip flexor muscle size, strength and recruitment pattern in patients with acetabular labral tears compared to healthy controls', *Manual Therapy*. Elsevier Ltd, 19(5), pp. 405–410. doi: 10.1016/j.math.2014.02.006.
- Millard, M., Kubica, E. and McPhee, J. (2011) 'Forward dynamic human gait simulation using a SLIP target model', in *Procedia IUTAM*, pp. 142–157. doi: 10.1016/j.piutam.2011.04.015.

- Miller, M. *et al.* (2006) 'Voluntary activation and central activation failure in the knee extensors in young women and men', *Scandinavian Journal of Medicine and Science in Sports*, 16(4), pp. 274–281. doi: 10.1111/j.1600-0838.2005.00479.x.
- Milovanovic, P., Potocnik, J., *et al.* (2012) 'Age-related deterioration in trabecular bone mechanical properties at material level: Nanoindentation study of the femoral neck in women by using AFM', *Experimental Gerontology*. Elsevier Inc., 47(2), pp. 154–159. doi: 10.1016/j.exger.2011.11.011.
- Milovanovic, P., Djonic, D., *et al.* (2012) 'Micro-structural basis for particular vulnerability of the superolateral neck trabecular bone in the postmenopausal women with hip fractures', *Bone*, 50(1), pp. 63–68. doi: 10.1016/j.bone.2011.09.044.
- Morcelli, M. H. *et al.* (2014) 'Hip muscles strength and activation in older fallers and non-fallers', *Isokinetics and Exercise Science*, 22(3), pp. 191–196. doi: 10.3233/IES-140538.
- Moreno, R., Borga, M. and Smedby, O. (2012) 'Generalizing the mean intercept length tensor for gray-level images', *Medical Physics*, 39(7), p. 4599. doi: 10.1118/1.4730502.
- Moreno, R., Borga, M. and Smedby, Ö. (2012a) 'Evaluation of the plate-rod model assumption of trabecular bone', in *Proceedings - International Symposium on Biomedical Imaging*, pp. 470–473. doi: 10.1109/ISBI.2012.6235586.
- Moreno, R., Borga, M. and Smedby, Ö. (2012b) 'Generalizing the mean intercept length tensor for gray-level images', *Medical Physics*, 39(7Part2), pp. 4599–4612. doi: 10.1118/1.4730502.
- Morgan, E. F., Bayraktar, H. H. and Keaveny, T. M. (2003) 'Trabecular bone modulus-density relationships depend on anatomic site', *Journal of Biomechanics*, 36(7), pp. 897–904. doi: 10.1016/S0021-9290(03)00071-X.
- Morgan, E. F. and Keaveny, T. M. (2001) 'Dependence of yield strain of human trabecular bone on anatomic site', *Journal of Biomechanics*, 34(5), pp. 569–577. doi: 10.1016/S0021-9290(01)00011-2.
- Murphy, A. J. *et al.* (1995) 'Isometric assessment of muscular function: The effect of joint angle', *Journal of Applied Biomechanics*, 11(2), pp. 205–215. doi: 10.1123/jab.11.2.205.
- Musy, S. N. *et al.* (2017) 'Not only stiffness, but also yield strength of the trabecular structure determined by non-linear  $\mu$ FE is best predicted by bone volume fraction and fabric tensor', *Journal of the Mechanical Behavior of Biomedical Materials*, 65, pp. 808–813. doi: 10.1016/j.jmbbm.2016.10.004.
- Myers, M. A. *et al.* (2008) 'Biological materials: Structure and mechanical properties', *Progress in Materials Science*, 53, pp. 1–206. doi: 10.1016/j.pmatsci.2007.05.002.
- Nankaku, M. *et al.* (2005) 'Evaluation of hip fracture risk in relation to fall direction', *Osteoporosis International*, 16(11), pp. 1315–1320. doi: 10.1007/s00198-005-1843-2.
- Nawathe, S. *et al.* (2014) 'Microstructural failure mechanisms in the human proximal femur for sideways fall loading', *Journal of Bone and Mineral Research*, 29(2), pp. 507–515. doi: 10.1002/jbmr.2033.
- Naylor, K. E. *et al.* (2012) 'The use of DXA based finite element analysis of the proximal femur in a longitudinal study of hip fracture.', *Journal of bone and mineral research : the official journal of the American Society for Bone and Mineral Research*, pp. 1–33. doi: 10.1002/jbmr.1856.

- Naylor, K. E. *et al.* (2013) 'Use of DXA-based finite element analysis of the proximal femur in a longitudinal study of hip fracture', *Journal of Bone and Mineral Research*, 28(5), pp. 1014–1021. doi: 10.1002/jbmr.1856.
- NICE (2011) 'Hip Fracture: The management of hip fracture in adults.', *Health Technology Assessment*, (June). doi: 10.1136/bmj.d2108.
- NICE (2013) 'NICE clinical guideline 161. Falls: Assessment and prevention of falls in older people', *National Institute of Health and Care Excellence*, 161(June), pp. 1–315. doi: 10.7748/nop.26.6.18.e586.
- Nicks, K. M. *et al.* (2012) 'Relationship of age to bone microstructure independent of areal bone mineral density', *Journal of Bone and Mineral Research*, 27(3), pp. 637–644. doi: 10.1002/jbmr.1468.
- NIH (2001) 'Osteoporosis prevention, diagnosis, and therapy', *JAMA*, 285, pp. 785–795.
- Nishiyama, K. K. *et al.* (2014) 'Classification of women with and without hip fracture based on quantitative computed tomography and finite element analysis', *Osteoporosis International*, 25(2), pp. 619–626. doi: 10.1007/s00198-013-2459-6.
- Odgaard, A. *et al.* (1997) 'Fabric and elastic principal directions of cancellous bone are closely related', *Journal of Biomechanics*, 30(5), pp. 487–495. doi: 10.1016/S0021-9290(96)00177-7.
- Oftadeh, R. *et al.* (2015) 'Biomechanics and Mechanobiology of Trabecular Bone: A Review', *Journal of Biomechanical Engineering*, 137(1), p. 10802. doi: 10.1115/1.4029176.
- Ohnaru, K. *et al.* (2013) 'Hip structural analysis: a comparison of DXA with CT in postmenopausal Japanese women.', *SpringerPlus*, 2(1), p. 331. doi: 10.1186/2193-1801-2-331.
- Otsu, N. (1979) 'A Threshold Selection Method from Gray-Level Histograms', *IEEE Transactions on Systems, Man, and Cybernetics*, 9(1), pp. 62–66. doi: 10.1109/TSMC.1979.4310076.
- Owen Lovejoy, C. *et al.* (2002) 'The Maka femur and its bearing on the antiquity of human walking: Applying contemporary concepts of morphogenesis to the human fossil record', *American Journal of Physical Anthropology*, 119(2), pp. 97–133. doi: 10.1002/ajpa.10111.
- Pandy, M. G. and Andriacchi, T. P. (2010) 'Muscle and Joint Function in Human Locomotion', *Annual Review of Biomedical Engineering*, 12(1), pp. 401–433. doi: 10.1146/annurev-bioeng-070909-105259.
- Pandy, M. G. and Andriacchi, T. P. (no date) *Muscle and Joint Function in Human Locomotion*. doi: 10.1146/annurev-bioeng-070909-105259.
- Parkkari, J. *et al.* (1999) 'Majority of hip fractures occur as a result of a fall and impact on the greater trochanter of the femur: A prospective controlled hip fracture study with 206 consecutive patients', *Calcified Tissue International*, 65(3), pp. 183–187. doi: 10.1007/s002239900679.
- Peng, L. *et al.* (2006) 'Comparison of isotropic and orthotropic material property assignments on femoral finite element models under two loading conditions', *Medical Engineering and Physics*, 28(3), pp. 227–233. doi: 10.1016/j.medengphy.2005.06.003.
- Phillips, A. T. M. (2009) 'The femur as a musculo-skeletal construct: A free boundary condition modelling approach', *Medical Engineering and Physics*, 31(6), pp. 673–680. doi:

10.1016/j.medengphy.2008.12.008.

Phillips, A. T. M. (2009) 'The femur as a musculo-skeletal construct: A free boundary condition modelling approach', *Medical Engineering and Physics*, 31(6), pp. 673–680. doi: 10.1016/j.medengphy.2008.12.008.

Phinyomark, A. *et al.* (2012) 'A preliminary study assessing time-domain EMG features of classifying exercises in preventing falls in the elderly', in *2012 9th International Conference on Electrical Engineering/Electronics, Computer, Telecommunications and Information Technology, ECTI-CON 2012*. doi: 10.1109/ECTICon.2012.6254117.

Piazza, S. J. (2006) 'Muscle-driven forward dynamic simulations for the study of normal and pathological gait', 7, pp. 1–7. doi: 10.1186/1743-0003-3-5.

Pijnappels, M. *et al.* (2008) 'Identification of elderly fallers by muscle strength measures', *European Journal of Applied Physiology*, 102(5), pp. 585–592. doi: 10.1007/s00421-007-0613-6.

Pilgram, R. *et al.* (2008) 'Proximal femur segmentation in conventional pelvic x ray.', *Medical physics*, 35(2008), pp. 2463–2472. doi: 10.1118/1.2919096.

Pulkkinen, P. *et al.* (2006) 'Association of geometric factors and failure load level with the distribution of cervical vs. trochanteric hip fractures.', *Journal of bone and mineral research : the official journal of the American Society for Bone and Mineral Research*, 21(6), pp. 895–901. doi: 10.1359/JBMR.060305.

Rajagopal, A. *et al.* (2016) 'Full body musculoskeletal model for muscle- driven simulation of human gait', *IEEE Transactions on Biomedical Engineering*, 63(10), pp. 2068–2079. doi: 10.1109/TBME.2016.2586891.

Ramos, A. and Simões, J. A. (2006) 'Tetrahedral versus hexahedral finite elements in numerical modelling of the proximal femur', *Medical Engineering and Physics*, 28(9), pp. 916–924. doi: 10.1016/j.medengphy.2005.12.006.

Rassier, Dilon E.; MacIntosh, B. R.; Herzog, W. (1999) 'Invited Review: Length dependence of active force production in skeletal muscle', *Journal of Appl*, 85(5), pp. 1445–1457.

Rassier, D. E. (2004) 'Considerations on the history dependence of muscle contraction', *Journal of Applied Physiology*, 96(2), pp. 419–427. doi: 10.1152/jappphysiol.00653.2003.

Raty, H. P. *et al.* (1999) 'Associations of isometric and isoinertial trunk muscle strength measurements and lumbar paraspinal muscle cross-sectional areas', *J Spinal Disord*, 12(3), pp. 266–270. doi: 10.1097/00024720-199906000-00018.

Reilly, D. T. and Burstein, A. H. (1975) 'The elastic and ultimate properties of compact bone tissue', *Journal of Biomechanics*, 8(6). doi: 10.1016/0021-9290(75)90075-5.

Ren, L., Howard, D. and Kenney, L. (2006) 'Computational Models to Synthesize Human Walking', 3.

Ren, L., Jones, R. K. and Howard, D. (2007a) 'Predictive modelling of human walking over a complete gait cycle', *Journal of Biomechanics*, 40(7), pp. 1567–1574. doi: 10.1016/j.jbiomech.2006.07.017.

Ren, L., Jones, R. K. and Howard, D. (2007b) 'Predictive modelling of human walking over a complete gait cycle', *Journal of Biomechanics*, 40(7), pp. 1567–1574. doi: 10.1016/j.jbiomech.2006.07.017.

- Ren, L., Jones, R. K. and Howard, D. (2008) 'Whole body inverse dynamics over a complete gait cycle based only on measured kinematics', *Journal of Biomechanics*, 41(12), pp. 2750–2759. doi: 10.1016/j.jbiomech.2008.06.001.
- Ren, L., Jones, R. K. and Howard, D. (2008) 'Whole body inverse dynamics over a complete gait cycle based only on measured kinematics', 41, pp. 2750–2759. doi: 10.1016/j.jbiomech.2008.06.001.
- Rho, J. Y., Kuhn-Spearing, L. and Zioupos, P. (1998) 'Mechanical properties and the hierarchical structure of bone', *Medical Engineering and Physics*, 20(2), pp. 92–102. doi: 10.1016/S1350-4533(98)00007-1.
- Rice, J. C., Cowin, S. C. and Bowman, J. A. (1988) 'On the dependence of the elasticity and strength of cancellous bone on apparent density', *Journal of Biomechanics*, 21(2), pp. 155–168. doi: 10.1016/0021-9290(88)90008-5.
- Rich, C. and Cafarelli, E. (2000) 'Submaximal motor unit firing rates after 8 wk of isometric resistance training.', *Medicine and science in sports and exercise*, 32(1), pp. 190–196. doi: 10.1097/00005768-200001000-00028.
- van Rietbergen, B. and Ito, K. (2015) 'A survey of micro-finite element analysis for clinical assessment of bone strength: The first decade', *Journal of Biomechanics*, 48(5), pp. 832–841. doi: 10.1016/j.jbiomech.2014.12.024.
- Riggs, B. L. *et al.* (2004) 'Population-Based Study of Age and Sex Differences in Bone Volumetric Density, Size, Geometry, and Structure at Different Skeletal Sites', *Journal of Bone and Mineral Research*, 19(12), pp. 1945–1954. doi: 10.1359/jbmr.040916.
- Riggs, B. L. and Melton, L. J. (1995) 'The worldwide problem of osteoporosis: Insights afforded by epidemiology', *Bone*, 17(5 SUPPL. 1). doi: 10.1016/8756-3282(95)00258-4.
- Robinovitch, S. N. *et al.* (2000) 'Prevention of falls and fall-related fractures through biomechanics.', *Exercise and sport sciences reviews*, 28(2), pp. 74–79.
- Robinovitch, S. N., Brumer, R. and Maurer, J. (2004) 'Effect of the "squat protective response" on impact velocity during backward falls', *Journal of Biomechanics*, 37(9), pp. 1329–1337. doi: 10.1016/j.jbiomech.2003.12.015.
- Robinovitch, S. N., Hayes, W. C. and McMahon, T. a (1991) 'Prediction of femoral impact forces in falls on the hip.', *Journal of biomechanical engineering*, 113(December 1991), pp. 366–374. doi: 10.1115/1.2895414.
- Robinovitch, S. N., McMahon, T. A. and Hayes, W. C. (1995) 'Force attenuation in trochanteric soft tissues during impact from a fall', *Journal of Orthopaedic Research*, 13(6), pp. 956–962. doi: 10.1002/jor.1100130621.
- Ruff, C. B., Holt, B. and Trinkaus, E. (2006) 'Who's afraid of the big bad wolff? "Wolff is law" and bone functional adaptation', *American Journal of Physical Anthropology*, 129(4), pp. 484–498. doi: 10.1002/ajpa.
- Saers, J. P. P. *et al.* (2016) 'Trabecular bone structural variation throughout the human lower limb', *Journal of Human Evolution*, 97, pp. 97–108. doi: 10.1016/j.jhevol.2016.05.012.
- Salguero, L., Saadat, F. and Sevostianov, I. (2014) 'Micromechanical modeling of elastic properties of cortical bone accounting for anisotropy of dense tissue', *Journal of Biomechanics*, 47(13), pp. 3279–3287. doi: 10.1016/j.jbiomech.2014.08.019.
- San Antonio, T. *et al.* (2012a) 'Orientation of orthotropic material properties in a femur FE

- model: A method based on the principal stresses directions', *Medical Engineering and Physics*. Institute of Physics and Engineering in Medicine, 34(7), pp. 914–919. doi: 10.1016/j.medengphy.2011.10.008.
- San Antonio, T. *et al.* (2012b) 'Orientation of orthotropic material properties in a femur FE model: A method based on the principal stresses directions', *Medical Engineering and Physics*, 34(7), pp. 914–919. doi: 10.1016/j.medengphy.2011.10.008.
- Sandercock, T. G. (2005) 'Summation of motor unit force in passive and active muscle.', *Exercise and sport sciences reviews*, 33(2), pp. 76–83. doi: 10.1097/00003677-200504000-00004.
- Sarvi, M. N. *et al.* (2014) 'Experimental Validation of Subject-Specific Dynamics Model for Predicting Impact Force in Sideways Fall', *Journal of Biomedical Science and ...*, (June), pp. 405–418. Available at: <http://www.scirp.org/journal/PaperInformation.aspx?paperID=46587>.
- Sasaki, K. and Neptune, R. R. (2006) 'Muscle mechanical work and elastic energy utilization during walking and running near the preferred gait transition speed', *Gait and Posture*, 23(3), pp. 383–390. doi: 10.1016/j.gaitpost.2005.05.002.
- Schaffler, M. B. and Burr, D. B. (1988) 'Stiffness of compact bone: Effects of porosity and density', *Journal of Biomechanics*, 21(1), pp. 13–16. doi: 10.1016/0021-9290(88)90186-8.
- Schileo, E. *et al.* (2007) 'Subject-specific finite element models can accurately predict strain levels in long bones', *Journal of Biomechanics*, 40(13), pp. 2982–2989. doi: 10.1016/j.jbiomech.2007.02.010.
- Schileo, E. *et al.* (2008) 'Subject-specific finite element models implementing a maximum principal strain criterion are able to estimate failure risk and fracture location on human femurs tested in vitro', *Journal of Biomechanics*, 41(2), pp. 356–367. doi: 10.1016/j.jbiomech.2007.09.009.
- Sellers, W. I. *et al.* (2004) 'Evaluating alternative gait strategies using evolutionary robotics', *J Anat*, 204(5), pp. 343–351. doi: 10.1111/j.0021-8782.2004.00294.x\rJOA294 [pii].
- Sellers, W. I. *et al.* (2010) 'Evolutionary robotic approaches in primate gait analysis', *International Journal of Primatology*, 31(2), pp. 321–338. doi: 10.1007/s10764-010-9396-4.
- Sellers, W. I., Dennis, L. A. and Crompton, R. H. (2003) 'Predicting the metabolic energy costs of bipedalism using evolutionary robotics', pp. 1127–1136. doi: 10.1242/jeb.00205.
- Sellers, W. I. and Manning, P. L. (2007) 'Estimating dinosaur maximum running speeds using evolutionary robotics.', *Proceedings. Biological sciences / The Royal Society*, 274(1626), pp. 2711–6. doi: 10.1098/rspb.2007.0846.
- Sevostianov, I. and Kachanov, M. (2000) 'Impact of the porous microstructure on the overall elastic properties of the osteonal cortical bone', *Journal of Biomechanics*, 33(7), pp. 881–888. doi: 10.1016/S0021-9290(00)00031-2.
- Shergold, I., Lyons, G. and Hubers, C. (2015) 'Future mobility in an ageing society - Where are we heading?', *Journal of Transport and Health*, 2(1), pp. 86–94. doi: 10.1016/j.jth.2014.10.005.
- Silder, A. *et al.* (2007) 'Identification of passive elastic joint moment-angle relationships in the lower extremity', *Journal of Biomechanics*, 40(12), pp. 2628–2635. doi: 10.1016/j.jbiomech.2006.12.017.

- Silverman, S. L. and Calderon, A. D. (2010) 'The utility and limitations of FRAX: A us perspective', *Current Osteoporosis Reports*, pp. 192–197. doi: 10.1007/s11914-010-0032-1.
- Siracuse, J. J. *et al.* (2012) 'Health care and socioeconomic impact of falls in the elderly', *American Journal of Surgery*, 203(3), pp. 335–338. doi: 10.1016/j.amjsurg.2011.09.018.
- Snyder, S. M. and Schneider, E. (1991) 'Estimation of mechanical properties of cortical bone by computed tomography', *Journal of Orthopaedic Research*, 9(3), pp. 422–431. doi: 10.1002/jor.1100090315.
- Sode, M. *et al.* (2008) 'Resolution Dependence of the Non-metric Trabecular Structure Indices', *Bone*, 42(4), pp. 728–736. doi: 10.1016/j.bone.2007.12.004.
- Sornay-Rendu, E. *et al.* (2017) 'Bone Microarchitecture Assessed by HR-pQCT as Predictor of Fracture Risk in Postmenopausal Women: The OFELY Study', *Journal of Bone and Mineral Research*, 32(6), pp. 1243–1251. doi: 10.1002/jbmr.3105.
- Speirs, A. D. *et al.* (2007) 'Physiologically based boundary conditions in finite element modelling', *Journal of Biomechanics*, 40(10), pp. 2318–2323. doi: 10.1016/j.jbiomech.2006.10.038.
- St-Jean-Pelletier, F. *et al.* (2017) 'The impact of ageing, physical activity, and pre-frailty on skeletal muscle phenotype, mitochondrial content, and intramyocellular lipids in men', *Journal of Cachexia, Sarcopenia and Muscle*, 8(2), pp. 213–228. doi: 10.1002/jcsm.12139.
- Stauber, M. and Müller, R. (2006) 'Age-related changes in trabecular bone microstructures: Global and local morphometry', *Osteoporosis International*, 17(4), pp. 616–626. doi: 10.1007/s00198-005-0025-6.
- Stevens, J. A. *et al.* (1999) 'Surveillance for injuries and violence among older adults.', *MMWR. CDC surveillance summaries : Morbidity and mortality weekly report. CDC surveillance summaries / Centers for Disease Control*, 48(8), pp. 27–50.
- Stinchcombe, A., Kuran, N. and Powell, S. (2014) 'Seniors' falls in Canada: Second report: Key highlights', *Chronic Diseases and Injuries in Canada*, pp. 171–174.
- Susan Standring, PhD, Ds. (2009) 'Gray's Anatomy 40th edition', *Churchill Livingstone*, pp. 196–200. doi: 10.1308/003588406X116873.
- Svedbom, A. *et al.* (2013) 'Osteoporosis in the European Union: A compendium of country-specific reports', *Archives of Osteoporosis*, 8(1–2). doi: 10.1007/s11657-013-0137-0.
- Synek, A. *et al.* (2015) 'The influence of bone density and anisotropy in finite element models of distal radius fracture osteosynthesis: Evaluations and comparison to experiments', *Journal of Biomechanics*, 48(15), pp. 4116–4123. doi: 10.1016/j.jbiomech.2015.10.012.
- Taghizadeh, E. *et al.* (2016) 'Biomechanical Role of Bone Anisotropy Estimated on Clinical CT Scans by Image Registration', *Annals of Biomedical Engineering*, 44(8), pp. 2505–2517. doi: 10.1007/s10439-016-1551-4.
- Tan, J. S. *et al.* (2006) 'Wrist impact velocities are smaller in forward falls than backward falls from standing', *Journal of Biomechanics*, 39(10), pp. 1804–1811. doi: 10.1016/j.jbiomech.2005.05.016.
- Tanck, E. *et al.* (2009) 'Predictive value of femoral head heterogeneity for fracture risk', *Bone*, 44(4), pp. 590–595. doi: 10.1016/j.bone.2008.12.022.
- Taylor, W. R. *et al.* (2002) 'Determination of orthotropic bone elastic constants using FEA

- and modal analysis', *Journal of Biomechanics*, 35(6), pp. 767–773. doi: 10.1016/S0021-9290(02)00022-2.
- The Mathworks Inc. (2016) *MATLAB - MathWorks*, [www.mathworks.com/products/matlab](http://www.mathworks.com/products/matlab). doi: 2016-11-26.
- Thigpen, M. T. *et al.* (2000a) 'Turning difficulty characteristics of adults aged 65 years or older.', *Physical therapy*, 80(12), pp. 1174–1187.
- Thigpen, M. T. *et al.* (2000b) 'Turning difficulty characteristics of adults aged 65 years or older.', *Journal of the American Physical Therapy Association*, 80(12), pp. 1174–1187.
- Thomsen, J. S., Ebbesen, E. N. and Mosekilde, L. i. (2002) 'Age-related differences between thinning of horizontal and vertical trabeculae in human lumbar bone as assessed by a new computerized method', *Bone*, 31(1), pp. 136–142. doi: 10.1016/S8756-3282(02)00801-3.
- Tian, Y. *et al.* (2013) 'Exploring the system-wide costs of falls in older people in Torbay', *London: The King's Fund*, pp. 1–12. Available at: [http://www.kingsfund.org.uk/sites/files/kf/field/field\\_publication\\_file/exploring-system-wide-costs-of-falls-in-torbay-kingsfund-aug13.pdf](http://www.kingsfund.org.uk/sites/files/kf/field/field_publication_file/exploring-system-wide-costs-of-falls-in-torbay-kingsfund-aug13.pdf).
- Topoliński, T. *et al.* (2012) 'Microarchitecture parameters describe bone structure and its strength better than BMD.', *TheScientificWorldJournal*, 2012, p. 502781. doi: 10.1100/2012/502781.
- Trabelsi, N. and Yosibash, Z. (2011) 'Patient-Specific Finite-Element Analyses of the Proximal Femur with Orthotropic Material Properties Validated by Experiments', *Journal of Biomechanical Engineering*, 133(6), p. 61001. doi: 10.1115/1.4004180.
- Trombetti, A. *et al.* (2016) 'Age-associated declines in muscle mass, strength, power, and physical performance: impact on fear of falling and quality of life', *Osteoporosis International*, 27(2), pp. 463–471. doi: 10.1007/s00198-015-3236-5.
- Turkylmaz, I. *et al.* (2006) 'Assessment of correlation between computerized tomography values of the bone, and maximum torque and resonance frequency values at dental implant placement', *Journal of Oral Rehabilitation*, 33(12), pp. 881–888. doi: 10.1111/j.1365-2842.2006.01692.x.
- Turner, C. H. *et al.* (1999) 'The elastic properties of trabecular and cortical bone tissues are similar: Results from two microscopic measurement techniques', *Journal of Biomechanics*, 32(4), pp. 437–441. doi: 10.1016/S0021-9290(98)00177-8.
- Unnanuntana, A. (2010) 'The Assessment of Fracture Risk', *The Journal of Bone and Joint Surgery (American)*, 92(3), p. 743. doi: 10.2106/JBJS.I.00919.
- Valero-Cuevas, F. J. *et al.* (2015) 'Exploring the high-dimensional structure of muscle redundancy via subject-specific and generic musculoskeletal models', *Journal of Biomechanics*, 48(11), pp. 2887–2896. doi: 10.1016/j.jbiomech.2015.04.026.
- Varga, P. *et al.* (2011) 'Validation of an HR-pQCT-based homogenized finite element approach using mechanical testing of ultra-distal radius sections', *Biomechanics and Modeling in Mechanobiology*, 10(4), pp. 431–444. doi: 10.1007/s10237-010-0245-3.
- Vaughan, C. L. (2003) 'Theories of bipedal walking: An odyssey', in *Journal of Biomechanics*, pp. 513–523. doi: 10.1016/S0021-9290(02)00419-0.
- Verhulp, E., van Rietbergen, B. and Huiskes, R. (2008) 'Load distribution in the healthy and osteoporotic human proximal femur during a fall to the side', *Bone*, 42(1), pp. 30–35. doi:

10.1016/j.bone.2007.08.039.

Viceconti, M. *et al.* (2004) 'Automatic generation of accurate subject-specific bone finite element models to be used in clinical studies', *Journal of Biomechanics*, 37(10), pp. 1597–1605. doi: 10.1016/j.jbiomech.2003.12.030.

Viceconti, M. *et al.* (2012a) 'Are spontaneous fractures possible? An example of clinical application for personalised, multiscale neuro-musculo-skeletal modelling', *Journal of Biomechanics*. Elsevier, 45(3), pp. 421–426. doi: 10.1016/j.jbiomech.2011.11.048.

Viceconti, M. *et al.* (2012b) 'Are spontaneous fractures possible? An example of clinical application for personalised, multiscale neuro-musculo-skeletal modelling', *Journal of Biomechanics*, 45(3), pp. 421–426. doi: 10.1016/j.jbiomech.2011.11.048.

Wakao, N. *et al.* (2009) 'The effect of impact direction on the fracture load of osteoporotic proximal femurs', *Medical Engineering and Physics*, 31(9), pp. 1134–1139. doi: 10.1016/j.medengphy.2009.07.010.

Wegrzyn, J. *et al.* (2010) 'Role of trabecular microarchitecture and its heterogeneity parameters in the mechanical behavior of ex vivo human L3 vertebrae', *Journal of Bone and Mineral Research*, 25(11), pp. 2324–2331. doi: 10.1002/jbmr.164.

Wei, T. S. *et al.* (2001) 'Fall characteristics, functional mobility and bone mineral density as risk factors of hip fracture in the community-dwelling ambulatory elderly', *Osteoporos Int*, 12(12), pp. 1050–1055. doi: <http://dx.doi.org/10.1007/PL00004184>.

Weinans, H. *et al.* (2000) 'Sensitivity of periprosthetic stress-shielding to load and the bone density-modulus relationship in subject-specific finite element models', *Journal of Biomechanics*, 33(7), pp. 809–817. doi: 10.1016/S0021-9290(00)00036-1.

Weiner, S. and Traub, W. (1992) 'Bone structure: from angstroms to microns', *FASEB Journal*, 6, pp. 879–885. doi: 10.1002/9780470114735.hawley01126.

Whitehouse, W. J. (1974) 'The quantitative morphology of anisotropic trabecular bone', *Journal of Microscopy*, 101(2), pp. 153–168. doi: 10.1111/j.1365-2818.1974.tb03878.x.

Wicke, R. W. and Oman, C. M. (1982) 'Visual and graviceptive influences on lower leg EMG activity in humans during brief falls', *Experimental Brain Research*, 46(3), pp. 324–330. doi: 10.1007/BF00238627.

Wickham, C. A. *et al.* (1989) 'Dietary calcium, physical activity, and risk of hip fracture: a prospective study.', *BMJ (Clinical research ed.)*, 299(6704), pp. 889–92. Available at: <http://www.pubmedcentral.nih.gov/articlerender.fcgi?artid=1837771&tool=pmcentrez&rendertype=abstract>.

Widler, K. S. *et al.* (2009) 'Assessment of hip abductor muscle strength. A validity and reliability study.', *The Journal of bone and joint surgery. American volume*, 91(11), pp. 2666–72. doi: 10.2106/JBJS.H.01119.

Wilson, F. (2015) 'Grieve's Modern Musculoskeletal Physiotherapy (Fourth edition)', *British Journal of Sports Medicine*, 49(20), pp. 1352–1352. doi: 10.1136/bjsports-2015-095310.

Wirtz, D. C. *et al.* (2000) 'Critical evaluation of known bone material properties to realize anisotropic FE-simulation of the proximal femur', *Journal of Biomechanics*, 33(10), pp. 1325–1330. doi: 10.1016/S0021-9290(00)00069-5.

Wolfram, U. *et al.* (2009) 'Vertebral trabecular main direction can be determined from clinical CT datasets using the gradient structure tensor and not the inertia tensor-A case

- study', *Journal of Biomechanics*, 42(10), pp. 1390–1396. doi: 10.1016/j.jbiomech.2009.04.006.
- World Health Organization (2004) *WHO SCIENTIFIC GROUP ON THE ASSESSMENT OF OSTEOPOROSIS AT PRIMARY HEALTH Care Level*, World Health Organization. doi: 10.1016/S0140-6736(02)08761-5.
- Yan, L. *et al.* (1999) 'Epidemiological study of hip fracture in Shenyang, People's Republic of China', *Bone*, 24(2), pp. 151–155. doi: 10.1016/S8756-3282(98)00168-9.
- Yang *et al.* (1996) 'The relationship between loading conditions and fracture patterns of the proximal femur.', *Journal of biomechanical engineering*, 118(4), pp. 575–8. doi: 10.1115/1.2796045.
- Yang, G. *et al.* (1998) 'Anisotropic Hooke's law for cancellous bone and wood', *Journal of Elasticity*, 53(2), pp. 125–146. doi: 10.1023/A:1007575322693.
- Yang, H., Ma, X. and Guo, T. (2010) 'Some factors that affect the comparison between isotropic and orthotropic inhomogeneous finite element material models of femur', *Medical Engineering and Physics*. Institute of Physics and Engineering in Medicine, 32(6), pp. 553–560. doi: 10.1016/j.medengphy.2010.01.004.
- Yang, L. *et al.* (2009) 'Use of DXA-Based Structural Engineering Models of the Proximal Femur to Discriminate Hip Fracture', *Journal of Bone and Mineral Research*, 24(1), pp. 33–42. doi: 10.1359/jbmr.080906.
- Yeni, Y. N. *et al.* (2005) 'Effect of microcomputed tomography voxel size on the finite element model accuracy for human cancellous bone.', *Journal of biomechanical engineering*, 127(1), pp. 1–8. doi: 10.1115/1.1835346.
- Yeni, Y. N. *et al.* (2011) 'Variability of trabecular microstructure is age-, gender-, race- and anatomic site-dependent and affects stiffness and stress distribution properties of human vertebral cancellous bone', *Bone*, 49(4), pp. 886–894. doi: 10.1016/j.bone.2011.07.006.
- Yeni, Y. N., Vashishth, D. and Fyhrie, D. P. (2001) 'Estimation of bone matrix apparent stiffness variation caused by osteocyte lacunar size and density', *Journal of biomechanical engineering*, 123(1), pp. 10–17. doi: 10.1115/1.1338123.
- Yokota, F. *et al.* (2009) 'Automated segmentation of the femur and pelvis from 3D CT data of diseased hip using hierarchical statistical shape model of joint structure', in *Lecture Notes in Computer Science (including subseries Lecture Notes in Artificial Intelligence and Lecture Notes in Bioinformatics)*, pp. 811–818. doi: 10.1007/978-3-642-04271-3\_98.
- Yosibash, Z., Tal, D. and Trabelsi, N. (2010) 'Predicting the yield of the proximal femur using high-order finite-element analysis with inhomogeneous orthotropic material properties', *Philosophical Transactions of the Royal Society A: Mathematical, Physical and Engineering Sciences*, 368(1920), pp. 2707–2723. doi: 10.1098/rsta.2010.0074.
- Zhou, B. *et al.* (2016) 'High-resolution peripheral quantitative computed tomography (HR-pQCT) can assess microstructural and biomechanical properties of both human distal radius and tibia: Ex vivo computational and experimental validations', *Bone*, 86, pp. 58–67. doi: 10.1016/j.bone.2016.02.016.
- Zysset, P. *et al.* (2015) 'Clinical Use of Quantitative Computed Tomography-Based Finite Element Analysis of the Hip and Spine in the Management of Osteoporosis in Adults: The 2015 ISCD Official Positions-Part II', *Journal of Clinical Densitometry*, 18(3), pp. 359–392. doi: 10.1016/j.jocd.2015.06.011.

Zysset, P. K. *et al.* (2013) 'Finite element analysis for prediction of bone strength.', *BoneKEy reports*, 2(August), p. 386. doi: 10.1038/bonekey.2013.120.

## APPENDIX A

---

Java script developed to automate the process of MIL analysis of trabecular bone cubes in BoneJ.

```
function processFolder(dir)
{list = getFileList(dir);
  n=0;
  for (i=0; i<list.length; i++)
    {if (endsWith(list[i], "/"))
      processFolder(""+dir+list[i]);
      else {n++;
            path = dir+list[i];
            if (n==1) {print("sequence "+path);

                                run ("Image Sequence...", "open=[path]
sort")run("Properties...", "channels=1 slices=68 frames=1 unit=mm
pixel_width=0.073000 pixel_height=0.073000 voxel_depth=0.073000");

setOption("BlackBackground", false);

run("Make Binary", "method=Otsu background=Default calculate");

run("Anisotropy", "auto radius=1.2 vectors=50000
vector_sampling=0.037 min_spheres=200 max_spheres=2000
tolerance=0.0050 record_eigens");

name1 = "Log";
saveAs("Text", ResultDir+name1);

name2 = "Eigens_all";
saveAs("Results", ResultDir+name2+".xls");
name = "Results";
index = lastIndexOf(list[i], ".");
  if (index!=-1)
    name = substring(list[i], 0, index);
    path = ResultDir + name + ".xls";
    saveAs("Results", path);
    }
  }
}
```

## APPENDIX B

---

Matlab code for trabecular analysis. Covers a suite of functions for analysis.

```
function menu
basedir=uigetdir('', 'Choose directory for analysing/storing data');
task=2;
while task~=1
    task=menu('Options', 'Exit', 'Generate cubes', 'Radiograph', 'Plot
EigenVectors - Whole Bone', 'Auto-Plot Eigens - Saggital
Slices', 'Manual Plot Eigen Slice/Region', 'Calculate Axis Angle', ...
'Calculate Trabecular Angles');
    if task==2, cube_generation(basedir); end
    if task==3, radiograph(basedir); end
    if task==4, Eigenvector_plot(basedir); end
    if task==5, plot_slice_auto(basedir); end
    if task==6, Slice_3D(basedir); end
    if task==7, NeckAngle(basedir); end
    if task==8, calculate_x_axis_angles(basedir); end
end
```

```
function radiograph(basedir)
tifdir=uigetdir('', 'Choose the original scan folder'); cd(tifdir);
infiles=dir('*.tif');
im=fliplr(imread(infiles(10).name, 'tif'));
D=[size(im) length(infiles)];
im(1:D(1), 1:D(2), 1:D(3))=uint16(0);
for i=1:D(3),
    j=D(3)-i+1;
    im(:, :, j)=fliplr(imread(infiles(i).name, 'tif'));
    imagesc(im(:, :, j)), axis equal, axis off, pause(0.01); end
imS=squeeze(sum(im, 1));
cd(basedir)
imagesc(imS), axis equal, axis off;
savefig ('Radiograph_col.fig');
saveas(gcf, 'Radiograph_col', 'jpeg');
imagesc(imS), axis equal, axis off, colormap(gray);
savefig ('Radiograph_grey.fig');
saveas(gcf, 'Radiograph_grey', 'jpeg');
filename = 'Radiograph.mat';
save('Radiograph.mat');
close all
```

```
function cube_generation(basedir)
cd(basedir);
listing = dir;
a = listing(10);
tit = a.name;
[X, map] = imread(tit);
Frame_Size = [size(X), size(listing, 1) - 2];
clear X tit a map
image_res = 0.0729;
cube_size = 5;
rve_size = round(cube_size/image_res); %
New_Frame_Size(1) = (ceil(Frame_Size(1)./rve_size))*rve_size;
New_Frame_Size(2) = (ceil(Frame_Size(2)./rve_size))*rve_size;
xd = [rve_size.*ones((New_Frame_Size(1)/rve_size), 1)];
yd = [rve_size.*ones((New_Frame_Size(2)/rve_size), 1)];
zd = rve_size;
delta_s = 3:rve_size:2000;
```

```

i3 = 0;
for k = 1:size(delta_s,2)
    k
    clear V
    n = 0;
    for i = delta_s(k):delta_s(k)+rve_size-1
        a = listing(i);
        tit = a.name;
        [X0,map] = imread(tit);
        X = zeros(New_Frame_Size(1),New_Frame_Size(2));
        X(1:Frame_Size(1),1:Frame_Size(2)) = double(X0);
        n = n+1;
        V(:, :, n) = X;
    end
    clear C
    C = mat2cell(V,xd,yd,zd);
    for i = 1:size(xd,2)
        for j = 1:size(yd,2)
            C_T = C{i,j};
            if (100*size(find(C_T>100),1)/(rve_size^3))>1
                disp('Keep go!!')
                cd(basedir);
                tit_box =
                ['Cube_', num2str(i), '_', num2str(j), '_', num2str(k)];
                mkdir(tit_box);
                i3 = i3+1;
                GRID(i3,:) = [i,j,k];
                for i2 = 1:rve_size
                    imwrite((C_T(:, :, i2))./255, [tit_box, '\image_', num2str(i2), '.tif'])
                end
            end
        end
    end
end
end
end
end
end

```

```

function Eigenvector_plot(basedir)
cd(basedir);
EV = xlsread('Results.xlsx','E:M');
[num,str]=xlsread('Results.xlsx','A:B');
EV2 = (str);
EV2(:,1) = [];
EV2(1,:) = [];
EV2 = cellfun(@(s) {s(6:end)}, EV2, 'UniformOutput', false);
str_tr = EV2';
all_coords = [str_tr{:}];
x_coords = cellfun(@(x) {x(1:2)}, all_coords, 'UniformOutput',
false);
x_coords = [x_coords{:}];
x_coords = regexprep(x_coords, '_+$', '');
x_coords = str2double(x_coords);
x_coords = x_coords.';
y_coords = cellfun(@(x) {x(3:5)}, all_coords, 'UniformOutput',
false);
y_coords = [y_coords{:}];
y_coords = regexprep(y_coords, '_+$', '');
y_coords = regexprep(y_coords, '^_', '');
y_coords = regexprep(y_coords, '_1+$', '');
y_coords = regexprep(y_coords, '_2+$', '');
y_coords = regexprep(y_coords, '_3+$', '');
y_coords = regexprep(y_coords, '_4+$', '');
y_coords = regexprep(y_coords, '_5+$', '');

```

```

y_coords = regexprep(y_coords, '_6+$', '');
y_coords = regexprep(y_coords, '_7+$', '');
y_coords = regexprep(y_coords, '_8+$', '');
y_coords = regexprep(y_coords, '_9+$', '');
y_coords = str2double(y_coords);
y_coords = y_coords.';
z_coords = cellfun(@(x) {x(end-1:end)}, all_coords, 'UniformOutput',
false);
z_coords = [z_coords{:}];
z_coords = regexprep(z_coords, '^_', '');
z_coords = str2double(z_coords);
z_coords = z_coords.';
ALL_COORDS = [x_coords y_coords z_coords];
index_ALLCOORDS = ALL_COORDS(1:end,:);
load('CUBES.mat');
[Lia2,LocB2] = (ismember(GRID, index_ALLCOORDS, 'rows'));
LocB2(LocB2==0)=[];
v=EV(:,1:9);
newmat2 = [index_ALLCOORDS v];
correct_eigen_positions = newmat2(LocB2,:);

%define a,b,c components of eigenvectors for each orthogonal
principal
%direction
v2=correct_eigen_positions(:,1:12);
p=correct_eigen_positions(:,1:3);
    x = p(:,1);
    y = p(:,2);
    z = p(:,3);
x2 = correct_eigen_positions(:,1);
y2 = correct_eigen_positions(:,2);
z2 = correct_eigen_positions(:,3);
    a1 = v2(:,4);
    b4 = v2(:,7);
    c7 = v2(:,10);
    a2 = v2(:,5);
    b5 = v2(:,8);
    c8 = v2(:,11);
    a3 = v2(:,6);
    b6 = v2(:,9);
    c9 = v2(:,12);
RVectors1 = [a1 b4 c7];
RVectors2 = [a2 b5 c8];
RVectors3 = [a3 b6 c9];
R = [cosd(-90) 0 sind(-90); 0 1 0; -sind(-90) 0 cosd(-90)];
Yrotate1 = (R*RVectors1.').';
Yrotate2 = (R*RVectors2.').';
Yrotate3 = (R*RVectors3.').';
a1R = Yrotate1(:,1);
b4R = Yrotate1(:,2);
c7R = Yrotate1(:,3);
a2R = Yrotate2(:,1);
b5R = Yrotate2(:,2);
c8R = Yrotate2(:,3);
a3R = Yrotate3(:,1);
b6R = Yrotate3(:,2);
c9R = Yrotate3(:,3);
scatter3(x2,y2,z2);
hold on
quiver3(x,y,z,a1R,c7R,b4R,0);
axis equal;

```

```

savefig('Eigens147.fig');
saveas(gcf,'Eigens147','png')
hold off
scatter3(x2,y2,z2);
hold on
quiver3(x,y,z,a2R,c8R,b5R,0);
axis equal;
savefig('Eigens258.fig');
saveas(gcf,'Eigens258','png')
hold off
scatter3(x2,y2,z2);
hold on
quiver3(x,y,z,a3R,c9R,b6R,0);
axis equal;
savefig('Eigens369.fig');
saveas(gcf,'Eigens369','png')
hold off
filename = 'Eigens.mat';
save('Eigens.mat'); %save all variables as mat file
close all
function plot_slice_auto(basedir)
cd(basedir);
load('Eigens.mat','x2','y2','z2','a3R','b6R','c9R');
xmin = min(x2);
xmax = max(x2);
ymin = min(y2);
ymax = max(y2);
zmin = min(z2);
zmax = max(z2);
ys = (y2);
hold on
set(gca,'XLim',[xmin xmax],'YLim',[ymin ymax],'ZLim',[zmin zmax])
axis equal
for is = 1:length(ys)
    if ys(is)==1
        scatter3(x2(is),y2(is),z2(is))
        quiver3(x2(is),y2(is),z2(is),a3R(is),c9R(is),b6R(is),0)
    end
end
savefig('slicel_3D.fig');
hold off
close
hold on
axis equal;
for is = 1:length(ys)
    if ys(is)==1
        scatter(x2(is),z2(is))
        quiver(x2(is),z2(is),a3R(is),b6R(is),0)
    end
end
savefig('slicel_2D.fig');
hold off
close

hold on
set(gca,'XLim',[xmin xmax],'YLim',[ymin ymax],'ZLim',[zmin zmax])
axis equal
for is = 1:length(ys)
    if ys(is)==2
        scatter3(x2(is),y2(is),z2(is))
        quiver3(x2(is),y2(is),z2(is),a3R(is),c9R(is),b6R(is),0)
    end
end

```

```

    end
end
savefig('slice2_3D.fig');
hold off
close
hold on
axis equal;
for is = 1:length(ys)
    if ys(is)==2
        scatter(x2(is),z2(is))
        quiver(x2(is),z2(is),a3R(is),b6R(is),0)
    end
end
savefig('slice2_2D.fig');
hold off
close
hold on
set(gca, 'XLim', [xmin xmax], 'YLim', [ymin ymax], 'ZLim', [zmin zmax])
axis equal
for is = 1:length(ys)
    if ys(is)==3
        scatter3(x2(is),y2(is),z2(is))
        quiver3(x2(is),y2(is),z2(is),a3R(is),c9R(is),b6R(is),0)
    end
end
savefig('slice3_3D.fig');
hold off
close
hold on
axis equal;
for is = 1:length(ys)
    if ys(is)==3
        scatter(x2(is),z2(is))
        quiver(x2(is),z2(is),a3R(is),b6R(is),0)
    end
end
savefig('slice3_2D.fig');
hold off
close
hold on
set(gca, 'XLim', [xmin xmax], 'YLim', [ymin ymax], 'ZLim', [zmin zmax])
axis equal
for is = 1:length(ys)
    if ys(is)==4
        scatter3(x2(is),y2(is),z2(is))
        quiver3(x2(is),y2(is),z2(is),a3R(is),c9R(is),b6R(is),0)
    end
end
savefig('slice4_3D.fig');
hold off
close
hold on
axis equal;
for is = 1:length(ys)
    if ys(is)==4
        scatter(x2(is),z2(is))
        quiver(x2(is),z2(is),a3R(is),b6R(is),0)
    end
end
savefig('slice4_2D.fig');
hold off

```

```

close
hold on
set(gca, 'XLim', [xmin xmax], 'YLim', [ymin ymax], 'ZLim', [zmin zmax])
axis equal
for is = 1:length(ys)
    if ys(is)==5
        scatter3(x2(is), y2(is), z2(is))
        quiver3(x2(is), y2(is), z2(is), a3R(is), c9R(is), b6R(is), 0)
    end
end
savefig('slice5_3D.fig');
hold off
close
hold on
axis equal;
for is = 1:length(ys)
    if ys(is)==5
        scatter(x2(is), z2(is))
        quiver(x2(is), z2(is), a3R(is), b6R(is), 0)
    end
end
savefig('slice5_2D.fig');
hold off
close
hold on
set(gca, 'XLim', [xmin xmax], 'YLim', [ymin ymax], 'ZLim', [zmin zmax])
axis equal
for is = 1:length(ys)
    if ys(is)==6
        scatter3(x2(is), y2(is), z2(is))
        quiver3(x2(is), y2(is), z2(is), a3R(is), c9R(is), b6R(is), 0)
    end
end
savefig('slice6_3D.fig');
hold off
close

hold on
axis equal;
for is = 1:length(ys)
    if ys(is)==6
        scatter(x2(is), z2(is))
        quiver(x2(is), z2(is), a3R(is), b6R(is), 0)
    end
end
savefig('slice6_2D.fig');
hold off
close
hold on
set(gca, 'XLim', [xmin xmax], 'YLim', [ymin ymax], 'ZLim', [zmin zmax])
axis equal
for is = 1:length(ys)
    if ys(is)==7
        scatter3(x2(is), y2(is), z2(is))
        quiver3(x2(is), y2(is), z2(is), a3R(is), c9R(is), b6R(is), 0)
    end
end
savefig('slice7_3D.fig');
hold off
close

```

```

hold on
axis equal;
for is = 1:length(ys)
    if ys(is)==7
        scatter(x2(is),z2(is))
        quiver(x2(is),z2(is),a3R(is),b6R(is),0)
    end
end
savefig('slice7_2D.fig');
hold off
close
hold on
set(gca,'XLim',[xmin xmax],'YLim',[ymin ymax],'ZLim',[zmin zmax])
axis equal
for is = 1:length(ys)
    if ys(is)==8
        scatter3(x2(is),y2(is),z2(is))
        quiver3(x2(is),y2(is),z2(is),a3R(is),c9R(is),b6R(is),0)
    end
end
savefig('slice8_3D.fig');
hold off
close
hold on
axis equal;
for is = 1:length(ys)
    if ys(is)==8
        scatter(x2(is),z2(is))
        quiver(x2(is),z2(is),a3R(is),b6R(is),0)
    end
end
savefig('slice8_2D.fig');
hold off
close
hold on
set(gca,'XLim',[xmin xmax],'YLim',[ymin ymax],'ZLim',[zmin zmax])
axis equal
for is = 1:length(ys)
    if ys(is)==9
        scatter3(x2(is),y2(is),z2(is))
        quiver3(x2(is),y2(is),z2(is),a3R(is),c9R(is),b6R(is),0)
    end
end
savefig('slice9_3D.fig');
hold off
close
hold on
axis equal;
for is = 1:length(ys)
    if ys(is)==9
        scatter(x2(is),z2(is))
        quiver(x2(is),z2(is),a3R(is),b6R(is),0)
    end
end
savefig('slice9_2D.fig');
hold off
close
hold on
set(gca,'XLim',[xmin xmax],'YLim',[ymin ymax],'ZLim',[zmin zmax])
axis equal
for is = 1:length(ys)

```

```

        if ys(is)==10
            scatter3(x2(is),y2(is),z2(is))
            quiver3(x2(is),y2(is),z2(is),a3R(is),c9R(is),b6R(is),0)
        end
    end
    savefig('slice10_3D.fig');
    hold off
    close
    hold on
    axis equal;
    for is = 1:length(ys)
        if ys(is)==10
            scatter(x2(is),z2(is))
            quiver(x2(is),z2(is),a3R(is),b6R(is),0)
        end
    end
    savefig('slice10_2D.fig');
    hold off
    close
    hold on
    set(gca,'XLim',[xmin xmax],'YLim',[ymin ymax],'ZLim',[zmin zmax])
    axis equal
    for is = 1:length(ys)
        if ys(is)==11
            scatter3(x2(is),y2(is),z2(is))
            quiver3(x2(is),y2(is),z2(is),a3R(is),c9R(is),b6R(is),0)
        end
    end
    savefig('slice11_3D.fig');
    hold off
    close
    hold on
    axis equal;
    for is = 11:length(ys)
        if ys(is)==11
            scatter(x2(is),z2(is))
            quiver(x2(is),z2(is),a3R(is),b6R(is),0)
        end
    end
    savefig('slice11_2D.fig');
    hold off
    close
    hold on
    set(gca,'XLim',[xmin xmax],'YLim',[ymin ymax],'ZLim',[zmin zmax])
    axis equal
    for is = 1:length(ys)
        if ys(is)==12
            scatter3(x2(is),y2(is),z2(is))
            quiver3(x2(is),y2(is),z2(is),a3R(is),c9R(is),b6R(is),0)
        end
    end
    savefig('slice12_3D.fig');
    hold off
    close
    hold on
    axis equal;
    for is = 1:length(ys)
        if ys(is)==12
            scatter(x2(is),z2(is))
            quiver(x2(is),z2(is),a3R(is),b6R(is),0)
        end
    end

```

```

end
savefig('slice12_2D.fig');
hold off
close
hold on
set(gca, 'XLim', [xmin xmax], 'YLim', [ymin ymax], 'ZLim', [zmin zmax])
axis equal
for is = 1:length(ys)
    if ys(is)==13
        scatter3(x2(is),y2(is),z2(is))
        quiver3(x2(is),y2(is),z2(is),a3R(is),c9R(is),b6R(is),0)
    end
end
savefig('slice13_3D.fig');
hold off
close
hold on
axis equal;
for is = 1:length(ys)
    if ys(is)==13
        scatter(x2(is),z2(is))
        quiver(x2(is),z2(is),a3R(is),b6R(is),0)
    end
end
savefig('slice13_2D.fig');
hold off
close
hold on
set(gca, 'XLim', [xmin xmax], 'YLim', [ymin ymax], 'ZLim', [zmin zmax])
axis equal
for is = 1:length(ys)
    if ys(is)==14
        scatter3(x2(is),y2(is),z2(is))
        quiver3(x2(is),y2(is),z2(is),a3R(is),c9R(is),b6R(is),0)
    end
end
savefig('slice14_3D.fig');
hold off
close
hold on
axis equal;
for is = 1:length(ys)
    if ys(is)==14
        scatter(x2(is),z2(is))
        quiver(x2(is),z2(is),a3R(is),b6R(is),0)
    end
end
savefig('slice14_2D.fig');
hold off
close
hold on
set(gca, 'XLim', [xmin xmax], 'YLim', [ymin ymax], 'ZLim', [zmin zmax])
axis equal
for is = 1:length(ys)
    if ys(is)==15
        scatter3(x2(is),y2(is),z2(is))
        quiver3(x2(is),y2(is),z2(is),a3R(is),c9R(is),b6R(is),0)
    end
end
savefig('slice15_3D.fig');
hold off

```

```

close
hold on
axis equal;
for is = 1:length(ys)
    if ys(is)==15
        scatter(x2(is),z2(is))
        quiver(x2(is),z2(is),a3R(is),b6R(is),0)
    end
end
savefig('slice15_2D.fig');
hold off
close
close all

function Slice_3D(basedir)
cd(basedir);
load('Eigens.mat','x2','y2','z2','a3R','b6R','c9R','Yrotate3','correct_eigen_positions');
openfig('Eigens369.fig');
hf1 = figure(1);
set(0,'CurrentFigure',hf1);
for count = 1;
    dcmObject = datacursormode;
    pause
    datacursormode off
    cursor = getCursorInfo(dcmObject);
end
close all
vectors = extractfield(cursor, 'Position');
vectors=reshape(vectors,3,[]);
vectors = vectors.';
v_index = vectors(1:end,:);
c_index = correct_eigen_positions(:,1:3);
[LocB, Lia] = (ismember(v_index, c_index, 'rows'));
uv = Yrotate3(Lia,:);
a3Ru = uv(:,1);
b6Ru = uv(:,2);
c9Ru = uv(:,3);
scatter3(x2,y2,z2);
hold on
quiver3(x2,y2,z2,a3Ru,c9Ru,b6Ru);
axis equal;
savefig('Manual_Slice3D.fig');
hold off
scatter3(x2,z2);
hold on
quiver3(x2,z2,a3Ru,b6Ru);
axis equal;
savefig('Manual_Slice_2D.fig');
filename = 'Manual_Slice.mat';
save('Manual_Slice.mat');
close all

function NeckAngle(basedir)
cd(basedir);
uiopen('figure');
hf1 = figure(1);
set(0,'CurrentFigure',hf1);
for count = 1;
    dcmObject = datacursormode;
    pause

```

```

        datacursormode off
        cursor = getCursorInfo(dcmObject);
end
NeckAngle_positions = extractfield(cursor, 'Position');
NA = reshape(NeckAngle_positions,3,[]);
NA = NA.';
v = diff(NA);
NA1 = NA(1,:);
NA1x = NA1(:,1);
NA1y = NA1(:,2);
NA1z = NA1(:,3);
NA2 = NA(2,:);
NA2x = NA2(:,1);
NA2y = NA2(:,2);
NA2z = NA2(:,3);
pts = [NA1; NA2];
plot3(pts(:,1), pts(:,2), pts(:,3));
savefig('Neck_Angle.fig');
Neckangle = atan2(sqrt(v(:,2).^2+v(:,3).^2),v(:,1));
Neckangle = Neckangle*180/pi;
NeckAngle = round(Neckangle);
save('Neck_Angle.mat');
close all

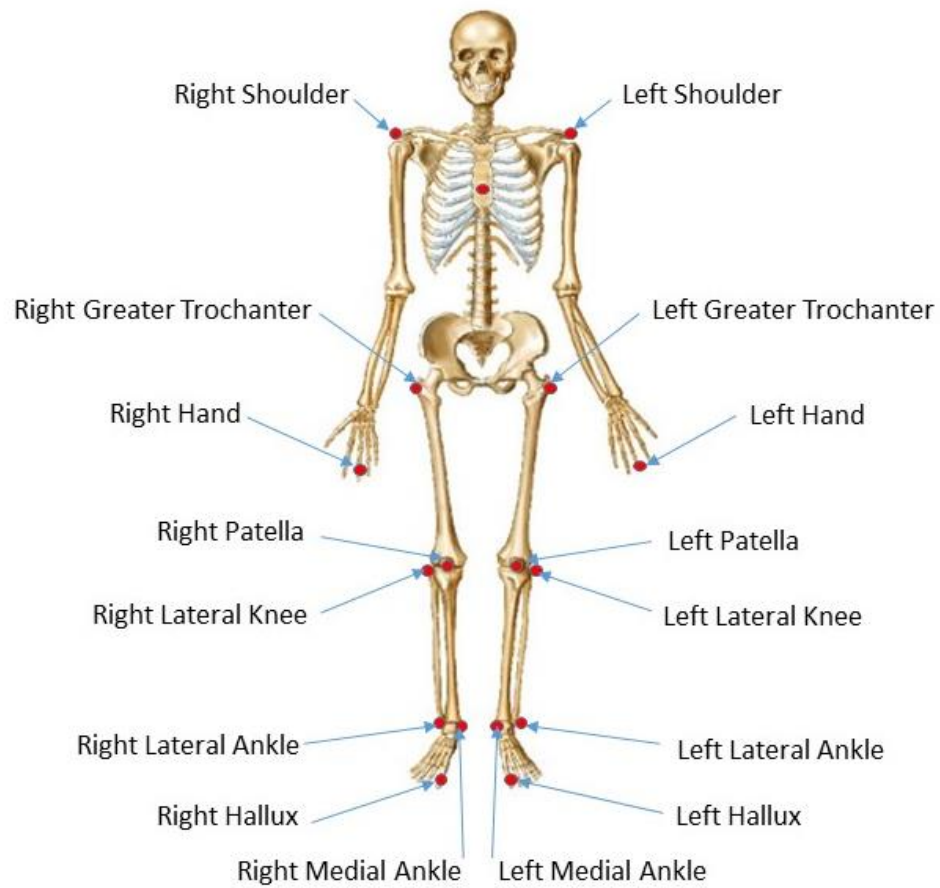
function calculate_x_axis_angles(basedir)
cd(basedir);
uiopen('figure');
load('Eigens.mat','x2','y2','z2','a3R','b6R','c9R','Yrotate3','correct_eigen_positions');
load('Neck_Angle.mat','v');
hf1 = figure(1);
set(0,'CurrentFigure',hf1);
for count = 1;
    dcmObject = datacursormode;
    pause
    datacursormode off
    cursor = getCursorInfo(dcmObject);
end
close all
vectors = extractfield(cursor, 'Position');
vectors=reshape(vectors,3,[]);
vectors = vectors.';
v_index = vectors(1:end,:);
c_index = correct_eigen_positions(:,1:3);
[LocB, Lia] = (ismember(v_index, c_index, 'rows'));
uv = Yrotate3(Lia,:);
a3Ru = uv(:,1);
b6Ru = uv(:,2);
c9Ru = uv(:,3);
R_all = [a3Ru b6Ru c9Ru];
for an = 1:length(cursor)
    ax(an) = atan2(sqrt(c9Ru(an).^2+b6Ru(an).^2),a3Ru(an));
    ax(an) = ax(an)*180/pi;
end
l = length(cursor);
for i = 1:length(l)
    v2 = repmat(v,[1 1 1]);
    for ij = 1:length(l)
        Relative_Angles = atan2(sqrt(c9Ru.^2+b6Ru.^2),a3Ru) -
atan2(sqrt(v2(:,2).^2+v2(:,3).^2),v2(:,1));
        Relative_Angles = Relative_Angles*180/pi;
    end
end

```

```
        end
    end
end
save('Trabecular_Angle_variables.mat');
save('Trabecular_Angles.mat', 'Relative_Angles');
close all
```

## APPENDIX C

---



Anterior view of retroreflective marker positions on the human subject determined by palpating relevant bony landmarks. Markers were used to capture the kinematics of sideways falls in chapter 4 for subsequent MDA modelling. There was also a single marker on each posterior borders of each calcaneus.

## APPENDIX D

---

Example of GaitSym code for the human musculoskeletal used for MDA simulations in chapter 5. The code defines relevant environmental and musculoskeletal parameters as well as the model's starting position in three-dimensional space e.g. at the point in time in which initiation of a sideways fall occurs.

```
<?xml version="1.0"?>
<GAITSYMODE>
<STATE SimulationTime="0.0000000000000000e+00"/>
<IOCONTROL OldStyleInputs="false" SanityCheckLeft="" SanityCheckRight="" SanityCheckAxis="Y"/>
<GLOBAL AllowInternalCollisions="true" BMR="0" CFM="1e-10" ContactMaxCorrectingVel="100"
ContactSurfaceLayer="0.001" DistanceTravelledBodyID="Trunk" ERP="0.2"
FitnessType="KinematicMatchMiniMax" GravityVector="0.0 0.0 -9.81" IntegrationStepSize="1e-4"
MechanicalEnergyLimit="0" MetabolicEnergyLimit="0" TimeLimit="0.6"/>
<INTERFACE BodyAxisSize="0.1 0.1 0.1" BodyColour="0.91 0.85 0.79 1.0"
DrawingOrder="Environment Joint Muscle Geom Body" EnvironmentAxisSize="1 1 1"
EnvironmentColour="0.5 0.5 1.0 1.0" GeomColour="0 0 1 0.5" JointAxisSize="0.05 0.05 0.05"
JointColour="0 1 0 1" StrapColour="1 0 0 1" StrapCylinderColour="0 1 1 0.5"
StrapCylinderLength="0.1" StrapForceColour="1 0 0 0.5" StrapForceRadius="0.01"
StrapForceScale="0.000001" StrapRadius="0.005" TrackBodyID="Trunk"/>
<ENVIRONMENT Plane="0 0 1 -0.025"/>
<BODY Badmesh="1" GraphicFile="HAT.obj" ID="Trunk" PositionHighBound="1000 4 4"
PositionLowBound="-10 -4 0" Scale="0.882000" Offset="0.0000000000000000e+00
0.0000000000000000e+00 2.1485832999999999e-02" Mass="5.1201000000000005e+01"
MOI="3.2398299999999999e+00 2.9809999999999987e+00 4.7168399999999992e-01 -
1.1221099999999992e-18 7.72926000000000030e-02 7.57251999999999944e-20" Density="-1"
Position="World 2.68258475465828994e+00 -1.53657117329301041e-01 9.84470601601357576e-
01" Quaternion="World 2.41224589388636339e+01d 5.35534865999291232e-01
6.14126625477246280e-01 5.79698969447981272e-01" LinearVelocity="World 1.0919 -0.90006 -
1.15" AngularVelocity="World 2.76537817857203216e-01 7.49540739272036294e-02
2.62413335055849350e-01"/>
<BODY Badmesh="1" GraphicFile="LeftThigh.obj" ID="LeftThigh" PositionHighBound="1000 4 4"
PositionLowBound="-10 -4 -0.5" Scale="0.933000" Offset="0.0000000000000000e+00
0.0000000000000000e+00 0.0000000000000000e+00" Mass="7.5000000000000000e+00"
MOI="1.39664420296205322e-01 1.39664420296205322e-01 1.96413405924106416e-02
0.0000000000000000e+00 0.0000000000000000e+00 0.0000000000000000e+00" Density="-1"
Position="Trunk -2.1827999999998545e-02 9.34960000000000235e-02 -2.55557000000000034e-
01 -1.35308431126190953e-16 -3.54539999999999161e-02 1.8380099999999964e-01"
Quaternion="Trunk 3.30745052477658845e+01d 5.84519098438421758e-01 -
6.37960290115195616e-01 5.01342290054280215e-01" LinearVelocity="World 0.599 -0.88155 -
0.51035" AngularVelocity="World 1.83283669082856315e+00 4.56016382707566892e-01
1.64982358225678394e+00"/>
```

<BODY Badmesh="1" GraphicFile="LeftShank.obj" ID="LeftShank" PositionHighBound="1000 4 4" PositionLowBound="-10 -4 -0.5" Scale="0.933000" Offset="0.0000000000000000e+00 0.0000000000000000e+00 0.0000000000000000e+00" Mass="3.4874999999999982e+00" MOI="6.36003177572906503e-02 6.36003177572906503e-02 4.20813551458132720e-03 0.0000000000000000e+00 0.0000000000000000e+00 0.0000000000000000e+00" Density="-1" Position="LeftThigh -2.332499999999998771e-02 -2.612400000000000777e-02 -2.40714000000000011e-01 -1.76941794549634324e-16 9.71445146547011973e-17 1.85853999999999908e-01" Quaternion="LeftThigh 2.45295769205255212e+01d -1.30657577825550648e-16 1.0000000000000000e+00 2.04152465352422894e-16" LinearVelocity="World 0.23135 -0.31815 -0.2409" AngularVelocity="World 1.83283669254230697e+00 4.56016383740070863e-01 1.64982358274291530e+00"/>

<BODY Badmesh="1" GraphicFile="Model4\_LeftPosteriorFoot.obj" ID="LeftRearFoot" PositionHighBound="1000 4 2" PositionLowBound="-10 -4 -0.5" Scale="1.039304" Offset="-3.30000000000000016e-02 -9.1999999999999984e-02 -3.8999999999999999e-02" Mass="4.9599999999999996e-01" MOI="4.12175890903932526e-03 4.12175890903932526e-03 9.37511568078650014e-04 0.0000000000000000e+00 0.0000000000000000e+00 0.0000000000000000e+00" Density="-1" Position="LeftShank 4.16333634234433703e-17 -6.93889390390722838e-17 -2.43325999999999987e-01 1.870699999999999459e-02 -2.078999999999999578e-03 3.741499999999999344e-02" Quaternion="LeftShank 1.91414942916024455e+00d 3.73877855771587282e-15 1.0000000000000000e+00 4.15419839746208047e-15" LinearVelocity="World 0.07275 0.05875 0.03275" AngularVelocity="World 2.77548678697791429e+00 -1.05120234713788929e+00 1.51369481205352230e+00"/>

<BODY Badmesh="1" GraphicFile="Model4\_LeftMidFoot.obj" ID="LeftMidFoot" PositionHighBound="1000 4 2" PositionLowBound="-10 -4 -0.5" Scale="1.039304" Offset="-9.1999999999999984e-02 -9.0999999999999997e-02 -4.2999999999999996e-02" Mass="2.21200000000000008e-01" MOI="4.12175890903932526e-03 4.12175890903932526e-03 9.37511568078650014e-04 0.0000000000000000e+00 0.0000000000000000e+00 0.0000000000000000e+00" Density="-1" Position="LeftRearFoot 4.09630000000001521e-02 -2.91300000000004923e-03 6.34000000000045118e-04 -2.03559999999998673e-02 -1.87300000000005409e-03 -3.52299999999994761e-03" Quaternion="LeftRearFoot 0.0000000000000000e+00d 1.0000000000000000e+00 0.0000000000000000e+00 0.0000000000000000e+00" LinearVelocity="World 0.07275 0.05875 0.03275" AngularVelocity="World 2.77548678697791429e+00 -1.05120234713788929e+00 1.51369481205352230e+00"/>

<BODY Badmesh="1" GraphicFile="LeftMetatarsals.obj" ID="LeftMTs" PositionHighBound="1000 4 2" PositionLowBound="-10 -4 -0.5" Scale="1.039304" Offset="-1.38000000000000012e-01 -1.0000000000000006e-01 -2.2999999999999996e-02" Mass="2.6740000000000027e-01" MOI="4.12175890903932526e-03 4.12175890903932526e-03 9.37511568078650014e-04 0.0000000000000000e+00 0.0000000000000000e+00 0.0000000000000000e+00" Density="-1" Position="LeftMidFoot 1.897099999999998144e-02 1.187200000000000336e-02 -1.02630000000000360e-02 -2.88370000000001958e-02 2.51800000000006359e-03 1.05229999999999421e-02" Quaternion="LeftMidFoot 0.0000000000000000e+00d 1.0000000000000000e+00 0.0000000000000000e+00 0.0000000000000000e+00" LinearVelocity="World 0.07275 0.05875 0.03275" AngularVelocity="World 2.77548678697791429e+00 -1.05120234713788929e+00 1.51369481205352230e+00"/>

<BODY Badmesh="1" GraphicFile="LeftFoot\_Toes.obj" ID="LeftToes" PositionHighBound="1000 4 2" PositionLowBound="-10 -4 -0.5" Scale="1.039304" Offset="-1.91000000000000003e-01 -1.0900000000000000e-01 -1.2000000000000002e-02" Mass="6.8599999999999943e-02" MOI="4.12175890903932526e-03 4.12175890903932526e-03 9.37511568078650014e-04

0.0000000000000000e+00 0.0000000000000000e+00 0.0000000000000000e+00" Density="-1"  
Position="LeftMTs 3.31019999999999648e-02 1.62119999999999626e-02 -  
7.135999999999998263e-03 -2.198099999999998965e-02 6.857999999999996742e-03  
4.296000000000004371e-03" Quaternion="LeftMTs 0.0000000000000000e+00d  
1.0000000000000000e+00 0.0000000000000000e+00 0.0000000000000000e+00"  
LinearVelocity="World 0.07275 0.05875 0.03275" AngularVelocity="World  
2.77548678697791429e+00 -1.05120234713788929e+00 1.51369481205352230e+00"/>

<BODY Badmesh="1" GraphicFile="RightThigh.obj" ID="RightThigh" PositionHighBound="1000 4 4"  
PositionLowBound="-10 -4 -0.5" Scale="0.933000" Offset="0.0000000000000000e+00  
0.0000000000000000e+00 0.0000000000000000e+00" Mass="7.5000000000000000e+00"  
MOI="1.39664420296205322e-01 1.39664420296205322e-01 1.96413405924106416e-02  
0.0000000000000000e+00 0.0000000000000000e+00 0.0000000000000000e+00" Density="-1"  
Position="Trunk -2.182799999999998822e-02 -9.34960000000000235e-02 -2.55557000000000090e-  
01 -1.00613961606654811e-16 3.5453999999999994e-02 1.83800999999999937e-01"  
Quaternion="Trunk 3.25973690950907908e+01d 6.71738100799669779e-01 -  
6.63524308889730907e-01 -3.29398566248333413e-01" LinearVelocity="World 0.9869 -0.5123 -  
0.9471" AngularVelocity="World 1.84381758306240418e+00 4.21635132474876828e-01  
1.09071047499057627e+00"/>

<BODY Badmesh="1" GraphicFile="RightShank.obj" ID="RightShank" PositionHighBound="1000 4 4"  
PositionLowBound="-10 -4 -0.5" Scale="0.933000" Offset="0.0000000000000000e+00  
0.0000000000000000e+00 0.0000000000000000e+00" Mass="3.4874999999999982e+00"  
MOI="6.36003177572906503e-02 6.36003177572906503e-02 4.20813551458132720e-03  
0.0000000000000000e+00 0.0000000000000000e+00 0.0000000000000000e+00" Density="-1"  
Position="RightThigh -2.332499999999997938e-02 2.61239999999999528e-02 -  
2.40714000000000011e-01 9.02056207507939689e-17 -2.77555756156289135e-17  
1.85854000000000130e-01" Quaternion="RightThigh 4.28568359331352582e+01d  
9.25911309710342777e-17 1.0000000000000000e+00 -2.37413156335985304e-18"  
LinearVelocity="World 0.4155 -0.172 -0.34105" AngularVelocity="World 1.85016538389823926e+00  
6.76195506621346087e-01 1.27138041734208462e+00"/>

<BODY Badmesh="1" GraphicFile="Model4\_RightPosteriorFoot.obj" ID="RightRearFoot"  
PositionHighBound="1000 4 4" PositionLowBound="-10 -4 -0.5" Scale="1.039304" Offset="-  
3.30000000000000016e-02 9.1999999999999984e-02 -3.8999999999999999e-02"  
Mass="4.9599999999999996e-01" MOI="4.12175890903932526e-03 4.12175890903932526e-03  
9.37511568078650014e-04 0.0000000000000000e+00 0.0000000000000000e+00  
0.0000000000000000e+00" Density="-1" Position="RightShank 6.93889390390722838e-17 -  
1.38777878078144568e-17 -2.4332599999999987e-01 1.87070000000001402e-02  
2.07899999999999231e-03 3.74150000000000316e-02" Quaternion="RightShank  
2.01927177664309880e+01d 3.16656209929168716e-16 -1.0000000000000000e+00  
7.91640524822921790e-17" LinearVelocity="World 0.04425 -0.0787 0.0114"  
AngularVelocity="World 1.83599901274737509e+00 1.08092748423344570e-01  
8.68178982462498028e-01"/>

<BODY Badmesh="1" GraphicFile="Model4\_RightMidFoot.obj" ID="RightMidFoot"  
PositionHighBound="1000 4 2" PositionLowBound="-10 -4 -0.5" Scale="1.039304" Offset="-  
9.1999999999999984e-02 9.0999999999999976e-02 -4.2999999999999966e-02"  
Mass="2.21200000000000008e-01" MOI="4.12175890903932526e-03 4.12175890903932526e-03  
9.37511568078650014e-04 0.0000000000000000e+00 0.0000000000000000e+00  
0.0000000000000000e+00" Density="-1" Position="RightRearFoot 4.09630000000000410e-02  
2.9129999999999979e-03 6.34000000000031240e-04 -2.03559999999999054e-02  
1.87300000000002330e-03 -3.52299999999996062e-03" Quaternion="RightRearFoot  
0.0000000000000000e+00d 1.0000000000000000e+00 0.0000000000000000e+00

0.0000000000000000e+00" LinearVelocity="World 0.04425 -0.0787 0.0114"  
AngularVelocity="World 1.83599901274737509e+00 1.08092748423344570e-01  
8.68178982462498028e-01"/>

<BODY Badmesh="1" GraphicFile="RightMetatarsals.obj" ID="RightMTs" PositionHighBound="1000  
4 2" PositionLowBound="-10 -4 -0.5" Scale="1.039304" Offset="-1.3800000000000012e-01  
1.0000000000000006e-01 -2.2999999999999996e-02" Mass="2.6740000000000027e-01"  
MOI="4.12175890903932526e-03 4.12175890903932526e-03 9.37511568078650014e-04  
0.0000000000000000e+00 0.0000000000000000e+00 0.0000000000000000e+00" Density="-1"  
Position="RightMidFoot 1.9266999999997635e-02 -1.1872000000000058e-02 -  
1.0263000000001123e-02 -2.8541000000002884e-02 -2.5180000000002196e-03  
1.0522999999998797e-02" Quaternion="RightMidFoot 0.0000000000000000e+00d  
1.0000000000000000e+00 0.0000000000000000e+00 0.0000000000000000e+00"  
LinearVelocity="World 0.04425 -0.0787 0.0114" AngularVelocity="World  
1.83599901274737509e+00 1.08092748423344570e-01 8.68178982462498028e-01"/>

<BODY Badmesh="1" GraphicFile="RightFoot\_Toes.obj" ID="RightToes" PositionHighBound="1000 4  
2" PositionLowBound="-10 -4 -0.5" Scale="1.039304" Offset="-1.9100000000000003e-01  
1.0900000000000000e-01 -1.2000000000000002e-02" Mass="6.859999999999943e-02"  
MOI="4.12175890903932526e-03 4.12175890903932526e-03 9.37511568078650014e-04  
0.0000000000000000e+00 0.0000000000000000e+00 0.0000000000000000e+00" Density="-1"  
Position="RightMTs 3.2062000000001529e-02 -1.6212000000000077e-02 -  
7.1359999999993580e-03 -2.3020999999998506e-02 -6.8580000000000472e-03  
4.2960000000006713e-03" Quaternion="RightMTs 0.0000000000000000e+00d  
1.0000000000000000e+00 0.0000000000000000e+00 0.0000000000000000e+00"  
LinearVelocity="World 0.04425 -0.0787 0.0114" AngularVelocity="World  
1.83599901274737509e+00 1.08092748423344570e-01 8.68178982462498028e-01"/>

<REPORTER BodyID="Trunk" ID="RightASIS" Type="Position" Position="Trunk  
6.10500000000002152e-02 -1.2688199999999995e-01 -1.9452600000000088e-01"  
Quaternion="Trunk 1.0000000000000000e+00 0.0000000000000000e+00  
0.0000000000000000e+00 0.0000000000000000e+00"/>

<REPORTER BodyID="Trunk" ID="LeftASIS" Type="Position" Position="Trunk  
6.10500000000001181e-02 1.2688199999999939e-01 -1.9452600000000088e-01"  
Quaternion="Trunk 1.0000000000000000e+00 0.0000000000000000e+00  
0.0000000000000000e+00 0.0000000000000000e+00"/>

<REPORTER BodyID="Trunk" ID="SternumMarker" Type="Position" Position="Trunk  
1.0527799999999886e-01 -5.26922255827955155e-17 2.2051699999999797e-02"  
Quaternion="Trunk 1.0000000000000000e+00 0.0000000000000000e+00  
0.0000000000000000e+00 0.0000000000000000e+00"/>

<REPORTER BodyID="RightThigh" ID="R\_GRTrochMarker" Type="Position" Position="RightThigh -  
2.44400000000013964e-03 -5.3414000000000448e-02 1.6251500000000021e-01"  
Quaternion="RightThigh 1.0000000000000000e+00 0.0000000000000000e+00  
0.0000000000000000e+00 0.0000000000000000e+00"/>

<REPORTER BodyID="RightThigh" ID="R\_LatKneeMarker" Type="Position" Position="RightThigh -  
1.4640000000001876e-02 -2.9363000000000141e-02 -2.421559999999982e-01"  
Quaternion="RightThigh 1.0000000000000000e+00 0.0000000000000000e+00  
0.0000000000000000e+00 0.0000000000000000e+00"/>

<REPORTER BodyID="RightThigh" ID="R\_PatellaMarker" Type="Position" Position="RightThigh 3.0997399999999995989e-02 1.175499999999999738e-02 -2.639246999999999790e-01" Quaternion="RightThigh 1.0000000000000000e+00 0.0000000000000000e+00 0.0000000000000000e+00 0.0000000000000000e+00"/>

<REPORTER BodyID="RightShank" ID="R\_LatAnkleMarker" Type="Position" Position="RightShank - 9.99999999985068388e-04 -3.95370000000000027e-02 -2.35079999999999956e-01" Quaternion="RightShank 1.0000000000000044e+00 0.0000000000000000e+00 0.0000000000000000e+00 -1.38777878078144568e-17"/>

<REPORTER BodyID="RightRearFoot" ID="R\_CalcaneusMarker" Type="Position" Position="RightRearFoot -4.53900000000000969e-02 -8.0300000000010520e-04 - 1.72810000000000359e-02" Quaternion="RightRearFoot 1.0000000000000044e+00 0.0000000000000000e+00 0.0000000000000000e+00 0.0000000000000000e+00"/>

<REPORTER BodyID="RightShank" ID="R\_MedAnkleMarker" Type="Position" Position="RightShank 3.29219999999967594e-03 4.0732199999999962e-02 -2.28277600000000164e-01" Quaternion="RightShank 1.0000000000000044e+00 0.0000000000000000e+00 0.0000000000000000e+00 -1.38777878078144568e-17"/>

<REPORTER BodyID="RightToes" ID="R\_HalluxMarker" Type="Position" Position="RightToes 4.23610000000000098e-02 2.0634999999999797e-02 1.0999999999999334e-02" Quaternion="RightToes 1.0000000000000044e+00 0.0000000000000000e+00 0.0000000000000000e+00 0.0000000000000000e+00"/>

<REPORTER BodyID="LeftThigh" ID="L\_GRTrochMarker" Type="Position" Position="LeftThigh - 2.44400000000009887e-03 5.34139999999999893e-02 1.6251500000000048e-01" Quaternion="LeftThigh 1.0000000000000044e+00 0.0000000000000000e+00 0.0000000000000000e+00 0.0000000000000000e+00"/>

<REPORTER BodyID="LeftThigh" ID="L\_LatKneeMarker" Type="Position" Position="LeftThigh - 1.4639999999997574e-02 2.9362999999998614e-02 -2.421599999999982e-01" Quaternion="LeftThigh 1.0000000000000044e+00 0.0000000000000000e+00 0.0000000000000000e+00 0.0000000000000000e+00"/>

<REPORTER BodyID="LeftThigh" ID="L\_PatellaMarker" Type="Position" Position="LeftThigh 3.09974000000002164e-02 -1.17550000000000293e-02 -2.63924700000000123e-01" Quaternion="LeftThigh 1.0000000000000044e+00 0.0000000000000000e+00 0.0000000000000000e+00 0.0000000000000000e+00"/>

<REPORTER BodyID="LeftShank" ID="L\_LatAnkleMarker" Type="Position" Position="LeftShank - 9.99999999985113491e-04 3.9536999999999472e-02 -2.3507999999999956e-01" Quaternion="LeftShank 1.0000000000000022e+00 0.0000000000000000e+00 0.0000000000000000e+00 6.93889390390722838e-18"/>

<REPORTER BodyID="LeftRearFoot" ID="L\_CalcaneusMarker" Type="Position" Position="LeftRearFoot -4.53900000000001247e-02 8.0299999999999461e-04 - 1.72810000000000290e-02" Quaternion="LeftRearFoot 1.0000000000000044e+00 0.0000000000000000e+00 0.0000000000000000e+00 0.0000000000000000e+00"/>

<REPORTER BodyID="LeftShank" ID="L\_MedAnkleMarker" Type="Position" Position="LeftShank 3.29220000000016166e-03 -4.07322000000001488e-02 -2.2827759999999914e-01" Quaternion="LeftShank 1.0000000000000022e+00 0.0000000000000000e+00 0.0000000000000000e+00 6.93889390390722838e-18"/>

<REPORTER BodyID="LeftToes" ID="L\_HalluxMarker" Type="Position" Position="LeftToes 4.23610000000003081e-02 -2.06350000000000387e-02 1.10000000000000549e-02"

Quaternion="LeftToes 1.0000000000000044e+00 0.0000000000000000e+00  
0.0000000000000000e+00 0.0000000000000000e+00"/>

<REPORTER BodyID="Trunk" ID="RightShoulderMarker" Type="Position" Position="Trunk -  
3.8807799999999548e-02 -1.8570100000000116e-01 2.5567000000000226e-01"  
Quaternion="Trunk 1.0000000000000000e+00 0.0000000000000000e+00  
0.0000000000000000e+00 0.0000000000000000e+00"/>

<REPORTER BodyID="Trunk" ID="LeftShoulderMarker" Type="Position" Position="Trunk -  
3.88077999999997328e-02 1.8570100000000005e-01 2.5567000000000170e-01"  
Quaternion="Trunk 1.0000000000000000e+00 0.0000000000000000e+00  
0.0000000000000000e+00 0.0000000000000000e+00"/>

<REPORTER BodyID="Trunk" ID="LeftHandMarker" Type="Position" Position="Trunk  
5.6891000000003024e-02 1.5922800000000008e-01 -4.988499999999905e-01"  
Quaternion="Trunk 1.0000000000000000e+00 0.0000000000000000e+00  
0.0000000000000000e+00 0.0000000000000000e+00"/>

<REPORTER BodyID="Trunk" ID="RightHandMarker" Type="Position" Position="Trunk  
5.6890999999999347e-02 -1.5922799999999981e-01 -4.9885000000000016e-01"  
Quaternion="Trunk 1.0000000000000000e+00 0.0000000000000000e+00  
0.0000000000000000e+00 0.0000000000000000e+00"/>

<JOINT Body1ID="Trunk" Body2ID="LeftThigh" ID="LeftHip" ParamHiStop="1.745329252"  
ParamLoStop="-0.261799388" Type="Ball" BallAxis="Trunk 0.0000000000000000e+00  
1.0000000000000000e+00 0.0000000000000000e+00" Body2HingeAnchor="LeftThigh -  
6.93889390390722838e-17 -3.5454000000000133e-02 1.838009999999992e-01"  
Body2HingeAxis="LeftThigh 0.0000000000000000e+00 1.0000000000000000e+00  
0.0000000000000000e+00" StartAngleReference="0.0000000000000000e+00" BallAnchor="Trunk  
-2.18279999999998545e-02 9.3496000000000235e-02 -2.5555700000000034e-01"  
Body2BallAnchor="LeftThigh -1.35308431126190953e-16 -3.5453999999999161e-02  
1.8380099999999964e-01" EulerReferenceVectors="0.0000000000000000e+00  
0.0000000000000000e+00 0.0000000000000000e+00 0.0000000000000000e+00  
0.0000000000000000e+00 0.0000000000000000e+00"/>

<JOINT Body1ID="LeftThigh" Body2ID="LeftShank" ID="LeftKnee" ParamHiStop="0.000"  
ParamLoStop="-2.35619449" Type="Hinge" HingeAnchor="LeftThigh -2.33249999999998771e-02 -  
2.61240000000000777e-02 -2.4071400000000011e-01" HingeAxis="LeftThigh -  
4.16333634234433703e-17 1.0000000000000022e+00 5.55111512312578270e-17"  
Body2HingeAnchor="LeftShank -1.76941794549634324e-16 9.71445146547011973e-17  
1.8585399999999908e-01" Body2HingeAxis="LeftShank -2.77555756156289135e-16  
1.0000000000000022e+00 2.22044604925031308e-16"  
StartAngleReference="0.0000000000000000e+00"/>

<JOINT Body1ID="LeftShank" Body2ID="LeftRearFoot" ID="LeftAnkle" ParamHiStop="1.919862177"  
ParamLoStop="1.047197551" Type="Hinge" HingeAnchor="LeftShank 4.16333634234433703e-17 -  
6.93889390390722838e-17 -2.4332599999999987e-01" HingeAxis="LeftShank  
2.77555756156289135e-17 1.0000000000000000e+00 2.22044604925031308e-16"  
Body2HingeAnchor="LeftRearFoot 1.8706999999999459e-02 -2.0789999999999578e-03  
3.7414999999999344e-02" Body2HingeAxis="LeftRearFoot 8.32667268468867405e-17  
1.0000000000000000e+00 0.0000000000000000e+00"  
StartAngleReference="1.57079633000000007e+00"/>

<JOINT Body1ID="LeftRearFoot" Body2ID="LeftMidFoot" ID="LeftMidFootJoint"  
ParamHiStop="0.261799388" ParamLoStop="-0.261799388" Type="Fixed" UniversalAxis1="World 1  
0 0" UniversalAxis2="World 1 0 0" HingeAnchor="LeftRearFoot 4.09630000000001521e-02 -  
2.91300000000004923e-03 6.34000000000045118e-04" HingeAxis="LeftRearFoot -  
2.63677968348474678e-16 9.9999999999999889e-01 5.55111512312578270e-17"  
Body2HingeAnchor="LeftMidFoot -2.03559999999998673e-02 -1.87300000000005409e-03 -  
3.52299999999994761e-03" Body2HingeAxis="LeftMidFoot -2.63677968348474678e-16  
9.9999999999999889e-01 5.55111512312578270e-17"  
StartAngleReference="0.0000000000000000e+00"/>

<JOINT Body1ID="LeftMidFoot" Body2ID="LeftMTs" ID="LeftMTJoint" ParamHiStop="0.261799388"  
ParamLoStop="-0.261799388" Type="Fixed" UniversalAxis1="World 1 0 0" UniversalAxis2="World 1  
0 0" HingeAnchor="LeftMidFoot 1.89709999999998144e-02 1.18720000000000336e-02 -  
1.02630000000000360e-02" HingeAxis="LeftMidFoot -2.25733059193240354e-01  
9.59365501571270429e-01 -1.69299794394930203e-01" Body2HingeAnchor="LeftMTs -  
2.88370000000001958e-02 2.51800000000006359e-03 1.05229999999999421e-02"  
Body2HingeAxis="LeftMTs -2.25733059193240354e-01 9.59365501571270429e-01 -  
1.69299794394930203e-01" StartAngleReference="0.0000000000000000e+00"/>

<JOINT Body1ID="LeftMTs" Body2ID="LeftToes" ID="LeftMTPJ" ParamHiStop="0.785398163"  
ParamLoStop="-0.087266463" Type="Fixed" HingeAnchor="LeftMTs 3.3101999999999648e-02  
1.62119999999999626e-02 -7.13599999999998263e-03" HingeAxis="LeftMTs -  
2.42535625036333191e-01 9.70142500145331876e-01 0.0000000000000000e+00"  
Body2HingeAnchor="LeftToes -2.19809999999998965e-02 6.85799999999996742e-03  
4.29600000000004371e-03" Body2HingeAxis="LeftToes -2.42535625036333191e-01  
9.70142500145331876e-01 0.0000000000000000e+00"  
StartAngleReference="0.0000000000000000e+00"/>

<JOINT Body1ID="Trunk" Body2ID="RightThigh" ID="RightHip" ParamHiStop="1.745329252"  
ParamLoStop="-0.261799388" Type="Ball" BallAxis="Trunk 0.0000000000000000e+00  
1.0000000000000000e+00 0.0000000000000000e+00" Body2HingeAnchor="RightThigh -  
8.32667268468867405e-17 3.54540000000000133e-02 1.83801000000000020e-01"  
Body2HingeAxis="RightThigh 0.0000000000000000e+00 1.0000000000000000e+00  
0.0000000000000000e+00" StartAngleReference="0.0000000000000000e+00" BallAnchor="Trunk  
-2.18279999999998822e-02 -9.34960000000000235e-02 -2.55557000000000090e-01"  
Body2BallAnchor="RightThigh -1.00613961606654811e-16 3.5453999999999994e-02  
1.8380099999999937e-01" EulerReferenceVectors="0.0000000000000000e+00  
0.0000000000000000e+00 0.0000000000000000e+00 0.0000000000000000e+00  
0.0000000000000000e+00 0.0000000000000000e+00"/>

<JOINT Body1ID="RightThigh" Body2ID="RightShank" ID="RightKnee" ParamHiStop="0.000"  
ParamLoStop="-2.35619449" Type="Hinge" HingeAnchor="RightThigh -2.33249999999997938e-02  
2.6123999999999528e-02 -2.4071400000000011e-01" HingeAxis="RightThigh -  
1.04083408558608426e-17 1.0000000000000000e+00 5.55111512312578270e-17"  
Body2HingeAnchor="RightShank 9.02056207507939689e-17 -2.77555756156289135e-17  
1.85854000000000130e-01" Body2HingeAxis="RightShank 5.55111512312578270e-17  
1.0000000000000000e+00 -1.11022302462515654e-16"  
StartAngleReference="0.0000000000000000e+00"/>

<JOINT Body1ID="RightShank" Body2ID="RightRearFoot" ID="RightAnkle"  
ParamHiStop="1.919862177" ParamLoStop="1.047197551" Type="Hinge" HingeAnchor="RightShank  
6.93889390390722838e-17 -1.38777878078144568e-17 -2.4332599999999987e-01"  
HingeAxis="RightShank 0.0000000000000000e+00 1.00000000000000044e+00 -  
5.55111512312578270e-17" Body2HingeAnchor="RightRearFoot 1.87070000000001402e-02  
2.0789999999999231e-03 3.74150000000000316e-02" Body2HingeAxis="RightRearFoot -

2.77555756156289135e-17 1.0000000000000044e+00 -5.55111512312578270e-17"  
StartAngleReference="1.57079633000000007e+00"/>

<JOINT Body1ID="RightRearFoot" Body2ID="RightMidFoot" ID="RightMidFootJoint"  
ParamHiStop="0.261799388" ParamLoStop="-0.261799388" Type="Fixed" UniversalAxis1="World 1  
0 0" UniversalAxis2="World 1 0 0" HingeAnchor="RightRearFoot 4.09630000000000410e-02  
2.9129999999999979e-03 6.34000000000031240e-04" HingeAxis="RightRearFoot -  
5.55111512312578270e-17 1.0000000000000022e+00 0.000000000000000e+00"  
Body2HingeAnchor="RightMidFoot -2.0355999999999054e-02 1.87300000000002330e-03 -  
3.5229999999996062e-03" Body2HingeAxis="RightMidFoot -5.55111512312578270e-17  
1.0000000000000022e+00 0.000000000000000e+00"  
StartAngleReference="0.000000000000000e+00"/>

<JOINT Body1ID="RightMidFoot" Body2ID="RightMTs" ID="RightMTJoint"  
ParamHiStop="0.261799388" ParamLoStop="-0.261799388" Type="Fixed" UniversalAxis1="World 1  
0 0" UniversalAxis2="World 1 0 0" HingeAnchor="RightMidFoot 1.9266999999997635e-02 -  
1.18720000000000058e-02 -1.02630000000001123e-02" HingeAxis="RightMidFoot  
2.25733059193240077e-01 9.59365501571270651e-01 1.69299794394930203e-01"  
Body2HingeAnchor="RightMTs -2.85410000000002884e-02 -2.51800000000002196e-03  
1.0522999999998797e-02" Body2HingeAxis="RightMTs 2.25733059193240077e-01  
9.59365501571270651e-01 1.69299794394930203e-01"  
StartAngleReference="0.000000000000000e+00"/>

<JOINT Body1ID="RightMTs" Body2ID="RightToes" ID="RightMTPJ" ParamHiStop="0.785398163"  
ParamLoStop="-0.087266463" Type="Fixed" HingeAnchor="RightMTs 3.20620000000001529e-02 -  
1.62120000000000077e-02 -7.1359999999993580e-03" HingeAxis="RightMTs  
2.42535625036332941e-01 9.70142500145331876e-01 0.000000000000000e+00"  
Body2HingeAnchor="RightToes -2.3020999999998506e-02 -6.85800000000000472e-03  
4.29600000000006713e-03" Body2HingeAxis="RightToes 2.42535625036332941e-01  
9.70142500145331876e-01 0.000000000000000e+00"  
StartAngleReference="0.000000000000000e+00"/>

<GEOM Abort="false" BodyID="RightThigh" ContactSoftERP="0.1" ID="RightThighContact1"  
Length="0.1" Mu="0.5" Radius="0.055" SpringConstant="68.9e4" DampingConstant="1.5e4"  
Type="CappedCylinder" Position="RightThigh -0.01 -0.005 0.1" Quaternion="RightThigh  
7.07106781186547351e-01 5.55111512312578393e-17 1.11022302462515679e-16 -  
7.07106781186547795e-01"/>

<GEOM Abort="false" BodyID="RightThigh" ContactSoftERP="0.1" ID="RightThighContact2"  
Length="0.15" Mu="0.5" Radius="0.05" SpringConstant="68.9e4" DampingConstant="1.5e4"  
Type="CappedCylinder" Position="RightThigh -0.025 0.01 -0.12" Quaternion="RightThigh  
7.07106781186547351e-01 5.55111512312578393e-17 1.11022302462515679e-16 -  
7.07106781186547795e-01"/>

<GEOM Abort="false" BodyID="RightShank" ContactSoftERP="0.1" ID="RightShankContact"  
Length="0.35" Mu="0.5" Radius="0.04" SpringConstant="68.9e4" DampingConstant="1.5e4"  
Type="CappedCylinder" Position="RightShank 0.01 -0.01 -0.035" Quaternion="RightShank  
7.07106781186547351e-01 5.55111512312578393e-17 1.11022302462515679e-16 -  
7.07106781186547795e-01"/>

<GEOM Abort="false" BodyID="LeftRearFoot" ContactSoftERP="0.1"  
ID="Main.Model.HumanModel.Left.Leg.Seg.Foot.HeelContactNode1" Length="0.02" Mu="1.0"  
Radius="0.01" SpringConstant="1e6" Type="CappedCylinder" Position="LeftRearFoot -  
1.7667999999999129e-02 -2.0789999999999231e-03 -2.91400000000000131e-02"

Quaternion="LeftRearFoot 7.07106781186547351e-01 -7.07106781186547795e-01  
5.55111512312578393e-17 1.11022302462515679e-16"/>

<GEOM Abort="false" BodyID="LeftRearFoot" ContactSoftERP="0.1"  
ID="Main.Model.HumanModel.Left.Leg.Seg.Foot.HeelContactNode2" Length="0.02" Mu="1.0"  
Radius="0.01" SpringConstant="1e6" Type="CappedCylinder" Position="LeftRearFoot  
7.27500000000012425e-03 -2.07900000000003048e-03 -2.8619999999999719e-02"  
Quaternion="LeftRearFoot 7.07106781186547351e-01 -7.07106781186547795e-01  
5.55111512312578393e-17 1.11022302462515679e-16"/>

<GEOM Abort="false" BodyID="LeftMidFoot" ContactSoftERP="0.1"  
ID="Main.Model.HumanModel.Left.Leg.Seg.Foot.MidFootLateralContactNode" Length="0.02"  
Mu="1.0" Radius="0.01" SpringConstant="1e6" Type="CappedCylinder" Position="LeftMidFoot  
1.6753999999999287e-02 -1.8526999999999602e-02 -2.34240000000000489e-02"  
Quaternion="LeftMidFoot 7.07106781186547351e-01 -7.07106781186547795e-01  
5.55111512312578393e-17 1.11022302462515679e-16"/>

<GEOM Abort="false" BodyID="LeftMidFoot" ContactSoftERP="0.1"  
ID="Main.Model.HumanModel.Left.Leg.Seg.Foot.MidFootMedialContactNode" Length="0.02"  
Mu="1.0" Radius="0.01" SpringConstant="1e6" Type="CappedCylinder" Position="LeftMidFoot -  
7.4599999999952430e-04 1.5586000000000096e-02 -2.8864000000000285e-02"  
Quaternion="LeftMidFoot 7.07106781186547351e-01 -7.07106781186547795e-01  
5.55111512312578393e-17 1.11022302462515679e-16"/>

<GEOM Abort="false" BodyID="LeftMTs" ContactSoftERP="0.1"  
ID="Main.Model.HumanModel.Left.Leg.Seg.Foot.MTHeadLateralContactNode" Length="0.02"  
Mu="1.0" Radius="0.01" SpringConstant="1e6" Type="CappedCylinder" Position="LeftMTs  
1.0496999999999525e-02 3.1178999999999949e-02 -1.1431999999999942e-02"  
Quaternion="LeftMTs 7.07106781186547351e-01 -7.07106781186547795e-01  
5.55111512312578393e-17 1.11022302462515679e-16"/>

<GEOM Abort="false" BodyID="LeftMTs" ContactSoftERP="0.1"  
ID="Main.Model.HumanModel.Left.Leg.Seg.Foot.MTMeadMedialContactNode" Length="0.02"  
Mu="1.0" Radius="0.01" SpringConstant="1e6" Type="CappedCylinder" Position="LeftMTs  
3.6479999999999985e-02 -1.2472000000000473e-02 -1.14319999999999561e-02"  
Quaternion="LeftMTs 7.07106781186547351e-01 -7.07106781186547795e-01  
5.55111512312578393e-17 1.11022302462515679e-16"/>

<GEOM Abort="false" BodyID="LeftToes" ContactSoftERP="0.1"  
ID="Main.Model.HumanModel.Left.Leg.Seg.Foot.ToeMedialContactNode" Length="0.025" Mu="1.0"  
Radius="0.01" SpringConstant="1e6" Type="CappedCylinder" Position="LeftToes  
1.3302999999999364e-02 -1.4777999999999960e-02 -1.56125112837912638e-17"  
Quaternion="LeftToes 7.07106781186547351e-01 -7.07106781186547795e-01  
5.55111512312578393e-17 1.11022302462515679e-16"/>

<GEOM Abort="false" BodyID="RightRearFoot" ContactSoftERP="0.1"  
ID="Main.Model.HumanModel.Right.Leg.Seg.Foot.HeelContactNode1" Length="0.02" Mu="1.0"  
Radius="0.01" SpringConstant="1e6" Type="CappedCylinder" Position="RightRearFoot -  
1.7668000000000205e-02 2.0789999999999752e-03 -2.9140000000000062e-02"  
Quaternion="RightRearFoot 7.07106781186547240e-01 -7.07106781186547906e-01  
9.71445146547012219e-17 1.38777878078144592e-16"/>

<GEOM Abort="false" BodyID="RightRearFoot" ContactSoftERP="0.1"  
ID="Main.Model.HumanModel.Right.Leg.Seg.Foot.HeelContactNode2" Length="0.02" Mu="1.0"  
Radius="0.01" SpringConstant="1e6" Type="CappedCylinder" Position="RightRearFoot  
7.27500000000014073e-03 2.07900000000002527e-03 -2.8619999999999719e-02"

Quaternion="RightRearFoot 7.07106781186547240e-01 -7.07106781186547906e-01  
9.71445146547012219e-17 1.38777878078144592e-16"/>

<GEOM Abort="false" BodyID="RightMidFoot" ContactSoftERP="0.1"  
ID="Main.Model.HumanModel.Right.Leg.Seg.Foot.MidFootLateralContactNode" Length="0.02"  
Mu="1.0" Radius="0.01" SpringConstant="1e6" Type="CappedCylinder" Position="RightMidFoot  
1.6754000000000744e-02 1.8527000000000018e-02 -2.3423999999999345e-02"  
Quaternion="RightMidFoot 7.07106781186547240e-01 -7.07106781186547906e-01  
9.71445146547012219e-17 1.38777878078144592e-16"/>

<GEOM Abort="false" BodyID="RightMidFoot" ContactSoftERP="0.1"  
ID="Main.Model.HumanModel.Right.Leg.Seg.Foot.MidFootMedialContactNode" Length="0.02"  
Mu="1.0" Radius="0.01" SpringConstant="1e6" Type="CappedCylinder" Position="RightMidFoot -  
7.4600000000225649e-04 -1.5586000000000130e-02 -2.88640000000001118e-02"  
Quaternion="RightMidFoot 7.07106781186547240e-01 -7.07106781186547906e-01  
9.71445146547012219e-17 1.38777878078144592e-16"/>

<GEOM Abort="false" BodyID="RightMTs" ContactSoftERP="0.1"  
ID="Main.Model.HumanModel.Right.Leg.Seg.Foot.MTHeadLateralContactNode" Length="0.02"  
Mu="1.0" Radius="0.01" SpringConstant="1e6" Type="CappedCylinder" Position="RightMTs  
1.0496999999999404e-02 -3.1179000000000053e-02 -1.14320000000000515e-02"  
Quaternion="RightMTs 7.07106781186547240e-01 -7.07106781186547906e-01  
9.71445146547012219e-17 1.38777878078144592e-16"/>

<GEOM Abort="false" BodyID="RightMTs" ContactSoftERP="0.1"  
ID="Main.Model.HumanModel.Right.Leg.Seg.Foot.MTMeadMedialContactNode" Length="0.02"  
Mu="1.0" Radius="0.01" SpringConstant="1e6" Type="CappedCylinder" Position="RightMTs  
3.64799999999997973e-02 1.2471999999999727e-02 -1.14320000000000758e-02"  
Quaternion="RightMTs 7.07106781186547240e-01 -7.07106781186547906e-01  
9.71445146547012219e-17 1.38777878078144592e-16"/>

<GEOM Abort="false" BodyID="RightToes" ContactSoftERP="0.1"  
ID="Main.Model.HumanModel.Right.Leg.Seg.Foot.ToeMedialContactNode" Length="0.025"  
Mu="1.0" Radius="0.01" SpringConstant="1e6" Type="CappedCylinder" Position="RightToes  
1.33030000000001845e-02 1.4777999999999908e-02 6.98226199080664856e-17"  
Quaternion="RightToes 7.07106781186547240e-01 -7.07106781186547906e-01  
9.71445146547012219e-17 1.38777878078144592e-16"/>

<MUSCLE ActivationK="0.17" ActivationKinetics="false" ActivationRate="500"  
FastTwitchProportion="0.5" FibreLength="0.1380000000000001" ForcePerUnitArea="300000"  
ID="Main.Model.HumanModel.Right.Leg.Mus.AdductorLongus" InsertionBodyID="RightThigh"  
OriginBodyID="Trunk" PCA="0.0014" ParallelStrainAtFmax="0.5999999999999998"  
ParallelStrainModel="Square" ParallelStrainRateAtFmax="0"  
SerialStrainAtFmax="0.0599999999999999" SerialStrainModel="Square"  
SerialStrainRateAtFmax="0" Strap="TwoPoint" TActivationA="80e-3" TActivationB="0.47e-3"  
TDeactivationA="90e-3" TDeactivationB="0.56e-3" Type="MinettiAlexanderComplete"  
VMMaxFactor="8.4" Width="1" TendonLength="5.99595918363138303e-02" InitialFibreLength="-1"  
StartActivation="1.0000000000000002e-03" Origin="Trunk 4.3439999999999231e-02 -  
7.055999999999977e-03 -3.0053900000000001e-01" Insertion="RightThigh -  
9.33000000000000843e-03 5.59800000000000575e-03 1.77809156287622727e-17"/>

<MUSCLE ActivationK="0.17" ActivationKinetics="false" ActivationRate="500"  
FastTwitchProportion="0.5" FibreLength="0.08699999999999994" ForcePerUnitArea="300000"  
ID="Main.Model.HumanModel.Right.Leg.Mus.AdductorMagnus1" InsertionBodyID="RightThigh"  
OriginBodyID="Trunk" PCA="0.00115" ParallelStrainAtFmax="0.5999999999999998"

ParallelStrainModel="Square" ParallelStrainRateAtFmax="0"  
SerialStrainAtFmax="0.059999999999999999" SerialStrainModel="Square"  
SerialStrainRateAtFmax="0" Strap="TwoPoint" TActivationA="80e-3" TActivationB="0.47e-3"  
TDeactivationA="90e-3" TDeactivationB="0.56e-3" Type="MinettiAlexanderComplete"  
VMaxFactor="8.4" Width="1" TendonLength="4.06675369857193159e-02" InitialFibreLength="-1"  
StartActivation="1.00000000000000002e-03" Origin="Trunk -2.53559999999999341e-02 -  
5.2919999999999983e-03 -3.2788099999999978e-01" Insertion="RightThigh -  
1.95930000000000340e-02 -8.3969999999998781e-03 7.2773999999999776e-02"/>

<MUSCLE ActivationK="0.17" ActivationKinetics="false" ActivationRate="500"  
FastTwitchProportion="0.5" FibreLength="0.121" ForcePerUnitArea="300000"  
ID="Main.Model.HumanModel.Right.Leg.Mus.AdductorMagnus2" InsertionBodyID="RightThigh"  
OriginBodyID="Trunk" PCA="0.00103333333333333334"  
ParallelStrainAtFmax="0.5999999999999998" ParallelStrainModel="Square"  
ParallelStrainRateAtFmax="0" SerialStrainAtFmax="0.059999999999999999"  
SerialStrainModel="Square" SerialStrainRateAtFmax="0" Strap="TwoPoint" TActivationA="80e-3"  
TActivationB="0.47e-3" TDeactivationA="90e-3" TDeactivationB="0.56e-3"  
Type="MinettiAlexanderComplete" VMaxFactor="8.4" Width="1"  
TendonLength="6.23739348980656139e-02" InitialFibreLength="-1"  
StartActivation="1.00000000000000002e-03" Origin="Trunk -2.53559999999999341e-02 -  
5.2919999999999983e-03 -3.2788099999999978e-01" Insertion="RightThigh -  
1.39950000000000421e-02 -9.32999999999989393e-04 -2.7056999999999665e-02"/>

<MUSCLE ActivationK="0.17" ActivationKinetics="false" ActivationRate="500"  
FastTwitchProportion="0.5" FibreLength="0.13100000000000001" ForcePerUnitArea="300000"  
ID="Main.Model.HumanModel.Right.Leg.Mus.AdductorMagnus3" InsertionBodyID="RightThigh"  
OriginBodyID="Trunk" PCA="0.00148333333333333332"  
ParallelStrainAtFmax="0.5999999999999998" ParallelStrainModel="Square"  
ParallelStrainRateAtFmax="0" SerialStrainAtFmax="0.059999999999999999"  
SerialStrainModel="Square" SerialStrainRateAtFmax="0" Strap="TwoPoint" TActivationA="80e-3"  
TActivationB="0.47e-3" TDeactivationA="90e-3" TDeactivationB="0.56e-3"  
Type="MinettiAlexanderComplete" VMaxFactor="8.4" Width="1"  
TendonLength="2.17347527621483183e-01" InitialFibreLength="-1"  
StartActivation="1.00000000000000002e-03" Origin="Trunk -2.53559999999999341e-02 -  
5.2919999999999983e-03 -3.2788099999999978e-01" Insertion="RightThigh -  
2.3324999999999638e-02 4.1052000000000052e-02 -2.1085799999999934e-01"/>

<MUSCLE ActivationK="0.17" ActivationKinetics="false" ActivationRate="500"  
FastTwitchProportion="0.5" FibreLength="0.172999999999999999" ForcePerUnitArea="300000"  
ID="Main.Model.HumanModel.Right.Leg.Mus.BicepsFemorisCaputBreve"  
InsertionBodyID="RightShank" MidpointBodyID="RightShank" OriginBodyID="RightThigh"  
PCA="0.00133333333333333333" ParallelStrainAtFmax="0.5999999999999998"  
ParallelStrainModel="Square" ParallelStrainRateAtFmax="0"  
SerialStrainAtFmax="0.059999999999999999" SerialStrainModel="Square"  
SerialStrainRateAtFmax="0" Strap="ThreePoint" TActivationA="80e-3" TActivationB="0.47e-3"  
TDeactivationA="90e-3" TDeactivationB="0.56e-3" Type="MinettiAlexanderComplete"  
VMaxFactor="8.4" Width="1" TendonLength="6.30983907166289826e-02" InitialFibreLength="-1"  
StartActivation="1.00000000000000002e-03" Origin="RightThigh -1.3061999999999521e-02  
0.0000000000000000e+00 -5.03820000000000448e-02" Insertion="RightShank -  
1.3994999999999658e-02 -4.0118999999999880e-02 1.5861000000000029e-01"  
MidPoint="RightShank -1.7259999999999559e-02 -4.0118999999999880e-02  
1.72605000000000092e-01"/>

<MUSCLE ActivationK="0.17" ActivationKinetics="false" ActivationRate="500"  
CylinderBodyID="RightThigh" FastTwitchProportion="0.5" FibreLength="0.11"  
ForcePerUnitArea="300000"  
ID="Main.Model.HumanModel.Right.Leg.Mus.BicepsFemorisCaputLongum"  
InsertionBodyID="RightShank" OriginBodyID="Trunk" PCA="0.002399999999999998"  
ParallelStrainAtFmax="0.5999999999999998" ParallelStrainModel="Square"  
ParallelStrainRateAtFmax="0" SerialStrainAtFmax="0.05999999999999999"  
SerialStrainModel="Square" SerialStrainRateAtFmax="0" Strap="CylinderWrap" TActivationA="80e-3"  
TActivationB="0.47e-3" TDeactivationA="90e-3" TDeactivationB="0.56e-3"  
Type="MinettiAlexanderComplete" VMaxFactor="8.4" Width="1"  
TendonLength="3.22589558691242340e-01" InitialFibreLength="-1"  
StartActivation="1.0000000000000002e-03" Origin="Trunk -7.2983999999999378e-02 -  
3.4397999999999980e-02 -3.1112300000000038e-01" Insertion="RightShank -  
1.39949999999999658e-02 -4.01189999999999880e-02 1.5861000000000029e-01"  
CylinderPosition="RightThigh -2.3324999999999222e-02 2.6124000000000083e-02 -  
2.4071399999999956e-01" CylinderRadius="2.5000000000000014e-02"  
CylinderQuaternion="RightThigh 7.07106781186547573e-01 7.07106781186547573e-01  
2.77555756156289135e-17 0.0000000000000000e+00"/>

<MUSCLE ActivationK="0.17" ActivationKinetics="false" ActivationRate="500"  
FastTwitchProportion="0.5" FibreLength="0.1000000000000001" ForcePerUnitArea="300000"  
ID="Main.Model.HumanModel.Right.Leg.Mus.ExtensorDigitorumLongus"  
InsertionBodyID="RightToes" OriginBodyID="RightShank" PCA="0.0011333333333333334"  
ParallelStrainAtFmax="0.5999999999999998" ParallelStrainModel="Square"  
ParallelStrainRateAtFmax="0" SerialStrainAtFmax="0.05999999999999999"  
SerialStrainModel="Square" SerialStrainRateAtFmax="0" Strap="NPoint" TActivationA="80e-3"  
TActivationB="0.47e-3" TDeactivationA="90e-3" TDeactivationB="0.56e-3"  
Type="MinettiAlexanderComplete" VMaxFactor="8.4" ViaPointBody0="RightRearFoot"  
ViaPointBody1="RightMTs" Width="1" TendonLength="4.62219772827661801e-01"  
InitialFibreLength="-1" StartActivation="1.0000000000000002e-03" Origin="RightShank -  
4.16333634234433703e-17 -9.3300000000000496e-03 1.4927999999999968e-01"  
Insertion="RightToes 2.0785999999999226e-02 -2.1824999999999972e-02 -  
4.15700000000005995e-03" ViaPoint0="RightRearFoot 6.54760000000000758e-02 -  
8.3140000000000194e-03 3.22180000000000660e-02" ViaPoint1="RightMTs  
3.57789999999999497e-02 -1.61799999999999861e-02 1.4159999999999549e-03"/>

<MUSCLE ActivationK="0.17" ActivationKinetics="false" ActivationRate="500"  
FastTwitchProportion="0.5" FibreLength="0.11" ForcePerUnitArea="300000"  
ID="Main.Model.HumanModel.Right.Leg.Mus.ExtensorHallucisLongus" InsertionBodyID="RightToes"  
OriginBodyID="RightShank" PCA="0.00036666666666666667"  
ParallelStrainAtFmax="0.5999999999999998" ParallelStrainModel="Square"  
ParallelStrainRateAtFmax="0" SerialStrainAtFmax="0.05999999999999999"  
SerialStrainModel="Square" SerialStrainRateAtFmax="0" Strap="NPoint" TActivationA="80e-3"  
TActivationB="0.47e-3" TDeactivationA="90e-3" TDeactivationB="0.56e-3"  
Type="MinettiAlexanderComplete" VMaxFactor="8.4" ViaPointBody0="RightRearFoot"  
ViaPointBody1="RightMTs" Width="1" TendonLength="2.50973055128590528e-01"  
InitialFibreLength="-1" StartActivation="1.0000000000000002e-03" Origin="RightShank -  
3.46944695195361419e-17 0.0000000000000000e+00 -4.66500000000000803e-02"  
Insertion="RightToes 3.4297000000000358e-02 2.0785999999999989e-02  
3.46944695195361419e-17" ViaPoint0="RightRearFoot 6.54760000000000758e-02  
2.07899999999999752e-03 3.22180000000000660e-02" ViaPoint1="RightMTs  
3.8289000000000036e-02 1.3715000000000050e-02 6.94200000000000893e-03"/>

<MUSCLE ActivationK="0.17" ActivationKinetics="false" ActivationRate="500"  
FastTwitchProportion="0.5" FibreLength="0.05999999999999998" ForcePerUnitArea="300000"  
ID="Main.Model.HumanModel.Right.Leg.Mus.FlexorDigitorumLongus" InsertionBodyID="RightToes"  
OriginBodyID="RightShank" PCA="0.0010333333333333334"  
ParallelStrainAtFmax="0.5999999999999998" ParallelStrainModel="Square"  
ParallelStrainRateAtFmax="0" SerialStrainAtFmax="0.05999999999999999"  
SerialStrainModel="Square" SerialStrainRateAtFmax="0" Strap="NPoint" TActivationA="80e-3"  
TActivationB="0.47e-3" TDeactivationA="90e-3" TDeactivationB="0.56e-3"  
Type="MinettiAlexanderComplete" VMaxFactor="8.4" ViaPointBody0="RightRearFoot"  
ViaPointBody1="RightMTs" Width="1" TendonLength="4.51191554813184126e-01"  
InitialFibreLength="-1" StartActivation="1.0000000000000002e-03" Origin="RightShank -  
4.16333634234433703e-17 9.33000000000000496e-03 3.73199999999999366e-02"  
Insertion="RightToes 2.07860000000000163e-02 -2.1824999999999972e-02 -  
1.03929999999999838e-02" ViaPoint0="RightRearFoot 1.69600000000006594e-03  
2.2864999999999964e-02 -4.15699999999996107e-03" ViaPoint1="RightMTs  
3.42730000000000395e-02 -1.63970000000000088e-02 -1.6851999999999573e-02"/>

<MUSCLE ActivationK="0.17" ActivationKinetics="false" ActivationRate="500"  
FastTwitchProportion="0.5" FibreLength="0.04000000000000001" ForcePerUnitArea="300000"  
ID="Main.Model.HumanModel.Right.Leg.Mus.FlexorHallucisLongus" InsertionBodyID="RightToes"  
MidpointBodyID="RightRearFoot" OriginBodyID="RightShank" PCA="0.0010666666666666667"  
ParallelStrainAtFmax="0.5999999999999998" ParallelStrainModel="Square"  
ParallelStrainRateAtFmax="0" SerialStrainAtFmax="0.05999999999999999"  
SerialStrainModel="Square" SerialStrainRateAtFmax="0" Strap="NPoint" TActivationA="80e-3"  
TActivationB="0.47e-3" TDeactivationA="90e-3" TDeactivationB="0.56e-3"  
Type="MinettiAlexanderComplete" VMaxFactor="8.4" ViaPointBody0="RightRearFoot"  
ViaPointBody1="RightMidFoot" ViaPointBody2="RightMTs" Width="1"  
TendonLength="4.11725452495137867e-01" InitialFibreLength="-1"  
StartActivation="1.0000000000000002e-03" Origin="RightShank 4.16333634234433703e-17 -  
9.33000000000000496e-03 -3.73199999999999366e-02" Insertion="RightToes  
3.42970000000000150e-02 2.0785999999999989e-02 -5.1969999999997768e-03"  
ViaPoint0="RightRearFoot -5.83000000000006863e-03 1.66290000000000049e-02 -  
2.893000000000003530e-03" ViaPoint1="RightMidFoot 1.5893999999999117e-02  
1.2513999999999973e-02 -2.56890000000000555e-02" ViaPoint2="RightMTs  
3.17939999999999404e-02 1.86250000000000027e-02 -2.04800000000000329e-02"/>

<MUSCLE ActivationK="0.17" ActivationKinetics="false" ActivationRate="500"  
FastTwitchProportion="0.5" FibreLength="0.05999999999999998" ForcePerUnitArea="300000"  
ID="Main.Model.HumanModel.Right.Leg.Mus.Gastrocnemius" InsertionBodyID="RightRearFoot"  
MidpointBodyID="RightShank" OriginBodyID="RightThigh" PCA="0.005349999999999997"  
ParallelStrainAtFmax="0.5999999999999998" ParallelStrainModel="Square"  
ParallelStrainRateAtFmax="0" SerialStrainAtFmax="0.05999999999999999"  
SerialStrainModel="Square" SerialStrainRateAtFmax="0" Strap="ThreePoint" TActivationA="80e-3"  
TActivationB="0.47e-3" TDeactivationA="90e-3" TDeactivationB="0.56e-3"  
Type="MinettiAlexanderComplete" VMaxFactor="8.4" Width="1"  
TendonLength="4.59448284649614125e-01" InitialFibreLength="-1"  
StartActivation="1.0000000000000002e-03" Origin="RightThigh -2.6124000000000569e-02  
2.1459000000000058e-02 -2.2112099999999984e-01" Insertion="RightRearFoot -  
3.11790000000000123e-02 3.11799999999999577e-03 4.1569999999997322e-03"  
MidPoint="RightShank -5.1314999999999301e-02 0.0000000000000000e+00  
5.5979999999999950e-02"/>

<MUSCLE ActivationK="0.17" ActivationKinetics="false" ActivationRate="500"  
FastTwitchProportion="0.5" FibreLength="0.14199999999999999" ForcePerUnitArea="300000"

ID="Main.Model.HumanModel.Right.Leg.Mus.GluteusMaximus1" InsertionBodyID="RightShank"  
OriginBodyID="Trunk" PCA="0.00127333333333333333"  
ParallelStrainAtFmax="0.5999999999999998" ParallelStrainModel="Square"  
ParallelStrainRateAtFmax="0" SerialStrainAtFmax="0.059999999999999999"  
SerialStrainModel="Square" SerialStrainRateAtFmax="0" Strap="NPoint" TActivationA="80e-3"  
TActivationB="0.47e-3" TDeactivationA="90e-3" TDeactivationB="0.56e-3"  
Type="MinettiAlexanderComplete" VMaxFactor="8.4" ViaPointBody0="Trunk"  
ViaPointBody1="RightThigh" Width="1" TendonLength="4.88436034776993044e-01"  
InitialFibreLength="-1" StartActivation="1.0000000000000002e-03" Origin="Trunk -  
5.9754000000000848e-02 -3.175200000000024e-02 -1.6206499999999904e-01"  
Insertion="RightShank -1.725999999999559e-02 -4.0118999999999880e-02  
1.726050000000092e-01" ViaPoint0="Trunk -6.592799999999866e-02 -  
9.172800000000040e-02 -2.202770000000056e-01" ViaPoint1="RightThigh -  
1.866000000000099e-02 -4.198499999999945e-02 1.492800000000024e-01"/>

<MUSCLE ActivationK="0.17" ActivationKinetics="false" ActivationRate="500"  
FastTwitchProportion="0.5" FibreLength="0.1469999999999999" ForcePerUnitArea="300000"  
ID="Main.Model.HumanModel.Right.Leg.Mus.GluteusMaximus2" InsertionBodyID="RightShank"  
OriginBodyID="Trunk" PCA="0.00182" ParallelStrainAtFmax="0.5999999999999998"  
ParallelStrainModel="Square" ParallelStrainRateAtFmax="0"  
SerialStrainAtFmax="0.059999999999999999" SerialStrainModel="Square"  
SerialStrainRateAtFmax="0" Strap="NPoint" TActivationA="80e-3" TActivationB="0.47e-3"  
TDeactivationA="90e-3" TDeactivationB="0.56e-3" Type="MinettiAlexanderComplete"  
VMaxFactor="8.4" ViaPointBody0="Trunk" ViaPointBody1="Trunk" ViaPointBody2="RightThigh"  
Width="1" TendonLength="4.31585222161969262e-01" InitialFibreLength="-1"  
StartActivation="1.0000000000000002e-03" Origin="Trunk -6.240000000000110e-02 -  
2.205000000000002e-02 -1.885250000000054e-01" Insertion="RightShank -  
1.725999999999559e-02 -4.0118999999999880e-02 1.726050000000092e-01"  
ViaPoint0="Trunk -7.4748000000000366e-02 -4.762799999999967e-02 -  
2.1586700000000031e-01" ViaPoint1="Trunk -7.4748000000000366e-02 -  
7.408800000000011e-02 -2.4673699999999984e-01" ViaPoint2="RightThigh -  
4.1985000000000431e-02 9.3300000000000496e-03 1.492799999999996e-01"/>

<MUSCLE ActivationK="0.17" ActivationKinetics="false" ActivationRate="500"  
FastTwitchProportion="0.5" FibreLength="0.1439999999999999" ForcePerUnitArea="300000"  
ID="Main.Model.HumanModel.Right.Leg.Mus.GluteusMaximus3" InsertionBodyID="RightThigh"  
MidpointBodyID="Trunk" OriginBodyID="Trunk" PCA="0.0012266666666666667"  
ParallelStrainAtFmax="0.5999999999999998" ParallelStrainModel="Square"  
ParallelStrainRateAtFmax="0" SerialStrainAtFmax="0.059999999999999999"  
SerialStrainModel="Square" SerialStrainRateAtFmax="0" Strap="ThreePoint" TActivationA="80e-3"  
TActivationB="0.47e-3" TDeactivationA="90e-3" TDeactivationB="0.56e-3"  
Type="MinettiAlexanderComplete" VMaxFactor="8.4" Width="1"  
TendonLength="8.57912036038013248e-02" InitialFibreLength="-1"  
StartActivation="1.0000000000000002e-03" Origin="Trunk -5.5344000000000598e-02 -  
1.763999999999994e-03 -2.132209999999994e-01" Insertion="RightThigh -  
1.492799999999587e-02 -8.3969999999998781e-03 6.997499999999539e-02"  
MidPoint="Trunk -7.4748000000000366e-02 -3.880800000000022e-02 -  
3.067130000000013e-01"/>

<MUSCLE ActivationK="0.17" ActivationKinetics="false" ActivationRate="500"  
FastTwitchProportion="0.5" FibreLength="0.05399999999999999" ForcePerUnitArea="300000"  
ID="Main.Model.HumanModel.Right.Leg.Mus.GluteusMedius1" InsertionBodyID="RightThigh"  
OriginBodyID="Trunk" PCA="0.00183333333333333333"  
ParallelStrainAtFmax="0.5999999999999998" ParallelStrainModel="Square"

ParallelStrainRateAtFmax="0" SerialStrainAtFmax="0.059999999999999999"  
SerialStrainModel="Square" SerialStrainRateAtFmax="0" Strap="TwoPoint" TActivationA="80e-3"  
TActivationB="0.47e-3" TDeactivationA="90e-3" TDeactivationB="0.56e-3"  
Type="MinettiAlexanderComplete" VMaxFactor="8.4" Width="1"  
TendonLength="7.93679121828035350e-02" InitialFibreLength="-1"  
StartActivation="1.0000000000000002e-03" Origin="Trunk 2.8445999999999713e-02 -  
1.1201400000000002e-01 -1.7353099999999880e-01" Insertion="RightThigh -  
9.3299999999991475e-03 -2.985599999999937e-02 1.651409999999954e-01"/>

<MUSCLE ActivationK="0.17" ActivationKinetics="false" ActivationRate="500"  
FastTwitchProportion="0.5" FibreLength="0.08400000000000005" ForcePerUnitArea="300000"  
ID="Main.Model.HumanModel.Right.Leg.Mus.GluteusMedius2" InsertionBodyID="RightThigh"  
OriginBodyID="Trunk" PCA="0.0012666666666666666"  
ParallelStrainAtFmax="0.599999999999998" ParallelStrainModel="Square"  
ParallelStrainRateAtFmax="0" SerialStrainAtFmax="0.059999999999999999"  
SerialStrainModel="Square" SerialStrainRateAtFmax="0" Strap="TwoPoint" TActivationA="80e-3"  
TActivationB="0.47e-3" TDeactivationA="90e-3" TDeactivationB="0.56e-3"  
Type="MinettiAlexanderComplete" VMaxFactor="8.4" Width="1"  
TendonLength="9.45413117460494196e-02" InitialFibreLength="-1"  
StartActivation="1.0000000000000002e-03" Origin="Trunk -1.3007999999999085e-02 -  
8.467199999999973e-02 -1.241389999999999e-01" Insertion="RightThigh -  
9.3299999999991475e-03 -2.985599999999937e-02 1.651409999999954e-01"/>

<MUSCLE ActivationK="0.17" ActivationKinetics="false" ActivationRate="500"  
FastTwitchProportion="0.5" FibreLength="0.06500000000000002" ForcePerUnitArea="300000"  
ID="Main.Model.HumanModel.Right.Leg.Mus.GluteusMedius3" InsertionBodyID="RightThigh"  
OriginBodyID="Trunk" PCA="0.0014499999999999999"  
ParallelStrainAtFmax="0.599999999999998" ParallelStrainModel="Square"  
ParallelStrainRateAtFmax="0" SerialStrainAtFmax="0.059999999999999999"  
SerialStrainModel="Square" SerialStrainRateAtFmax="0" Strap="TwoPoint" TActivationA="80e-3"  
TActivationB="0.47e-3" TDeactivationA="90e-3" TDeactivationB="0.56e-3"  
Type="MinettiAlexanderComplete" VMaxFactor="8.4" Width="1"  
TendonLength="1.24873642193960077e-01" InitialFibreLength="-1"  
StartActivation="1.0000000000000002e-03" Origin="Trunk -5.7107999999999366e-02 -  
4.057199999999970e-02 -1.356049999999976e-01" Insertion="RightThigh -  
9.3299999999991475e-03 -2.985599999999937e-02 1.651409999999954e-01"/>

<MUSCLE ActivationK="0.17" ActivationKinetics="false" ActivationRate="500"  
FastTwitchProportion="0.5" FibreLength="0.06800000000000005" ForcePerUnitArea="300000"  
ID="Main.Model.HumanModel.Right.Leg.Mus.GluteusMinimus1" InsertionBodyID="RightThigh"  
OriginBodyID="Trunk" PCA="0.0005999999999999995"  
ParallelStrainAtFmax="0.599999999999998" ParallelStrainModel="Square"  
ParallelStrainRateAtFmax="0" SerialStrainAtFmax="0.059999999999999999"  
SerialStrainModel="Square" SerialStrainRateAtFmax="0" Strap="TwoPoint" TActivationA="80e-3"  
TActivationB="0.47e-3" TDeactivationA="90e-3" TDeactivationB="0.56e-3"  
Type="MinettiAlexanderComplete" VMaxFactor="8.4" Width="1"  
TendonLength="4.50398159941884091e-02" InitialFibreLength="-1"  
StartActivation="1.0000000000000002e-03" Origin="Trunk -6.5999999999882903e-04 -  
1.0231200000000000e-01 -1.8499700000000078e-01" Insertion="RightThigh  
2.7989999999989185e-03 -3.452099999999961e-02 1.6140900000000025e-01"/>

<MUSCLE ActivationK="0.17" ActivationKinetics="false" ActivationRate="500"  
FastTwitchProportion="0.5" FibreLength="0.05600000000000001" ForcePerUnitArea="300000"  
ID="Main.Model.HumanModel.Right.Leg.Mus.GluteusMinimus2" InsertionBodyID="RightThigh"

OriginBodyID="Trunk" PCA="0.00063333333333333333"  
ParallelStrainAtFmax="0.5999999999999998" ParallelStrainModel="Square"  
ParallelStrainRateAtFmax="0" SerialStrainAtFmax="0.059999999999999999"  
SerialStrainModel="Square" SerialStrainRateAtFmax="0" Strap="TwoPoint" TActivationA="80e-3"  
TActivationB="0.47e-3" TDeactivationA="90e-3" TDeactivationB="0.56e-3"  
Type="MinettiAlexanderComplete" VMaxFactor="8.4" Width="1"  
TendonLength="7.47975534939395448e-02" InitialFibreLength="-1"  
StartActivation="1.0000000000000002e-03" Origin="Trunk -1.56540000000000568e-02 -  
8.0262000000000000e-02 -1.7617700000000028e-01" Insertion="RightThigh  
2.7989999999999989185e-03 -3.4520999999999961e-02 1.6140900000000025e-01"/>

<MUSCLE ActivationK="0.17" ActivationKinetics="false" ActivationRate="500"  
FastTwitchProportion="0.5" FibreLength="0.037999999999999999" ForcePerUnitArea="300000"  
ID="Main.Model.HumanModel.Right.Leg.Mus.GluteusMinimus3" InsertionBodyID="RightThigh"  
OriginBodyID="Trunk" PCA="0.00071666666666666667"  
ParallelStrainAtFmax="0.5999999999999998" ParallelStrainModel="Square"  
ParallelStrainRateAtFmax="0" SerialStrainAtFmax="0.059999999999999999"  
SerialStrainModel="Square" SerialStrainRateAtFmax="0" Strap="TwoPoint" TActivationA="80e-3"  
TActivationB="0.47e-3" TDeactivationA="90e-3" TDeactivationB="0.56e-3"  
Type="MinettiAlexanderComplete" VMaxFactor="8.4" Width="1"  
TendonLength="1.02804829462628783e-01" InitialFibreLength="-1"  
StartActivation="1.0000000000000002e-03" Origin="Trunk -3.59400000000000830e-02 -  
5.4684000000000034e-02 -1.8499700000000078e-01" Insertion="RightThigh  
2.7989999999999989185e-03 -3.4520999999999961e-02 1.6140900000000025e-01"/>

<MUSCLE ActivationK="0.17" ActivationKinetics="false" ActivationRate="500"  
FastTwitchProportion="0.5" FibreLength="0.3519999999999998" ForcePerUnitArea="300000"  
ID="Main.Model.HumanModel.Right.Leg.Mus.Gracilis" InsertionBodyID="RightShank"  
OriginBodyID="Trunk" PCA="0.00036000000000000002"  
ParallelStrainAtFmax="0.5999999999999998" ParallelStrainModel="Square"  
ParallelStrainRateAtFmax="0" SerialStrainAtFmax="0.059999999999999999"  
SerialStrainModel="Square" SerialStrainRateAtFmax="0" Strap="NPoint" TActivationA="80e-3"  
TActivationB="0.47e-3" TDeactivationA="90e-3" TDeactivationB="0.56e-3"  
Type="MinettiAlexanderComplete" VMaxFactor="8.4" ViaPointBody0="RightShank"  
ViaPointBody1="RightShank" Width="1" TendonLength="1.49051553907173284e-01"  
InitialFibreLength="-1" StartActivation="1.0000000000000002e-03" Origin="Trunk  
9.0419999999999449e-03 -6.1739999999999980e-03 -3.1376899999999965e-01"  
Insertion="RightShank 1.67940000000000519e-02 1.4927999999999968e-02  
1.2129000000000037e-01" ViaPoint0="RightShank -3.06489999999999541e-02  
1.6794000000000034e-02 1.6794000000000089e-01" ViaPoint1="RightShank -  
4.66499999999994697e-03 3.9185999999999986e-02 1.3995000000000047e-01"/>

<MUSCLE ActivationK="0.17" ActivationKinetics="false" ActivationRate="500"  
CylinderBodyID="Trunk" FastTwitchProportion="0.5" FibreLength="0.1000000000000001"  
ForcePerUnitArea="300000" ID="Main.Model.HumanModel.Right.Leg.Mus.Iliopsoas"  
InsertionBodyID="RightThigh" OriginBodyID="Trunk" PCA="0.0026666666666666666"  
ParallelStrainAtFmax="0.5999999999999998" ParallelStrainModel="Square"  
ParallelStrainRateAtFmax="0" SerialStrainAtFmax="0.059999999999999999"  
SerialStrainModel="Square" SerialStrainRateAtFmax="0" Strap="CylinderWrap" TActivationA="80e-  
3" TActivationB="0.47e-3" TDeactivationA="90e-3" TDeactivationB="0.56e-3"  
Type="MinettiAlexanderComplete" VMaxFactor="8.4" Width="1"  
TendonLength="1.17962624962018203e-01" InitialFibreLength="-1"  
StartActivation="1.0000000000000002e-03" Origin="Trunk -1.01880000000000859e-02 -  
7.0559999999999977e-02 -1.4089700000000050e-01" Insertion="RightThigh

9.33000000000010210e-04 7.4639999999999841e-03 1.1195999999999907e-01"  
CylinderPosition="Trunk -1.30079999999999085e-02 -4.2335999999999986e-02 -  
2.8201699999999962e-01" CylinderRadius="3.00000021249149269e-02"  
CylinderQuaternion="Trunk 4.06838449131298407e-01 -9.13500123868869474e-01  
0.0000000000000000e+00 0.0000000000000000e+00"/>

<MUSCLE ActivationK="0.17" ActivationKinetics="false" ActivationRate="500"  
FastTwitchProportion="0.5" FibreLength="0.05000000000000003" ForcePerUnitArea="300000"  
ID="Main.Model.HumanModel.Right.Leg.Mus.PeroneusBrevis" InsertionBodyID="RightMTs"  
MidpointBodyID="RightRearFoot" OriginBodyID="RightShank" PCA="0.001166666666666668"  
ParallelStrainAtFmax="0.5999999999999998" ParallelStrainModel="Square"  
ParallelStrainRateAtFmax="0" SerialStrainAtFmax="0.05999999999999999"  
SerialStrainModel="Square" SerialStrainRateAtFmax="0" Strap="ThreePoint" TActivationA="80e-3"  
TActivationB="0.47e-3" TDeactivationA="90e-3" TDeactivationB="0.56e-3"  
Type="MinettiAlexanderComplete" VMaxFactor="8.4" Width="1"  
TendonLength="2.52934358523857872e-01" InitialFibreLength="-1"  
StartActivation="1.0000000000000002e-03" Origin="RightShank 4.16333634234433703e-17 -  
2.79899999999999871e-02 -3.7319999999999366e-02" Insertion="RightMTs -  
5.40439999999999809e-02 -2.70220000000000043e-02 -4.15699999999998362e-03"  
MidPoint="RightRearFoot 8.31400000000006613e-03 -1.66290000000000049e-02  
1.35110000000000577e-02"/>

<MUSCLE ActivationK="0.17" ActivationKinetics="false" ActivationRate="500"  
FastTwitchProportion="0.5" FibreLength="0.025999999999999999" ForcePerUnitArea="300000"  
ID="Main.Model.HumanModel.Right.Leg.Mus.Piriformis" InsertionBodyID="RightThigh"  
MidpointBodyID="Trunk" OriginBodyID="Trunk" PCA="0.0009833333333333324"  
ParallelStrainAtFmax="0.5999999999999998" ParallelStrainModel="Square"  
ParallelStrainRateAtFmax="0" SerialStrainAtFmax="0.05999999999999999"  
SerialStrainModel="Square" SerialStrainRateAtFmax="0" Strap="ThreePoint" TActivationA="80e-3"  
TActivationB="0.47e-3" TDeactivationA="90e-3" TDeactivationB="0.56e-3"  
Type="MinettiAlexanderComplete" VMaxFactor="8.4" Width="1"  
TendonLength="1.19067000404308787e-01" InitialFibreLength="-1"  
StartActivation="1.0000000000000002e-03" Origin="Trunk -5.53440000000000598e-02 -  
1.8522000000000003e-02 -2.0528299999999993e-01" Insertion="RightThigh -  
1.2128999999999940e-02 -2.4258000000000018e-02 1.69806000000000012e-01"  
MidPoint="Trunk -3.94680000000000586e-02 -7.93800000000000061e-02 -  
2.3791699999999934e-01"/>

<MUSCLE ActivationK="0.17" ActivationKinetics="false" ActivationRate="500"  
CylinderBodyID="RightThigh" FastTwitchProportion="0.5" FibreLength="0.08400000000000005"  
ForcePerUnitArea="300000" ID="Main.Model.HumanModel.Right.Leg.Mus.RectusFemoris"  
InsertionBodyID="RightShank" OriginBodyID="Trunk" PCA="0.0025999999999999999"  
ParallelStrainAtFmax="0.5999999999999998" ParallelStrainModel="Square"  
ParallelStrainRateAtFmax="0" SerialStrainAtFmax="0.05999999999999999"  
SerialStrainModel="Square" SerialStrainRateAtFmax="0" Strap="CylinderWrap" TActivationA="80e-  
3" TActivationB="0.47e-3" TDeactivationA="90e-3" TDeactivationB="0.56e-3"  
Type="MinettiAlexanderComplete" VMaxFactor="8.4" Width="1"  
TendonLength="4.84929924409269020e-01" InitialFibreLength="-1"  
StartActivation="1.0000000000000002e-03" Origin="Trunk 5.51400000000001889e-03 -  
8.8200000000000006e-02 -2.36153000000000057e-01" Insertion="RightShank  
2.9856000000000006e-02 -9.3300000000000496e-03 1.0262999999999985e-01"  
CylinderPosition="RightThigh -2.3324999999999222e-02 2.61240000000000083e-02 -  
2.4071399999999956e-01" CylinderRadius="2.999999999999989e-02"

CylinderQuaternion="RightThigh -7.07106781186547573e-01 7.07106781186547573e-01  
0.0000000000000000e+00 0.0000000000000000e+00"/>

<MUSCLE ActivationK="0.17" ActivationKinetics="false" ActivationRate="500"  
FastTwitchProportion="0.5" FibreLength="0.5789999999999996" ForcePerUnitArea="300000"  
ID="Main.Model.HumanModel.Right.Leg.Mus.Sartorius" InsertionBodyID="RightShank"  
OriginBodyID="Trunk" PCA="0.0003466666666666667"  
ParallelStrainAtFmax="0.5999999999999998" ParallelStrainModel="Square"  
ParallelStrainRateAtFmax="0" SerialStrainAtFmax="0.05999999999999999"  
SerialStrainModel="Square" SerialStrainRateAtFmax="0" Strap="NPoint" TActivationA="80e-3"  
TActivationB="0.47e-3" TDeactivationA="90e-3" TDeactivationB="0.56e-3"  
Type="MinettiAlexanderComplete" VMaxFactor="8.4" ViaPointBody0="RightThigh"  
ViaPointBody1="RightShank" ViaPointBody2="RightShank" Width="1"  
TendonLength="5.60366472734018517e-02" InitialFibreLength="-1"  
StartActivation="1.0000000000000002e-03" Origin="Trunk 3.8148000000000707e-02 -  
1.1995200000000003e-01 -1.8764300000000004e-01" Insertion="RightShank  
1.6794000000000519e-02 1.4927999999999968e-02 1.2129000000000037e-01"  
ViaPoint0="RightThigh 3.2655000000000798e-02 2.7990000000000010e-02  
1.8660000000000064e-02" ViaPoint1="RightShank -2.0105999999999989e-02  
3.545399999999994e-02 1.6794000000000034e-01" ViaPoint2="RightShank  
2.77555756156289135e-17 4.3851000000000011e-02 1.3994999999999963e-01"/>

<MUSCLE ActivationK="0.17" ActivationKinetics="false" ActivationRate="500"  
CylinderBodyID="RightThigh" FastTwitchProportion="0.5" FibreLength="0.08000000000000002"  
ForcePerUnitArea="300000" ID="Main.Model.HumanModel.Right.Leg.Mus.Semimembranosus"  
InsertionBodyID="RightShank" OriginBodyID="Trunk" PCA="0.0034333333333333334"  
ParallelStrainAtFmax="0.5999999999999998" ParallelStrainModel="Square"  
ParallelStrainRateAtFmax="0" SerialStrainAtFmax="0.05999999999999999"  
SerialStrainModel="Square" SerialStrainRateAtFmax="0" Strap="CylinderWrap" TActivationA="80e-  
3" TActivationB="0.47e-3" TDeactivationA="90e-3" TDeactivationB="0.56e-3"  
Type="MinettiAlexanderComplete" VMaxFactor="8.4" Width="1"  
TendonLength="3.37657679256022136e-01" InitialFibreLength="-1"  
StartActivation="1.0000000000000002e-03" Origin="Trunk -7.29839999999999378e-02 -  
3.4397999999999980e-02 -3.1112300000000038e-01" Insertion="RightShank -  
2.5191000000000606e-02 1.6794000000000034e-02 1.5860999999999918e-01"  
CylinderPosition="RightThigh -2.3324999999999222e-02 2.6124000000000083e-02 -  
2.4071399999999956e-01" CylinderRadius="3.5000000000000033e-02"  
CylinderQuaternion="RightThigh 7.07106781186547573e-01 7.07106781186547573e-01  
2.77555756156289135e-17 0.0000000000000000e+00"/>

<MUSCLE ActivationK="0.17" ActivationKinetics="false" ActivationRate="500"  
FastTwitchProportion="0.5" FibreLength="0.20100000000000001" ForcePerUnitArea="300000"  
ID="Main.Model.HumanModel.Right.Leg.Mus.Semitendinosus" InsertionBodyID="RightShank"  
MidpointBodyID="RightShank" OriginBodyID="Trunk" PCA="0.0011000000000000001"  
ParallelStrainAtFmax="0.5999999999999998" ParallelStrainModel="Square"  
ParallelStrainRateAtFmax="0" SerialStrainAtFmax="0.05999999999999999"  
SerialStrainModel="Square" SerialStrainRateAtFmax="0" Strap="ThreePoint" TActivationA="80e-3"  
TActivationB="0.47e-3" TDeactivationA="90e-3" TDeactivationB="0.56e-3"  
Type="MinettiAlexanderComplete" VMaxFactor="8.4" Width="1"  
TendonLength="2.77209427004380338e-01" InitialFibreLength="-1"  
StartActivation="1.0000000000000002e-03" Origin="Trunk -7.29839999999999378e-02 -  
3.4397999999999980e-02 -3.1112300000000038e-01" Insertion="RightShank  
1.6794000000000519e-02 1.4927999999999968e-02 1.2129000000000037e-01"

MidPoint="RightShank -2.3325000000000471e-02 3.9185999999999986e-02  
1.3994999999999908e-01"/>

<MUSCLE ActivationK="0.17" ActivationKinetics="false" ActivationRate="500"  
FastTwitchProportion="0.5" FibreLength="0.04000000000000001" ForcePerUnitArea="300000"  
ID="Main.Model.HumanModel.Right.Leg.Mus.Soleus" InsertionBodyID="RightRearFoot"  
OriginBodyID="RightShank" PCA="0.009433333333333335"  
ParallelStrainAtFmax="0.5999999999999998" ParallelStrainModel="Square"  
ParallelStrainRateAtFmax="0" SerialStrainAtFmax="0.05999999999999999"  
SerialStrainModel="Square" SerialStrainRateAtFmax="0" Strap="TwoPoint" TActivationA="80e-3"  
TActivationB="0.47e-3" TDeactivationA="90e-3" TDeactivationB="0.56e-3"  
Type="MinettiAlexanderComplete" VMaxFactor="8.4" Width="1"  
TendonLength="3.82929072067645981e-01" InitialFibreLength="-1"  
StartActivation="1.0000000000000002e-03" Origin="RightShank -1.8660000000000793e-02  
0.0000000000000000e+00 1.20543999999999887e-01" Insertion="RightRearFoot -  
3.1179000000000123e-02 3.1179999999999577e-03 4.156999999997322e-03"/>

<MUSCLE ActivationK="0.17" ActivationKinetics="false" ActivationRate="500"  
FastTwitchProportion="0.5" FibreLength="0.09500000000000001" ForcePerUnitArea="300000"  
ID="Main.Model.HumanModel.Right.Leg.Mus.TensorFasciaeLatae" InsertionBodyID="RightShank"  
MidpointBodyID="RightThigh" OriginBodyID="Trunk" PCA="0.0005166666666666668"  
ParallelStrainAtFmax="0.5999999999999998" ParallelStrainModel="Square"  
ParallelStrainRateAtFmax="0" SerialStrainAtFmax="0.05999999999999999"  
SerialStrainModel="Square" SerialStrainRateAtFmax="0" Strap="ThreePoint" TActivationA="80e-3"  
TActivationB="0.47e-3" TDeactivationA="90e-3" TDeactivationB="0.56e-3"  
Type="MinettiAlexanderComplete" VMaxFactor="8.4" Width="1"  
TendonLength="4.75012228506116352e-01" InitialFibreLength="-1"  
StartActivation="1.0000000000000002e-03" Origin="Trunk 3.8148000000000707e-02 -  
1.1995200000000003e-01 -1.8764300000000004e-01" Insertion="RightShank -  
1.7259999999999559e-02 -4.0118999999999880e-02 1.7260500000000092e-01"  
MidPoint="RightThigh -9.3299999999995638e-03 -3.9185999999999986e-02  
1.2128999999999940e-01"/>

<MUSCLE ActivationK="0.17" ActivationKinetics="false" ActivationRate="500"  
FastTwitchProportion="0.5" FibreLength="0.05600000000000001" ForcePerUnitArea="300000"  
ID="Main.Model.HumanModel.Right.Leg.Mus.TibialisAnterior" InsertionBodyID="RightMidFoot"  
MidpointBodyID="RightMidFoot" OriginBodyID="RightShank" PCA="0.002"  
ParallelStrainAtFmax="0.5999999999999998" ParallelStrainModel="Square"  
ParallelStrainRateAtFmax="0" SerialStrainAtFmax="0.05999999999999999"  
SerialStrainModel="Square" SerialStrainRateAtFmax="0" Strap="ThreePoint" TActivationA="80e-3"  
TActivationB="0.47e-3" TDeactivationA="90e-3" TDeactivationB="0.56e-3"  
Type="MinettiAlexanderComplete" VMaxFactor="8.4" Width="1"  
TendonLength="2.55749622953320432e-01" InitialFibreLength="-1"  
StartActivation="1.0000000000000002e-03" Origin="RightShank -5.89805981832114412e-17  
9.3300000000000496e-03 1.0729999999999653e-02" Insertion="RightMidFoot  
1.974699999999937e-02 2.182499999999972e-02 2.0789999999998711e-03"  
MidPoint="RightMidFoot 4.1569999999990903e-03 1.143199999999977e-02  
2.8060999999999263e-02"/>

<MUSCLE ActivationK="0.17" ActivationKinetics="false" ActivationRate="500"  
FastTwitchProportion="0.5" FibreLength="0.02999999999999999" ForcePerUnitArea="300000"  
ID="Main.Model.HumanModel.Right.Leg.Mus.TibialisPosterior" InsertionBodyID="RightMidFoot"  
MidpointBodyID="RightRearFoot" OriginBodyID="RightShank" PCA="0.004233333333333337"  
ParallelStrainAtFmax="0.5999999999999998" ParallelStrainModel="Square"

ParallelStrainRateAtFmax="0" SerialStrainAtFmax="0.059999999999999999"  
SerialStrainModel="Square" SerialStrainRateAtFmax="0" Strap="ThreePoint" TActivationA="80e-3"  
TActivationB="0.47e-3" TDeactivationA="90e-3" TDeactivationB="0.56e-3"  
Type="MinettiAlexanderComplete" VMaxFactor="8.4" Width="1"  
TendonLength="4.66945158597317000e-01" InitialFibreLength="-1"  
StartActivation="1.0000000000000002e-03" Origin="RightShank -4.85722573273505986e-17  
0.0000000000000000e+00 1.2128999999999953e-01" Insertion="RightMidFoot  
5.9410000000000357e-03 2.7464000000000023e-02 -8.50700000000000761e-03"  
MidPoint="RightRearFoot 6.57400000000005029e-03 3.1178999999999984e-02  
1.3511000000000369e-02"/>

<MUSCLE ActivationK="0.17" ActivationKinetics="false" ActivationRate="500"  
CylinderBodyID="RightThigh" FastTwitchProportion="0.5" FibreLength="0.08699999999999994"  
ForcePerUnitArea="300000" ID="Main.Model.HumanModel.Right.Leg.Mus.VastusIntermedius"  
InsertionBodyID="RightShank" OriginBodyID="RightThigh" PCA="0.004116666666666669"  
ParallelStrainAtFmax="0.5999999999999998" ParallelStrainModel="Square"  
ParallelStrainRateAtFmax="0" SerialStrainAtFmax="0.059999999999999999"  
SerialStrainModel="Square" SerialStrainRateAtFmax="0" Strap="CylinderWrap" TActivationA="80e-  
3" TActivationB="0.47e-3" TDeactivationA="90e-3" TDeactivationB="0.56e-3"  
Type="MinettiAlexanderComplete" VMaxFactor="8.4" Width="1"  
TendonLength="2.63531912563401249e-01" InitialFibreLength="-1"  
StartActivation="1.0000000000000002e-03" Origin="RightThigh 1.30619999999999487e-02  
0.0000000000000000e+00 6.67868538251070731e-17" Insertion="RightShank  
2.9856000000000006e-02 -9.3300000000000496e-03 1.0262999999999985e-01"  
CylinderPosition="RightThigh -2.3324999999999222e-02 2.6124000000000083e-02 -  
2.4071399999999956e-01" CylinderRadius="2.500000000000014e-02"  
CylinderQuaternion="RightThigh -7.07106781186547573e-01 7.07106781186547573e-01  
0.0000000000000000e+00 0.0000000000000000e+00"/>

<MUSCLE ActivationK="0.17" ActivationKinetics="false" ActivationRate="500"  
CylinderBodyID="RightThigh" FastTwitchProportion="0.5" FibreLength="0.08400000000000005"  
ForcePerUnitArea="300000" ID="Main.Model.HumanModel.Right.Leg.Mus.VastusLateralis"  
InsertionBodyID="RightShank" OriginBodyID="RightThigh" PCA="0.006233333333333329"  
ParallelStrainAtFmax="0.5999999999999998" ParallelStrainModel="Square"  
ParallelStrainRateAtFmax="0" SerialStrainAtFmax="0.059999999999999999"  
SerialStrainModel="Square" SerialStrainRateAtFmax="0" Strap="CylinderWrap" TActivationA="80e-  
3" TActivationB="0.47e-3" TDeactivationA="90e-3" TDeactivationB="0.56e-3"  
Type="MinettiAlexanderComplete" VMaxFactor="8.4" Width="1"  
TendonLength="2.68468498031746716e-01" InitialFibreLength="-1"  
StartActivation="1.0000000000000002e-03" Origin="RightThigh 0.0000000000000000e+00 -  
1.2129000000000009e-02 0.0000000000000000e+00" Insertion="RightShank  
2.9856000000000006e-02 -9.3300000000000496e-03 1.0262999999999985e-01"  
CylinderPosition="RightThigh -2.3324999999999222e-02 2.6124000000000083e-02 -  
2.4071399999999956e-01" CylinderRadius="2.750000000000001e-02"  
CylinderQuaternion="RightThigh -7.07106781186547573e-01 7.07106781186547573e-01  
0.0000000000000000e+00 0.0000000000000000e+00"/>

<MUSCLE ActivationK="0.17" ActivationKinetics="false" ActivationRate="500"  
CylinderBodyID="RightThigh" FastTwitchProportion="0.5" FibreLength="0.08899999999999996"  
ForcePerUnitArea="300000" ID="Main.Model.HumanModel.Right.Leg.Mus.VastusMedialis"  
InsertionBodyID="RightShank" OriginBodyID="RightThigh" PCA="0.004316666666666666"  
ParallelStrainAtFmax="0.5999999999999998" ParallelStrainModel="Square"  
ParallelStrainRateAtFmax="0" SerialStrainAtFmax="0.059999999999999999"  
SerialStrainModel="Square" SerialStrainRateAtFmax="0" Strap="CylinderWrap" TActivationA="80e-

3" TActivationB="0.47e-3" TDeactivationA="90e-3" TDeactivationB="0.56e-3"  
Type="MinettiAlexanderComplete" VMaxFactor="8.4" Width="1"  
TendonLength="3.02574678296056554e-01" InitialFibreLength="-1"  
StartActivation="1.0000000000000002e-03" Origin="RightThigh -2.77555756156289135e-17  
1.3062000000000042e-02 3.8253000000000370e-02" Insertion="RightShank  
2.9856000000000006e-02 -9.3300000000000496e-03 1.026299999999985e-01"  
CylinderPosition="RightThigh -2.332499999999222e-02 2.6124000000000083e-02 -  
2.407139999999956e-01" CylinderRadius="2.750000000000001e-02"  
CylinderQuaternion="RightThigh -7.07106781186547573e-01 7.07106781186547573e-01  
0.000000000000000e+00 0.000000000000000e+00"/>

<MUSCLE ActivationK="0.17" ActivationKinetics="false" ActivationRate="500"  
FastTwitchProportion="0.5" FibreLength="0.06" ForcePerUnitArea="300000"  
ID="Main.Model.HumanModel.Right.Leg.Mus.PeroneusLongus" InsertionBodyID="RightMTs"  
MidpointBodyID="RightRearFoot" OriginBodyID="RightShank" PCA="0.002144"  
ParallelStrainAtFmax="0.599999999999998" ParallelStrainModel="Square"  
ParallelStrainRateAtFmax="0" SerialStrainAtFmax="0.0599999999999999"  
SerialStrainModel="Square" SerialStrainRateAtFmax="0" Strap="ThreePoint" TActivationA="80e-3"  
TActivationB="0.47e-3" TDeactivationA="90e-3" TDeactivationB="0.56e-3"  
Type="MinettiAlexanderComplete" VMaxFactor="8.4" Width="1"  
TendonLength="4.510000000000012e-01" InitialFibreLength="-1"  
StartActivation="1.000000000000002e-03" Origin="RightShank 9.1470000000000929e-03 -  
3.5028000000000036e-02 1.1908599999999942e-01" Insertion="RightMTs -  
1.8777000000000020e-02 2.079999999999990e-02 -2.7840000000000175e-03"  
MidPoint="RightRearFoot 7.70600000000004615e-03 -2.4317000000000053e-02 -  
3.4224999999999499e-02"/>

<MUSCLE ActivationK="0.17" ActivationKinetics="false" ActivationRate="500"  
FastTwitchProportion="0.5" FibreLength="0.1380000000000001" ForcePerUnitArea="300000"  
ID="Main.Model.HumanModel.Left.Leg.Mus.AdductorLongus" InsertionBodyID="LeftThigh"  
OriginBodyID="Trunk" PCA="0.0014" ParallelStrainAtFmax="0.599999999999998"  
ParallelStrainModel="Square" ParallelStrainRateAtFmax="0"  
SerialStrainAtFmax="0.0599999999999999" SerialStrainModel="Square"  
SerialStrainRateAtFmax="0" Strap="TwoPoint" TActivationA="80e-3" TActivationB="0.47e-3"  
TDeactivationA="90e-3" TDeactivationB="0.56e-3" Type="MinettiAlexanderComplete"  
VMaxFactor="8.4" Width="1" TendonLength="5.99595918363138303e-02" InitialFibreLength="-1"  
StartActivation="1.000000000000002e-03" Origin="Trunk 4.3439999999999231e-02  
7.055999999999977e-03 -3.005390000000001e-01" Insertion="LeftThigh -  
9.3299999999999494e-03 -5.59800000000000575e-03 3.23092247400680321e-17"/>

<MUSCLE ActivationK="0.17" ActivationKinetics="false" ActivationRate="500"  
FastTwitchProportion="0.5" FibreLength="0.08699999999999994" ForcePerUnitArea="300000"  
ID="Main.Model.HumanModel.Left.Leg.Mus.AdductorMagnus1" InsertionBodyID="LeftThigh"  
OriginBodyID="Trunk" PCA="0.00115" ParallelStrainAtFmax="0.599999999999998"  
ParallelStrainModel="Square" ParallelStrainRateAtFmax="0"  
SerialStrainAtFmax="0.0599999999999999" SerialStrainModel="Square"  
SerialStrainRateAtFmax="0" Strap="TwoPoint" TActivationA="80e-3" TActivationB="0.47e-3"  
TDeactivationA="90e-3" TDeactivationB="0.56e-3" Type="MinettiAlexanderComplete"  
VMaxFactor="8.4" Width="1" TendonLength="4.06675369857193159e-02" InitialFibreLength="-1"  
StartActivation="1.000000000000002e-03" Origin="Trunk -2.5355999999999341e-02  
5.291999999999983e-03 -3.278809999999978e-01" Insertion="LeftThigh -  
1.95930000000000687e-02 8.3969999999998781e-03 7.2774000000000192e-02"/>

<MUSCLE ActivationK="0.17" ActivationKinetics="false" ActivationRate="500"  
FastTwitchProportion="0.5" FibreLength="0.121" ForcePerUnitArea="300000"  
ID="Main.Model.HumanModel.Left.Leg.Mus.AdductorMagnus2" InsertionBodyID="LeftThigh"  
OriginBodyID="Trunk" PCA="0.0010333333333333334"  
ParallelStrainAtFmax="0.5999999999999998" ParallelStrainModel="Square"  
ParallelStrainRateAtFmax="0" SerialStrainAtFmax="0.05999999999999999"  
SerialStrainModel="Square" SerialStrainRateAtFmax="0" Strap="TwoPoint" TActivationA="80e-3"  
TActivationB="0.47e-3" TDeactivationA="90e-3" TDeactivationB="0.56e-3"  
Type="MinettiAlexanderComplete" VMaxFactor="8.4" Width="1"  
TendonLength="6.23739348980656139e-02" InitialFibreLength="-1"  
StartActivation="1.0000000000000002e-03" Origin="Trunk -2.53559999999999341e-02  
5.2919999999999983e-03 -3.2788099999999978e-01" Insertion="LeftThigh -  
1.39949999999999485e-02 -9.329999999999998393e-04 -2.70569999999999700e-02"/>

<MUSCLE ActivationK="0.17" ActivationKinetics="false" ActivationRate="500"  
FastTwitchProportion="0.5" FibreLength="0.1310000000000001" ForcePerUnitArea="300000"  
ID="Main.Model.HumanModel.Left.Leg.Mus.AdductorMagnus3" InsertionBodyID="LeftThigh"  
OriginBodyID="Trunk" PCA="0.0014833333333333332"  
ParallelStrainAtFmax="0.5999999999999998" ParallelStrainModel="Square"  
ParallelStrainRateAtFmax="0" SerialStrainAtFmax="0.05999999999999999"  
SerialStrainModel="Square" SerialStrainRateAtFmax="0" Strap="TwoPoint" TActivationA="80e-3"  
TActivationB="0.47e-3" TDeactivationA="90e-3" TDeactivationB="0.56e-3"  
Type="MinettiAlexanderComplete" VMaxFactor="8.4" Width="1"  
TendonLength="2.17347527621483183e-01" InitialFibreLength="-1"  
StartActivation="1.0000000000000002e-03" Origin="Trunk -2.53559999999999341e-02  
5.2919999999999983e-03 -3.2788099999999978e-01" Insertion="LeftThigh -  
2.33250000000000540e-02 -4.1052000000000052e-02 -2.1085799999999990e-01"/>

<MUSCLE ActivationK="0.17" ActivationKinetics="false" ActivationRate="500"  
FastTwitchProportion="0.5" FibreLength="0.17299999999999999" ForcePerUnitArea="300000"  
ID="Main.Model.HumanModel.Left.Leg.Mus.BicepsFemorisCaputBreve"  
InsertionBodyID="LeftShank" MidpointBodyID="LeftShank" OriginBodyID="LeftThigh"  
PCA="0.0013333333333333333" ParallelStrainAtFmax="0.5999999999999998"  
ParallelStrainModel="Square" ParallelStrainRateAtFmax="0"  
SerialStrainAtFmax="0.05999999999999999" SerialStrainModel="Square"  
SerialStrainRateAtFmax="0" Strap="ThreePoint" TActivationA="80e-3" TActivationB="0.47e-3"  
TDeactivationA="90e-3" TDeactivationB="0.56e-3" Type="MinettiAlexanderComplete"  
VMaxFactor="8.4" Width="1" TendonLength="6.30983907166289826e-02" InitialFibreLength="-1"  
StartActivation="1.0000000000000002e-03" Origin="LeftThigh -1.30620000000001013e-02  
0.0000000000000000e+00 -5.03820000000000379e-02" Insertion="LeftShank -  
1.39950000000000144e-02 4.01189999999999880e-02 1.5861000000000001e-01"  
MidPoint="LeftShank -1.72599999999999178e-02 4.01189999999999880e-02  
1.72605000000000064e-01"/>

<MUSCLE ActivationK="0.17" ActivationKinetics="false" ActivationRate="500"  
CylinderBodyID="LeftThigh" FastTwitchProportion="0.5" FibreLength="0.11"  
ForcePerUnitArea="300000"  
ID="Main.Model.HumanModel.Left.Leg.Mus.BicepsFemorisCaputLongum"  
InsertionBodyID="LeftShank" OriginBodyID="Trunk" PCA="0.0023999999999999998"  
ParallelStrainAtFmax="0.5999999999999998" ParallelStrainModel="Square"  
ParallelStrainRateAtFmax="0" SerialStrainAtFmax="0.05999999999999999"  
SerialStrainModel="Square" SerialStrainRateAtFmax="0" Strap="CylinderWrap" TActivationA="80e-  
3" TActivationB="0.47e-3" TDeactivationA="90e-3" TDeactivationB="0.56e-3"  
Type="MinettiAlexanderComplete" VMaxFactor="8.4" Width="1"

TendonLength="3.22589558691242340e-01" InitialFibreLength="-1"  
StartActivation="1.0000000000000002e-03" Origin="Trunk -7.29839999999999378e-02  
3.4397999999999980e-02 -3.1112300000000038e-01" Insertion="LeftShank -  
1.39950000000000144e-02 4.01189999999999880e-02 1.5861000000000001e-01"  
CylinderPosition="LeftThigh -2.33249999999999083e-02 -2.61240000000000083e-02 -  
2.4071399999999984e-01" CylinderRadius="2.5000000000000014e-02"  
CylinderQuaternion="LeftThigh 7.07106781186547573e-01 7.07106781186547573e-01  
1.38777878078144568e-17 1.38777878078144568e-17"/>

<MUSCLE ActivationK="0.17" ActivationKinetics="false" ActivationRate="500"  
FastTwitchProportion="0.5" FibreLength="0.1000000000000001" ForcePerUnitArea="300000"  
ID="Main.Model.HumanModel.Left.Leg.Mus.ExtensorDigitorumLongus" InsertionBodyID="LeftToes"  
OriginBodyID="LeftShank" PCA="0.0011333333333333334"  
ParallelStrainAtFmax="0.5999999999999998" ParallelStrainModel="Square"  
ParallelStrainRateAtFmax="0" SerialStrainAtFmax="0.05999999999999999"  
SerialStrainModel="Square" SerialStrainRateAtFmax="0" Strap="NPoint" TActivationA="80e-3"  
TActivationB="0.47e-3" TDeactivationA="90e-3" TDeactivationB="0.56e-3"  
Type="MinettiAlexanderComplete" VMaxFactor="8.4" ViaPointBody0="LeftRearFoot"  
ViaPointBody1="LeftMTs" Width="1" TendonLength="4.62219772827661801e-01"  
InitialFibreLength="-1" StartActivation="1.0000000000000002e-03" Origin="LeftShank -  
1.04083408558608426e-17 9.33000000000000496e-03 1.49280000000000024e-01"  
Insertion="LeftToes 2.0785999999999157e-02 2.1824999999999972e-02 -  
4.1569999999999403e-03" ViaPoint0="LeftRearFoot 6.54760000000000064e-02  
8.31400000000000194e-03 3.2218000000000036e-02" ViaPoint1="LeftMTs  
3.57790000000000677e-02 1.6179999999999861e-02 1.4159999999999777e-03"/>

<MUSCLE ActivationK="0.17" ActivationKinetics="false" ActivationRate="500"  
FastTwitchProportion="0.5" FibreLength="0.11" ForcePerUnitArea="300000"  
ID="Main.Model.HumanModel.Left.Leg.Mus.ExtensorHallucisLongus" InsertionBodyID="LeftToes"  
OriginBodyID="LeftShank" PCA="0.0003666666666666667"  
ParallelStrainAtFmax="0.5999999999999998" ParallelStrainModel="Square"  
ParallelStrainRateAtFmax="0" SerialStrainAtFmax="0.05999999999999999"  
SerialStrainModel="Square" SerialStrainRateAtFmax="0" Strap="NPoint" TActivationA="80e-3"  
TActivationB="0.47e-3" TDeactivationA="90e-3" TDeactivationB="0.56e-3"  
Type="MinettiAlexanderComplete" VMaxFactor="8.4" ViaPointBody0="LeftRearFoot"  
ViaPointBody1="LeftMTs" Width="1" TendonLength="2.50973055128590528e-01"  
InitialFibreLength="-1" StartActivation="1.0000000000000002e-03" Origin="LeftShank  
2.25514051876984922e-17 0.0000000000000000e+00 -4.66500000000000387e-02"  
Insertion="LeftToes 3.42970000000000566e-02 -2.0785999999999989e-02 -  
2.81892564846231153e-18" ViaPoint0="LeftRearFoot 6.54760000000000064e-02 -  
2.0789999999999752e-03 3.2218000000000036e-02" ViaPoint1="LeftMTs  
3.82890000000000244e-02 -1.3715000000000050e-02 6.9420000000000025e-03"/>

<MUSCLE ActivationK="0.17" ActivationKinetics="false" ActivationRate="500"  
FastTwitchProportion="0.5" FibreLength="0.05999999999999998" ForcePerUnitArea="300000"  
ID="Main.Model.HumanModel.Left.Leg.Mus.FlexorDigitorumLongus" InsertionBodyID="LeftToes"  
OriginBodyID="LeftShank" PCA="0.0010333333333333334"  
ParallelStrainAtFmax="0.5999999999999998" ParallelStrainModel="Square"  
ParallelStrainRateAtFmax="0" SerialStrainAtFmax="0.05999999999999999"  
SerialStrainModel="Square" SerialStrainRateAtFmax="0" Strap="NPoint" TActivationA="80e-3"  
TActivationB="0.47e-3" TDeactivationA="90e-3" TDeactivationB="0.56e-3"  
Type="MinettiAlexanderComplete" VMaxFactor="8.4" ViaPointBody0="LeftRearFoot"  
ViaPointBody1="LeftMTs" Width="1" TendonLength="4.51191554813184126e-01"  
InitialFibreLength="-1" StartActivation="1.0000000000000002e-03" Origin="LeftShank -



1.72605000000000064e-01" ViaPoint0="Trunk -6.5927999999999866e-02  
9.17280000000000040e-02 -2.20277000000000056e-01" ViaPoint1="LeftThigh -  
1.86599999999999648e-02 4.1984999999999945e-02 1.492799999999996e-01"/>

<MUSCLE ActivationK="0.17" ActivationKinetics="false" ActivationRate="500"  
FastTwitchProportion="0.5" FibreLength="0.1469999999999999" ForcePerUnitArea="300000"  
ID="Main.Model.HumanModel.Left.Leg.Mus.GluteusMaximus2" InsertionBodyID="LeftShank"  
OriginBodyID="Trunk" PCA="0.00182" ParallelStrainAtFmax="0.5999999999999998"  
ParallelStrainModel="Square" ParallelStrainRateAtFmax="0"  
SerialStrainAtFmax="0.0599999999999999" SerialStrainModel="Square"  
SerialStrainRateAtFmax="0" Strap="NPoint" TActivationA="80e-3" TActivationB="0.47e-3"  
TDeactivationA="90e-3" TDeactivationB="0.56e-3" Type="MinettiAlexanderComplete"  
VMaxFactor="8.4" ViaPointBody0="Trunk" ViaPointBody1="Trunk" ViaPointBody2="LeftThigh"  
Width="1" TendonLength="4.31585222161969262e-01" InitialFibreLength="-1"  
StartActivation="1.0000000000000002e-03" Origin="Trunk -6.2400000000000110e-02  
2.2050000000000002e-02 -1.8852500000000054e-01" Insertion="LeftShank -  
1.7259999999999178e-02 4.0118999999999880e-02 1.7260500000000064e-01"  
ViaPoint0="Trunk -7.4748000000000366e-02 4.7627999999999967e-02 -  
2.1586700000000031e-01" ViaPoint1="Trunk -7.4748000000000366e-02  
7.4088000000000011e-02 -2.4673699999999984e-01" ViaPoint2="LeftThigh -  
4.1984999999999599e-02 -9.3300000000000496e-03 1.492799999999996e-01"/>

<MUSCLE ActivationK="0.17" ActivationKinetics="false" ActivationRate="500"  
FastTwitchProportion="0.5" FibreLength="0.1439999999999999" ForcePerUnitArea="300000"  
ID="Main.Model.HumanModel.Left.Leg.Mus.GluteusMaximus3" InsertionBodyID="LeftThigh"  
MidpointBodyID="Trunk" OriginBodyID="Trunk" PCA="0.0012266666666666667"  
ParallelStrainAtFmax="0.5999999999999998" ParallelStrainModel="Square"  
ParallelStrainRateAtFmax="0" SerialStrainAtFmax="0.0599999999999999"  
SerialStrainModel="Square" SerialStrainRateAtFmax="0" Strap="ThreePoint" TActivationA="80e-3"  
TActivationB="0.47e-3" TDeactivationA="90e-3" TDeactivationB="0.56e-3"  
Type="MinettiAlexanderComplete" VMaxFactor="8.4" Width="1"  
TendonLength="8.57912036038013248e-02" InitialFibreLength="-1"  
StartActivation="1.0000000000000002e-03" Origin="Trunk -5.5344000000000598e-02  
1.7639999999999994e-03 -2.1322099999999994e-01" Insertion="LeftThigh -  
1.4927999999999257e-02 8.3969999999998781e-03 6.9975000000000233e-02"  
MidPoint="Trunk -7.4748000000000366e-02 3.8808000000000022e-02 -3.0671300000000013e-  
01"/>

<MUSCLE ActivationK="0.17" ActivationKinetics="false" ActivationRate="500"  
FastTwitchProportion="0.5" FibreLength="0.0539999999999999" ForcePerUnitArea="300000"  
ID="Main.Model.HumanModel.Left.Leg.Mus.GluteusMedius1" InsertionBodyID="LeftThigh"  
OriginBodyID="Trunk" PCA="0.0018333333333333333"  
ParallelStrainAtFmax="0.5999999999999998" ParallelStrainModel="Square"  
ParallelStrainRateAtFmax="0" SerialStrainAtFmax="0.0599999999999999"  
SerialStrainModel="Square" SerialStrainRateAtFmax="0" Strap="TwoPoint" TActivationA="80e-3"  
TActivationB="0.47e-3" TDeactivationA="90e-3" TDeactivationB="0.56e-3"  
Type="MinettiAlexanderComplete" VMaxFactor="8.4" Width="1"  
TendonLength="7.93679121828035350e-02" InitialFibreLength="-1"  
StartActivation="1.0000000000000002e-03" Origin="Trunk 2.8445999999999713e-02  
1.1201400000000002e-01 -1.73530999999999880e-01" Insertion="LeftThigh -  
9.33000000000009863e-03 2.9855999999999937e-02 1.6514100000000010e-01"/>

<MUSCLE ActivationK="0.17" ActivationKinetics="false" ActivationRate="500"  
FastTwitchProportion="0.5" FibreLength="0.08400000000000005" ForcePerUnitArea="300000"

ID="Main.Model.HumanModel.Left.Leg.Mus.GluteusMedius2" InsertionBodyID="LeftThigh"  
OriginBodyID="Trunk" PCA="0.0012666666666666666"  
ParallelStrainAtFmax="0.5999999999999998" ParallelStrainModel="Square"  
ParallelStrainRateAtFmax="0" SerialStrainAtFmax="0.05999999999999999"  
SerialStrainModel="Square" SerialStrainRateAtFmax="0" Strap="TwoPoint" TActivationA="80e-3"  
TActivationB="0.47e-3" TDeactivationA="90e-3" TDeactivationB="0.56e-3"  
Type="MinettiAlexanderComplete" VMaxFactor="8.4" Width="1"  
TendonLength="9.45413117460494196e-02" InitialFibreLength="-1"  
StartActivation="1.0000000000000002e-03" Origin="Trunk -1.30079999999999985e-02  
8.4671999999999973e-02 -1.2413899999999999e-01" Insertion="LeftThigh -  
9.33000000000009863e-03 2.9855999999999937e-02 1.6514100000000010e-01"/>

<MUSCLE ActivationK="0.17" ActivationKinetics="false" ActivationRate="500"  
FastTwitchProportion="0.5" FibreLength="0.06500000000000002" ForcePerUnitArea="300000"  
ID="Main.Model.HumanModel.Left.Leg.Mus.GluteusMedius3" InsertionBodyID="LeftThigh"  
OriginBodyID="Trunk" PCA="0.0014499999999999999"  
ParallelStrainAtFmax="0.5999999999999998" ParallelStrainModel="Square"  
ParallelStrainRateAtFmax="0" SerialStrainAtFmax="0.05999999999999999"  
SerialStrainModel="Square" SerialStrainRateAtFmax="0" Strap="TwoPoint" TActivationA="80e-3"  
TActivationB="0.47e-3" TDeactivationA="90e-3" TDeactivationB="0.56e-3"  
Type="MinettiAlexanderComplete" VMaxFactor="8.4" Width="1"  
TendonLength="1.24873642193960077e-01" InitialFibreLength="-1"  
StartActivation="1.0000000000000002e-03" Origin="Trunk -5.71079999999999366e-02  
4.0571999999999970e-02 -1.3560499999999976e-01" Insertion="LeftThigh -  
9.33000000000009863e-03 2.9855999999999937e-02 1.6514100000000010e-01"/>

<MUSCLE ActivationK="0.17" ActivationKinetics="false" ActivationRate="500"  
FastTwitchProportion="0.5" FibreLength="0.06800000000000005" ForcePerUnitArea="300000"  
ID="Main.Model.HumanModel.Left.Leg.Mus.GluteusMinimus1" InsertionBodyID="LeftThigh"  
OriginBodyID="Trunk" PCA="0.0005999999999999995"  
ParallelStrainAtFmax="0.5999999999999998" ParallelStrainModel="Square"  
ParallelStrainRateAtFmax="0" SerialStrainAtFmax="0.05999999999999999"  
SerialStrainModel="Square" SerialStrainRateAtFmax="0" Strap="TwoPoint" TActivationA="80e-3"  
TActivationB="0.47e-3" TDeactivationA="90e-3" TDeactivationB="0.56e-3"  
Type="MinettiAlexanderComplete" VMaxFactor="8.4" Width="1"  
TendonLength="4.50398159941884091e-02" InitialFibreLength="-1"  
StartActivation="1.0000000000000002e-03" Origin="Trunk -6.599999999999882903e-04  
1.0231200000000000e-01 -1.8499700000000078e-01" Insertion="LeftThigh  
2.79899999999989185e-03 3.4520999999999961e-02 1.6140900000000025e-01"/>

<MUSCLE ActivationK="0.17" ActivationKinetics="false" ActivationRate="500"  
FastTwitchProportion="0.5" FibreLength="0.05600000000000001" ForcePerUnitArea="300000"  
ID="Main.Model.HumanModel.Left.Leg.Mus.GluteusMinimus2" InsertionBodyID="LeftThigh"  
OriginBodyID="Trunk" PCA="0.0006333333333333333"  
ParallelStrainAtFmax="0.5999999999999998" ParallelStrainModel="Square"  
ParallelStrainRateAtFmax="0" SerialStrainAtFmax="0.05999999999999999"  
SerialStrainModel="Square" SerialStrainRateAtFmax="0" Strap="TwoPoint" TActivationA="80e-3"  
TActivationB="0.47e-3" TDeactivationA="90e-3" TDeactivationB="0.56e-3"  
Type="MinettiAlexanderComplete" VMaxFactor="8.4" Width="1"  
TendonLength="7.47975534939395448e-02" InitialFibreLength="-1"  
StartActivation="1.0000000000000002e-03" Origin="Trunk -1.5654000000000568e-02  
8.0262000000000000e-02 -1.7617700000000028e-01" Insertion="LeftThigh  
2.79899999999989185e-03 3.4520999999999961e-02 1.6140900000000025e-01"/>

<MUSCLE ActivationK="0.17" ActivationKinetics="false" ActivationRate="500"  
FastTwitchProportion="0.5" FibreLength="0.03799999999999999" ForcePerUnitArea="300000"  
ID="Main.Model.HumanModel.Left.Leg.Mus.GluteusMinimus3" InsertionBodyID="LeftThigh"  
OriginBodyID="Trunk" PCA="0.00071666666666666667"  
ParallelStrainAtFmax="0.59999999999999998" ParallelStrainModel="Square"  
ParallelStrainRateAtFmax="0" SerialStrainAtFmax="0.05999999999999999"  
SerialStrainModel="Square" SerialStrainRateAtFmax="0" Strap="TwoPoint" TActivationA="80e-3"  
TActivationB="0.47e-3" TDeactivationA="90e-3" TDeactivationB="0.56e-3"  
Type="MinettiAlexanderComplete" VMaxFactor="8.4" Width="1"  
TendonLength="1.02804829462628783e-01" InitialFibreLength="-1"  
StartActivation="1.0000000000000002e-03" Origin="Trunk -3.5940000000000830e-02  
5.4684000000000034e-02 -1.8499700000000078e-01" Insertion="LeftThigh  
2.798999999999989185e-03 3.4520999999999961e-02 1.6140900000000025e-01"/>

<MUSCLE ActivationK="0.17" ActivationKinetics="false" ActivationRate="500"  
FastTwitchProportion="0.5" FibreLength="0.35199999999999998" ForcePerUnitArea="300000"  
ID="Main.Model.HumanModel.Left.Leg.Mus.Gracilis" InsertionBodyID="LeftShank"  
OriginBodyID="Trunk" PCA="0.00036000000000000002"  
ParallelStrainAtFmax="0.59999999999999998" ParallelStrainModel="Square"  
ParallelStrainRateAtFmax="0" SerialStrainAtFmax="0.05999999999999999"  
SerialStrainModel="Square" SerialStrainRateAtFmax="0" Strap="NPoint" TActivationA="80e-3"  
TActivationB="0.47e-3" TDeactivationA="90e-3" TDeactivationB="0.56e-3"  
Type="MinettiAlexanderComplete" VMaxFactor="8.4" ViaPointBody0="LeftShank"  
ViaPointBody1="LeftShank" Width="1" TendonLength="1.49051553907173284e-01"  
InitialFibreLength="-1" StartActivation="1.0000000000000002e-03" Origin="Trunk  
9.0419999999999449e-03 6.1739999999999980e-03 -3.1376899999999965e-01"  
Insertion="LeftShank 1.67940000000000277e-02 -1.4927999999999968e-02  
1.2129000000000023e-01" ViaPoint0="LeftShank -3.06489999999999679e-02 -  
1.6794000000000034e-02 1.6794000000000061e-01" ViaPoint1="LeftShank -  
4.66499999999990880e-03 -3.9185999999999986e-02 1.3994999999999991e-01"/>

<MUSCLE ActivationK="0.17" ActivationKinetics="false" ActivationRate="500"  
CylinderBodyID="Trunk" FastTwitchProportion="0.5" FibreLength="0.10000000000000001"  
ForcePerUnitArea="300000" ID="Main.Model.HumanModel.Left.Leg.Mus.Iliopsoas"  
InsertionBodyID="LeftThigh" OriginBodyID="Trunk" PCA="0.0026666666666666666"  
ParallelStrainAtFmax="0.59999999999999998" ParallelStrainModel="Square"  
ParallelStrainRateAtFmax="0" SerialStrainAtFmax="0.05999999999999999"  
SerialStrainModel="Square" SerialStrainRateAtFmax="0" Strap="CylinderWrap" TActivationA="80e-  
3" TActivationB="0.47e-3" TDeactivationA="90e-3" TDeactivationB="0.56e-3"  
Type="MinettiAlexanderComplete" VMaxFactor="8.4" Width="1"  
TendonLength="1.17962624962018203e-01" InitialFibreLength="-1"  
StartActivation="1.0000000000000002e-03" Origin="Trunk -1.0188000000000859e-02  
7.055999999999977e-02 -1.4089700000000050e-01" Insertion="LeftThigh  
9.33000000000063986e-04 -7.4639999999999841e-03 1.1195999999999893e-01"  
CylinderPosition="Trunk -1.3007999999999085e-02 4.233599999999986e-02 -  
2.8201699999999962e-01" CylinderRadius="3.0000021249149269e-02"  
CylinderQuaternion="Trunk 9.13500123868869474e-01 -4.06838449131298407e-01  
0.0000000000000000e+00 0.0000000000000000e+00"/>

<MUSCLE ActivationK="0.17" ActivationKinetics="false" ActivationRate="500"  
FastTwitchProportion="0.5" FibreLength="0.05000000000000003" ForcePerUnitArea="300000"  
ID="Main.Model.HumanModel.Left.Leg.Mus.PeroneusBrevis" InsertionBodyID="LeftMTs"  
MidpointBodyID="LeftRearFoot" OriginBodyID="LeftShank" PCA="0.0011666666666666668"  
ParallelStrainAtFmax="0.59999999999999998" ParallelStrainModel="Square"

ParallelStrainRateAtFmax="0" SerialStrainAtFmax="0.059999999999999999"  
SerialStrainModel="Square" SerialStrainRateAtFmax="0" Strap="ThreePoint" TActivationA="80e-3"  
TActivationB="0.47e-3" TDeactivationA="90e-3" TDeactivationB="0.56e-3"  
Type="MinettiAlexanderComplete" VMaxFactor="8.4" Width="1"  
TendonLength="2.52934358523857872e-01" InitialFibreLength="-1"  
StartActivation="1.0000000000000002e-03" Origin="LeftShank 5.89805981832114412e-17  
2.7989999999999871e-02 -3.7320000000000059e-02" Insertion="LeftMTs -  
5.4044000000000850e-02 2.7022000000000043e-02 -4.1569999999999577e-03"  
MidPoint="LeftRearFoot 8.3139999999992909e-03 1.6629000000000049e-02  
1.3511000000000074e-02"/>

<MUSCLE ActivationK="0.17" ActivationKinetics="false" ActivationRate="500"  
FastTwitchProportion="0.5" FibreLength="0.025999999999999999" ForcePerUnitArea="300000"  
ID="Main.Model.HumanModel.Left.Leg.Mus.Piriformis" InsertionBodyID="LeftThigh"  
MidpointBodyID="Trunk" OriginBodyID="Trunk" PCA="0.0009833333333333324"  
ParallelStrainAtFmax="0.5999999999999998" ParallelStrainModel="Square"  
ParallelStrainRateAtFmax="0" SerialStrainAtFmax="0.059999999999999999"  
SerialStrainModel="Square" SerialStrainRateAtFmax="0" Strap="ThreePoint" TActivationA="80e-3"  
TActivationB="0.47e-3" TDeactivationA="90e-3" TDeactivationB="0.56e-3"  
Type="MinettiAlexanderComplete" VMaxFactor="8.4" Width="1"  
TendonLength="1.19067000404308787e-01" InitialFibreLength="-1"  
StartActivation="1.0000000000000002e-03" Origin="Trunk -5.5344000000000598e-02  
1.8522000000000003e-02 -2.0528299999999993e-01" Insertion="LeftThigh -  
1.2128999999999315e-02 2.4258000000000018e-02 1.6980600000000040e-01"  
MidPoint="Trunk -3.9468000000000586e-02 7.9380000000000061e-02 -2.3791699999999934e-  
01"/>

<MUSCLE ActivationK="0.17" ActivationKinetics="false" ActivationRate="500"  
CylinderBodyID="LeftThigh" FastTwitchProportion="0.5" FibreLength="0.08400000000000005"  
ForcePerUnitArea="300000" ID="Main.Model.HumanModel.Left.Leg.Mus.RectusFemoris"  
InsertionBodyID="LeftShank" OriginBodyID="Trunk" PCA="0.0025999999999999999"  
ParallelStrainAtFmax="0.5999999999999998" ParallelStrainModel="Square"  
ParallelStrainRateAtFmax="0" SerialStrainAtFmax="0.059999999999999999"  
SerialStrainModel="Square" SerialStrainRateAtFmax="0" Strap="CylinderWrap" TActivationA="80e-  
3" TActivationB="0.47e-3" TDeactivationA="90e-3" TDeactivationB="0.56e-3"  
Type="MinettiAlexanderComplete" VMaxFactor="8.4" Width="1"  
TendonLength="4.84929924409269020e-01" InitialFibreLength="-1"  
StartActivation="1.0000000000000002e-03" Origin="Trunk 5.51400000000001889e-03  
8.8200000000000006e-02 -2.3615300000000057e-01" Insertion="LeftShank  
2.9855999999999000e-02 9.3300000000000496e-03 1.0262999999999999e-01"  
CylinderPosition="LeftThigh -2.3324999999999083e-02 -2.6124000000000083e-02 -  
2.4071399999999984e-01" CylinderRadius="2.999999999999989e-02"  
CylinderQuaternion="LeftThigh -7.07106781186547573e-01 7.07106781186547573e-01  
1.38777878078144568e-17 1.38777878078144568e-17"/>

<MUSCLE ActivationK="0.17" ActivationKinetics="false" ActivationRate="500"  
FastTwitchProportion="0.5" FibreLength="0.5789999999999996" ForcePerUnitArea="300000"  
ID="Main.Model.HumanModel.Left.Leg.Mus.Sartorius" InsertionBodyID="LeftShank"  
OriginBodyID="Trunk" PCA="0.0003466666666666667"  
ParallelStrainAtFmax="0.5999999999999998" ParallelStrainModel="Square"  
ParallelStrainRateAtFmax="0" SerialStrainAtFmax="0.059999999999999999"  
SerialStrainModel="Square" SerialStrainRateAtFmax="0" Strap="NPoint" TActivationA="80e-3"  
TActivationB="0.47e-3" TDeactivationA="90e-3" TDeactivationB="0.56e-3"  
Type="MinettiAlexanderComplete" VMaxFactor="8.4" ViaPointBody0="LeftThigh"

ViaPointBody1="LeftShank" ViaPointBody2="LeftShank" Width="1"  
TendonLength="5.60366472734018517e-02" InitialFibreLength="-1"  
StartActivation="1.0000000000000002e-03" Origin="Trunk 3.8148000000000707e-02  
1.1995200000000003e-01 -1.8764300000000004e-01" Insertion="LeftShank  
1.6794000000000277e-02 -1.4927999999999968e-02 1.2129000000000023e-01"  
ViaPoint0="LeftThigh 3.2655000000000243e-02 -2.7990000000000010e-02  
1.8659999999999981e-02" ViaPoint1="LeftShank -2.0105999999999954e-02 -  
3.5453999999999994e-02 1.6794000000000006e-01" ViaPoint2="LeftShank -  
4.51028103753969845e-17 -4.3851000000000011e-02 1.3994999999999991e-01"/>

<MUSCLE ActivationK="0.17" ActivationKinetics="false" ActivationRate="500"  
CylinderBodyID="LeftThigh" FastTwitchProportion="0.5" FibreLength="0.0800000000000002"  
ForcePerUnitArea="300000" ID="Main.Model.HumanModel.Left.Leg.Mus.Semimembranosus"  
InsertionBodyID="LeftShank" OriginBodyID="Trunk" PCA="0.0034333333333333334"  
ParallelStrainAtFmax="0.5999999999999998" ParallelStrainModel="Square"  
ParallelStrainRateAtFmax="0" SerialStrainAtFmax="0.05999999999999999"  
SerialStrainModel="Square" SerialStrainRateAtFmax="0" Strap="CylinderWrap" TActivationA="80e-  
3" TActivationB="0.47e-3" TDeactivationA="90e-3" TDeactivationB="0.56e-3"  
Type="MinettiAlexanderComplete" VMaxFactor="8.4" Width="1"  
TendonLength="3.37657679256022136e-01" InitialFibreLength="-1"  
StartActivation="1.0000000000000002e-03" Origin="Trunk -7.2983999999999378e-02  
3.4397999999999980e-02 -3.11123000000000038e-01" Insertion="LeftShank -  
2.5190999999999773e-02 -1.67940000000000034e-02 1.5861000000000001e-01"  
CylinderPosition="LeftThigh -2.3324999999999083e-02 -2.61240000000000083e-02 -  
2.4071399999999984e-01" CylinderRadius="3.50000000000000033e-02"  
CylinderQuaternion="LeftThigh 7.07106781186547573e-01 7.07106781186547573e-01  
1.38777878078144568e-17 1.38777878078144568e-17"/>

<MUSCLE ActivationK="0.17" ActivationKinetics="false" ActivationRate="500"  
FastTwitchProportion="0.5" FibreLength="0.20100000000000001" ForcePerUnitArea="300000"  
ID="Main.Model.HumanModel.Left.Leg.Mus.Semitendinosus" InsertionBodyID="LeftShank"  
MidpointBodyID="LeftShank" OriginBodyID="Trunk" PCA="0.0011000000000000001"  
ParallelStrainAtFmax="0.5999999999999998" ParallelStrainModel="Square"  
ParallelStrainRateAtFmax="0" SerialStrainAtFmax="0.05999999999999999"  
SerialStrainModel="Square" SerialStrainRateAtFmax="0" Strap="ThreePoint" TActivationA="80e-3"  
TActivationB="0.47e-3" TDeactivationA="90e-3" TDeactivationB="0.56e-3"  
Type="MinettiAlexanderComplete" VMaxFactor="8.4" Width="1"  
TendonLength="2.77209427004380338e-01" InitialFibreLength="-1"  
StartActivation="1.0000000000000002e-03" Origin="Trunk -7.2983999999999378e-02  
3.4397999999999980e-02 -3.11123000000000038e-01" Insertion="LeftShank  
1.6794000000000277e-02 1.4927999999999968e-02 1.2129000000000023e-01"  
MidPoint="LeftShank -2.33250000000000644e-02 3.9185999999999986e-02  
1.3994999999999991e-01"/>

<MUSCLE ActivationK="0.17" ActivationKinetics="false" ActivationRate="500"  
FastTwitchProportion="0.5" FibreLength="0.04000000000000001" ForcePerUnitArea="300000"  
ID="Main.Model.HumanModel.Left.Leg.Mus.Soleus" InsertionBodyID="LeftRearFoot"  
OriginBodyID="LeftShank" PCA="0.0094333333333333335"  
ParallelStrainAtFmax="0.5999999999999998" ParallelStrainModel="Square"  
ParallelStrainRateAtFmax="0" SerialStrainAtFmax="0.05999999999999999"  
SerialStrainModel="Square" SerialStrainRateAtFmax="0" Strap="TwoPoint" TActivationA="80e-3"  
TActivationB="0.47e-3" TDeactivationA="90e-3" TDeactivationB="0.56e-3"  
Type="MinettiAlexanderComplete" VMaxFactor="8.4" Width="1"  
TendonLength="3.82929072067645981e-01" InitialFibreLength="-1"

StartActivation="1.0000000000000002e-03" Origin="LeftShank -1.86599999999999475e-02  
0.0000000000000000e+00 1.2054399999999984e-01" Insertion="LeftRearFoot -  
3.11790000000000331e-02 -3.1179999999999577e-03 4.15700000000000271e-03"/>

<MUSCLE ActivationK="0.17" ActivationKinetics="false" ActivationRate="500"  
FastTwitchProportion="0.5" FibreLength="0.09500000000000001" ForcePerUnitArea="300000"  
ID="Main.Model.HumanModel.Left.Leg.Mus.TensorFasciaeLatae" InsertionBodyID="LeftShank"  
MidpointBodyID="LeftThigh" OriginBodyID="Trunk" PCA="0.00051666666666666668"  
ParallelStrainAtFmax="0.5999999999999998" ParallelStrainModel="Square"  
ParallelStrainRateAtFmax="0" SerialStrainAtFmax="0.05999999999999999"  
SerialStrainModel="Square" SerialStrainRateAtFmax="0" Strap="ThreePoint" TActivationA="80e-3"  
TActivationB="0.47e-3" TDeactivationA="90e-3" TDeactivationB="0.56e-3"  
Type="MinettiAlexanderComplete" VMaxFactor="8.4" Width="1"  
TendonLength="4.75012228506116352e-01" InitialFibreLength="-1"  
StartActivation="1.0000000000000002e-03" Origin="Trunk 3.81480000000000707e-02  
1.1995200000000003e-01 -1.8764300000000004e-01" Insertion="LeftShank -  
1.7259999999999178e-02 4.0118999999999880e-02 1.7260500000000064e-01"  
MidPoint="LeftThigh -9.3299999999990261e-03 3.9185999999999986e-02  
1.2128999999999981e-01"/>

<MUSCLE ActivationK="0.17" ActivationKinetics="false" ActivationRate="500"  
FastTwitchProportion="0.5" FibreLength="0.05600000000000001" ForcePerUnitArea="300000"  
ID="Main.Model.HumanModel.Left.Leg.Mus.TibialisAnterior" InsertionBodyID="LeftMidFoot"  
MidpointBodyID="LeftMidFoot" OriginBodyID="LeftShank" PCA="0.002"  
ParallelStrainAtFmax="0.5999999999999998" ParallelStrainModel="Square"  
ParallelStrainRateAtFmax="0" SerialStrainAtFmax="0.05999999999999999"  
SerialStrainModel="Square" SerialStrainRateAtFmax="0" Strap="ThreePoint" TActivationA="80e-3"  
TActivationB="0.47e-3" TDeactivationA="90e-3" TDeactivationB="0.56e-3"  
Type="MinettiAlexanderComplete" VMaxFactor="8.4" Width="1"  
TendonLength="2.55749622953320432e-01" InitialFibreLength="-1"  
StartActivation="1.0000000000000002e-03" Origin="LeftShank 6.93889390390722838e-17 -  
9.3300000000000496e-03 1.0730000000000104e-02" Insertion="LeftMidFoot  
1.9746999999999382e-02 -2.182499999999972e-02 2.0790000000000012e-03"  
MidPoint="LeftMidFoot 4.1569999999996888e-03 -1.143199999999977e-02  
2.806099999999957e-02"/>

<MUSCLE ActivationK="0.17" ActivationKinetics="false" ActivationRate="500"  
FastTwitchProportion="0.5" FibreLength="0.02999999999999999" ForcePerUnitArea="300000"  
ID="Main.Model.HumanModel.Left.Leg.Mus.TibialisPosterior" InsertionBodyID="LeftMidFoot"  
MidpointBodyID="LeftRearFoot" OriginBodyID="LeftShank" PCA="0.004233333333333337"  
ParallelStrainAtFmax="0.5999999999999998" ParallelStrainModel="Square"  
ParallelStrainRateAtFmax="0" SerialStrainAtFmax="0.05999999999999999"  
SerialStrainModel="Square" SerialStrainRateAtFmax="0" Strap="ThreePoint" TActivationA="80e-3"  
TActivationB="0.47e-3" TDeactivationA="90e-3" TDeactivationB="0.56e-3"  
Type="MinettiAlexanderComplete" VMaxFactor="8.4" Width="1"  
TendonLength="4.66945158597317000e-01" InitialFibreLength="-1"  
StartActivation="1.0000000000000002e-03" Origin="LeftShank 8.67361737988403547e-17  
0.0000000000000000e+00 1.2129000000000051e-01" Insertion="LeftMidFoot  
5.9409999999991683e-03 -2.7464000000000023e-02 -8.506999999999720e-03"  
MidPoint="LeftRearFoot 6.5740000000010493e-03 -3.117899999999984e-02  
1.3510999999999987e-02"/>

<MUSCLE ActivationK="0.17" ActivationKinetics="false" ActivationRate="500"  
CylinderBodyID="LeftThigh" FastTwitchProportion="0.5" FibreLength="0.08699999999999994"

ForcePerUnitArea="300000" ID="Main.Model.HumanModel.Left.Leg.Mus.VastusIntermedius"  
InsertionBodyID="LeftShank" OriginBodyID="LeftThigh" PCA="0.004116666666666669"  
ParallelStrainAtFmax="0.5999999999999998" ParallelStrainModel="Square"  
ParallelStrainRateAtFmax="0" SerialStrainAtFmax="0.05999999999999999"  
SerialStrainModel="Square" SerialStrainRateAtFmax="0" Strap="CylinderWrap" TActivationA="80e-3"  
TActivationB="0.47e-3" TDeactivationA="90e-3" TDeactivationB="0.56e-3"  
Type="MinettiAlexanderComplete" VMaxFactor="8.4" Width="1"  
TendonLength="2.63531912563401249e-01" InitialFibreLength="-1"  
StartActivation="1.0000000000000002e-03" Origin="LeftThigh 1.306199999999999833e-02  
0.0000000000000000e+00 3.77302356024955543e-17" Insertion="LeftShank  
2.985599999999999000e-02 9.33000000000000496e-03 1.0262999999999999e-01"  
CylinderPosition="LeftThigh -2.332499999999999083e-02 -2.61240000000000083e-02 -  
2.40713999999999984e-01" CylinderRadius="2.5000000000000014e-02"  
CylinderQuaternion="LeftThigh -7.07106781186547573e-01 7.07106781186547573e-01  
1.38777878078144568e-17 1.38777878078144568e-17"/>

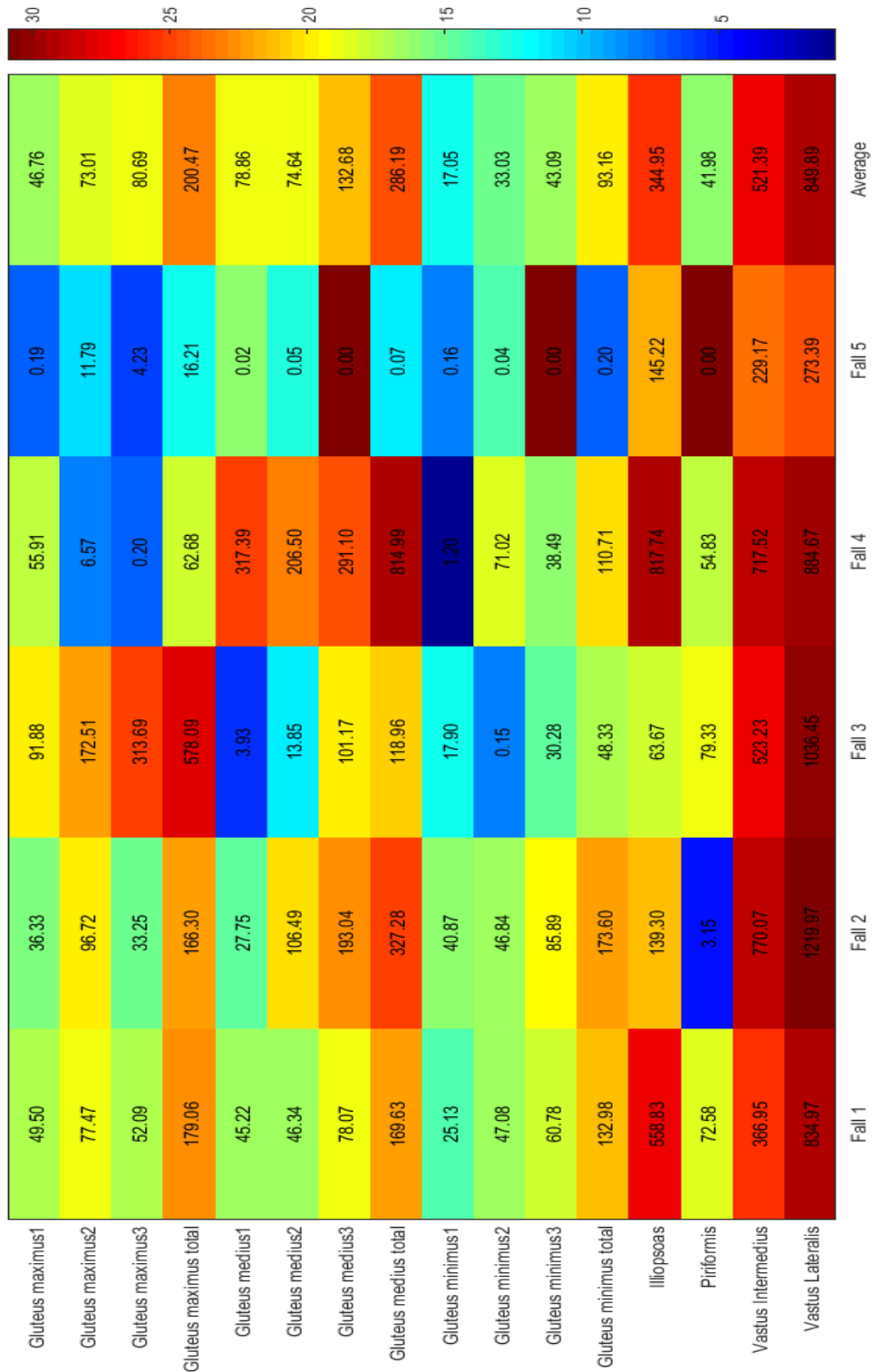
<MUSCLE ActivationK="0.17" ActivationKinetics="false" ActivationRate="500"  
CylinderBodyID="LeftThigh" FastTwitchProportion="0.5" FibreLength="0.08400000000000005"  
ForcePerUnitArea="300000" ID="Main.Model.HumanModel.Left.Leg.Mus.VastusLateralis"  
InsertionBodyID="LeftShank" OriginBodyID="LeftThigh" PCA="0.006233333333333329"  
ParallelStrainAtFmax="0.5999999999999998" ParallelStrainModel="Square"  
ParallelStrainRateAtFmax="0" SerialStrainAtFmax="0.05999999999999999"  
SerialStrainModel="Square" SerialStrainRateAtFmax="0" Strap="CylinderWrap" TActivationA="80e-3"  
TActivationB="0.47e-3" TDeactivationA="90e-3" TDeactivationB="0.56e-3"  
Type="MinettiAlexanderComplete" VMaxFactor="8.4" Width="1"  
TendonLength="2.68468498031746716e-01" InitialFibreLength="-1"  
StartActivation="1.0000000000000002e-03" Origin="LeftThigh 0.0000000000000000e+00  
1.2129000000000009e-02 0.0000000000000000e+00" Insertion="LeftShank  
2.985599999999999000e-02 9.33000000000000496e-03 1.0262999999999999e-01"  
CylinderPosition="LeftThigh -2.332499999999999083e-02 -2.61240000000000083e-02 -  
2.40713999999999984e-01" CylinderRadius="2.7500000000000001e-02"  
CylinderQuaternion="LeftThigh -7.07106781186547573e-01 7.07106781186547573e-01  
1.38777878078144568e-17 1.38777878078144568e-17"/>

<MUSCLE ActivationK="0.17" ActivationKinetics="false" ActivationRate="500"  
CylinderBodyID="LeftThigh" FastTwitchProportion="0.5" FibreLength="0.08899999999999996"  
ForcePerUnitArea="300000" ID="Main.Model.HumanModel.Left.Leg.Mus.VastusMedialis"  
InsertionBodyID="LeftShank" OriginBodyID="LeftThigh" PCA="0.004316666666666666"  
ParallelStrainAtFmax="0.5999999999999998" ParallelStrainModel="Square"  
ParallelStrainRateAtFmax="0" SerialStrainAtFmax="0.05999999999999999"  
SerialStrainModel="Square" SerialStrainRateAtFmax="0" Strap="CylinderWrap" TActivationA="80e-3"  
TActivationB="0.47e-3" TDeactivationA="90e-3" TDeactivationB="0.56e-3"  
Type="MinettiAlexanderComplete" VMaxFactor="8.4" Width="1"  
TendonLength="3.02574678296056554e-01" InitialFibreLength="-1"  
StartActivation="1.0000000000000002e-03" Origin="LeftThigh -8.84708972748171618e-17 -  
1.30620000000000042e-02 3.82530000000000023e-02" Insertion="LeftShank  
2.985599999999999000e-02 9.33000000000000496e-03 1.0262999999999999e-01"  
CylinderPosition="LeftThigh -2.332499999999999083e-02 -2.61240000000000083e-02 -  
2.40713999999999984e-01" CylinderRadius="2.7500000000000001e-02"  
CylinderQuaternion="LeftThigh -7.07106781186547573e-01 7.07106781186547573e-01  
1.38777878078144568e-17 1.38777878078144568e-17"/>

<MUSCLE ActivationK="0.17" ActivationKinetics="false" ActivationRate="500"  
FastTwitchProportion="0.5" FibreLength="0.06" ForcePerUnitArea="300000"

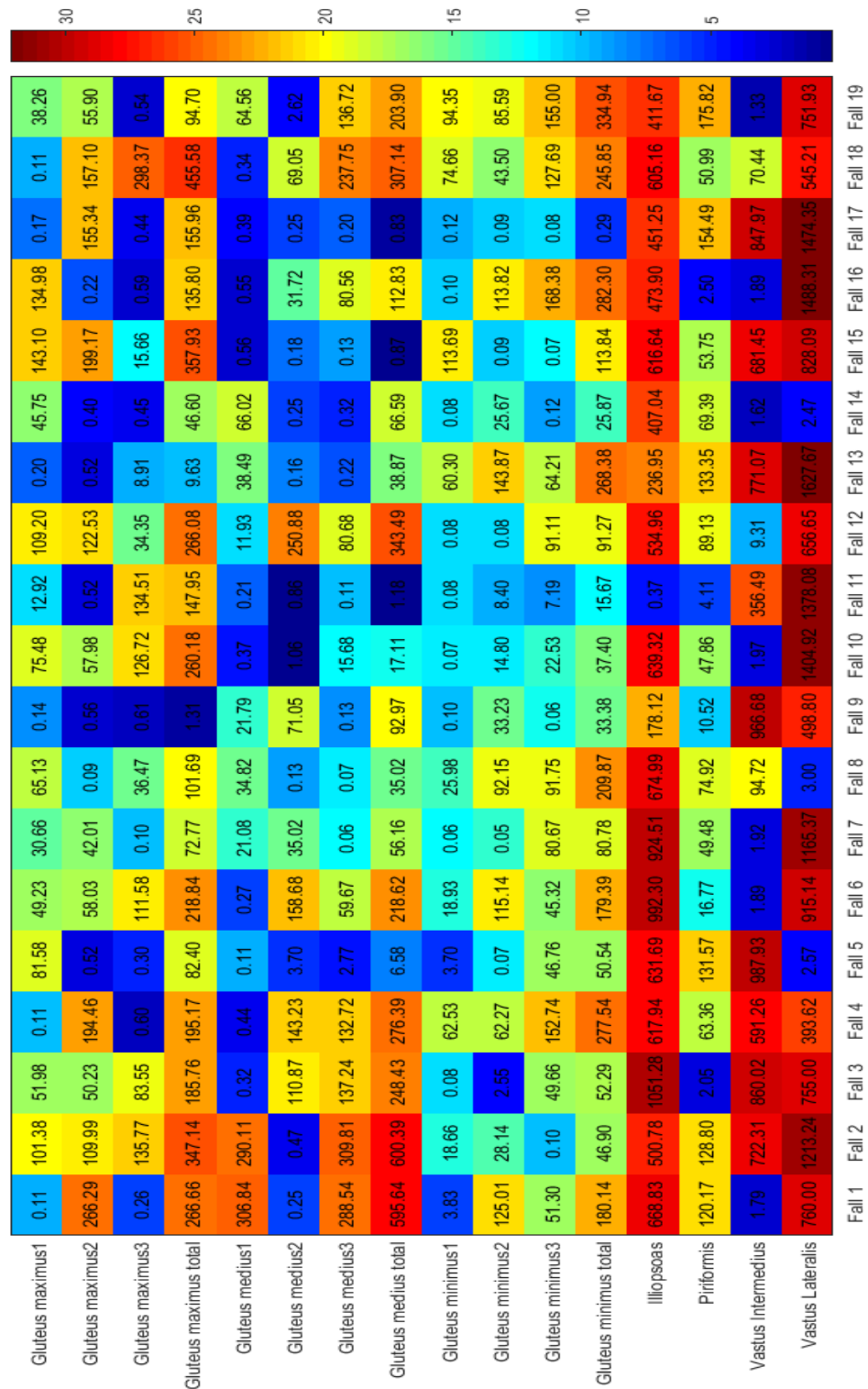
ID="Main.Model.HumanModel.Left.Leg.Mus.PeroneusLongus" InsertionBodyID="LeftMTs"  
MidpointBodyID="LeftRearFoot" OriginBodyID="LeftShank" PCA="0.002144"  
ParallelStrainAtFmax="0.5999999999999998" ParallelStrainModel="Square"  
ParallelStrainRateAtFmax="0" SerialStrainAtFmax="0.05999999999999999"  
SerialStrainModel="Square" SerialStrainRateAtFmax="0" Strap="ThreePoint" TActivationA="80e-3"  
TActivationB="0.47e-3" TDeactivationA="90e-3" TDeactivationB="0.56e-3"  
Type="MinettiAlexanderComplete" VMaxFactor="8.4" Width="1"  
TendonLength="4.51000000000000012e-01" InitialFibreLength="-1"  
StartActivation="1.0000000000000002e-03" Origin="LeftShank 9.14700000000007521e-03  
3.50280000000000036e-02 1.1908599999999984e-01" Insertion="LeftMTs -  
1.8776999999999951e-02 -2.079999999999990e-02 -2.7840000000000305e-03"  
MidPoint="LeftRearFoot 7.70600000000006263e-03 2.4317000000000053e-02 -  
3.4225000000000054e-02"/>

# APPENDIX E1



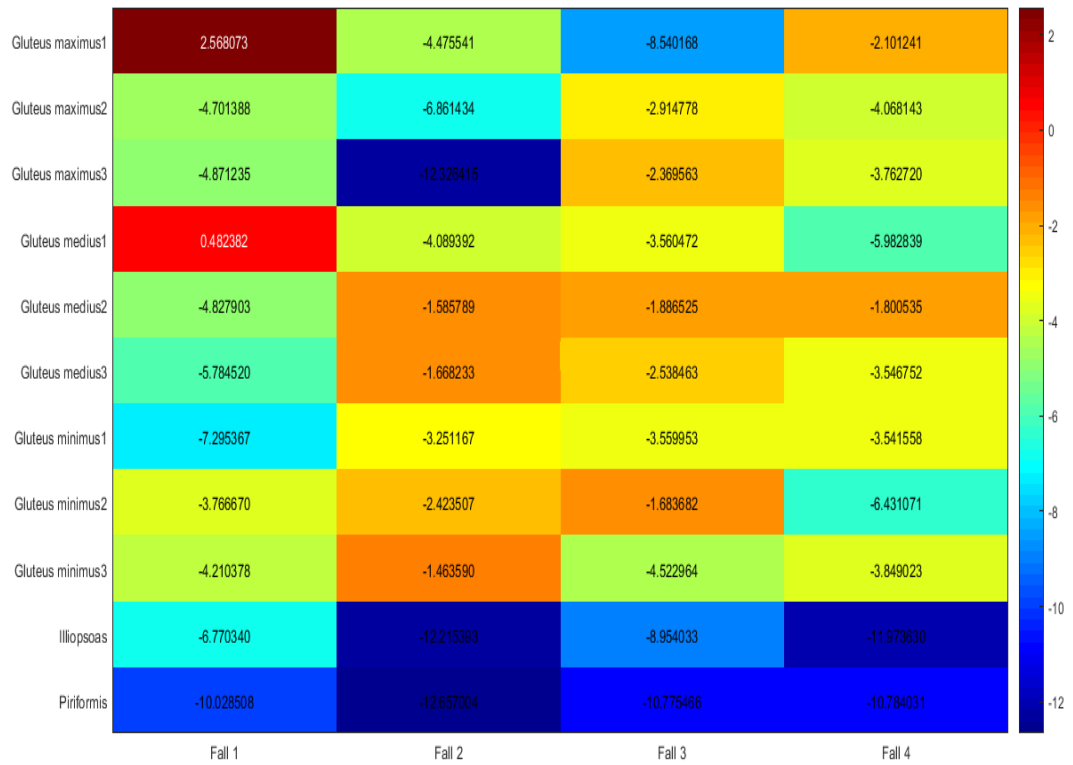
**Colour map: average muscle forces (N).** Colour map of mean muscle force values for all simulations, grouped by the real-world fall they modelled. Red colours = high values, blue colours = low values. Iliopsoas and the vastii muscles were relatively consistent in force production compared to all other muscles across simulations.

## APPENDIX E2



**Colour map of muscle forces (N): fall 1 simulations.** Colour map of muscle force magnitudes for each of the simulations modelling real-world fall 1. The colour map shows the wide range and inconsistent nature of muscle forces which correspond to colour, despite the fact these simulations were modelling the same real-world fall. Red colours = high values, blue colours = low values. Iliopsoas and the vastii muscles were relatively consistent in force production compared to all other muscles across simulations.

## APPENDIX F



**Colour map: tendon length changes.** Colour map of tendon length changes during impact in mm. Negative values represent an increase in tendon length with dark blue colours showing the largest increases in length. Positive values represent a decrease in tendon length with dark red colours showing the largest decreases in tendon length.





## APPENDIX H

---

Example of matlab code for assigning elements the correct orientations by creating the necessary python script and commands.

```
%cortical surface based orientation
for ik = 1:100
dlnname = 'cortical_orientations.py';
header1 = {'p = mdb.models["FINAL_187K"].parts["PART2_187K"]};
header2 = {'region = p.sets["PART2_187K VOLUME' num2str(ik) '"]};
header3 = {'p = mdb.models["FINAL_187K"].parts["PART2_187K"]};
header4 = {'normalAxisRegion = p-surfaces["SURFACE1"]};
header5 =
{'primaryAxisDatum=mdb.models["FINAL_187K"].parts["PART2_187K"].datu
ms[2230]};
header6 =
{'mdb.models["FINAL_187K"].parts["PART2_187K"].MaterialOrientation(r
egion=region,');
header7 = {'orientationType=DISCRETE, axis=AXIS_1,');
header8 = {'normalAxisDefinition=SURFACE,');
header9 = {'normalAxisRegion=normalAxisRegion,');
header10 = {'flipNormalDirection=False,');
header11 = {'normalAxisDirection=AXIS_1,
primaryAxisDefinition=DATUM,');
header12 = {'primaryAxisDatum=primaryAxisDatum,');
header13 = {'primaryAxisDirection=AXIS_3,');
header14 = {'flipPrimaryDirection=False,');
header15 = {'additionalRotationType=ROTATION_NONE,');
header16 = {'angle=0.0, additionalRotationField="",');
header17 = {'stackDirection=STACK_3)');
header18 = {'#: Specified material orientation has been assigned to
the selected regions.});
dlmwrite(dlnname, header1,'delimiter','', '-append');
dlmwrite(dlnname, header2,'delimiter','', '-append');
dlmwrite(dlnname, header3,'delimiter','', '-append');
dlmwrite(dlnname, header4,'delimiter','', '-append');
dlmwrite(dlnname, header5,'delimiter','', '-append');
dlmwrite(dlnname, header6,'delimiter','', '-append');
dlmwrite(dlnname, header7,'delimiter','', '-append');
dlmwrite(dlnname, header8,'delimiter','', '-append');
dlmwrite(dlnname, header9,'delimiter','', '-append');
dlmwrite(dlnname, header10,'delimiter','', '-append');
dlmwrite(dlnname, header11,'delimiter','', '-append');
dlmwrite(dlnname, header12,'delimiter','', '-append');
dlmwrite(dlnname, header13,'delimiter','', '-append');
dlmwrite(dlnname, header14,'delimiter','', '-append');
dlmwrite(dlnname, header15,'delimiter','', '-append');
dlmwrite(dlnname, header16,'delimiter','', '-append');
dlmwrite(dlnname, header17,'delimiter','', '-append');
dlmwrite(dlnname, header18,'delimiter','', '-append');
end

%trabecular cube orientation
load('fea_orient.mat','new_positions');
norm_vector = new_positions(:,4:6);
norm_vector1 = new_positions(:,4);
norm_vector2 = new_positions(:,5);
norm_vector3 = new_positions(:,6);
```

```

primary_vector = new_positions(:,10:12);
primary_vector1 = new_positions(:,10);
primary_vector2 = new_positions(:,11);
primary_vector3 = new_positions(:,12);

from abaqus import*
from part import *
from assembly import *
from interaction import *
from job import *
from sketch import *
from abaqusConstants import*

for ij = 1:606
dlmname = 'Material_orientations.py';
header1 = {'p = mdb.models["FINAL_187K"].parts["PART2_187K"]};
header2 = {'region = p.sets["FINAL_VOLUME' num2str(ij+100) '"']};
header3 =
{'mdb.models["FINAL_187K"].parts["PART2_187K"].MaterialOrientation(r
egion=region,');
header4 = {'orientationType=DISCRETE, axis=AXIS_1,');
header5 = {'normalAxisDefinition=VECTOR,');
header6 = {'normalAxisVector=(' num2str(norm_vector1(ij,:)) ', '
num2str(norm_vector2(ij,:)) ',');
header7 = {'num2str(norm_vector3(ij,:)) '),
flipNormalDirection=False,');
header8 = {'normalAxisDirection=AXIS_1,');
header9 = {'primaryAxisDefinition=VECTOR,');
header10 = {'primaryAxisVector=(' num2str(primary_vector1(ij,:))
',');
header11 = {'num2str(primary_vector2(ij,:)) ', '
num2str(primary_vector3(ij,:)) '),');
header12 = {'primaryAxisDirection=AXIS_3,');
header13 = {'flipPrimaryDirection=False,');
header14 = {'additionalRotationType=ROTATION_NONE,');
header15 = {'angle=0.0, additionalRotationField="",');
header16 = {'stackDirection=STACK_3)');
header17 = {'#: Specified material orientation has been assigned to
the selected regions.}';
dlmwrite(dlmname, header1, 'delimiter', ',', '-append');
dlmwrite(dlmname, header2, 'delimiter', ',', '-append');
dlmwrite(dlmname, header3, 'delimiter', ',', '-append');
dlmwrite(dlmname, header4, 'delimiter', ',', '-append');
dlmwrite(dlmname, header5, 'delimiter', ',', '-append');
dlmwrite(dlmname, header6, 'delimiter', ',', '-append');
dlmwrite(dlmname, header7, 'delimiter', ',', '-append');
dlmwrite(dlmname, header8, 'delimiter', ',', '-append');
dlmwrite(dlmname, header9, 'delimiter', ',', '-append');
dlmwrite(dlmname, header10, 'delimiter', ',', '-append');
dlmwrite(dlmname, header11, 'delimiter', ',', '-append');
dlmwrite(dlmname, header12, 'delimiter', ',', '-append');
dlmwrite(dlmname, header13, 'delimiter', ',', '-append');
dlmwrite(dlmname, header14, 'delimiter', ',', '-append');
dlmwrite(dlmname, header15, 'delimiter', ',', '-append');
dlmwrite(dlmname, header16, 'delimiter', ',', '-append');
dlmwrite(dlmname, header17, 'delimiter', ',', '-append');
end

```

## APPENDIX I

---

Matlab code for FE models. Creates cubes made of elements with the same three-dimensional coordinates as in chapter 4 and then associates each cube with the correct orthotropic orientations.

```
load('Eigens.mat','ALL_COORDS','Yrotate1','Yrotate2','Yrotate3');
load('fea_orient.mat','nodes','elements');
abaqus_coords = (ALL_COORDS/2)*10; %convert cube_coords to mm's
ab_c_x = abaqus_coords(:,1);
ab_c_y = abaqus_coords(:,2);
ab_c_z = abaqus_coords(:,3);
ab_c_x2 = ab_c_x-5;
ab_c_y2 = ab_c_y-5;
ab_c_z2 = ab_c_z-5;
for i=1:length(ab_c_x)
    plotcube([5 5 5],[ab_c_x2(i) ab_c_y2(i) ab_c_z2(i)],.8,[1 1 1]);
    axis equal;
    ((:,:,i)) = [ab_c_x(i) ab_c_y(i) ab_c_z(i)];
end
handles = get(gca,'children');
vertices = get(handles,'Vertices');
vertices2 = cell2mat(vertices);
vertices3 = reshape(vertices2, 24, [], 3);
vert = permute(vertices3,[1 3 2]);
elements = elements(:,2:11);
nodes1 = nodes(:,2:4);
minbounds = min(vert);
maxbounds = max(vert);
isinbounds = all(bsxfun(@gt, nodes1, minbounds) & bsxfun(@lt,
nodes1, maxbounds), 2);
for i = 1:size(isinbounds,3)
    Elset = find(isinbounds(:,:,i));
    textfilename = ['nodes_set' num2str(i) '.txt'];
    fileID = fopen(textfilename,'w');
    fprintf(fileID, '%d \r\n',Elset);
    fclose(fileID);
end
for j = 1:size(isinbounds,3)
    nodefilename = ['nodes_set' num2str(j) '.txt'];
    fileID = fopen(nodefilename,'r');
    formatSpec = '%d';
    nodes_file = fscanf(fileID,formatSpec);
    [Lia,LocB] = ismember(nodes_file,elements(:,1:10));
    elementfilename = ['element_set' num2str(j) '.txt'];
    fileID2 = fopen(elementfilename,'w');
    fprintf(fileID2, '%d \r\n',LocB);
    fclose(fileID2);
    fclose(fileID);
    fclose all;
end
lengthy = length(elements);
for k = 1:size(isinbounds,3)
    elfilename = ['element_set' num2str(k) '.txt'];
    [fid, message] = fopen(elfilename);
    elements_file = fscanf(fid,formatSpec);
        for ij = 1:length(elements_file)
            if any(elements_file(ij)>lengthy) &&
any(elements_file(ij)<lengthy*2)
                elements_file(ij) = elements_file(ij)-(lengthy);
            end
        end
    end
end
```

```

        elseif any(elements_file(ij)>lengthy*2) &&
any(elements_file(ij)<lengthy*3)
        elements_file(ij) = elements_file(ij)-(lengthy*2);
        elseif any(elements_file(ij)>lengthy*3) &&
any(elements_file(ij)<lengthy*4)
        elements_file(ij) = elements_file(ij)-(lengthy*3);
        elseif any(elements_file(ij)>lengthy*4) &&
any(elements_file(ij)<lengthy*5)
        elements_file(ij) = elements_file(ij)-(lengthy*4);
        elseif any(elements_file(ij)>lengthy*5) &&
any(elements_file(ij)<lengthy*6)
        elements_file(ij) = elements_file(ij)-(lengthy*5);
        elseif any(elements_file(ij)>lengthy*6) &&
any(elements_file(ij)<lengthy*7)
        elements_file(ij) = elements_file(ij)-(lengthy*6);
        elseif any(elements_file(ij)>lengthy*7) &&
any(elements_file(ij)<lengthy*8)
        elements_file(ij) = elements_file(ij)-(lengthy*7);
        elseif any(elements_file(ij)>lengthy*8) &&
any(elements_file(ij)<lengthy*9)
        elements_file(ij) = elements_file(ij)-(lengthy*8);
        elseif any(elements_file(ij)>lengthy*9) &&
any(elements_file(ij)<lengthy*10)
        elements_file(ij) = elements_file(ij)-(lengthy*9);
    end
end
    dlmname = ['Final_element_set' num2str(k) '.dat']
    dlmname2 = 'Final_element_set_all.dat';
    fclose(fid);
    dlmwrite(dlmname, elements_file, 'delimiter', ',', 'precision', 8, '-
append');
    dlmwrite(dlmname2, elements_file, 'precision', 8, '-
append', 'roffset', 1);
end
for ii = 201:length(ALL_COORDS)+200
    dlmname3 = 'Input_commands.inp';
    header={'*Elset, elset=CALIBRATED_210_FINAL_VOLUME'
num2str(ii)};
    header2={'*Include, input=Final_element_set' num2str(ii-200)
'.dat'};
    dlmwrite(dlmname3, header, 'delimiter', ',', '-append');
    dlmwrite(dlmname3, header2, 'delimiter', ',', '-append');
end
for j = 1:length(ALL_COORDS)
    nodefilename = ['nodes_set' num2str(j) '.txt'];
    fileID = fopen(nodefilename, 'r');
    formatSpec = '%d';
    nodes_file = fscanf(fileID, formatSpec);
    node_coords2(j) = nodes_file(1, :);
    fclose(fileID);
end
node_coords2 = node_coords2';
node_coords3 = nodes1(node_coords2, :);
node_coords3 = (node_coords3*2)/10;
node_coords4 = ceil(node_coords3);
Yrotate_all = [Yrotate1 Yrotate2 Yrotate3];
old_positions = [ALL_COORDS Yrotate_all];
[Lia, LocB] = ismember(node_coords4, ALL_COORDS, 'rows');
new_positions = old_positions(LocB, :);

```